

Abstract

Measurement of (π^- -Ar) and (K^+ -Ar) total hadronic cross sections in the LArIAT experiment

Elena Gramellini

2018

The Liquid Argon Time Projection Chamber (LArTPC) represents one of the most advanced experimental technologies for physics at the Intensity Frontier due to its full 3D-imaging, excellent particle identification and precise calorimetric energy reconstruction. By deploying a LArTPC in a dedicated calibration test beam line at Fermilab, LArIAT (Liquid Argon In A Testbeam) aims to experimentally calibrate this technology in a controlled environment and to provide physics results key to the neutrino oscillation physics and proton decay searches of the Short Baseline Neutrino and Long Baseline Neutrino programs.

¹⁴ LArIAT's physics program entails a vast set of topics with a particular focus on
¹⁵ the study of nuclear effects such as pion and kaon characteristic interaction modes.

This thesis presents two world's first measurements: the measurement of (π^- -Ar) total hadronic cross section in the 100-1050 MeV kinetic energy range and the measurement of the (K^+ -Ar) total hadronic cross section in the 100-650 MeV kinetic energy range. The analyses devised for these measurements use both the core elements of LArIAT: beamline and TPC. The first step in each analysis is the development of an event selection based on beamline and TPC information geared towards the identification of the hadron of interest. We then proceed to match the beamline candidate to a suitable TPC track. Finally, we apply the “thin slice method” technique and measure the cross section, correcting for background and detector effects. The thin slice technique is a new method to measure hadron-argon cross sections possible only thanks to the combination of the tracking and calorimetry capability of the

27 LArTPC technology. Albeit never on argon, the hadronic cross section of pions has
28 been measured before on several different elements in thin target experiments, leading
29 to solid predictions in the argon case. Through the use of a different technique, our
30 measurement of the (π^- -Ar) total hadronic cross section is in general agreement with
31 the prediction by the Geant4 Bertini Cascade model which are based on data from
32 thin target experiments. On the contrary, cross section measurements for kaons are
33 extremely rare, thus more difficult to model. Not surprisingly, our measurement of
34 the (K^+ -Ar) total hadronic cross section is mostly in disagreement with the Geant4
35 prediction.

36 This thesis also reports two ancillary detector physics measurements necessary
37 for the cross section analyses: the measurements of the LArIAT electric field and
38 calorimetry constants. We developed a technique to measure the LArIAT electric field
39 using cathode-anode piercing tracks with cosmic data. We applied a new technique
40 for the measurement of the calorimetry calibration constants based on the particles'
41 momentum measurement.

42 The (π^- -Ar) and the (K^+ -Ar) total hadronic cross measurements are the first
43 physics results of the LArIAT experiment and will be the basis for the future LArIAT
44 measurements of pion and kaon cross sections in the exclusive channels.

45 **Measurement of (π^- -Ar) and (K^+ -Ar)**

46 **total hadronic cross sections in the**

47 **LArIAT experiment**

48 A Dissertation
49 Presented to the Faculty of the Graduate School
50 of
51 Yale University
52 in Candidacy for the Degree of
53 Doctor of Philosophy

54 by
55 Elena Gramellini

56 Dissertation Director: Bonnie T. Fleming

57 Date you'll receive your degree

58

Copyright © 2018 by Elena Gramellini

59

All rights reserved.

60

A mia mamma e mio babbo,

61

grazie per le radici e grazie per le ali.

62

To my mom and dad,

63

thank you for the roots and thank you for the wings.

⁶⁴ Contents

⁶⁵	Acknowledgements	viii
⁶⁶	Introduction	ix
⁶⁷	1 The theoretical framework	1
⁶⁸	1.1 The Standard Model	1
⁶⁹	1.2 Neutrinos: tiny cracks in the Standard Model	4
⁷⁰	1.2.1 Neutrinos in the Standard Model	4
⁷¹	1.2.2 Neutrino Oscillations	6
⁷²	1.2.3 Make up of Neutrino Interactions	7
⁷³	1.3 Beyond the Standard Model	9
⁷⁴	1.3.1 Open Questions in Neutrino Physics	11
⁷⁵	1.3.2 Towards a more fundamental theory: GUTs	15
⁷⁶	1.4 Motivations for Hadronic Cross Sections in Argon	18
⁷⁷	1.4.1 Pion-Argon Total Hadronic Cross Section	18
⁷⁸	1.4.2 Kaon-Argon Total Hadronic Cross Section	29
⁷⁹	2 Liquid Argon Detectors at the Intensity Frontier	34
⁸⁰	2.1 The Liquid Argon Time Projection Chamber Technology	34
⁸¹	2.1.1 TPCs, Neutrinos & Argon	35
⁸²	2.1.2 LArTPC: Principles of Operation	37

83	2.1.3	Liquid Argon: Ionization Charge	40
84	2.1.4	Liquid Argon: Scintillation Light	45
85	2.1.5	Signal Processing and Event Reconstruction	49
86	2.2	The Intensity Frontier Program	53
87	2.2.1	Prospects for LArTPCs in Neutrino Physics: SBN and DUNE	54
88	2.2.2	Prospects for LArTPCs in GUT Physics: DUNE	55
89	2.2.3	Enabling the next generation of discoveries: LArIAT	57
90	3	LArIAT: Liquid Argon In A Testbeam	60
91	3.1	The Particles' Path to LArIAT	60
92	3.2	LArIAT Tertiary Beam Instrumentation	62
93	3.2.1	Bending Magnets	63
94	3.2.2	Multi-Wire Proportional Chambers	65
95	3.2.3	Time-of-Flight System	67
96	3.2.4	Punch-Through and Muon Range Stack Instruments	68
97	3.2.5	LArIAT Cosmic Ray Paddle Detectors	70
98	3.3	In the Cryostat	71
99	3.3.1	Cryogenics and Argon Purity	71
100	3.3.2	LArTPC: Charge Collection	74
101	3.3.3	LArTPC: Light Collection System	77
102	3.4	Trigger and DAQ	80
103	3.5	Control Systems	81
104	4	Total Hadronic Cross Section Measurement Methodology	87
105	4.1	Event Selection	88
106	4.1.1	Selection of Beamline Events	88
107	4.1.2	Particle Identification in the Beamline	89
108	4.1.3	TPC Selection: Halo Mitigation	89

109	4.1.4	TPC Selection: Shower Removal	90
110	4.2	Beamline and TPC Handshake: the Wire Chamber to TPC Match . .	91
111	4.3	The Thin Slice Method	93
112	4.3.1	Cross Sections on Thin Target	93
113	4.3.2	Not-so-Thin Target: Slicing the Liquid Argon Volume	94
114	4.3.3	Corrections to the Raw Cross Section	96
115	4.4	Procedure testing with MC truth quantities	98
116	5	Data and MC preparation for the Cross Section Measurements	100
117	5.1	Cross Section Analyses Data Sets	100
118	5.2	Construction of a Monte Carlo Simulation for LArIAT	102
119	5.2.1	G4Beamline	102
120	5.2.2	Data Driven MC	106
121	5.3	Estimate of Backgrounds in the Pion Cross Section	108
122	5.3.1	Background from Pion Capture and Decay	110
123	5.3.2	Contributions from the Beamline Background	113
124	5.4	Estimate of Energy Loss before the TPC	117
125	5.5	Tracking Studies	119
126	5.5.1	Angular Resolution	121
127	5.6	Calorimetry Studies	128
128	5.6.1	Kinetic Energy Measurement	128
129	6	Negative Pion Cross Section Measurement	131
130	6.1	Raw Cross Section	131
131	6.1.1	Statistical Uncertainty	133
132	6.1.2	Treatment of Systematics	135
133	6.2	Corrections to the Raw Cross Section	136
134	6.2.1	Background subtraction	137

¹³⁵	6.2.2 Correction for Reconstruction Effects	138
¹³⁶	6.3 Results	144
¹³⁷	7 Positive Kaon Cross Section Measurement	146
¹³⁸	7.1 Raw Cross Section	146
¹³⁹	7.2 Corrections to the Raw Cross Section	148
¹⁴⁰	7.3 Results	150
¹⁴¹	8 Conclusions	153
¹⁴²	A Measurement of LArIAT Electric Field	155
¹⁴³	B Additional Tracking Studies for LArIAT Cross Section Analyses	163
¹⁴⁴	B.0.1 Study of WC to TPC Match	164
¹⁴⁵	B.0.2 Tracking Optimization	166
¹⁴⁶	C Energy Calibration	169

¹⁴⁷ Acknowledgements

¹⁴⁸

“Dunque io ringrazio tutti quanti.

¹⁴⁹

Specie la mia mamma che mi ha fatto così funky.”

¹⁵⁰

– Articolo 31, Tanqi Funky, 1996 –

¹⁵¹

“At last, I thank everyone.

¹⁵²

Especially my mom who made me so funky.”

¹⁵³

– Articolo 31, Tanqi Funky, 1996 –

¹⁵⁴

A lot of people are awesome, especially you, since you probably agreed to read
this when it was a draft.

¹⁵⁶

‘

¹⁵⁷ Introduction

¹⁵⁸ This thesis work concerns the first measurement of the (π^- -Ar) total hadronic cross
¹⁵⁹ section in the 100-1000 MeV kinetic energy range and the first measurement of the
¹⁶⁰ (K^+ -Ar) total hadronic cross section in the 100-650 MeV kinetic energy range. We
¹⁶¹ performed these measurements at the LArIAT experiment, a small (0.25 ton) Liquid
¹⁶² Argon Time Projection Chamber (LArTPC) on a beam of charged particles at the
¹⁶³ Fermilab Test Beam Facility. Albeit particle and nuclear physics have a long history
¹⁶⁴ of hadronic cross section measurements, the work outlined in this thesis presents a
¹⁶⁵ new methodology – the “thin slice method” – for cross section measurements in argon,
¹⁶⁶ possible only thanks to the detection capabilities of the LArTPC technology. The
¹⁶⁷ combination of fine-grained tracking and excellent calorimetric information provided
¹⁶⁸ by the LArTPC technology allows to see unprecedented details of particle interactions
¹⁶⁹ in argon and, in LArIAT, to measure the kinetic energy of a hadron at each step
¹⁷⁰ of the tracking. A renewed interest for precision measurements of hadronic cross
¹⁷¹ sections, particularly in argon, arises from the current panorama of experimental
¹⁷² particle physics at the intensity frontier.

¹⁷³ The discovery of the Higgs boson in 2012 marked the triumph of the Standard
¹⁷⁴ Model of Particle Physics; exploring what lays beyond is the real challenge in our field
¹⁷⁵ today. Since their formulation in 1930, neutrinos have been a source of surprises (and
¹⁷⁶ Nobel Prizes) for particle physicists, tiny cracks in our understanding of Nature. In
¹⁷⁷ particular, the discovery of neutrino oscillation represents the first evidence of physics

178 Beyond the Standard Model (BSM). From a theoretical point of view, the field is
179 developing new theories to account for the small but non-zero mass of neutrinos,
180 while trying to remain consistent with the rest of the Standard Model. From an
181 experimental point of view, we are developing technologies and huge collaborations
182 to probe these theories. As we enter the era of precision measurements of neutrino
183 interaction, neutrinos might hold the key to the next generation of discoveries in
184 particle physics.

185 Experimentally, precision measurements can be achieved only if the detector tech-
186 nology is able to resolve the fine details of a neutrino interaction and to record a
187 statistically relevant number of neutrinos. With “fine details” here we mean the abil-
188 ity to distinguish the many products of the neutrino interaction, such as protons,
189 pions, muons and electrons, and to measure their energy. Historically, bubble cham-
190 ber neutrino detectors were the first revolution in neutrino detection: for example,
191 the spatial resolution of Gargamelle allowed the discovery of neutrino neutral current
192 interaction. Despite the high precision of bubble chambers images, this technology
193 is hard to scale to massive size, making statistical analyses on neutrino interactions
194 almost impossible to perform. To make up for the small neutrino interaction cross
195 section, neutrino experiments moved to very large size, at the expenses of spatial
196 precision. This is the case for the detectors which discovered neutrino oscillation:
197 both Super-Kamiokande and SNO are massive Cherenkov detectors. With LArT-
198 PCs, the field is gaining again bubble-chamber like precision but at massive scales.
199 Following the recommendations of the latest Particle Physics Project Prioritization
200 Panel [106], the US particle physics panorama is directing a substantial effort to-
201 wards the exploration of the intensity frontier through the construction of massive
202 LArTPCs. In particular, the near future will see the development of a Short Baseline
203 Neutrino Program (SBN) and long baseline neutrino program (DUNE), both based
204 on the LArTPC detector technology. The US liquid argon program has the potential

205 to answer many of the fundamental open questions in particle physics today, such
206 as: is there a fourth generation neutrino? is CP violated in the lepton sector? are
207 there any additional symmetries? and, can we find an indication of Grand Unified
208 Theories?

209 The SBN program at Fermilab is tasked with conclusively addressing the existence
210 of a fourth neutrino generation in the $\Delta m^2 = \Delta m_{14}^2 \sim [0.1 - 10] \text{ eV}^2$ parameter space.
211 The SBN program entails three surface LArTPCs positioned on the Booster Neutrino
212 Beam at different distances from the neutrino production in oder to fully exploit the
213 L/E dependence of the oscillation pattern: SBND (100 m from the decay pipe),
214 MicroBooNE (450 m), and ICARUS (600 m). SBN will also perform an extensive
215 program of neutrino cross section measurements, fundamental to abate systematics
216 in the oscillation analyses in both SBN and DUNE.

217 DUNE has a vast neutrino and non-accelerator physics reach. For what it concerns
218 neutrino physics, oscillation analyses in DUNE have the capability of solving the mass
219 hierarchy and octant problem, and discovering CP violation in the neutrino sector.
220 Besides its neutrino program, DUNE can open an experimental window on Grand
221 Unified Theories (GUTs). GUTs could potentially answer fundamental questions
222 such as the existence of non-zero neutrino masses and matter-antimatter asymmetry,
223 explaining some “accidents” in the Standard Models, such as the exact cancellation of
224 the proton and the electron charge. Directly probing GUTs at the unification energy
225 scale is impossible by any foreseeable collider experiment. We then need an indirect
226 proof such as baryon number violation, which is predicted by almost every GUT in the
227 form of proton decay, bounded nucleon decay or $n - \bar{n}$ oscillations on long time-scales.
228 Historically, the main technology used in these searches has been water Cherenkov
229 detectors, with Super-Kamiokande setting all the current experimental limits on the
230 decay lifetimes at the order of $\sim 10^{34}$ years. The DUNE far detector and its non-
231 accelerator physics program is a interesting new actor on this stage. LArTPCs can in

fact complement nucleon decay searches in modes where water Cherenkov detectors are less sensitive, especially $p \rightarrow K^+ \bar{\nu}$ [11].

Such a diverse physics program speaks to the versatility of the LArTPC technology. LArTPCs provide excellent electron/photon separation [9] lacking in Cherenkov detectors which can be leveraged to abate the photon background from neutral current interactions in ν_e searches. LArTPCs also share superb tracking capability with bubble chamber detectors, with several additional benefits. They are electronically read out and self triggered detectors; they provide full 3D-imaging with millimeter resolution, precise calorimetric reconstruction and excellent particle identification.

The amount of information a LArTPC can provide makes these detectors rather complex: a series of dedicated measurements is necessary to obtain meaningful physics results from a LArTPC. The complexity of the LArTPC technology for neutrino detection is due to several reasons. Argon is a fairly heavy element, which means that nuclear effects play an important role in the looks of the interaction topology. For example, pions are one of the main products of neutrino interactions; yet, since data on charged particle interaction in argon is scarce, neutrino event generators have big uncertainties in the re-scattering simulation of pion in argon. The amount of details in an LArTPC event is easily parsed by human eye, but can make automatic event reconstruction rather challenging. Thus, reconstruction algorithms in LArTPC need to be tune to recognize the different topologies of the neutrino interaction products in argon. This is particularly true for pions, since they are an abundant product of the neutrino interactions: the occurrence of a pion interaction in argon can modify the topology of the neutrino event, causing a misidentification of the neutrino interaction.

The LArIAT [38] experiment is performing precise cross section measurements of charged particles in argon to bridge this gap of knowledge. The LArIAT LArTPC sits on a beam of charged particles at the Fermilab Test Beam Facility which provides charge particles of the type and energy range relevant for neutrino interaction of

259 both SBN and DUNE. The (π^- -Ar) hadronic cross section is a fundamental input for
260 neutrino detectors in liquid argon, as pion interactions can modify the topology and
261 energy reconstruction of neutrino events in the GeV range, where pion production
262 is abundant. The (K^+ -Ar) total hadronic differential cross section in LArIAT is
263 particularly relevant for a high identification efficiency in the context of proton decay
264 searches in DUNE in the $p \rightarrow K^+ \bar{\nu}$ channel. In fact, the kaon-argon cross section
265 affects the kaon topology by modifying the kaon tracking and energy reconstruction,
266 impacting the basis for kaon identification in a LArTPC.

267 The cross section analyses exploit the totality of LArIAT’s experimental handles;
268 they rely on beam line detector information as well as both calorimetry and tracking
269 in the TPC. These analyses are LArIAT’s first physics results. In order to measure
270 total hadronic argon cross sections, several steps are necessary. The analyses start by
271 identifying a sample of the hadron of interest in the beam line and assessing the beam
272 line contaminations. It proceeds with tracking the hadron candidates in the TPC and
273 measuring their kinetic energy at each point in the tracking: the fine sampling of an
274 hadron in the TPC forms the set of “incident” hadrons. Then, the hadronic interac-
275 tion point is identified and the raw cross section is calculated. Two corrections are
276 then applied to the raw cross section – a background subtraction and a correction
277 for detector effects – to obtain the true cross section measurement.

278

279 This body of work is organized in 8 chapters. We provide a description of the
280 theoretical framework for the measurements in Chapter 1. Chapter 2 outlines the
281 LArTPC detector technology, while Chapter 3 describes LArIAT experimental setup.
282 We present the event selection for both the pion and kaon analyses, as well as the
283 “thin slice method” in Chapter 4. Chapter 5 describes the work done on the data
284 and Monte Carlo samples in preparation of the cross section analyses. Chapter 6
285 shows the results for the (π^- -Ar) total hadronic cross section measurement. Chapter

²⁸⁶ 7 shows the results for the (K^+ -Ar) total hadronic cross section measurement. We
²⁸⁷ draw the final remarks on this work in Chapter 8

²⁸⁸ A series of additional studies and calibrations were necessary to perform the cross
²⁸⁹ section analyses. Appendix A shows a measurement of the LArIAT LArTPC electric
²⁹⁰ field using cosmic data. Appendix B shows an optimization of the tracking algorithms
²⁹¹ geared towards maximizing the efficiency of finding the hadronic interaction point.
²⁹² Appendix C shows the calorimetry calibration of the LArIAT LArTPC, which is a
²⁹³ pivotal measurement to enable any physics analysis with TPC data.

²⁹⁴ **Chapter 1**

²⁹⁵ **The theoretical framework**



²⁹⁶

– J. S. Bach, 1720 ca. –

²⁹⁷ In this chapter, we set the (π^- - Ar) and (K^+ - Ar) total hadronic cross section
²⁹⁸ measurements into the greater theoretical and phenomenological framework. We start
²⁹⁹ by briefly describing the Standard Model (Section 1.1), with particular attention to
³⁰⁰ neutrinos and neutrino interactions (Section 1.2). We then describe some of the
³⁰¹ open questions in neutrino physics today and Beyond Standard Model theories (1.3)
³⁰² setting the stage for the measurements reported in this work (Section 1.4).

³⁰³ **1.1 The Standard Model**

³⁰⁴ The Standard Model (SM) of particle physics is the most accurate theoretical descrip-
³⁰⁵ tion of the subatomic world and, in general, one of the most precisely tested theories
³⁰⁶ in the history of physics. The SM describes the strong, electromagnetic and weak
³⁰⁷ interactions among elementary particles in the framework of quantum field theory,

308 accounting for the unification of electromagnetic and weak interactions for energies
309 above the vacuum expectation value (VEV) of the Higgs field. The SM does not
310 describe gravity or general relativity.

311 The Standard Model is a gauge theory based on the local symmetry group

$$G_{SM} = SU(3)_C \otimes SU(2)_L \otimes U(1)_Y \quad (1.1)$$

312 where the subscripts C indicates the conserved strong charge (color), and the
313 subscripts Y indicates the conserved hypercharge. If we indicated with T the weak
314 isospin T and with T3 its third component, hypercharge can be related to the electric
315 charge Q through the Gell-Mann-Nishijima relation:

$$Q = \frac{Y}{2} + T_3. \quad (1.2)$$

316 In the quantum field framework, the SM fields correspond to the irreducible rep-
317 resentations of the G_{SM} symmetry group. In particular, the particles are divided in
318 two categories, fermions and bosons, according to their spin-statistics. Described by
319 the Fermi-Dirac statistics, fermions have half-integer spin and are sometimes called
320 “matter-particles”. Bosons or “force carriers” have integer spin, follow the Bose-
321 Einstein statistics and mediate the interaction between fermions. The fundamental
322 fermions and their quantum numbers are listed in Tab 1.1.

323 Quarks can interact via all three the fundamental forces; they are triplets of
324 $SU(3)_C$, that is they can exist in three different colors. If one chooses a base where
325 u , c and t quarks are simultaneously eigenstates of both the strong and the weak
326 interactions, the remaining eigenstates are usually written as d , s and b for the strong
327 interaction and d' , s' and b' for the weak interaction, because the latter ones are
328 the result of a CKM rotation on the first ones. Charged leptons interact via the
329 weak and the electromagnetic forces, while neutrinos only interact via the weak force.

Generation	I	II	III	T	Y	Q
Leptons	$\begin{pmatrix} \nu_e \\ e \end{pmatrix}_L$	$\begin{pmatrix} \nu_\mu \\ \mu \end{pmatrix}_L$	$\begin{pmatrix} \nu_\tau \\ \tau \end{pmatrix}_L$	1/2 -1/2	-1 -1	0 -1
	e_R	μ_R	τ_R	0	-2	1
Quarks	$\begin{pmatrix} u \\ d' \end{pmatrix}_L$	$\begin{pmatrix} c \\ s' \end{pmatrix}_L$	$\begin{pmatrix} t \\ b' \end{pmatrix}_L$	1/2 -1/2	1/3 1/3	2/3 -1/3
	u_R d'_R	c_R s'_R	t_R b'_R	0 0	4/3 -2/3	2/3 -1/3

Table 1.1: SM elementary fermionic fields. The subscripts L and R indicate respectively the negative chirality (left-handed) and the positive chirality (right-handed).

- 330 The gauge group univocally determines the number of gauge bosons that carry the
 331 interaction; the gauge bosons correspond to the generators of the group: eight gluons
 332 (g) for the strong interaction, one photon (γ) and three bosons (W^\pm , Z^0) for the
 333 electroweak interaction. A gauge theory by itself cannot provide a description of
 334 massive particles, but it is experimentally well known that most of the elementary
 335 particles have non-zero masses. The introduction of massive fields in the Standard
 336 Model lagrangian would make the theory not gauge invariant, resulting ill-defined.
 337 This problem is solved in the SM by the introduction of a scalar iso-doublet $\Phi(x)$, the
 338 Higgs field, which gives mass to W^\pm and Z^0 gauge bosons through the electroweak
 339 symmetry breaking mechanism and to the fermions through Yukawa coupling [75, 76].
 340 The discovery of the Higgs boson in 2012 by the LHC experiments [41, 42] marked
 341 the ultimate confirmation of a long history of successful predictions by the SM.

342 1.2 Neutrinos: tiny cracks in the Standard Model

343 To our current knowledge, neutrinos are the most abundant fermion in the Universe.
344 And yet, they are maybe the most mysterious particle in the SM: they generate
345 theoretical puzzles and experimental challenges. In this section, we treat neutrinos
346 within and beyond the SM and describe the make up of their interaction with matter.

347 1.2.1 Neutrinos in the Standard Model

348 Neutrino can be introduced in the SM as left-handed massless Weyl spinors. The
349 Dirac equation of motion for a free field

$$(i\gamma^\mu \partial_\mu - m)\psi = 0 \quad (1.3)$$

350 for a fermionic field

$$\psi = \psi_L + \psi_R \quad (1.4)$$

351 is equivalent to the equations

$$i\gamma^\mu \partial_\mu \psi_L = m\psi_R \quad (1.5)$$

352

$$i\gamma^\mu \partial_\mu \psi_R = m\psi_L \quad (1.6)$$

353 for the chiral fields ψ_R and ψ_L , whose evolution in space and time is coupled
354 through the mass m . If the fermion is massless, the chiral fields decouple and the
355 fermion can be described by a single Weyl spinor with two independent compo-
356 nents [116]. Pauli initially rejected the description of a physical particle through
357 a single Weyl spinor because of its implication of parity violation. In fact, since
358 the spatial inversion operator throws $\psi_R \leftrightarrow \psi_L$, parity is conserved only if both chi-
359 ral components exist at the same time. For the neutrino introduction in the SM,
360 experiments came in help of the theoretical description. The constraint of parity

³⁶¹ conservation weakened after Wu's experiment in 1957 [119]. Additionally, there was
³⁶² no experimental indication for massive neutrinos, nor evidence of interaction via the
³⁶³ neutrino right-handed component.

³⁶⁴ The symmetry group $SU(2)_L \otimes U(1)_Y$ is the only group relevant for neutrino
³⁶⁵ interactions. The SM electroweak lagrangian is the most general renormalizable la-
³⁶⁶ grangian invariant under the local symmetry group $SU(2)_L \otimes U(1)_Y$. The lagrangian
³⁶⁷ couples the weak isotopic spin doublets and singlets described in Table 1.1 with the
³⁶⁸ gauge bosons A_a^μ ($a = 1, 2, 3$) and B^μ , and Higgs doublet $\Phi(x)$:

$$\begin{aligned} \mathcal{L} = & i \sum_{\alpha=e,\mu,\tau} \bar{L}'_{\alpha L} \not{\partial} L'_{\alpha L} + i \sum_{\alpha=1,2,3} \bar{Q}'_{\alpha L} \not{\partial} Q'_{\alpha L} \\ & + i \sum_{\alpha=e,\mu,\tau} \bar{l}'_{\alpha R} \not{\partial} l'_{\alpha R} + i \sum_{\alpha=d,s,b} \bar{q}'^D_{\alpha R} \not{\partial} q'^D_{\alpha R} + i \sum_{\alpha=u,c,t} \bar{q}'^U_{\alpha R} \not{\partial} q'^U_{\alpha R} \\ & - \frac{1}{4} A_{\mu\nu} A^{\mu\nu} - \frac{1}{4} B_{\mu\nu} B^{\mu\nu} \\ & + (D_\rho \Phi)^\dagger (D^\rho \Phi) - \mu^2 \Phi^\dagger \Phi - \lambda (\Phi^\dagger \Phi)^2 \\ & - \sum_{\alpha,\beta=e,\mu,\tau} \left(Y_{\alpha\beta}^l \bar{L}'_{\alpha L} \Phi l'_{\beta R} + Y_{\alpha\beta}^{l*} \bar{l}'_{\beta R} \Phi^\dagger L'_{\alpha L} \right) \\ & - \sum_{\alpha=1,2,3} \sum_{\beta=d,s,b} \left(Y_{\alpha\beta}^D \bar{Q}'_{\alpha L} \Phi q'^D_{\beta R} + Y_{\alpha\beta}^{D*} \bar{q}'^D_{\beta R} \Phi^\dagger Q'_{\alpha L} \right) \\ & - \sum_{\alpha=1,2,3} \sum_{\beta=u,c,t} \left(Y_{\alpha\beta}^U \bar{Q}'_{\alpha L} \tilde{\Phi} q'^U_{\beta R} + Y_{\alpha\beta}^{U*} \bar{q}'^U_{\beta R} \tilde{\Phi}^\dagger Q'_{\alpha L} \right). \end{aligned} \quad (1.7)$$

³⁶⁹ The first two lines of the lagrangian summarize the kinetic terms for the fermionic
³⁷⁰ fields and their coupling to the gauge bosons $A_a^{\mu\nu}$, $B^{\mu\nu}$ ¹. The third line describes
³⁷¹ the kinetic terms and the self-coupling terms of the gauge bosons. The forth line is
³⁷² the Higgs lagrangian, which results in the spontaneous symmetry breaking. The last
³⁷³ three lines describe the Yukawa coupling between fermions and the Higgs field, origin
³⁷⁴ of the fermions' mass.

1. In gauge theories the ordinary derivative ∂_μ is substituted with the covariant derivative D_μ . Here $D_\mu = \partial_\mu + igA_\mu \cdot I + ig'B_\mu \frac{Y}{2}$, where I and Y are the $SU(2)_L$ and $U(1)_Y$ generators, respectively.

375 The coupling between left-handed and right-handed field generates the mass term
376 for fermions. The SM assumes only left-handed components for neutrinos, thus im-
377 plying zero neutrino mass. Since any linear combination of massless fields results in a
378 massless field, the flavor eigenstates are identical to the mass eigenstates in the SM.

379 1.2.2 Neutrino Oscillations

380 The determination of the flavor of a neutrino dynamically arises from the correspond-
381 ing charged lepton associated in a change current interaction; for example, a ν_e is a
382 neutrino which produces an e^- , a $\bar{\nu}_\mu$ is a neutrino which produces a μ^+ , *etc.* The
383 neutrino flavor eigenstates $|\nu_\alpha\rangle$, with $\alpha = e, \mu, \tau$, are orthogonal to each other and
384 form a base for the weak interaction matrix.

385 Overwhelming experimental data show that neutrinos change flavor during their
386 propagation [101]. This phenomenon, called “neutrino oscillations”, was predicted
387 first by Bruno Pontecorvo in 1957 [102]. Neutrino oscillations are possible only if
388 the neutrino flavor eigenstate are not identical to the mass eigenstates. Thus, the
389 observation of neutrino oscillation results in the first evidence of physics beyond the
390 Standard Model. A minimal extension of the SM introduces three mass eigenstates,
391 $|\nu_i\rangle$ ($i = 1, 2, 3$), whose mass m_i is well defined. The unitary Pontecorvo-Maki-
392 Nakagawa-Sakata matrix transforms the mass base into the flavor base as follows

$$|\nu_\alpha\rangle = U_{PMNS} |\nu_i\rangle, \quad (1.8)$$

393 with

$$U_{PMNS} = \begin{bmatrix} c_{12} & s_{12} & 0 \\ -s_{12} & c_{12} & 0 \\ 0 & 0 & 1 \end{bmatrix} \begin{bmatrix} c_{13} & 0 & s_{13}e^{-i\delta} \\ 0 & 1 & 0 \\ -s_{13}e^{-i\delta} & 0 & c_{13} \end{bmatrix} \begin{bmatrix} 1 & 0 & 0 \\ 0 & c_{23} & s_{23} \\ 0 & -s_{23} & c_{23} \end{bmatrix} \begin{bmatrix} e^{i\alpha_1} & 0 & 0 \\ 0 & e^{i\alpha_2} & 0 \\ 0 & 0 & 1 \end{bmatrix} \quad (1.9)$$

394 where c e s stand respectively for cosine and sine of the corresponding mixing
 395 angles (θ_{12} , θ_{23} and θ_{13}), δ is the Dirac CP violation phase, α_1 and α_2 are the eventual
 396 Majorana CP violation phases. Experimental results on neutrino oscillations are
 397 generally reported in terms of the mixing angles and of the squared mass splitting
 398 $\Delta m_{ab}^2 = m_a^2 - m_b^2$, where a and b represent the mass eigenstates. A summary of the
 399 current status of experimental results, albeit partial, is given in table 1.2.

Table 1.2: Summary of experimental results on neutrino oscillation parameters. **ADD CITATIONS**

	Value	Precision	Experiment
θ_{23}	45°	9.0%	Super Kamiokande, MINOS,
$-\Delta m_{32}^2$	$2.5 \cdot 10^{-3} \text{ eV}^2$	1.8%	Nova, MACRO
θ_{12}	34°	5.8%	SNO, Gallex,
$-\Delta m_{12}^2$	$7.4 \cdot 10^{-5} \text{ eV}^2$	2.8%	SAGE, KamLAND
θ_{13}	9°	4.7%	DAYA Bay,
$-\Delta m_{32}^2$	$2.5 \cdot 10^{-3} \text{ eV}^2$	1.8%	RENO

400 1.2.3 Make up of Neutrino Interactions

401 All neutrino experiments involving the detection of single neutrinos are concerned
 402 with neutrino interactions (and neutrino cross sections) on nuclei. Given the invisible
 403 nature of the neutrino, characterizing the products of its interaction is the only
 404 method to a) assess the neutrino presence, b) detect its flavor in case of a charge
 405 current interaction and c) eventually reconstruct its energy.

406 Historically, neutrino interactions with the nucleus in the GeV region are divided
 407 into three categories into three categories whose contributions change as a function

408 of increasing neutrino energy:: quasi elastic (QE), resonant (RES), and deep inelastic
409 (DIS) scattering. All current and forthcoming oscillation experiments on neutrino
410 beams live in the 0.1-10 GeV transition region, which encompasses the energy where
411 the QE neutrino-nucleus interaction transitions into RES and then into DIS. For
412 scattering off free nucleons, neutrino and antineutrino QE charge current scattering
413 refers to the process $\nu_l n \rightarrow l^- p$ and $\bar{\nu}_l p \rightarrow l^+ n$ where a charged lepton and single
414 nucleon are ejected in the elastic interaction. Resonant scattering refers to an inelas-
415 tic collision producing a nucleon excited state (Δ, N^*) – the resonance – which then
416 quickly decays, most often to a nucleon and single-pion final state. DIS refers to the
417 head-on collision between the neutrino and a parton inside the nucleon, producing
418 hadronization and subsequent abundant production of mesons and nucleons. In addi-
419 tion to such interactions between the neutrino and a single component of the nucleus,
420 neutrinos can also interact with the nucleus as a whole, albeit more rarely, a well
421 documented process called coherent meson production scattering [58]; the signature
422 of such process is the production of a distinctly forward-scattered single meson final
423 state, most often a pion. This simple picture of neutrino interactions works rather
424 well for scattering off of light nuclear targets, such as the H₂ and D₂ of bubble cham-
425 ber experiments [64], but the complexity of the nuclear structure for heavier nuclei
426 such as argon complicates this model.

427 As we will discuss in Chapter 2, the properties of argon make it a good candidate
428 for an interacting medium in neutrino experiments; in particular the density of its
429 interaction centers increases the yield of neutrino interactions and allows for relatively
430 compact detectors. Though, the choice of a relatively heavy nuclear target comes at
431 the cost of enhancing nuclear effects which modify the kinematic and final state of
432 the neutrino interaction products.

433 Nuclear effects can potentially affect neutrino event rates, final state particle emis-
434 sion, neutrino energy reconstruction, and the neutrino/antineutrino ratios, carrying

435 deep implications for oscillation experiments. Even in the case of “simple” QE scat-
436 tering, intra-nuclear hadron rescattering and correlation effects between the target
437 nucleons can cause the ejection of additional nucleons in the final state, modifying
438 the final state kinematics and topology. In the case of resonant and DIS scattering,
439 the hadronic interactions of meson and nucleons produced in the decay of the res-
440 onance or during hadronization complicate this picture even more. A large source
441 of uncertainty in modeling nuclear effects in neutrino interactions come from mesons
442 interactions (and re-interactions) in the nucleus, e.g., pion re-scattering, charge ex-
443 change, and absorption.

444 A renewed interest for neutrino cross section measurements surged in recent years,
445 along with a lively discussion on the data reporting; the historical method of reporting
446 the neutrino cross section as a function of the neutrino energy or momentum trans-
447 fered shakes under the weight of its dependency on the chosen nuclear model. On one
448 hand, correcting for nuclear effects in neutrino interaction can introduce unwanted
449 sources of uncertainty and model dependency especially due to the mis-modeling of
450 the meson interactions. On the other, avoiding this correction makes a comparison
451 between neutrino interactions on different target nuclei extremely difficult.

452 Data on neutrino scattering off many different nuclei are available for both charged
453 current (CC) and neutral current (NC) channels, as summarized in [64]. A summary
454 of the results on QE, resonant and DIS scattering for neutrinos and antineutrinos from
455 accelerators on different target is reported in Figure 1.1, where the (NUANCE) [37]
456 event generator is used as comparison with the theory.

457 1.3 Beyond the Standard Model

458 The discovery of neutrino oscillation and its implication of non-zero neutrino mass
459 mark the beginning of a new, exciting era in neutrino physics: the era of physics Be-

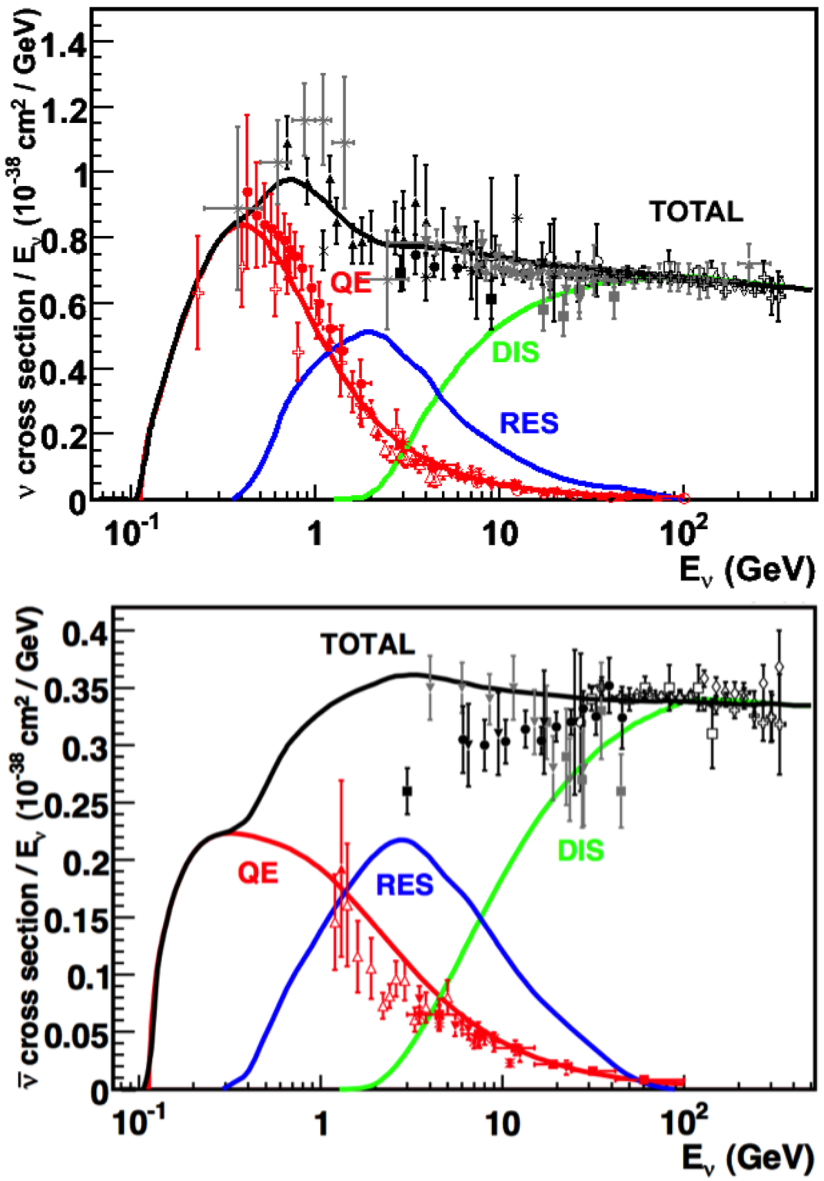


Figure 1.1: Total neutrino (top) and antineutrino (bottom) CC cross sections per nucleon divided by neutrino energy as a function of energy as reported in [64]. Predictions for the total (black), the QE (red), resonant (blue) and DIS (green) are provided by the NUANCE generator. The quasi-elastic scattering data and predictions have been averaged over neutron and proton targets (isoscalar target).

460 yond the Standard Model (BSM) at the intensity frontier. We are currently searching
461 for new, deeper theories that can accommodate neutrinos with tiny but non-zero
462 masses, while remaining consistent with the rest of the Standard Model.

463 **1.3.1 Open Questions in Neutrino Physics**

464 On one hand, the last three decades of experiments in neutrino oscillations brought
465 spectacular advancements in the understanding of the oscillations pattern, measuring
466 the neutrino mixing angles and mass splitting with a precision of less than 10%. On
467 the other, they opened the field for a series of questions needing experimental answers.

468 **Sterile neutrinos.** Hints to the existence of at least one additional neutrino,
469 in the form of various anomalies, have been puzzling physicists almost from the be-
470 ginning of neutrino oscillation searches. Originally designed to look for evidence of
471 neutrino oscillation, the Liquid Scintillator Neutrino Detector (LSND) [54] provided
472 a first conflicting result with the Standard Model expectation of only three neutrinos.
473 A second conflicting result has also been provided by the MiniBooNE experiment [50].

474 The LSND and MiniBooNE ν_e and $\bar{\nu}_e$ appearance results, known as the “LSND and
475 MiniBooNE anomalies” [14, 15, 23], may be interpreted under the assumption of a new
476 right-handed neutrino. The additional neutrino needs to be “sterile”, i.e needs not
477 to couple with the electroweak force carriers, in order to meet the constraint imposed
478 by the measurement of the width of the Z boson [2]. The new sterile neutrino would
479 mainly be composed of a heavy neutrino ν_4 with mass m_4 such that $m_1, m_2, m_3 \ll m_4$
480 and $\Delta m^2 = \Delta m_{14}^2 \sim [0.1 - 10]$ eV². The introduction of sterile neutrinos is an ap-
481 pealing line of thinking, since this renormalizable generalization of the SM has the
482 potential to impact long standing questions in high energy physics and cosmology:
483 light sterile neutrinos are candidates for dark matter particles and there are ideas
484 that the theory could be adjusted to explain the baryon asymmetry of the Universe
485 via leptogenesis [71].

486 **CP Violation In Lepton Sector.** The measurement of non-zero value for the
 487 oscillation parameter θ_{13} allows the exploration of low-energy CP violation in the lep-
 488 ton sector at neutrino long baseline oscillation experiments, enabling the possibility
 489 to measure the Dirac CP-violating phase δ . Exciting theoretical results tie δ directly
 490 to the generation of the baryon asymmetry of the Universe at the Grand Unified
 491 Theory scale **a couple of cit would be nice**. According to the theoretical model de-
 492 scribed in [100], for example, leptogenesis can be achieved if $|\sin \theta_{13} \sin \delta| > 0.11$, i.e.
 493 $\sin \delta > 0.7$.
 494 The asymmetry in the oscillation probability of neutrinos and antineutrinos is the ob-
 495 servable sensitive to the Dirac CP-violating phase δ leveraged in neutrino oscillation
 496 experiments. Using the parameterization of the PMNS matrix shown in Equation
 497 1.9, the difference between the probability of $\nu_e \rightarrow \nu_\mu$ oscillation and the probability
 498 of $\bar{\nu}_e \rightarrow \bar{\nu}_\mu$ oscillation can be parametrized as follows [39],

$$P_{\nu_e \rightarrow \nu_\mu} - P_{\bar{\nu}_e \rightarrow \bar{\nu}_\mu} = J \cos \left(\pm \delta - \frac{\Delta_{31} L}{2} \right) \sin \left(\frac{\Delta_{21} L}{2} \right) \sin \left(\frac{\Delta_{31} L}{2} \right) \quad (1.10)$$

499 where

$$J = \cos \theta_{13} \sin 2\theta_{13} \sin 2\theta_{12} \sin 2\theta_{23} \quad (1.11)$$

500 is the Jarlskog invariant [81], L the neutrino baseline, i.e. the distance between
 501 the neutrino production and detection points, and Δ_{ab} a factor proportional to the
 502 sign and magnitude of the mass splitting. From these equations, it is clear how the
 503 relative large value of θ_{13} is a happy accident necessary not to completely suppress
 504 the sensitivity to CP violation. The equations also show how the sensitivity to δ is
 505 tied to the measurement of the least precisely measured mixing angle, θ_{23} (via the
 506 $\sin 2\theta_{23}$ term) and to an other unknown quantity, the neutrino “mass hierarchy” (via
 507 the Δ_{ab} terms). The precise determination of θ_{23} is often referred as to “the octant
 508 problem”. Current experimental results [3, 12] are consistent with $\theta_{23} = 45^\circ$, which

509 would imply maximal mixing between ν_μ - ν_τ , hinting to an intriguing new symmetry.
510 Therefore, a precise measurement of θ_{23} is of great interest for theoretical models of
511 quark-lepton universality [74, 92, 105], whose quark and lepton mixing matrices are
512 proportional to the deviation of θ_{23} from 45°.

513 **Neutrino mass hierarchy.** The “mass hierarchy” problem refers to the unknown
514 ordering of the value of absolute mass of the neutrino mass eigenstates. Current
515 oscillation experiments are sensitive only to the magnitude of the mass splitting, and
516 not directly to its sign. In a framework where the lightest neutrino mass (arbitrarily)
517 corresponds to the first eigenstate m_1 , it is unknown whether $m_2 - m_1 < m_3 - m_1$
518 (Normal Hierarchy) or $m_2 - m_1 > m_3 - m_1$ (Inverted Hierarchy). The mass hierarchy
519 affects not only the sensitivity to CP violation searches in long baseline oscillation
520 experiments, but also the sensitivity to determine whether neutrinos are Majorana
521 particles in neutrinoless double beta decay experiments.

522 **Majorana or Dirac?** Evidence of neutrino oscillations demands the introduction
523 of a mechanism which can give mass to the neutrinos. This mechanism should possibly
524 also explain why neutrino masses are at least six orders of magnitude lower than the
525 electron mass (the second lightest SM fermion). In a description of neutrinos as Dirac
526 4-component spinors, the neutrino field acquires mass via the Higgs mechanism as
527 any other fermion of the SM. In this case, the neutrino mass is given by $m_a = \frac{y_a^\nu v}{\sqrt{2}}$,
528 where v is the Higgs VEV and y_a^ν is the Yukawa coupling between the Higgs and the
529 neutrino. The smallness of neutrino masses can only be pinned on a tiny Yukawa
530 coupling which is not justified by the theory.

531 In 1937, Majorana demonstrated that the introduction of a two components spinor is
532 sufficient to describe a massive fermion [91]. The Dirac equations of motion for the
533 chiral fields (equations 1.5 and 1.6) hold true in the case of two components spinor
534 under the assumption that the chiral components ψ_R and ψ_L are correlated through
535 the charge conjugation matrix \mathcal{C} , $\psi_R = \mathcal{C}\bar{\psi}_L$. Therefore the theory is applicable only

536 to neutral fermions. Neutrinos are the only neutral elementary particles in the SM
537 – the only possible Majorana particle candidate. This theory constructs a neutrino
538 Majorana mass term \mathcal{L}_5 of the following form in the Higgs unitary gauge

$$\mathcal{L}_5 = \frac{1}{2} \frac{gv^2}{\mathcal{M}} \nu_L^T \mathcal{C}^\dagger \nu_L, \quad (1.12)$$

539 where g is the coupling coefficient, v the Higgs VEV and \mathcal{M} a constant with the
540 dimension of the mass proportional to the scale of new physics. The \mathcal{L}_5 term would
541 introduce a non-renormalizable term in the lagrangian, since it has dimensions of
542 energy to the fifth power. This is not allowed in the SM lagrangian; however, the
543 existence of such terms is plausible if we consider the SM as an effective theory
544 at low energy, manifestation of the symmetry breaking of a more general theory at
545 higher energy, e.g. a Grand Unified Theory (GUT), and not the definitive theory.
546 The mass term in eq 1.12 implies the neutrino mass to be $m = \frac{gv^2}{\mathcal{M}}$. The coupling
547 coefficient can be of the order of any other fermion's coupling coefficient, since the
548 smallness of neutrino masses is achieved by the big value of the new physics mass
549 scale alone. This vanilla formulation is the conceptual basis for many flavors of *see-*
550 *saw mechanism* [121], which we will not discuss here in any detail. However, it is
551 fascinating how the puzzle of the neutrino mass hints to the existence of a deeper and
552 more complete theory.

553 From a kinematic point of view, Dirac and Majorana neutrinos satisfy the same
554 energy-momentum dispersion relationship. Thus, it is impossible to discern the neu-
555 trino nature through kinematic effects such as neutrino oscillations. Neutrinoless
556 double beta decay searches are the most promising way to understand the nature of
557 the neutrino and are therefore subject of great theoretical and experimental interest.
558 Observation of the lepton number violating process $0\nu\beta\beta$ would imply neutrinos have
559 a Majorana component. Depending on the mass hierarchy, the theory also predicts

560 $0\nu\beta\beta$ exclusion regions and confirmation of the sole Dirac component for neutrinos [44].
561
562

563 1.3.2 Towards a more fundamental theory: GUTs

564 Despite its highly predictive power, a number of conceptual issues arise in the SM
565 which disfavor it to be a good candidate for a fundamental theory.

566 The SM does not include a suitable dark matter candidate and a mechanisms
567 that accounts for the baryon asymmetry of the universe. Additionally, up to a total
568 of 25 parameters remain seemingly arbitrary and need to be fitted to data: 3 gauge
569 couplings, 9 charged fermion masses, 3 mixing angles and one CP phase in the CKM
570 matrix, the Higgs mass and quartic coupling, θ_{QCD} , 3 neutrino mixing angles, 1 Dirac
571 phase and, eventually, 2 Majorana phases.

572 From a group theory perspective, the SM has a rather complex group structure,
573 where a gauge group is formed with the direct product of other three groups as shown
574 in eq. 1.1. Drawing a parallel with the electroweak symmetry breaking mechanism,
575 where the $SU(2)_L \otimes U(1)_Y$ is recovered from $U(1)_{EM}$, an interesting line of simplification
576 for the SM group structure would be to devise a similar mechanism where
577 $SU(3)_C \otimes SU(2)_L \otimes U(1)_Y$ is recovered from an hypothetical larger group. IS THIS
578 CORRECT? Just as the electroweak unification becomes evident at energies higher
579 than the Higgs VEV, a direct manifestation of Grand Unification Theories (GUTs)
580 would occur at even higher energies.

581 As the smallness of neutrino masses suggests the existence of a higher mass scale,
582 an other, even stronger, hint to Grand Unification comes from the slope of running
583 of the coupling constants. The coupling constants for the electromagnetic, weak and
584 strong interactions in the SM vary as a function of the interaction energy as shown
585 in figure 1.2; they do not exactly meet under the current experimental constraints,

⁵⁸⁶ but their trend is interesting enough to push for the construction of theories where
⁵⁸⁷ perfect unification is achieved through the addition of new particles.

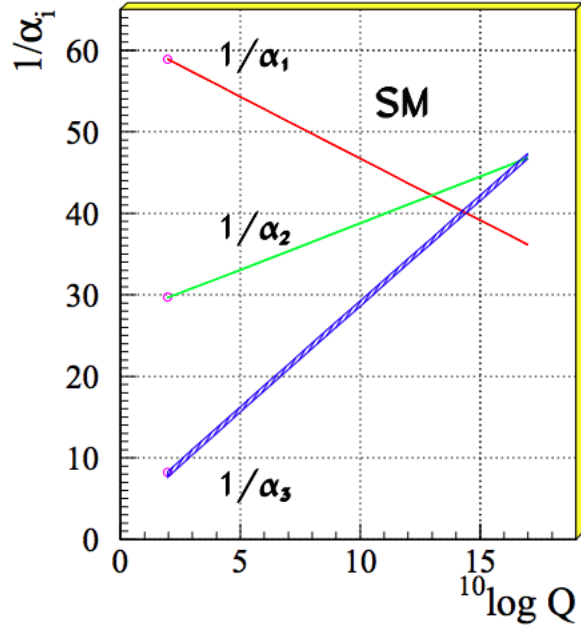


Figure 1.2: Evolution of the inverse of the three coupling constants in the Standard Model as a function of the momentum transferred, [85].

SU(5). The smallest simple group containing $SU(3)_C \otimes SU(2)_L \otimes U(1)_Y$ is SU(5), as shown first by Georgi and Glashow in [68]. Quarks and leptons in this group fit the $\bar{5}$ and 10 representations. The representation for left-handed fermions are the following

$$\bar{5} = (\nu_e, e^-)_L + \bar{d}_L \quad (1.13)$$

$$10 = e_L^+ + \bar{u}_L + (u, d)_L, \quad (1.14)$$

⁵⁸⁸ while the boson structure gains a new couple of super heavy bosons (X,Y)

$$24 = \underbrace{(8, 1)}_{\text{gluons}} + \underbrace{(1, 3) + (1, 1)}_{W^\pm, Z, \gamma} + \underbrace{(3, 2) + (\bar{3}, 2)}_{X, Y \text{ bosons}}. \quad (1.15)$$

⁵⁸⁹ Nice features such as charge quantization and the identity between the positron

590 and proton charge value come directly from the group structure. The new super
591 heavy bosons are colored and form a weak doublet. Their are the mediator of the
592 interaction that turns quarks into leptons, leading to predict the existence of processes
593 that violate baryon number, such as $p \rightarrow \pi^0 + e^+$ (see fig 1.8, right). The prediction
594 for proton decay lifetime, $\tau_p \sim \frac{M_X^4}{m_p^5} \sim 10^{30 \pm 1.5}$ years, is unfortunately experimentally
595 disproved by IMB and Super-Kamiokande [4, 28].

596 **SO(10).** More complicated group structures, such as SO(10) are still viable
597 candidates for GUT. SO(10) includes the same type of X and Y bosons as SU(5).
598 Right-handed massive neutrinos are embedded in the construction of the irreducible
599 representation of SO(10). Different patterns of SO(10) symmetry breaking to recover
600 the SM are possible and lead to different predictions for the proton decay lifetime;
601 some of these predictions are not excluded by the experiments [86].

602 **SUSY GUTs.** Supersymmetry theories allow for another family of GUTs. In
603 SUSY, every fundamental particle in the SM has a “superpartner”, identical in each
604 quantum number except for the spin-statistics: the fermion supersymmetric partners
605 are bosons and vice versa. Collider experiments (mainly LHC) constrain the mass of
606 the supersymmetric partners to be very heavy [?]. The SU(5), SU(10) groups with
607 a SUSY twist are the basic groups for SUSY GUTs. From the phenomenology point
608 of view, SUSY models tend to push the proton decay life time higher by a factor of
609 four, they solve the “hierarchy problem”, and they also predict new channels for the
610 proton decay. In particular they predict the presence of kaons in the final product,
611 with a dominant mode of $p \rightarrow K^+ \bar{\nu}$. Predictions on the proton decay lifetime depend
612 on the chosen SUSY model; again, some of the predictions are not excluded by the
613 experiments [89, 90, 109].

614 **1.4 Motivations for Hadronic Cross Sections in Ar-**
615 **gon**

616 Critical challenges await the next decade of high energy physics at the intensity
617 frontier. Following the recommendation of the latest Particle Physics Project Priori-
618 tization Panel [106], the US is dedicating substantial resources to the development of
619 a short- and long- baseline neutrino program to address many of open questions in
620 neutrino physics today. This program pivots on the Liquid Argon Time Projection
621 Chamber (LArTPC) detector technology which will be described in Chapter 2.

622 The main goals of these research programs include:

- 623 - the assessment of the existence of right-handed sterile neutrinos via the study
624 of accelerator neutrinos on a short baseline (SBN),
- 625 - the determination of the sign of Δm_{13}^2 (or Δm_{23}^2), i.e., the neutrino mass hier-
626 archy via the study of accelerator neutrinos on a long baseline (DUNE),
- 627 - the determination of the octant, i.e. whether θ_{23} is maximal, via the study of
628 accelerator neutrinos on a long baseline (DUNE),
- 629 - the determination the status of CP symmetry in the lepton sector, via the study
630 of accelerator neutrinos on a long baseline (DUNE),
- 631 - the search for observables predicted by GUTs, such as proton decay via the
632 study of non accelerator physics in massive underground detectors (DUNE).

633 **1.4.1 Pion-Argon Total Hadronic Cross Section**

634 This section outlines the importance of the pion-argon total hadronic cross section in
635 the context of the current and upcoming liquid argon neutrino experiments, SBN and
636 DUNE. We describe the signal signature and historic measurements of pion-nucleus

637 cross section, as well as the implementation of these cross sections in the current
638 version of the simulation package used by LArIAT.

639 **π^- Ar Cross Section in the Context of Neutrino Searches**

640 As outlined in 1.2.3, neutrino experiments use the products of neutrino interactions
641 to identify the energy and flavor of the incoming neutrino. Pions are a common
642 product of neutrino interaction, especially in resonant scattering, DIS and coherent
643 pion production. For neutrino experiments in argon, there are two main reasons
644 why understanding pion hadronic interactions with argon is important: to model the
645 behavior of the pion inside the target nucleus and to model the behavior of the pion
646 during its propagation inside the detector medium.

647 Assumptions on the nuclear modeling and on the interaction of hadrons inside the
648 nucleus performed at the level of the neutrino event generator bridge the measure-
649 ment of the products of a neutrino interaction to the reconstruction of the neutrino
650 energy and flavor. Thus, understanding pion hadronic interactions with the nucleus is
651 particularly important to model correctly resonant, DIS and coherent pion production
652 in neutrino interactions. For example, in case of resonant scattering,

$$\nu_l + N \rightarrow l + \Delta/N^* \rightarrow l + \pi + N', \quad (1.16)$$

653 the Δ and N^* and excited states will decay hadronically in matters of $\sim 10^{-24}$ s
654 inside the nucleus producing pions which will have many chances to re-interact
655 as they exit the target medium. The decay modes for the lower mass Δ (1232) and
656 $N^*(1440)$ are listed in table 1.3.

657 The key elements of a neutrino event generators for resonance and DIS events
658 are the nuclear model and the hadron treatment (both production and transporta-
659 tion). We illustrate here the conceptual basis of the GENIE Neutrino Generator [18]

660 as an example, since GENIE is one the most popular event generators for liquid ar-
661 gon experiments. For example, the nuclear model used by GENIE for all processes
662 is a Relativistic Fermi Gas (RFG) model modified to incorporate nucleon-nucleon
663 correlations [30]. This means that the initial momentum and binding energy of the
664 struck nucleon is determined by assuming nucleons inside the nucleus are quasi-free,
665 acting independently in the mean field of the nucleus. For $A > 20$ such as argon, the
666 2-parameter Woods-Saxon shell model for density function is used. The GENIE mod-
667 ule INTRANUKE [84] is used to simulate final-state interactions (FSI) which model
668 hadron re-interactions inside the nucleus. This module places the outgoing parti-
669 cles in the nucleus and propagates them using the “hA model”. In the INTRANUKE
670 hA model, hadrons can undergo at most one FSI per event. When possible, external
671 hadron-nucleus scattering data are used to tune INTRANUKE. Since no data is avail-
672 able for Argon, GENIE uses an interpolation of data from heavier and lighter nuclei
673 for the pion-argon cross section leading to large (10?s of %) resultant uncertainties in
674 the INTRANUKE module.

675 Once the pion has left the target nucleus, the pion-argon hadronic cross section also
676 plays an important role in the pion transportation inside the argon medium: processes
677 such as pion absorption or pion charge exchange can greatly modify the topology of
678 a neutrino interactions in the detector and lead to significant modifications in the
679 event classification. Being able to reconstruct the details of pions inside the detector
680 is an imperative for modern liquid argon neutrino experiment to achieve the design
681 resolution for their key physics measurements.

682 π^- -Ar Hadronic Interaction: Signal Signatures

683 Strong hadronic interaction models [49,69] predict the pion interaction processes with
684 argon in the [100 - 1200] MeV energy range. The total hadronic π^- -Ar interaction
685 cross section is defined as the one related to the single process driven only by the

686 strong interaction which is dominant in the considered energy range. In measuring
687 the “total” cross section, we include both the elastic and reaction channels, regardless
688 of the final state,

$$\sigma_{Tot} = \sigma_{Elastic} + \sigma_{Reaction}; \quad (1.17)$$

689 the reaction channel is further characterized by several exclusive channels with defined
690 topologies,

$$\sigma_{Reaction} = \sigma_{Inelastic} + \sigma_{abs} + \sigma_{chex} + \sigma_{\pi prod}. \quad (1.18)$$

691 A summary of the pion final states in order of pion multiplicity for the reaction
692 channel is given in table 1.4. Pion capture and pion decay at rest dominate the
693 cross section under 100 MeV. We define pion capture as the process determining the
694 formation of a pionic atom and the subsequent pion’s end of life. Stopping negative
695 pions can form pionic argon, where the negative pion plays the role of an orbital
696 electron. Since the pion mass is two orders of magnitude greater than the electron
697 mass, the spatial wave form of the pion will overlap more with the nucleus compared
698 to the electron case. After the electromagnetic formation of the pionic atom, the
699 pion will get quickly absorbed by the nucleus, which is put in an excited state. The
700 nucleus then de-excites with the emission of low energy nucleons and photons. Pion
701 capture is dominant compared to pion decay, the other important process for very
702 low energy pions. The decay of a pion is governed by the weak force; the pion decay
703 life time is $\tau_\pi = 2.6 \times 10^{-8}$ s and the main decay mode is $\pi^- \rightarrow \mu^- + \bar{\nu}_\mu$ (BR 99.98%).
704 Since pion capture can be considered an electromagnetic process and pion decay is a
705 weak process, this energy region is purposely excluded from the hadronic cross section
706 measurement.

707 **Previous measurements: Lighter and Heavier Nuclei**

708 Many experiments with pion beams have studied the hadronic interaction of pions on
709 light and heavy materials, such as He, Li, C, Fe, Pb [36]. However, data on argon are
710 rare: the total differential hadronic cross section has never been measured before on
711 argon. Simulation packages such as Geant4 base their pion transportation for argon
712 on data from lighter and heavier nuclei: the goal of LArIAT’s dedicated measurement
713 on argon is to bridge this gap in data, thus reducing the uncertainties related to pion
714 interactions in argon in both neutrino event generators and in simulation packages of
715 pion transportation.

716 The shape of the pion-nucleus interaction cross section in the energy range con-
717 sidered shows the distinct features indicating the presence of a resonance. In fact, the
718 mean free path of a pion of kinetic energy between 100 and 400 MeV is much shorter
719 than the average distance between nucleons (which is of the order of 1 fm). There-
720 fore, the pion interacts with surface nucleons. A Δ resonance is often produced in
721 the interaction, which subsequently decays inside the nucleus. Experimental results
722 on several nuclei as reported in [36] are shown in Figure 1.3; it is interesting to notice
723 here how the shape of the Δ resonance becomes less pronounced as a function of the
724 mass number of the target nucleus. Pion interactions with heavier nuclei also shift the
725 peak of the resonance at lower energy; this effect is due to kinematic considerations
726 and to the difference in propagation of the Δ inside the nucleus. Multiple scattering
727 effect modify the resonance width, which is larger than the natural-decay width. As
728 an example of a fairly well studied target, Figure 1.4 reports the negative pion cross
729 section on Carbon for the elastic and reaction² channels, and their sum [55].

2. This paper calls “inelastic interaction” what we refer as to “reaction channel”.

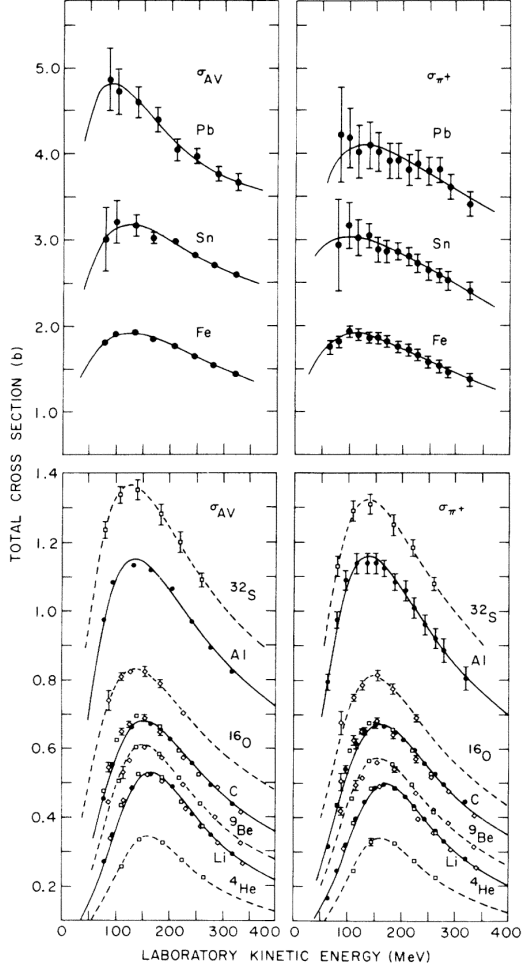


Figure 1.3: Pion-nucleus total cross sections: σ_{π^+} for positive pions (right) and σ_{AV} (left) for the average between positive and negative pions $\sigma_{AV} = \frac{\sigma_{\pi^+} + \sigma_{\pi^-}}{2}$ in the Δ resonance region. The error bars include estimates of systematic uncertainties. The curves are the results of fits to the data assuming a Breit-Wigner shape. This summary plot is reported in [36] and uses data from [52, 117].

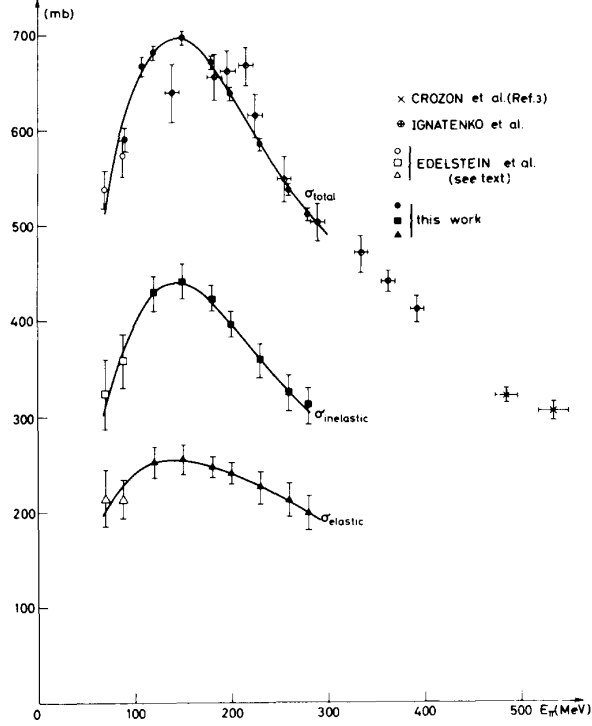


Figure 1.4: Negative pion nucleus total, elastic and reaction cross sections on ^{12}C as from [55].

730 Negative Pion Interaction Cross Section in Simulation Packages

731 LArIAT uses Geant4 as the default simulation package. In particular, pions (and
 732 kaons) transportation is achieved through the Geant4 FTFP_BERT physics list. In
 733 this physics list, Geant4 uses the Bertini cascade model [118] to simulate the products
 734 of the pion-nucleus interaction as well as secondary hadronic re-interactions inside
 735 the target nucleus (intra-nuclear cascade). The target nucleus is represented as a
 736 continuous gas where the nuclear potential follows concentrical shells whose depths
 737 approximate the Woods-Saxon shape. The CERN-HERA compilations [113, 114] of
 738 hadron-nucleon interaction data is the data base used for the decision making process
 739 after the cascade is invoked. The cross section model determines if the pion inter-
 740 acts, the eventual type of interaction and the interaction multiplicity. For hadron
 741 projectiles with energy less than 20 GeV, Geant4 reports the uncertainty on the cross

742 section model to be about the size of the error bars on the data used, or about 10%,
743 increasing to 20-30% in energy regions where data is sparse.

744 The relevance of the GENIE generator for neutrino physics and its basic working
745 principles have been outlined earlier in this section. Given GENIE’s modularity,
746 information on hadron-nucleus interactions can be extracted from the INTRANUKE
747 module and directly compared against the Geant4 predictions. The work in [97]
748 reviews the current status of negative and positive pion simulation in Geant4 and
749 GENIE for ^{12}C , ^{56}Fe , and ^{40}Ca . From that work, we report the results for ^{12}C in
750 Figure 1.5 as it allows a direct comparison between Geant4, GENIE and and pion
751 re-scattering data. Geant4 predictions for π^- on Carbon are in good agreement with
752 data over the entire spectrum spectrum, while GENIE predictions seem to show some
753 features at around 500 MeV and 900 MeV, maybe due to higher resonances in the hA
754 model. From the same work, we also report the negative pion cross section on ^{40}Ca
755 in Figure 1.6, since this is the nuclear medium closest to argon. The predictions from
756 both Geant4 and GENIE agree with data in the high energy region; the Geant4 and
757 GENIE predictions diverge in the resonance region, where data is not available. These
758 few examples highlight how cross section data for the specific nucleus considered in
759 the neutrino experiments is fundamental to inform the Monte Carlo simulation.

760 For the LArIAT simulation of the MC sample used in the π^- argon total hadronic
761 cross section measurement we use the Geant4 Bertini Cascade model, whose predic-
762 tions for the total, elastic and reaction hadronic cross sections are show in Figure
763 1.7.

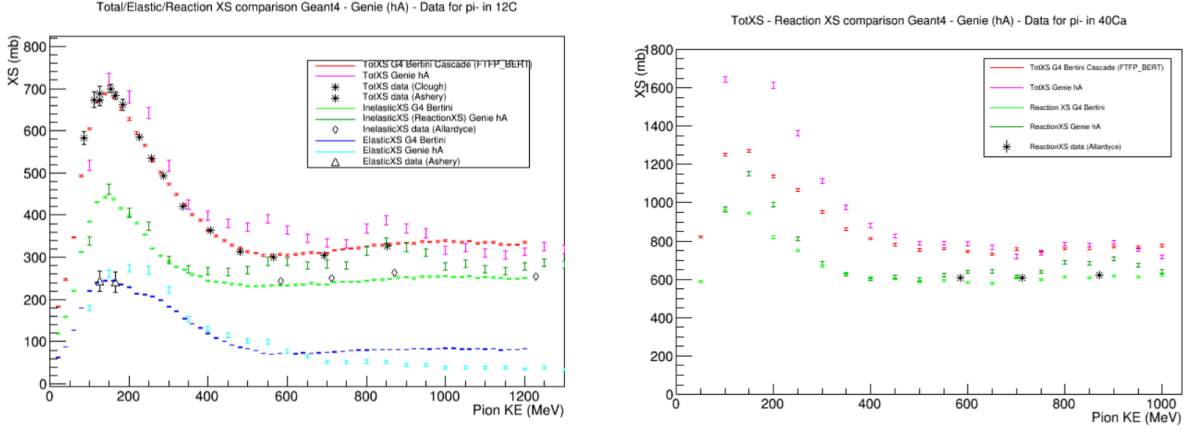


Figure 1.5: Total, elastic and reaction cross section for π^- on ^{12}C . Comparison between results from Geant4 simulation (Bertini cascade model), Genie simulation (hA model), and experimental data [22, 52, 53, 108].

Figure 1.6: Total, elastic and reaction cross section for π^- on ^{40}Ca . Comparison between results from Geant4 simulation (Bertini cascade model), Genie simulation (hA model), and experimental data [53].

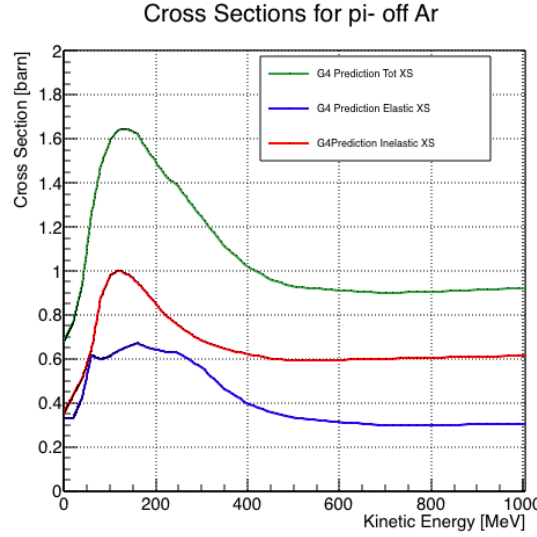


Figure 1.7: Total, elastic and reaction hadronic cross section for π^- -argon implemented in Geant4 10.01.p3.

Resonance	Decay Mode	Lifetime (s)
Δ (1232) $3/2^+$	$\Delta^{++}(\text{uuu}) \rightarrow p\pi^+$ $\Delta^+(\text{uud}) \rightarrow n\pi^+$ $\Delta^+(\text{uud}) \rightarrow p\pi^0$ $\Delta^0(\text{udd}) \rightarrow n\pi^0$ $\Delta^0(\text{udd}) \rightarrow p\pi^-$ $\Delta^-(\text{ddd}) \rightarrow n\pi^-$	$\sim 5.6 \times 10^{-24}$
N^* (1440) $1/2^+$	$N^* \rightarrow N\pi$ $N^* \rightarrow N\pi\pi$	$\sim 2.2 \times 10^{-24}$

Table 1.3: Main decay modes of the lightest Delta resonance and Nucleon excited state.

N π in FS	Channel Name	Reaction	Notes
0	Pion Absorption, σ_{abs}	$\pi^-(np) \rightarrow nn$ (2-body abs) $\pi^-(nnp) \rightarrow nnn$ (3-body abs) $\pi^-(npp) \rightarrow pnn$ (3-body abs) $\pi^-(nnpp) \rightarrow pmn$ (Multi-body abs)	Suppressed on single nucleon by energy conservation: the process occurs on at least two nucleons system.
1	Elastic Scattering, σ_{el}	$\pi^- + N \rightarrow \pi^- + N$	Scattering on nucleon or nucleus, the target is left in ground state
1	Charge Exchange, σ_{chea}	$\pi^- + p \rightarrow \Delta^0 \rightarrow \pi^0 + n$ $\pi^- + N \rightarrow \pi^+ +$ nucleons	Single charge exchange: charged pion converts into neutral pion Double charge exchange: charged pion converts into opposite charge pion
1	Inelastic Scattering, σ_{inel}	$\pi^- + p \rightarrow \Delta^0 \rightarrow \pi^- + p$ (knock-out) $\pi^- + n \rightarrow \Delta^- \rightarrow \pi^- + n$ (knock-out)	Other possible reactions: Pure Inelastic scattering: population of low energy bound excited states Nuclear break-up with nucleons or fragments knock-out
2+	Pion Production, $\sigma_{\pi prod}$	$\pi^- + N \rightarrow \geq 2\pi +$ nucleons	Possible if pion K.E ≥ 500 MeV/c

Table 1.4: Summary of negative pion hadronic interactions of the reaction channel as a function of the pion multiplicity in the final state in the energy range [100-1200] MeV.

764 **1.4.2 Kaon-Argon Total Hadronic Cross Section**

765 This section outlines the importance of the kaon-argon total hadronic cross section.
766 We start by discussing the measurement in the context of nucleon decay searches. We
767 then describe the signal signature and historical measurements of kaon-nucleus cross
768 section, as well as the implementation of this cross sections in the current version of
769 the simulation package used by LArIAT.

770 **K⁺Ar Cross section in the Context of Nucleon Decay Searches**

771 Baryon number is accidentally conserved in the Standard Model. Even though no
772 baryon number violation has been experimentally observed thus far, no underlying
773 symmetry in line with the Noether paradigm [96] explains its conservation. As shown
774 in section 1.3.2, almost all Grand Unified Theories predict at some level baryon num-
775 ber violation in the form of nucleon decay on long time-scales. Given the impossibil-
776 ity to reach grand unification energy scales with collider experiments (Energy Scale
777 > 10¹⁵ GeV), an indirect proof of GUTs is needed. The experimental observation of
778 nucleon decay may be the only viable way to explore these theories.

779 In case of nucleon decay discovery, the dominant decay mode may uncover addi-
780 tional information about the GUT type. Supersymmetric GUTs [24, 46] prefer the
781 presence of kaons in the products of the decay, e.g. $p \rightarrow K^+ \bar{\nu}$ (see fig 1.8, left).
782 Gauge mediated GUTs, in which new gauge bosons are introduced that allow for the
783 transformation of quarks into leptons, and vice versa, prefer the mode $p \rightarrow e^+ \pi^0$ (see
784 fig 1.8, right).

785 LArIAT tiny active volume makes it impossible for the experiment to place com-
786 petitive limits on nucleon decay searches. However, LArIAT provides excellent data
787 to characterize kaons in liquid argon for the “LAr golden mode”, $p \rightarrow K^+ \bar{\nu}$. The
788 result of these studies will affect future proton decay searches in LArTPCs. Previous
789 work has been done to assess the potential identification efficiency for different decay

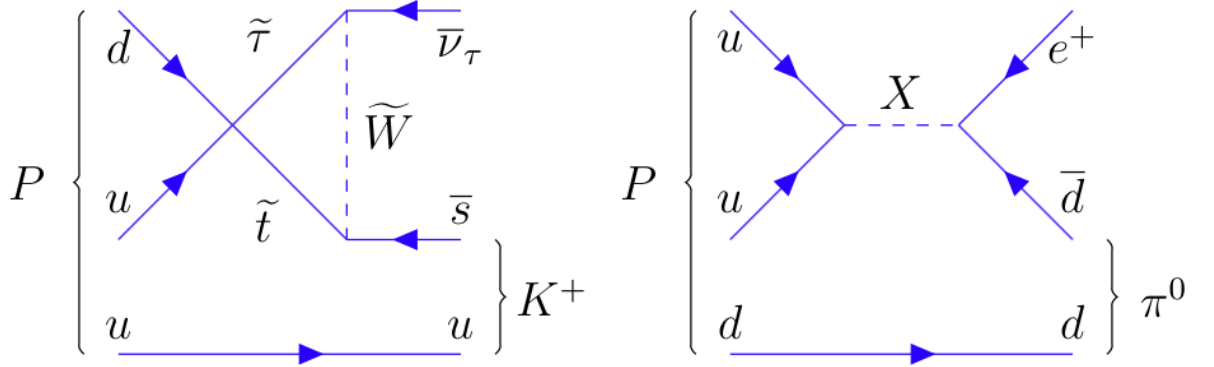


Figure 1.8: Feynman diagrams for proton decay “golden modes”: $p \rightarrow K^+\bar{\nu}$ for supersymmetric GUTs on the left and $p \rightarrow e^+\pi^0$ for gauge-mediated GUTs on the right.

790 modes in a LArTPC [51], but, as the time of this writing, no study of kaon selection
 791 efficiency in LArTPCs has been performed on data. The K^+ -Ar interaction cross
 792 section has never been measured before and can affect the possibility of detecting
 793 and measuring kaons when produced in a proton decay event. Kaon interactions with
 794 argon can distort the kaon energy spectrum as well as change the topology of single
 795 kaon events. In a LArTPC, non-interacting kaons appear as straight tracks with a
 796 high ionization depositions at the end (Bragg peak). The topology of interacting
 797 kaons can be quite different. In case of elastic scattering, a distinct kink will be
 798 present in the track. In case of inelastic scattering the Bragg peak will not be present
 799 and additional tracks will populate the event. Performing the total hadronic K^+ -Ar
 800 cross section measurement on data serves the double purpose of identifying the rate
 801 of “unusual” topologies (kinks and additional tracks) and of developing tools for kaon
 802 tracking in LAr.

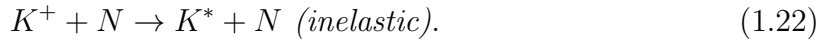
803 K^+ Ar Hadronic Interaction: Signal Signatures

The interaction of a mildly relativistic charged kaon with an argon nucleus is determined largely by the strong force. The total hadronic K^+ -Ar interaction cross section

is defined as the one related to the single (hadronic) process driven only by the strong interaction. In this case, “total” indicates all strong interactions regardless of the final state. This condition purposefully includes both elastic and inelastic (reaction) channels. Indeed, the total cross section section can be then decomposed into

$$\sigma_{Tot} = \sigma_{Elastic} + \sigma_{Reaction}.$$

804 For the LArIAT cross section analysis, the kaons considered span a momentum
 805 inside the TPC from 100 MeV/c to 800 MeV/c. In this energy range, the relevant
 806 K-Nucleon interactions are according to [63]:



807 **Previous Measurements: Lighter and Heavier Nuclei**

808 In general, measurements on kaon cross sections are extremely scarce. The mea-
 809 surement of the kaon interaction cross section would bring the additional benefit
 810 of reducing the uncertainties associated with hadron interaction models adopted in
 811 MC simulations for argon targets, beneficial for both proton decay studies and kaon
 812 production from neutrino interaction studies, where the uncertainties for final state
 813 interaction models are big [47].

814 Figure 1.9 shows a 1997 measurement on several elements as performed by Fried-
 815 mann et al. [65]. As a reference, this paper measures a σ_{Tot} for Si of 366.5 ± 4.8
 816 mb and a σ_{Tot} for Ca of 494.6 ± 7.7 mb at 488 MeV/c. The cross section for argon

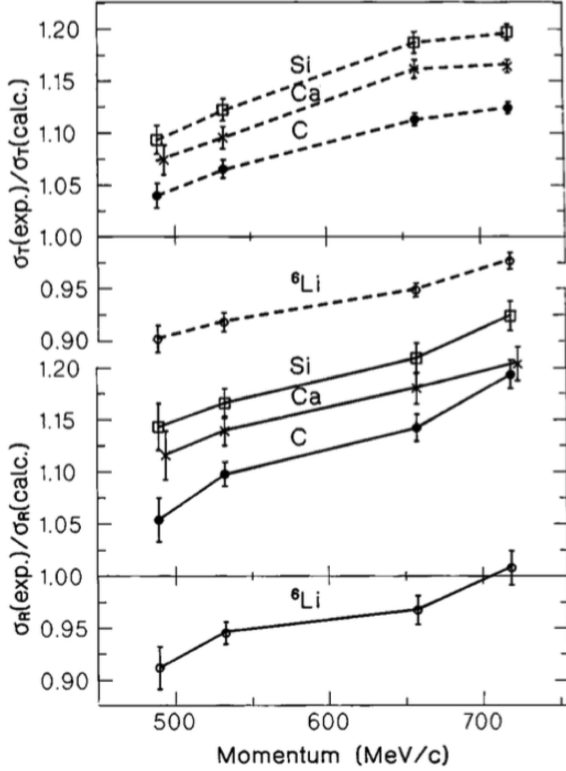


Figure 1.9: Ratios between experimental and calculated cross sections as from [65].
Top: Total cross sections.
Bottom: reaction cross sections.

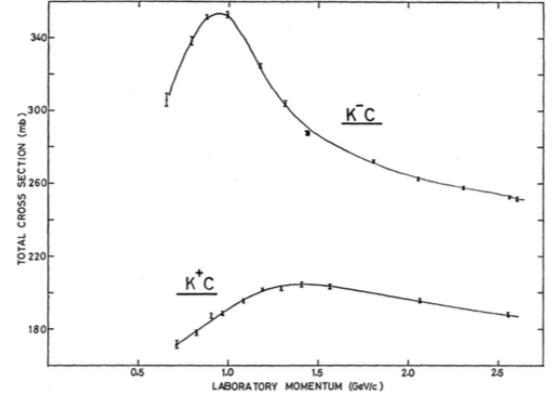


Figure 1.10: Total K^+ and K^- cross sections on carbon as from [32].

is expected to lie in between these two measurements. Additional data on the kaon cross section are provided by Bugg et al. [32]. Bugg performs a measurement of the total K^+ and K^- cross sections on protons and deuterons over the range of 0.6-2.65 GeV/c, as well as a measurement of the total K^+ and K^- cross sections on carbon for a number of momenta; the results of this paper on carbon are reported in Figure 1.10.

823 Kaon Interaction Cross Section for thin target in Geant4

824 Since the kaon cross section in argon has never been measured before, simulation
825 packages tune kaon transportation in argon by extrapolation from lighter and heavier
826 nuclei. LArIAT uses the Geant4 suite for particle transportation. Since kaon data on

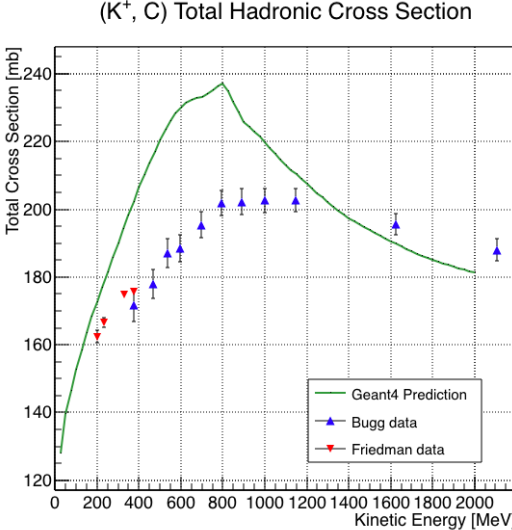


Figure 1.11: Total hadronic cross section for carbon implemented in Geant4 10.01.p3 with overlaid with the Bugg and Friedman data.

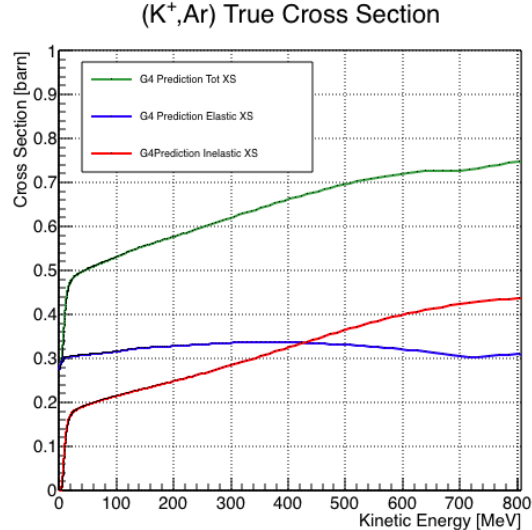


Figure 1.12: Total, elastic and reaction hadronic cross section for K^+ -argon implemented in Geant4 10.01.p3.

carbon are available, we used it as a metric to evaluate the Geant4 prediction performances. Figure 1.11 shows the total hadronic cross section for carbon implemented in Geant4 10.01.p3 overlaid with the Bugg and Friedman data. Unfortunately, version 10.01.p3³ of Geant4, which is the version used for the simulation in this work, does not reproduce the data for carbon closely. On one hand, this evidence makes us even more wary when using the Monte Carlo in simulating the kaon-argon interactions. On the other, it further highlights the importance of the kaon measurement. For the LArIAT simulation of the MC sample used in the K^+ argon total hadronic cross section measurement we use the Geant4 Bertini Cascade model, whose predictions for the total, elastic and reaction hadronic cross sections are show in Figure 1.12.

3. It should be noted that the latest Geant4 version, 10.03.p3, uses a different parametrization for the kaon cross section and retrieves a better agreement with data.

⁸³⁷ **Chapter 2**

⁸³⁸ **Liquid Argon Detectors at the**
⁸³⁹ **Intensity Frontier**

⁸⁴⁰ “*Don’t you know, honey,*
⁸⁴¹ *Ain’t nobody ever gonna love you, the way I try to do?*”
⁸⁴² – Janis Joplin, 1971 –

⁸⁴³ In the next few years, LArTPCs will be the tools to answer some of the burning
⁸⁴⁴ questions in neutrino physics today. This chapter illustrates the operational principles
⁸⁴⁵ of this detector technology, as well as the scope of the key detectors in the US liquid
⁸⁴⁶ argon program – SBN, DUNE and LArIAT.

⁸⁴⁷ **2.1 The Liquid Argon Time Projection Chamber**
⁸⁴⁸ **Technology**

⁸⁴⁹ In this section, we outline an extremely brief history of Time Projection Chambers
⁸⁵⁰ as particle detectors, focusing on their incarnation as Argon detectors for neutrino
⁸⁵¹ physics. We further describe the working principles of Liquid Argon Time Projection

852 Chambers, leading to the description of the event reconstruction in LArTPC.

853 2.1.1 TPCs, Neutrinos & Argon

854 David Nygren designed the first Time Projection Chamber (TPC) in the late 1970s [98]
855 for the PEP-4 experiment, a detector apt to study electron-positron collisions at the
856 PEP storage ring at the SLAC National Accelerator Laboratory. From the original
857 design in the seventies – a cylindrical chamber filled with methane gas – the TPC
858 detector concept has seen many incarnations, the employment of several different
859 active media and a variety of different particle physics applications, including, but
860 not limited to the study of electron/positron storage rings (e.g. PEP4, TOPAZ,
861 ALEPH and DELPHI), heavy ions collisions in fixed target and collider experiments
862 (e.g. EOS/HISSL and ALICE), dark matter (ArDM), rare decays and capture (e.g.
863 TRIUMF, MuCap), neutrino detectors and nucleon decay (ICARUS, SBN, DUNE),
864 and neutrino less double beta decay (Next). A nice review of the history of TPCs
865 and working principles is provided in [77].

866 Several features of the TPC technology make these detectors a more versatile tool
867 compared to other ionization detectors and explain such a wide popularity. TPCs are
868 the only electronically read detector which deliver simultaneous three-dimensional
869 track information and a measurement of the particle energy loss. Leveraging on both
870 tracking and calorimetry, particle identification (PID) capabilities are enhanced over
871 a wide momentum range.

872 Historically, the active medium in ionization detectors has been in the gaseous
873 form. Carlo Rubbia first proposed the use of a Liquid Argon TPC for a neutrino
874 experiment, ICARUS [107], in 1977. Using nobles elements in the liquid form for
875 neutrino detectors is advantageous for several reasons. The density of liquids is \sim 1000
876 times greater than gases, augmenting the number of targets for neutrino's interaction
877 in the same volume, in a effort to balance the smallness of neutrino cross section. Since

Element	LAr	LXe
Atomic Number	18	54
Atomic weight A	40	131
Boiling Point Tb at 1 atm	87.3 K	165.0 K
Density	1.4 g/cm ³	3.0 g/cm ³
Radiation length	14.0 cm	2.8 cm
Moliere Radius	10.0 cm	5.7 cm
Work function	23.6 eV	15.6 eV
Electron Mobility at $E_{field} = 10^4$ V/m	0.047 m ² /Vs	0.22 m ² /Vs
Average dE/dx MIP	2.1 MeV/cm	3.8 MeV/cm
Average Scintillation Light Yield	40000 γ /MeV	42000 γ /MeV
Scintillation λ	128 nm	175 nm

Table 2.1: LAr, LXe summary of properties relevant for neutrino detectors.

the energy loss of charged particle is proportional to the target material density, as shown in the Bethe-Block equation (eq. 2.1), the increased density reflects into a proportionally higher energy loss, enhancing the calorimetry capability of detectors with a liquid active medium. Additionally, the ionization energy of liquids is smaller than gasses by the order of tens of eV. Thus, at the passage of charged particles, liquids generally produce more ionization electrons than gases for the same deposited energy, forcing the particles to deposit more energy in a shorter range. The downside of using noble liquid elements in experiments is that they require expensive cryogenic systems to cool the gas until it transitions to its the liquid form. The properties of liquid argon in comparison liquid xenon – a popular choice for dark matter and neutrinoless double beta decay detectors – are summarized in table 2.1. Albeit xenon would be more desirable than argon given some superior properties such as lower ionization energy and higher density and light yield, argon relative abundance abates the cost of argon compared to xenon, making argon a more viable choice for the construction of ton (and kilo-ton) scale neutrino detectors.

LArTPCs are some times referred as to “electronic” bubble-chambers, for the similarity in the tracking and energy resolution which is coupled with an electronic readout of the imaging information in LArTPCs. Compared to these historic detectors

896 however, LArTPC bestow tridimensional tracking and a self triggering mechanism
897 provided by the scintillation light in the liquid argon. An event display of a ν_μ CC
898 interaction candidate in the MicroBooNE detector is shown in picture 2.1 to display
899 the level of spatial details these detectors are capable of; the color scale of the image
900 is proportional to the energy deposited, hinting to these calorimetry capabilities of
the detectors.

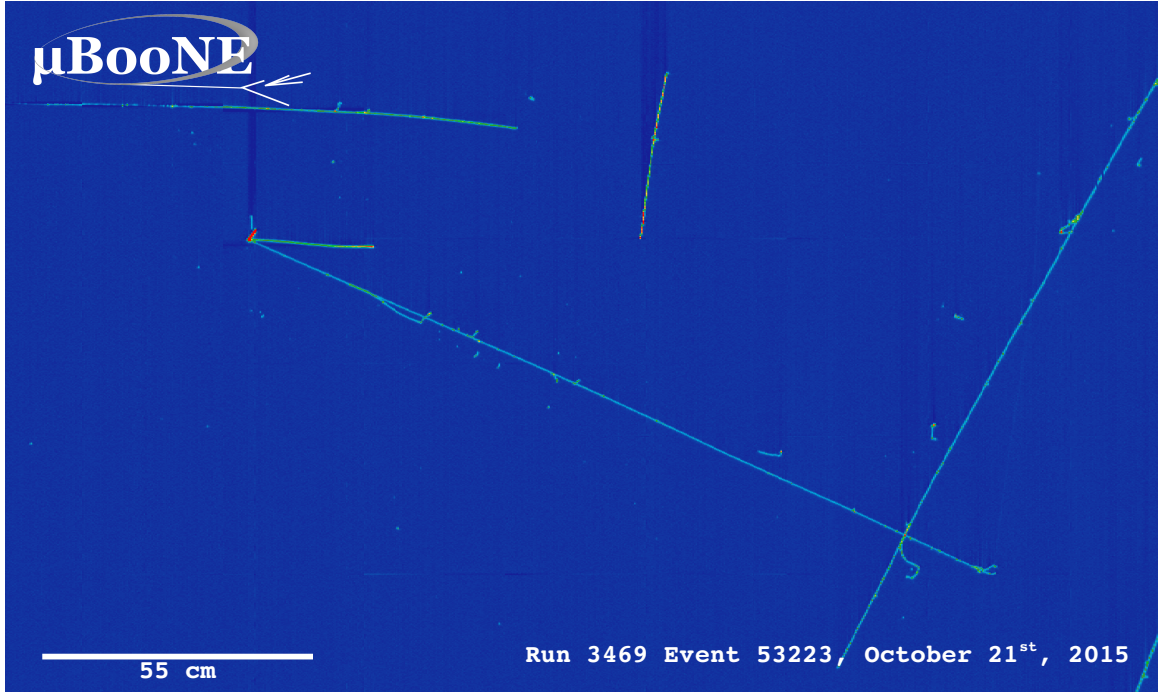


Figure 2.1: Event display of a ν_μ CC interaction candidate in the MicroBooNE detector.

901

902 2.1.2 LArTPC: Principles of Operation

903 To the bare bones, a LArTPC is a bulk of liquid argon sandwiched in a flat capacitor,
904 equipped with a light collection system, as the cartoon in 2.2 shows. A uniform
905 electric field of the order of 500 V/cm is maintained constant between the faces of the
906 capacitor. The anode is sensitive to ionization charge and it is usually made of two
907 or more planes segmented into several hundreds parallel sense wires a few millimeters
908 apart; different geometries for the anode segmentation are under study [48].

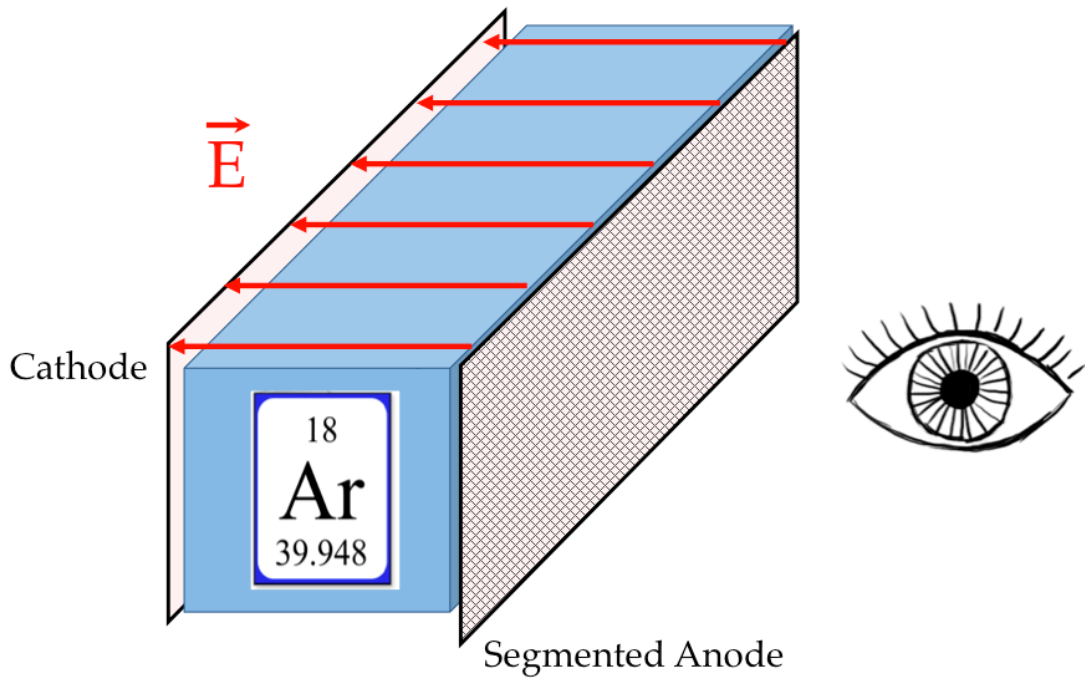


Figure 2.2: A cartoonish sketch of a LArTPC.

Argon ionization and scintillation are the processes leveraged to detect particles in the LArTPC active volume. When a ionizing radiation traverses the argon active volume it leaves a trail of ionization electrons along its trajectory and it excites the argon producing scintillation light – details on the production and detection of ionization charge and scintillation light are provided in 2.1.4 and 2.1.4 respectively. The optical detector sees the argon scintillation light in matters of nanoseconds. This flash of light determines the start time of an event in the chamber, t_0 . The uniform electric field drifts the ionization electrons from the production point towards the anode in order of hundreds of microseconds or more depending on the chamber dimensions¹. The anode sense wires see either an induced current by the drifting ionization charge (on induction planes) or an injection of such charge (collection

1. The ionized argon also drifts, but in the opposite directions compared to the electrons. Since the drift time is proportional to the particle mass, the ions' drift time is much longer than the electrons'. Ionized argon is collected on the cathode which is not instrumented, so it is not used to infer information about the interactions in the chamber.

920 plane). An appropriate choice of the voltage bias on each wire plane assures ideal
921 charge transparency, so that all the ionization charge is collected on the collection
922 plane and none on the induction planes.

923 The arrival time of the charge on the anode sense wires is used to measure the
924 position of the original ionizing radiation in the drift direction. In fact, since the
925 constant electric field implies that the drift velocity is also constant, the position of
926 the original ionization is simply given by the multiplication of the drift velocity by the
927 drift time, where the “drift time” is the difference between t_0 and the charge arrival
928 time on the wire planes. The spacial resolution on this dimension is limited by the
929 time resolution of the electronics or by longitudinal diffusion of the electrons. The
930 spatial information on the different wire planes maps a bi-dimensional projection of
931 the interaction pattern in the plane perpendicular to the drift direction. The spacial
932 resolution on this dimension is limited by the transverse electron diffusion in argon
933 and by the grain of the anode segmentation, i.e. the spacing between the wires in
934 the sense planes [45]. The off-line combination of the 2-D information on the wire
935 planes with the timing information allows for the 3D reconstruction of the event in
936 the chamber.

937 Since the charge deposited by the ionizing radiation is proportional to the de-
938 posited energy and the charge collected on the sense plane is a function of the de-
939 posited charge, LArTPCs allow the measurement of the energy deposit in the active
940 volume. Effects due to the presence of free charge and impurities in the active vol-
941 ume, such as a finite electron lifetime, recombination and space charge, complicate
942 the relationship between deposited and collected charge affecting the measurement of
943 the particle’s energy, as described in the next section.

944 **2.1.3 Liquid Argon: Ionization Charge**

945 The mean rate of energy loss by moderately relativistic elementary charge particles
 946 heavier than electrons is well described by the modified Bethe-Bloch [101] equation

$$-\frac{dE}{dx} = K z^2 \frac{Z}{A} \varrho \frac{1}{\beta^2} \left[\frac{1}{2} \ln \frac{2m_e c^2 \beta^2 \gamma^2 T_{max}}{I^2} - \beta^2 - \frac{\delta}{2} \right], \quad (2.1)$$

947 where z is the number of unit charge of the ionizing radiation, Z , A and ϱ are the
 948 atomic number, mass number and density of the medium, m_e is the electron mass,
 949 $\gamma = \frac{\beta}{\sqrt{1-\beta^2}}$ is the Lorentz factor of the ionizing radiation, T_{max} is the maximum kinetic
 950 energy which can be imparted to a free electron in a single collision, I is the mean
 951 excitation energy on eV, δ is the density correction and $K = 0.307075 \text{ MeV g}^{-1} \text{ cm}^2$ is
 952 a numerical conversion factor. The Bethe-Bloch treats the energy loss by an ionizing
 953 radiation via quantum-mechanical collisions producing ionization or an excitation in
 954 the medium as an uniform and continuous process. The density correction terms
 955 becomes relevant for incident particle with high energy, where screening effects due
 956 to the polarization of the medium by high energy particles occur.

957 Excitation and ionization of the detector medium occur in similar amounts. Since
 958 the ionizing collisions occur randomly, we can parametrize their number k in a segment
 959 of length s along the track with a Poissonian function

$$P(k) = \frac{s^k}{k! \lambda^k} e^{-s/\lambda}, \quad (2.2)$$

960 where $\lambda = 1/N_e \sigma_i$, with N_e being the electron density of σ_i the ionization cross-
 961 section per electron. About 66% of the ionizing collisions in Argon produce only
 962 a single electron/ion pair [77]; in the other cases, the transferred kinetic energy is
 963 enough for the primary electron to liberate one or more secondary electrons, which
 964 usually stay close to the original pair. Occasionally, electrons can receive enough

965 energy to be ejected with high energy, forming a so-called “ δ -ray”: a detectable short
966 track off the particle trajectory, as shown in figure 2.3. The average number of δ -ray
967 with energy $E > E_0$ per cm follows the empirical form

$$P(E > E_0) \sim \frac{y}{\beta^2 E_0}, \quad (2.3)$$

968 where y is an empirical factor depending on the medium (0.114 for gaseous Ar), and
969 β is v/c .

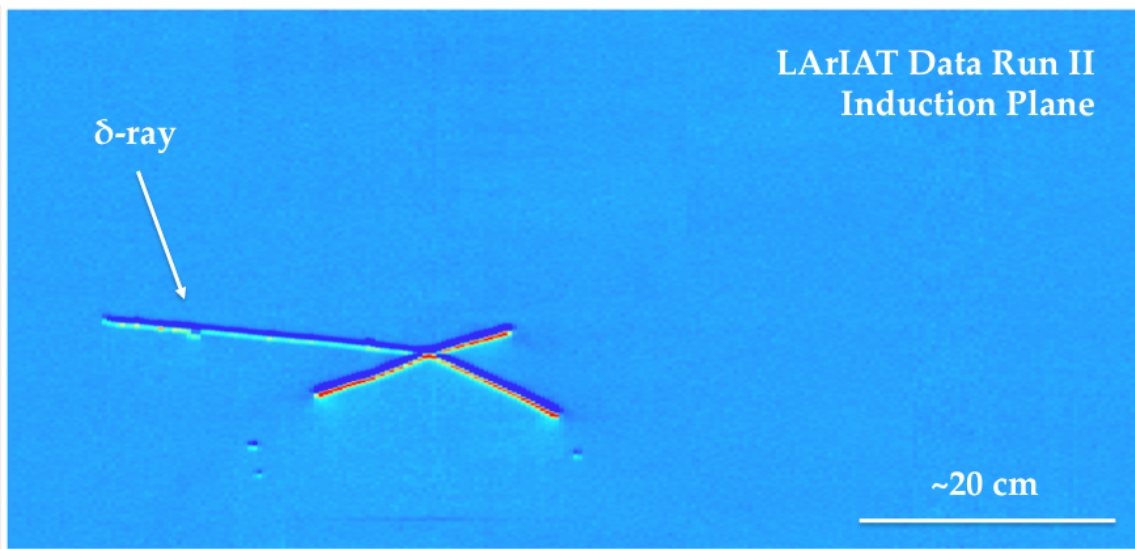


Figure 2.3: Events display for a LArIAT pion absorption candidate on the induction plane, with highlighted delta ray.

970 Purity & Electron Life Time

971 The presence of electronegative contaminants in liquid argon, such as oxygen O_2
972 and water H_2O , is particularly pernicious, since these molecules quench the charge
973 produced by the ionizing radiation. Thus, amount of charge per unit of length dQ/dx
974 collected on the collection plane depends on the charge's production point in the
975 detector: ionization produced close to the cathode will see more impurities along its
976 journey to the collection plane than ionization produced close to the anode, resulting

977 in greater attenuation of its charge. As a result, the amount of charge collected on
 978 the sense wires as a function of the traveled distance follows an exponential decay
 979 trend. The traveled distance is generally measured in terms of drift time and the
 980 characteristic time constant of the exponential decay is called electron lifetime τ_e .
 981 Figure 2.4 shows the typical life time for LArIAT data. The procedure to measure
 982 the electron lifetime in LArIAT is outlined in [104]. LArIAT small drift distance (47
 983 cm) allows for a relatively short electron life time. The life time for bigger detectors
 984 such as MicroBooNE, whose drift distance is 2.6 m, needs to be of the order of
 985 tens of milliseconds to allow a charge collection usable for physics analyses. Energy
 986 reconstruction in LArTPC applies a correction for the finite lifetime to calibrate the
 987 detector calorimetric response; details for LArIAT are provided in Section C.

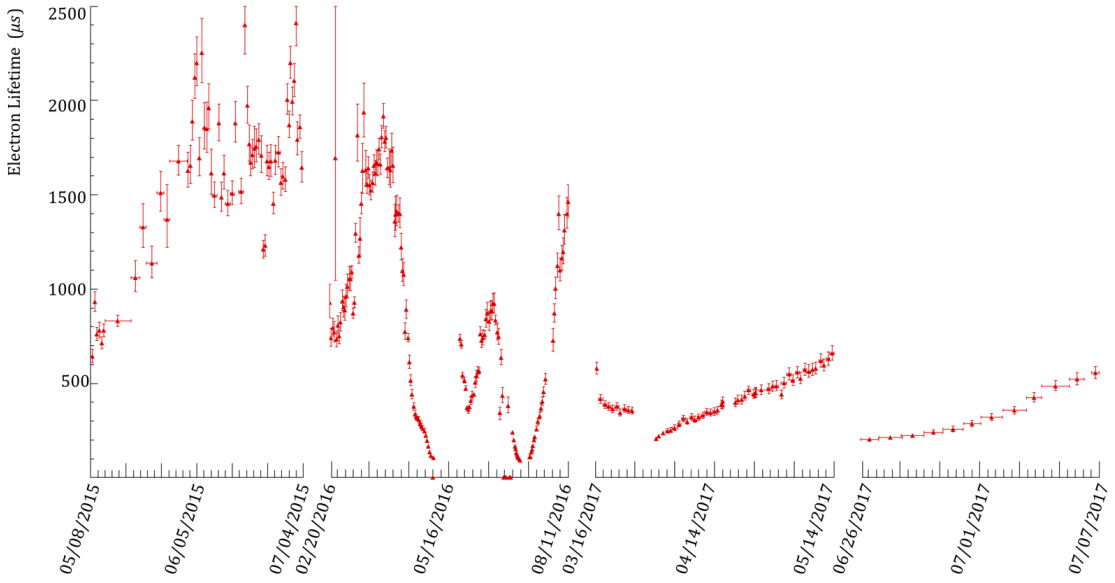


Figure 2.4: Electron lifetime during the LArIAT run period [43].

988 LArTPCs use hermetically sealed and leak-checked vessels to abate the leakage
989 and diffusion of contaminants into the system. The liquid argon filling of the volume
990 occurs after the vessel is evacuated or purged with gaseous argon [10] to reduce re-
991 maining gases in the volume. Even so, the construction of a pure tank of argon is
992 unviable, as several sources of impurity remain. In particular, impurities can come
993 from the raw argon supply, the argon filtration system and from the outgassing from
994 internal surfaces. Outgassing is a continuous diffusive process producing contami-
995 nants, especially water, even after the vessel is sealed, particularly from materials in
996 the ullage region². Since research-grade argon comes from the industrial distillation
997 of air, the impurities with the highest concentration are nitrogen, oxygen and water,
998 generally maintained under the 1 part per million level by the vendor. Even so, a
999 higher level of purity is necessary to achieve a free electron life time usable in meter
1000 scale detectors. Thus, argon is constantly filtered in the cryogenic system, which
1001 reduce the oxygen and water contamination to less than 100 parts per trillion. The
1002 filtration system depends on the size and drift distance of the experiment and, for
1003 experiments on several meters scale, it includes an argon recirculation system.

1004 **Recombination Effect**

1005 After production, ionization electrons thermalize with the surrounding medium and
1006 may recombine with nearby ions. Recombination might occur either between the
1007 electron and the parent ion through Coulomb attraction, as described in the geminate
1008 theory [99], or thanks to the collective charge density of electrons and ions from
1009 multiple ionizations in a cylindrical volume surrounding the particle trajectory, as
1010 described in the columnar model [80]. Consideration on the average electron-ion
1011 distance and the average ion-ion distance for argon show that the probability of

2. While the liquid argon low temperature reduces outgassing in the liquid, this process remains significant for absorptive material (such as plastic) above the surface of the liquid phase.

1012 geminate recombination is low; thus recombination in argon is mainly due to collective
1013 effects [5]. Since protons, kaons and stopping particles present a higher ionization
1014 compared to MIPs, recombination effects are more prominent when considering the
1015 reconstruction of energy deposited by these particles.

1016 Theoretical descriptions of recombination based on the Birks model and the Box
1017 model are provided in [29] and [112], respectively. The Birks model assumes a gaus-
1018 sian spatial distribution around the particle trajectory during the entire recombina-
1019 tion phase and identical charge mobility for ions and electrons. The Box model also
1020 assumes that electron diffusion and ion mobility are negligible in liquid argon during
1021 recombination. In these models, the fraction of ionization electrons surviving recom-
1022 bination is a function of the number of ion-electron pairs per unit length, the electric
1023 field, the average ion-electron separation distance after thermalization and the angle
1024 of the particle with respect to the direction of the electric field – plus the diffusion
1025 coefficient in the Birks model. Given the stringent assumptions, it is perhaps not sur-
1026 prising that these models are in accordance to data only in specific regimes: the Birks
1027 model is generally used to describe recombination for low dE/dx , the Box model for
1028 high dE/dX . In LArTPC, the ICARUS and ArgoNeut experiments have measured
1029 recombination in [16] and [5] respectively. Since LArIAT uses the refurbished Ar-
1030 goNeut TPC and cryostat at the same electric field, LArIAT currently corrects for
1031 recombination using the ArgoNeut measured recombination parameters in [5].

1032 **Space Charge Effect**

1033 Slow-moving positive argon ions created during ionization can build-up in LArTPC,
1034 causing the distortion of the electric field within the detector. This effect, called
1035 “space charge effect” leads to a displacement in the reconstructed position of the
1036 signal ionization electrons. In surface LArTPCs the space charge effect is primarily
1037 due to the rate of ionization produced by cosmic rays which is slowly drifting in the

1038 chamber at all times. Surface LArTPC of the size of several meters are expected
1039 to be modestly impacted from the space charge effect, where charge build-up create
1040 anisotropy of the electric field magnitude of the order of 5% at a drift field of 500
1041 V/cm [93]. The smallness of the LArIAT drift volume and its relatively high electric
1042 field are such that the effect of space charge is expected to be negligible.

1043 2.1.4 Liquid Argon: Scintillation Light

1044 Liquid argon emits scintillation light at the passage of charged particles. LArTPCs
1045 leverage this property to determine when the ionization charge begins to drift towards
1046 the anode plane.

1047 Scintillation Process

1048 Scintillation light in argon peaks in the ultraviolet at a 128 nm, shown in comparison
1049 to Xenon and Kypton in Figure 2.5, from [94]. The light yield collected by the optical
1050 detector depends on the argon purity, the electric field, the dE/dx and particle type,
1051 averaging at the tens of thousands of photons per MeV.

1052 The de-excitation of Rydberg dimers in the argon is responsible for the scintillation
1053 light. Rydberg dimers exist in two states: singlets and a triplets. The time constant
1054 for the singlet radiative decay is 6 ns, resulting in a prompt component for the scin-
1055 tillation light. The decay of the triplet is delayed by intersystem crossing, producing
1056 a slow component with a time constant of \sim 1500 ns. “Self-trapped exciton lumines-
1057 cence” and “recombination luminescence” are the two processes responsible for the
1058 creation of the Rydberg dimers [83]. In the first process, a charged particle excites an
1059 argon atom which becomes self-trapped in the surrounding bulk of argon, forming a
1060 dimer; the dimer is in the singlet state 65% of the times and in the triplet state 35%
1061 of the times. In case of recombination luminescence, the charged particle transfers
1062 enough energy to ionize the argon. The argon ion forms a charged argon dimer state,

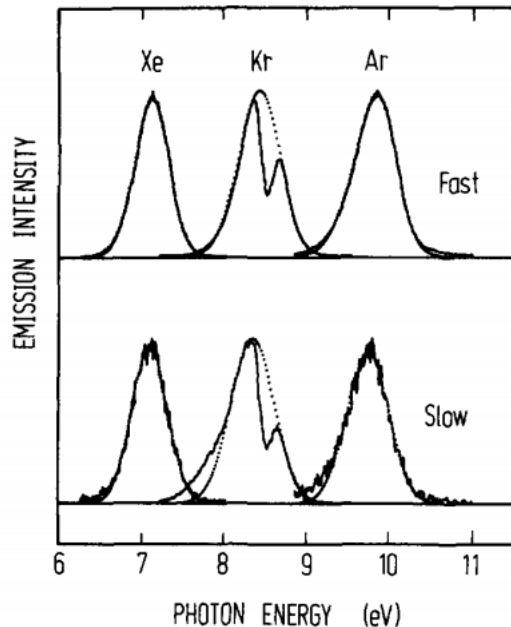


Figure 2.5: Emission spectra of the fast and slow emission components in Xenon, Krypton and Argon according to [94]. The dotted lines correspond to the Gaussian fits.

which quickly recombines with the thermalized free electron cloud. Excimer states are produced in the recombination, roughly half in the singlet and half in the triplet state. The light yield dependency on the electric field, on the dE/dx and particle type derives from the role of free charge in the recombination luminescence process. The spacial separation between the argon ions and the free electron cloud depends on the electric field. On one hand, a strong electric field diminishes the recombination probability, leading to a smaller light yield; on the other, it increases the free charge drifting towards the anode plane. Hence, the amount of measurable charge and light anti-correlates as a function of the electric field. Ionizing particles in the argon modify the local density of both free electrons and ions depending on their dE/dx . Since the recombination rate is proportional to the square of the local ionization density, highly ionizing particles boost recombination and the subsequent light yield compared to MIPs. The possibility to leverage this dependency for pulseshape-based particle identification has been shown in [31, 88].

1077 **Effects Modifying the Light Yield**

1078 The production mechanism through emission from bound excimer states implies that
1079 argon is transparent to its own scintillation light. In fact, the photons emitted from
1080 these metastable states are not energetic enough to re-excite the argon bulk, greatly
1081 suppressing absorption mechanisms. In a LArTPC however, several processes modify
1082 the light yield in between the location where light is produced and the optical detector.
1083 In a hypothetical pure tank of argon, Rayleigh scattering would be the most important
1084 processes modifying the light yield. Rayleigh scattering changes the path of light
1085 propagation in argon, prolonging the time between light production and detection.
1086 The scattering length has been measured to be 66 cm [78] , shorter than the theoretical
1087 prediction of ~ 90 cm [111]; this value is short enough to be relevant for the current
1088 size of LArTPCs detectors. In fact, Rayleigh scattering worsen the resolution on t_0 ,
1089 the start time for charge drifting, and alters the light directionality, complicating the
1090 matching between light and charge coming from the same object in case of multiple
1091 charged particles in the detector.

1092 Traces of impurities in argon such as oxygen, water and nitrogen also affect the
1093 light yield, mainly via absorption and quenching mechanisms. Absorption occurs as
1094 the interaction of a 128 nm photon directly with the impurity dissolved in the liquid
1095 argon. Differently, quenching occurs as the interaction of an argon excimer and an
1096 impurity, where the excimer transfers its excitation to the impurity and dissociates
1097 non-radiatively. Given this mechanism, it is evident how quenching is both a function
1098 of the impurity concentrations and the excimer lifetime. Since the triplet states
1099 live much longer than the singlet states, quenching occurs mainly on triplet states,
1100 affecting primarily the slow component of the light, reducing the scintillation yield
1101 and a shortening of the scintillation time constants.

1102 The stringent constraints for the electron life time limit the presence of oxygen and
1103 water to such a low level that both absorption and quenching on these impurity is not

1104 expected to be significant. Contrarily, the nitrogen level is not bound by the electron
1105 life time constraints – nitrogen being an inert gas, expensive to filter. Thus, nitrogen
1106 is often present at the level provided by the vendor. The effects of nitrogen on argon
1107 scintillation light have been studied in the WArP R&D program and at several test
1108 stands. The quenching process induced by nitrogen in liquid Ar has been measured
1109 to be proportional to the nitrogen concentration, with a rate constant of ~ 0.11
1110 μs^{-1} ppm $^{-1}$; appreciable decreasing in lifetime and relative amplitude of the slow
1111 component have been shown for contamination as high as a few ppm of nitrogen [6].
1112 For a nitrogen concentration of 2 parts per million, typical of the current generation
1113 of LArTPC, the attenuation length due to nitrogen has been measured to be ~ 30
1114 meters [82].

1115 **Wavelength Shifting of LAr Scintillation Light**

1116 Liquid argon scintillation light is invisible for most optical detectors deployed in a
1117 LArTPC, such as cryogenic PMTs and SiPMs, since a wavelength of 128 nm is gen-
1118 erally too short to be absorbed from most in glasses, polymers and semiconductor
1119 materials. Research on prototype SiPMs absorbing directly VUV light and their
1120 deployment in noble gasses experiment is ongoing but not mature [120]. Thus, ex-
1121 periments need to shift the wavelength of scintillation light to be able to detect it.
1122 Albeit deployed in different ways, neutrinos and dark matter experiments commonly
1123 use 1,1,4,4-tetraphenyl-butadiene (TPB) to shift the scintillation light. TPB absorbs
1124 the vacuum ultraviolet (VUV) light and emits in the visible at ~ 425 nm [33], with
1125 a ratio of visible photon emitted per VUV photon absorbed of $\sim 1.2:1$ [66].

1126 Neutrino experiments typically coat their optical detector system evaporating a
1127 layer of TPB either directly on the PMTs glass surface or on acrylic plates mounted in
1128 front of the PMTs [60]; this technique allows the fast detection light coming directly
1129 from the neutrino interaction. Dark matter experiments typically evaporate TPB on

reflective foils mounted on the inside walls of the sensitive volume and detect the light after it has been reflected; this technique leads to a higher and more uniform light yield, though scattering effects for both the visible and VUV light augment the propagation time and hinder directionality information [61]. In order to take advantage of both these techniques, hybrid systems with PMT coating and foils are being considered for the next generation of large neutrino detectors.

2.1.5 Signal Processing and Event Reconstruction

In this section we illustrate the processing and reconstruction chain of the TPC signals, from the pulses on the sense wire to the construction of three dimensional objects with associated calorimetry. Different experiments can chose different software packages for their off line signal processing and event reconstruction, but a popular choice for US based LArTPCs is LArSoft [40]. Based on the Art framework [72], LArSoft is an event-based toolkit to perform simulation, analysis and reconstruction of LArTPCs events.

1144

LArTPC signal processing develops in several consecutive stages that we summarize here in the following categories: *Deconvolution*, *Hit Reconstruction*, *2D Clustering*, *3D Tracking*, *Calorimetry Reconstruction*. A visualization of the signal processing workflow is shown in figure 2.6.

1149

Deconvolution. Induction and collection planes have different field responses, given the different nature of the signals on these planes: the wires on the induction planes see the inductive signal of the drifting charge, while the wires on the collection planes see the current derived from the charge entering the conductor. Thus, signals on the induction plane are bi-polar pulse and signal on the collection plane are unipolar pulses, see Figure 2.6 panel a). The first step in signal processing is deconvolution,

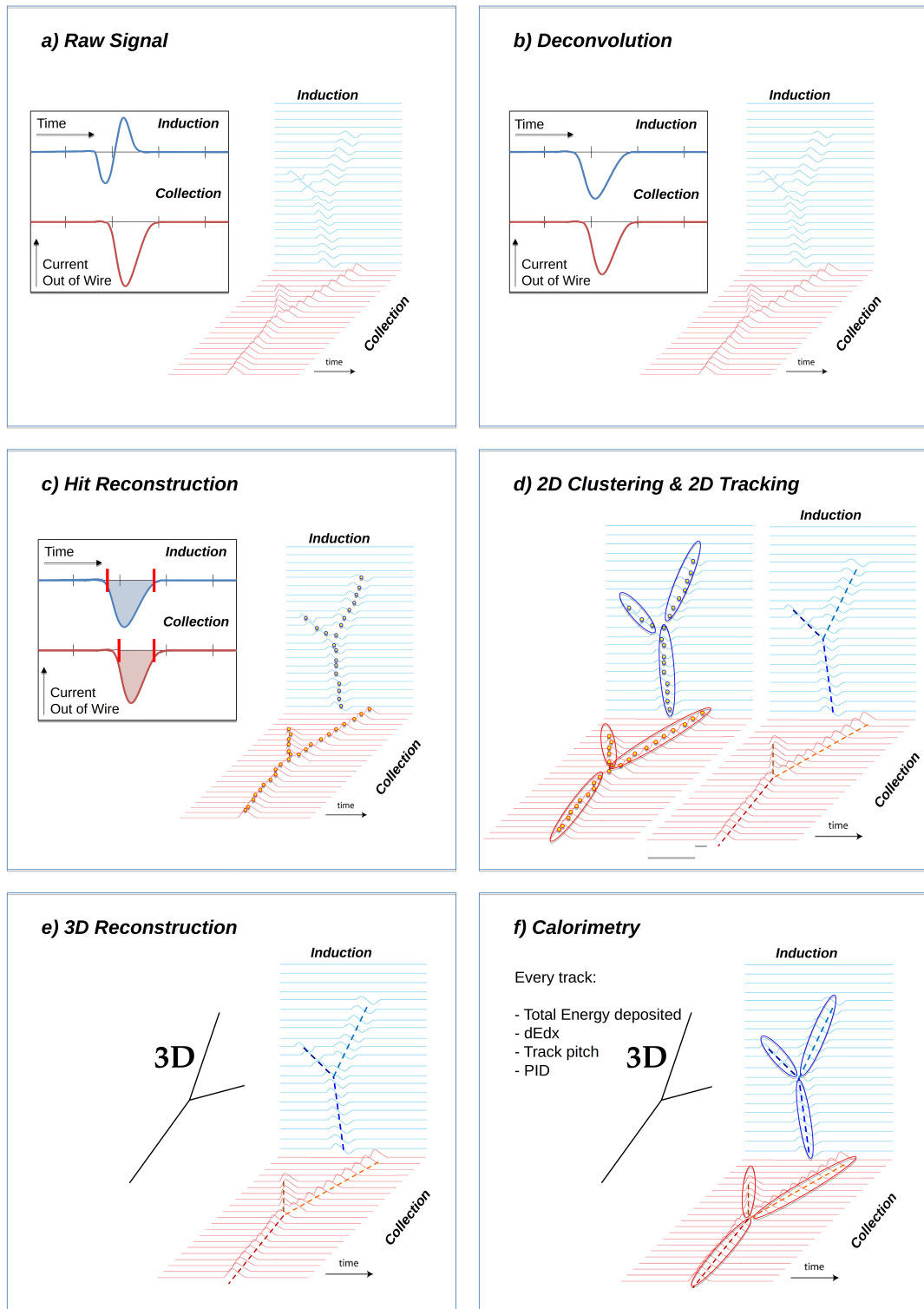


Figure 2.6: A scheme of a typical signal processing workflow in LArSoft.

1156 that is a series of off-line algorithms geared towards undoing the detector effects. The
1157 result of the deconvolution step is the production of a comparable set waveforms on
1158 all planes presenting unipolar, approximately gaussian-like pulses (Figure 2.6 panel
1159 b). Signal from all planes are treated on equal footage beyond this point. Some
1160 LArTPC apply noise filtering in the frequency domain just after the deconvolution
1161 to clean up wire cross talk. Since signals from the LArIAT TPC are extremely clean,
1162 noise filtering is not necessary.

1163

1164 **Hit Reconstruction.** The second stage of the signal processing is the recon-
1165 struction of hits, indicating an energy deposition in the detector. A peak finder scans
1166 the deconvolved TPC waveforms for each wire on the whole readout time looking for
1167 spikes above the waveform’s baseline. It then fits these peaks with gaussian shapes
1168 and stores the fit parameters such as the quality of the fit, the peak time, height and
1169 area under the gaussian fit. The information resulting from this process on a single
1170 spike form a single reconstructed “hit”, see Figure 2.6 panel c). The next steps in
1171 the event reconstruction chain will then decide if rejecting hits with poor fits. It is
1172 important to notice how the height and width of the hit depend on the topology of
1173 the event: for example, a particle running parallel to the wire planes will leave a series
1174 of sharp hits on many consecutive wires, while a particle traveling towards the planes
1175 will leave a long, wide hit on very few wires. The height of the hits and their integral
1176 is proportional to the charge collected on the wire, so it depends on the particle type.

1177

1178 The event reconstruction chain uses collection of hits to form more complex objects
1179 associated with the particles in the detector. The development of different approaches
1180 to accomplish this task is an extremely hot topic in LArTPC event reconstruction
1181 which spans from more traditional approaches such as line-clustering [26] to the use of
1182 machine learning tools [59]. Generally speaking, the scope of hit clustering and event

1183 reconstruction to provide shower-like or track like-objects with an associated energy
1184 reconstruction. This is because different particles have different topology in the de-
1185 tector – electrons and photon create electromagnetic showers, resulting in shower-like
1186 topologies, while muons and hadrons leave track-like signals. For the scope of these
1187 thesis, we will describe only LArIAT’s approach to track reconstruction even if we
1188 recognize the breath of LArTPC event reconstruction is much wider. We are inter-
1189 ested in the reconstruction of pions and kaons in the active volume, whose topology
1190 is track-like.

1191

1192 **2D Clustering Reconstruction.** The LArIAT reconstruction of track-like ob-
1193 jects starts by clustering hits on the collection and induction planes separately with
1194 the use of the TrajCluster clustering package [25]. TrajCluster looks for a collection
1195 of hits in the wire-time 2D space which can be described with a line-like 2D trajec-
1196 tory. TrajCluster reconstructs trajectories by adding trajectory points to the leading
1197 edge of the trajectory while stepping through the 2D space of hits. Several factors
1198 determine whether a hit is added to the trajectory, including but not limited to

- 1199 1. the goodness of the fit of the single hit,
- 1200 2. the charge of the hit compared to the average charge and RMS of the hits
1201 already forming the trajectory,
- 1202 3. the goodness of trajectory fit with and without the hit addition,
- 1203 4. the angle between the two lines formed by the collection of hits before and after
1204 the considered hit in the trajectory.

1205 The final product of this reconstruction stage is the collection of bidimensional clusters
1206 on each wire plane, see Figure 2.6 panel d).

1207 **3D Tracking.** The 3D tracking set of algorithms uses clusters close in time on
1208 the induction and collection planes as starting point to form a 3D track. Firstly, it

1209 construct a tentative 3D trajectory using the edges of the clusters. Then, it projected
1210 back the tentative trajectory on to the planes and adjusts the parameters of the 3D
1211 track fit such that they minimize the distance between the fit projections and the
1212 track hits in all wire planes simultaneously. Tridimensional tracking can use multiple
1213 clusters in one plane, but it can never break them in smaller groups of hits. This
1214 algorithm was first developed for the ICARUS collaboration [20]. The final product
1215 of this reconstruction stage is the formation of tridimensional objects in the TPC
1216 active volume, see Figure 2.6 panel e).

1217

1218 **Calorimetry.** The last step in the event reconstruction chain is to assign calorimetric
1219 information to the track (or shower) objects. Calorimetry is performed separately on the different planes. A multi-step procedure is needed to retrieve the energy
1220 deposited in the TPC from the charge seen by the wires. For each hit associated with
1221 the track object, the calorimetry algorithms calculate the charge seen on every wire
1222 using the area underneath the gaussian fit; then, they correct this raw charge by the
1223 electron life time, the electronic noise on the considered wire and the recombination
1224 effect. Lastly an overall calibration of the energy, explained in detail in section C,
1225 is applied and the calorimetric information for the given track is assigned. Even if
1226 calorimetry is done in 2D, it benefits from the 3D tracking information; typical information available after the calorimetric reconstruction are the total energy deposited
1227 by the particle and its stopping power dE/dx at each “track pitch”, i.e. at each 2D
1228 projection on the wire plane of the 3D trajectory.

1231 2.2 The Intensity Frontier Program

1232 This section highlights the role of Liquid Argon Time Projection Chambers at the
1233 Intensity frontier. In particular, we show the prospects for the exploration of neutrino

1234 physics (Section 2.2.1) and GUT models (Section 2.2.2) in current and forthcoming
1235 LAr experiments. In Section , we introduce LArIAT and its role in the Intensity
1236 Frontier panorama.

1237 **2.2.1 Prospects for LArTPCs in Neutrino Physics: SBN and**
1238 **DUNE**

1239 The ArgoNeut experiment [17] together the LAr R&D experiments TallBo and the
1240 Yale TPC initiated the US LArTPC neutrino program. Following the success of the
1241 ArgoNeut small TPC on the NuMI beam, a wide program of LArTPCs on neutrino
1242 beams has flourished. The construction of LArTPCs as near and far detectors at
1243 different baseline allows for the exploration of some of the fundamental questions in
1244 neutrino physics today illustrated in section 1.3.1.

1245 The Short-Baseline Neutrino (SBN) [21] program at Fermilab is tasked with con-
1246 clusively assess the nature of the “LSND and MiniBooNE anomalies” [14, 15, 23],
1247 resolving the mystery of sterile neutrinos at the eV² scale. The SBN program entails
1248 three surface LArTPCs positioned on the Booster Neutrino Beam at different dis-
1249 tances from the neutrino production in oder to fully exploit the L/E dependence of
1250 the oscillation pattern: SBND (100 m from the decay pipe), MicroBooNE (450 m),
1251 and ICARUS (600 m). Within the oscillation context, the choice of the LArTPC tech-
1252 nology for the SBN detectors changes the set of systematics with respect to LSND
1253 and MiniBooNE, whose detection techniques were both based on Cherenkov light.
1254 In particular, LArTPCs provide excellent electron/photon separation [9] lacking in
1255 Cherenkov detectors which can be leveraged to abate the photon background from
1256 neutral current interactions in ν_e searches. MicroBooNE [8], the first detector of the
1257 SBN program to be fully operational, started its first neutrino run in October 2015.
1258 MicroBooNE is a 89 ton active volume LArTPC, single drift chamber with TPC di-
1259 mensions of 2.6 m (drift) x 2.3 m (heigh) x 10.4 m (depth). MicroBooNE is positioned

at a very similar L/E on the Booster neutrino beam as MiniBooNE has the scope to directly cross check the MiniBooNE oscillation measurement. In case MicroBooNE confirms the presence of the “low energy excess” anomaly, SBND and ICARUS will provide the full measurement of the oscillation parameters. SBND and ICARUS are both dual drift chambers, whose active volume is respectively 112 ton and 600 ton. ICARUS is scheduled to become operational by the end of 2018 and SBND shortly after. Besides the oscillation analysis, the second main goals of SBN is to perform an extensive campaign of neutrino cross section measurements in argon. Given the importance of nuclear effects in (relatively) heavy materials, as discussed in section 1.2.3, both the oscillation analysis of the SBN program and the measurements of neutrino properties in DUNE will benefit from such a campaign.

On a different neutrino beam and baseline, the DUNE experiment, née LBNE [11], is the flagship experiment on the medium-long term of US-based neutrino physics, scheduled to start data taking in 2026. Shooting neutrinos from Fermilab for 800 miles to the SURF laboratory in South Dakota, DUNE is tasked with performing conclusive measurements of CP violation in the lepton sector, the neutrino mass ordering and the θ_{23} octant. The DUNE far detector will count four 10 kton LArTPCs, roughly of dimensions of 19 m (horizontally) x 18 m (vertically) x 66 m (depth).

2.2.2 Prospects for LArTPCs in GUT Physics: DUNE

The experimental exploration of a manifestation of Grand Unified Theory is possible in DUNE thanks to its sheer mass. In particular, proton decay searches are a capital topic of DUNE’s wide non-accelerator physics program. The key elements for a rare decay experiment are: massive active volume, long exposure, high identification efficiency and low background. Figure 2.7 shows the current best experimental limits on nucleon decay lifetime over branching ratio (dots). Historically, the dominant technology used in these searches has been water Cherenkov detectors: all the best

1286 experimental limits on every decay mode are indeed set by Super-Kamiokande [?, ?].
 1287 As shown in section 1.3.2, different family of GUTs predict the proton to decay in
 1288 different modes. In particular, SUSY flavored GUTs prefer the presence of kaons
 1289 in the decay products, e.g. $p \rightarrow K^+ \bar{\nu}$. It is particularly important to notice that
 1290 the kaon energy for the proton decay mode $p \rightarrow K^+ \bar{\nu}$ is under Cherenkov threshold
 1291 in water. Thus, Super-Kamiokande set the limit on the lifetime for the $p \rightarrow K^+ \bar{\nu}$
 1292 mode by relying on photons from nuclear de-excitation and on the muon tagging in
 1293 the kaon decay leptonic mode. For this reason, an attractive alternative approach to
 1294 identifying nucleon decay is the use of a LArTPCs, where the kaon is directly visible
 1295 in the detector. According to [11], DUNE will have an active volume large enough,
 1296 have sufficient shielding from the surface, and will run for lengths of time sufficient
 1297 to compete with Hyper-K, opening up the opportunity for the discovery of nucleon
 1298 decay.

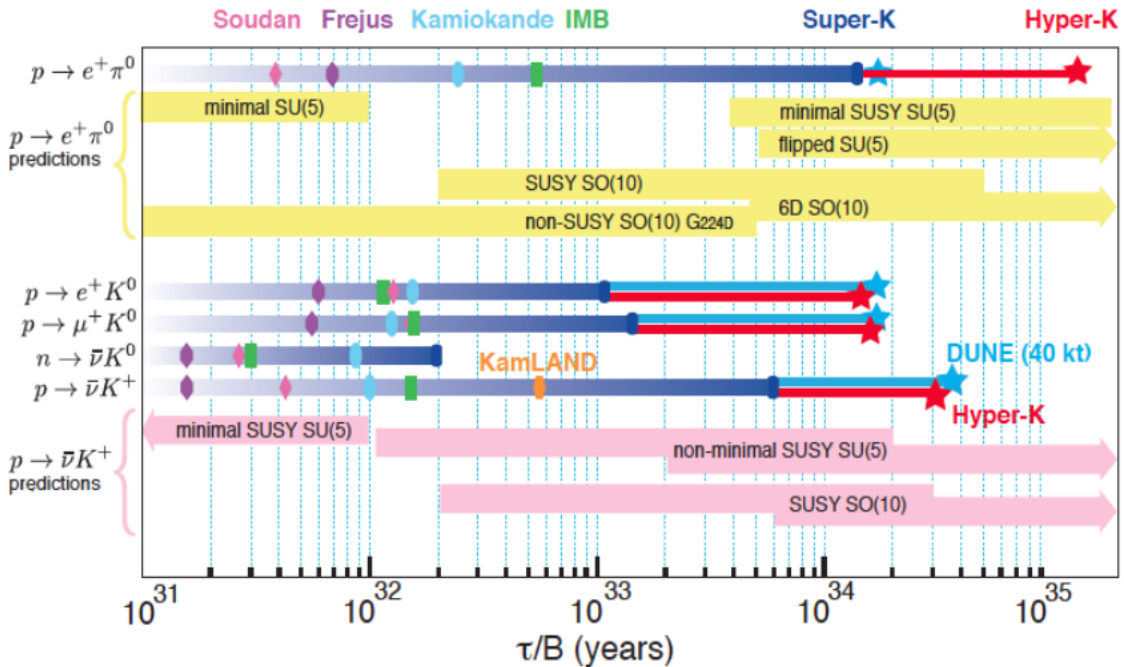


Figure 2.7: Proton decay lifetime limits from passed and future experiments.

1299 **2.2.3 Enabling the next generation of discoveries: LArIAT**

1300 LArIAT, a small LArTPC in a test beam, is designed to perform an extensive physics
1301 campaign centered on charged particle cross section measurements while characteriz-
1302 ing the detector performance for future LArTPCs. Since LArTPCs represent the most
1303 advanced experiments for physics at the Intensity Frontier, their complex technology
1304 needs a thorough calibration and dedicated measurements of some key quantities to
1305 achieve the precision required for the next generation of discoveries. LArIAT’s goal
1306 is to provide such calibration and dedicated measurements. The LArIAT LArTPC is
1307 deployed in a dedicated calibration test beamline at Fermilab. We use the LArIAT
1308 beamline to characterize the charge particles before they enter the TPC: the particle
1309 type and initial momentum is known from beamline information. The precise calori-
1310 metric energy reconstruction of the LArTPC technology enables the measurement of
1311 the total differential cross section for tagged hadrons. The Pion-Nucleus and Kaon-
1312 Nucleus total hadronic interaction cross section have never been measured before in
1313 argon and they are a fundamental step to shed light on light meson interaction in nu-
1314 clei per se, while providing a key input to neutrino physics and proton decay studies
1315 in future LArTPC experiments like SBN and DUNE.

1316 In order to showcase LArIAT’s utility to SBN and DUNE, we illustrate briefly
1317 two comparisons as examples: one regarding neutrino interactions and the second
1318 regarding proton decay studies.

1319 The left side of figure 2.8 shows the distribution of products in momentum spectrum
1320 and particle type as simulated in a ν_e CC interaction in DUNE (according to [87]);
1321 the range of these distribution is to compare with the momentum distribution of
1322 light particles in the LArIAT beamline – shown on the right side of figure 2.8. The
1323 momentum spectrum in the LArIAT beamline for electrons, muons and pions – the
1324 most abundant particles produced in a ν_e CC interaction – covers a wide range of the
1325 expected momentum distribution in a neutrino event.

1326 The signature of a proton decay event in the “LAr golden mode” is the presence of
 1327 a single kaon of about 400 MeV in the detector; the momentum spectrum of the kaon
 1328 pre and post FSI in such an event as simulated by GENIE is shown on the left side
 1329 of figure 2.9. The right side of figure 2.9 shows the momentum spectrum of kaons in
 1330 the LArIAT beamline. Kaons arriving to the LArIAT TPC are ideal for proton decay
 1331 studies, since their momentum in the beamline is just above the typical momentum
 1332 for kaons in a proton decay event: the majority of LArIAT kaons slow down in the
 1333 TPC enough to enter the desired momentum window.

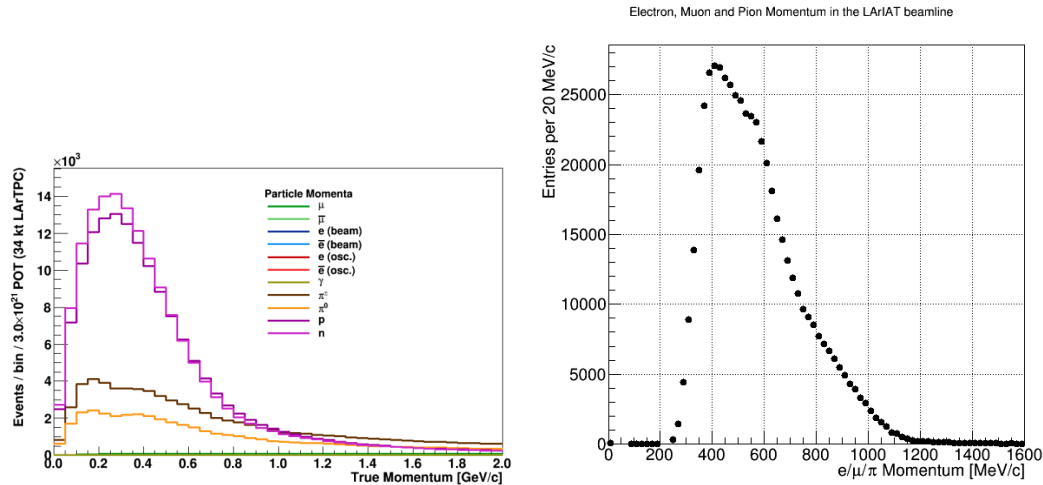


Figure 2.8: *Left.* Simulation of the products of a ν_e CC interaction in DUNE, both in particles type and momentum.
Right. Momentum spectrum for low mass particles (e, μ, π) in the LArIAT beamline, negative tune, Run II, Picky Tracks see section 3.2.2.

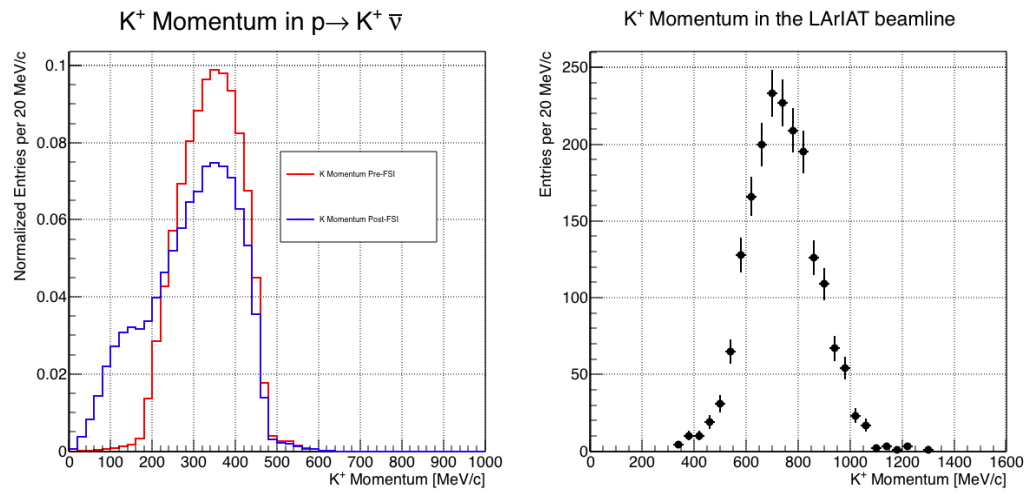


Figure 2.9: *Left.* Momentum of the kaon outgoing a proton decay $p \rightarrow K^+ \bar{\nu}$ event as simulated by the Genie 2.8.10 event generator in argon. The red line represents the kaon momentum distribution before undergoing the simulated final state interaction inside the argon nucleus, while the blue line represents the momentum distribution after FSI.

Right. Positive Kaon momentum spectrum in the LArIAT beamline, positive tune, Run II, Picky Tracks see section 3.2.2.

¹³³⁴ **Chapter 3**

¹³³⁵ **LArIAT: Liquid Argon In A**

¹³³⁶ **Testbeam**

¹³³⁷ “*But, hey we need to be somewhat foolish...*”

¹³³⁸ – Agnes Obel, 2010 –

¹³³⁹ In this chapter, we describe the LArIAT experimental setup. We start by illus-
¹³⁴⁰ trating the journey of the charged particles in the Fermilab accelerator complex, from
¹³⁴¹ the gaseous thermal hydrogen at the Fermilab ion source to the delivery of the LAr-
¹³⁴² IAT tertiary beam at MC7. We then describe the LArIAT beamline detectors, the
¹³⁴³ LArTPC, the DAQ and the monitoring system.

¹³⁴⁴ **3.1 The Particles’ Path to LArIAT**

¹³⁴⁵ LArIAT’s particle history begins in the Fermilab accelerator complex with a beam of
¹³⁴⁶ protons. The process of proton acceleration develops in gradual stages (see picture
¹³⁴⁷ 3.1): gaseous hydrogen is ionized in order to form H⁻ ions; these ions are boosted
¹³⁴⁸ to 750 keV by a Cockcroft-Walton accelerator and injected into the linear accelerator
¹³⁴⁹ (Linac) that increases their energy up to 400 MeV; then, H⁻ ions pass through a

1350 carbon foil and lose the two electrons; the resulting protons are then injected into a
1351 rapid cycling synchrotron, called the Booster; at this stage, protons reach 8 GeV of
1352 energy and are compacted into bunches; the next stage of acceleration is the Main
1353 Injector, a synchrotron which accelerates the bunches up to 120 GeV; in the Main
1354 Injector, several bunches are merged into one and are ready for delivery.

1355 The Fermilab accelerator complex works in supercycles of 60 seconds in duration.
1356 A 120 GeV primary proton beam with variable intensity is extracted in four-second
1357 “spills” and sent to the Meson Center beam line.

1358 LArIAT’s home at Fermilab is the Fermilab Test Beam Facility (FTBF), where
1359 the experiment characterizes a beam of charged particles in the Meson Center beam
1360 line. At FTBF, the primary beam is focused onto a tungsten target to create LAr-
1361 IAT’s secondary beam. The secondary beamline is set such that the composition of
1362 the secondary particle beam is mainly positive pions. The momentum peak of the
1363 secondary beam was fixed at 64 GeV/c for the LArIAT data considered in this work,
1364 although the beam is tunable in momentum between 8-80 GeV/c; this configuration
1365 of the secondary beamline assured a stable beam delivery at the LArIAT experimental
1366 hall.

1367 The secondary beam impinges then on a copper target within a steel collimator
1368 inside the LArIAT experimental hall (MC7) to create the LArIAT tertiary beam,
1369 (shown in Fig. 3.2). The steel collimator selects particles produced with a 13° pro-
1370 duction angle. The particles are then bent by roughly 10° through a pair of dipole
1371 magnets. By configuring the field intensity of the magnets we allow the particles of
1372 LArIAT’s tertiary beam to span a momentum range from 0.2 to 1.4 GeV/c. The
1373 polarity of the magnet is also configurable and determines the sign of the beamline
1374 particles which are focused on the LArTPC. If the magnet polarity is positive the
1375 tertiary beam composition is mostly pions and protons with a small fraction of elec-
1376 trons, muons, and kaons. It is the job of the LArIAT beamline equipment to select the

Fermilab Accelerator Complex

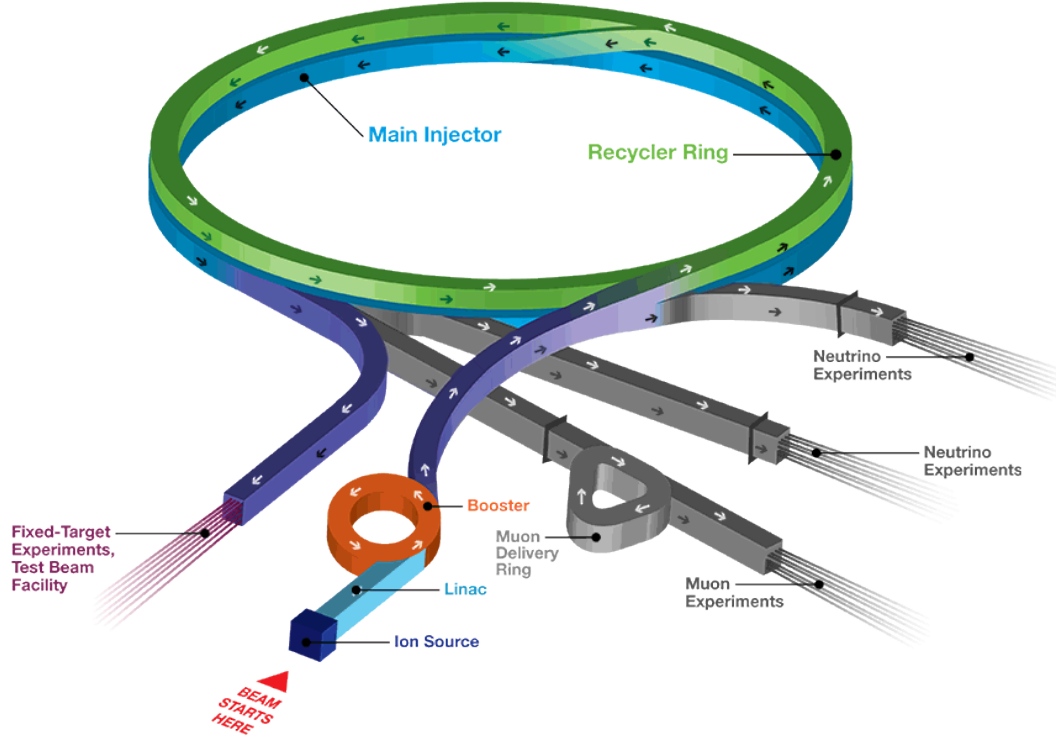


Figure 3.1: Layout of Fermilab Accelerator complex.

1377 particles polarity, to perform particle identification in the beamline and to measure
1378 the momentum of the tertiary beam particles before they get to the LArTPC. The
1379 LArIAT detectors are described in the following paragraphs.

1380 3.2 LArIAT Tertiary Beam Instrumentation

1381 The instrumentation of LArIAT tertiary beam and the TPC components have changed
1382 several times during the three years of LArIAT data taking. The following paragraphs
1383 describe the components operational during “Run II”, the data taking period relevant
1384 to the hadron cross section measurements considered in this thesis.

1385 The key components of the tertiary beamline instrumentation for the hadron cross
1386 section analyses are the two bending magnets, a set of four wire chambers (WCs)

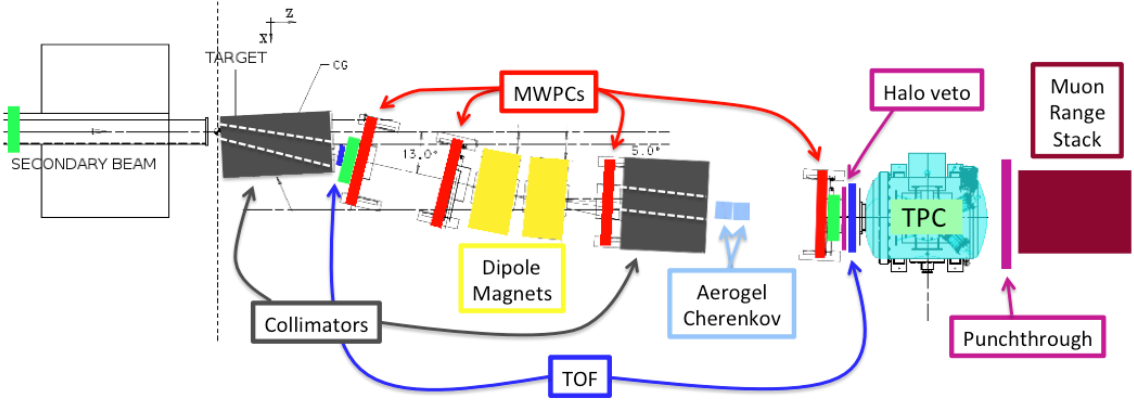


Figure 3.2: Bird’s eye view of the LArIAT tertiary beamline. In grey: upstream and downstream collimators; in yellow: bending magnets; in red: multi wire proportional chambers; in blue: time of flight; in green: liquid argon TPC volume; in maroon: muon range stack.

and two time-of-flight scintillating paddles (TOF) and, of course, the LArTPC. The magnets determine the polarity of the particles in the tertiary beam; the combination of magnets and wire chambers determines the particles’ momenta, which is used to determine the particle species in conjunction with the TOF. A muon range stack downstream from the TPC and two sets of cosmic paddles configured as a telescope surrounding the TPC are also used for calibration purposes. A couple of Aerogel Cherenkov counters, which we will not describe here as they are not used in the hadron cross section measurements, completes the beamline instrumentation.

3.2.1 Bending Magnets

LArIAT uses a pair of identical Fermilab type “NDB” electromagnets, recycled from the Tevatron’s anti-proton ring, in a similar configuration used for the MINERvA T-977 test beam calibration [56]. The magnets are a fundamental piece of the LArIAT beamline equipment, as they are used for the selection of the particle polarity and for the momentum measurement before the LArTPC. The sign of the current in the magnets allows us to select either positively or negatively charged particles; the value

1402 of the magnetic field is used in the momentum determination and in the subsequent
1403 particle identification.

1404 We describe here the characteristics and response of one magnet, as the second one
1405 has a similar response, given its identical shape and history. Each magnet is a box with
1406 a rectangular aperture gap in the center to allow for the particle passage. The magnet
1407 aperture measures 14.22 cm in height, 31.75 cm in width, and 46.67 cm in length.
1408 Since the wire chambers aperture ($\sim 12.8 \text{ cm}^2$) is smaller than the magnet aperture,
1409 only the central part of the magnet gap is utilized. The field is extremely uniform
1410 over this limited aperture and was measured with two hall probes, both calibrated
1411 with nuclear magnetic resonance probes. The probes measured the excitation curve
1412 shown in Figure 3.3.

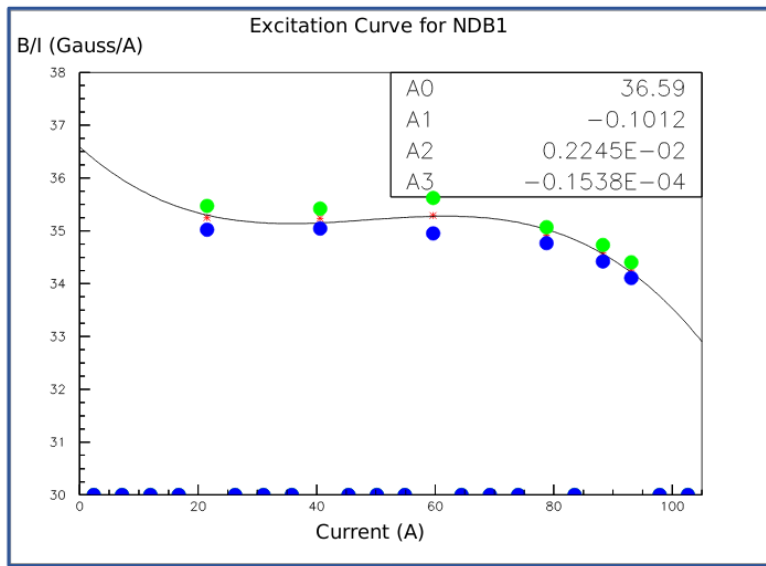


Figure 3.3: Magnetic field over current as a function of the current, for one NDB magnet (excitation curve). The data was collected using two hall probes (blue and green). We fit the readings with a cubic function (black) to average of measurements (red) given in the legend [43].

1413 The current through the magnets at a given time is identical in both magnets.
1414 For the Run II data taking period, the current settings explored were 60A ($B \sim 0.21$
1415 T) and 100A ($B \sim 0.35$ T) in both polarities. Albeit advantageous to enrich the
1416 tertiary beam composition with high mass particles such as kaons, we never pushed

1417 the magnets current over 100 A, not to incur in overheating. During operation, we
1418 operated an air and water cooling system on the magnets and we remotely monitored
1419 the magnet temperatures.

1420 **3.2.2 Multi-Wire Proportional Chambers**



Figure 3.4: One of the four Multi Wire Proportional Chambers (WC) used in the LArIAT tertiary beamline and related read-out electronics.

1421 LArIAT uses four multi-wire proportional chambers, or wire chambers (WC) for
1422 short, two upstream and two downstream from the bending magnets. The geometry of
1423 one chamber is shown in Figure 3.4: the WC effective aperture is a square of 12.8 cm
1424 perpendicular to the beam direction. Inside the chamber, the 128 horizontal and 128
1425 vertical wires strung at a distance of 1 mm from each other in a mixture of 85% Argon
1426 and 15% isobutane gas. The WC operating voltage is between 2400 V and 2500 V.
1427 The LArIAT wire chambers are an upgraded version of the Fenker Chambers [62],
1428 where an extra grounding improves the signal to noise ratio of the electronic readout.

1429 Two ASDQ chips [95] mounted on a mother board plugged into the chamber serve
1430 as front end amplifier/discriminator. The chips are connected to a multi-hit TDC [73]
1431 which provides a fast OR output used as first level trigger. The TDC time resolution
1432 is 1.18 ns/bin and can accept 2 edges per 9 ns. The maximum event rate acceptable
1433 by the chamber system is 1 MHz: this rate is not a limiting factor considering that

1434 the rate of the tertiary particle beam at the first wire chamber is estimated to be less
1435 than 15 kHz. A full spill of data occurring once per supercycle is stored on the TDC
1436 board memory at once and read out by a specially designed controller. We use LVDS
1437 cables to carry both power and data between the controller and the TDCs and from
1438 the controller to the rest of the DAQ.

1439 Multi-Wire Proportional Chambers functionality

1440 We use the wire chamber system together with the bending magnets to measure the
1441 particle's momentum.

1442 In the simplest scenario, only one hit on each and every of the four wire chambers
1443 is recorded during a single readout of the detector systems. Thus, we use the hit
1444 positions in the two wire chambers upstream of the magnets to form a trajectory
1445 before the bend, and the hit positions in the two wire chambers downstream of the
1446 magnets to form a trajectory after the bend. We use the angles in the XZ plane
1447 between the upstream and downstream trajectories to calculate the Z component of
1448 the momentum as follows:

$$P_z = \frac{B_{eff}L_{eff}}{3.3(\sin(\theta_{DS}) - \sin(\theta_{US}))}, \quad (3.1)$$

1449 where B_{eff} is the effective maximum field in a square field approximation, L_{eff}
1450 is the effective length of both magnets (twice the effective length of one magnet),
1451 θ_{US} is the angle off the z axis of the upstream trajectory, θ_{DS} is the angle off the
1452 z axis of the downstream trajectory and $3.3 c^{-1}$ is the conversion factor from [T·m]
1453 to [MeV/c]. By using the hit positions on the third and fourth wire chamber, we
1454 estimate the azimuthal and polar angles of the particle trajectory, and we are able to
1455 calculate the other components of the momentum.

1456 The presence of multiple hits in a single wire chamber or the absence of hits in one
1457 (or more) wire chambers can complicate this simple scenario. The first complication

1458 is due to beam pile up, while the latter is due to wire chamber inefficiency. In the
1459 case of multiple hits on a single WC, at most one wire chamber track is reconstructed
1460 per event. Since the magnets bend particles only in the X direction, we assume
1461 the particle trajectory to be roughly constant in the YZ plane, thus we keep the
1462 combination of hits which fit best with a straight line. It is still possible to reconstruct
1463 the particle’s momentum even if the information is missing in either of the two middle
1464 wire chambers (WC2 or WC3), by constraining the particle trajectory to cross the
1465 plane in between the magnets.

1466 Events satisfying the simplest scenario of one single hit in each of the four wire
1467 chambers form the “Picky Track” sample. We construct another, higher statistics
1468 sample, where we loosen the requirements on single hit and wire chamber efficiency:
1469 the “High Yield” sample. For LArIAT Run II, the High Yield sample is about three
1470 times the Picky Tracks statistics. We assume an uncertainty of 2% for four-point WC
1471 track, momentum uncertainty as reported for the same beamline in [56].

1472 3.2.3 Time-of-Flight System

1473 Two scintillator paddles, one upstream of the first set of WCs and one downstream
1474 of the second set of WCs form LArIAT time-of-flight (TOF) detector system.

1475 The upstream paddle is made of a 10 x 6 x 1 cm scintillator piece, read out by
1476 two PMTs mounted on the beam left side which collect the light from light guides
1477 mounted on all four edges of the scintillator. The downstream paddle is a 14 x 14 x
1478 1 cm scintillator piece read out by two PMTs on the opposite ends of the scintillator,
1479 as shown in figure 3.5. The relatively thin width in the beamline direction minimizes
1480 energy loss of beam particles traveling through the scintillator material.

1481 The CAEN 1751 digitizer is used to digitize the TOF PMTs signals at a sampling
1482 rate of 1 GHz. The 12 bit samples are stored in a circular memory buffer. At trigger
1483 time, data from the TOF PMTs are recorded to output in a 28.7 μ s windows starting

1484 approximately 8.4 μ s before the trigger time.

1485 **TOF functionality**

1486 The TOF signals rise time (10-90%) is 4 ns and a full width, half-maximum of 9 ns
1487 consistent in time. The signal amplitudes from the upstream TOF and downstream
1488 TOF are slightly different: 200 mV for the upstream PMTs but only 50 mV for
1489 downstream PMTs. The time of the pulses was calculated utilizing an oversampled
1490 template derived from the data itself. We take the pulse pedestal from samples
1491 far from the pulse and subtract it from the pulse amplitude. We then vertically
1492 stretch a template to match the pedestal-subtracted pulse amplitude and we move
1493 it horizontally to find the time. With this technique, we find a pulse time-pickoff
1494 resolution better than 100 ps. The pulse pile up is not a significant problem given
1495 the TOF timing resolution and the rate of the particle beam. Leveraging on the
1496 pulses width uniformity of any given PMT, we flag events where two pulses overlap
1497 as closely in time as 4 ns with a 90% efficiency according to simulation.

1498 We combine the pulses from the two PMTs on each paddle to determine the
1499 particles' arrival time by averaging the time measured from the single PMT, so to
1500 minimize errors due to optical path differences in the scintillator. However, a time
1501 spread of approximately 300 ps is present in both the upstream and downstream
1502 detectors, likely due to transit time jitter in the PMTs themselves.

1503 **3.2.4 Punch-Through and Muon Range Stack Instruments**

1504 The punch-through and the muon range stack (MuRS) detectors are located down-
1505 stream of the TPC. These detectors provide a sample of TPC crossing tracks without
1506 relying on TPC information and can be used to improve particle ID for muons and
1507 pions with momentum higher than 450 MeV/c.

1508 The punch-through is simple sheet of scintillator material, read out by two PMTs.



Figure 3.5: Image of the down stream time of flight paddle, PMTs and relative support structure before mounting.

1509 The MuRS is a segmented block of steel with four slots instrumented with scintillation
1510 bars. The four steel layers in front of each instrumented slot are 2 cm, 2 cm, 14 cm
1511 and 16 cm deep in the beam direction. Each instrumented slot is equipped with
1512 four scintillation bars each, positioned horizontally in the direction orthogonal to the
1513 beam. Each scintillator bar measures ? x ? x 2 cm and it is read out by one PMT.

1514 The signals from both the punch-thorough and the MuRS PMTs are sent to a
1515 NIM discriminator. If the signal crosses the discriminator threshold, it is digitized in
1516 the CAEN V1740, same as the TPC. The sampling time of the CAEN V1740 is slow
1517 (of the order of 128 ns) and that the pulse shape information from the PMT is lost.
1518 A Punch-thorough and MuRS signal will then be simply a “hit” at a given time in
1519 the beamline event.

1520 It is worth mentioning here the presence of an additional scintillation paddle
1521 between WC4 and the downstream paddle of the TOF system, called halo. The
1522 halo is a 39x38x1 cm³ paddle with a 6.5 cm radius hole in the center, whose original
1523 function was to reject beam particles slightly offset from the beamline center. Data

1524 from this paddle turned out to be unusable, so our data events include both particle
1525 going through the halo scintillation material or through the halo hole.

1526 **3.2.5 LArIAT Cosmic Ray Paddle Detectors**

1527 LArIAT triggers both on beam events and on cosmic rays events. We perform this
1528 latter trigger by using two sets of cosmic ray paddle detectors (a.k.a. “cosmic towers”.)
1529 The cosmic towers frame the LArIAT cryostat, as one sits in the downstream left
1530 corner and the other sits in the upstream right corner of the cryostat. Two paddle
1531 sets of four scintillators pieces each make up each cosmic tower, an upper set and a
1532 lower set per tower. Of the four paddles, a couple of two matched paddles stands
1533 upright while the a second matched pair lies across the top of the assembly in the top
1534 sets (or across the bottom of the assembly in the bottom sets). The horizontal couple
1535 is used as a veto for particles traveling from inside the TPC out. The four signals
1536 from the vertical paddles along one of the body diagonals of the TPC are combined
1537 in a logical “AND”. This allows to select track due to cosmic muons at the ground
1538 level crossing the TPC along one of its diagonals. Cosmic ray muons whose average
1539 energy is in the few GeV range crossing both anode and cathode populate the events
1540 triggered this way. This particularly useful sample of tracks is associated can be used
1541 for many tasks; for example, we use anode-cathode piercing tracks to cross check
1542 the TPC electric field on data (see Appendix A), to calibrate the charge response of
1543 the TPC wires for the full TPC volume and to measure the electron lifetime in the
1544 chamber [104].

1545 We retrieved the scintillation paddles from the decommissioning of the CDF de-
1546 tector at Fermilab and we used only the paddles with a counting efficiency greater
1547 than 95% and low noise at working voltage. The measured trigger rate of the whole
1548 system is 0.032 Hz, corresponding to ~ 2 muons per minute.



Figure 3.6: Photograph of one of the scintillation counters used in the cosmic towers.

1549 3.3 In the Cryostat

1550 The heart of the LArIAT experiment lives in the LArIAT cryostat. In this section,
1551 we describe the cryogenic system and the argon purity (Section 3.3.1), the LArIAT
1552 TPC (Section 3.3.2) and light collection system (3.3.3).

1553 3.3.1 Cryogenics and Argon Purity

1554 LArIAT repurposed the ArgoNeuT cryostat [17] in order to use it in a beam of charged
1555 particles, and added a new process piping and a new liquid argon filtration system in
1556 FTBF. Inside the LArIAT experimental hall, the cryostat sits in the beam of charged
1557 particles with its horizontal main axis oriented parallel to the secondary beam, 3°
1558 off axis from the tertiary beam

1559 Two volumes make up LArIAT cryostat, shown in Figure 3.7: the inner vessel and
1560 the outer vessel. Purified liquid argon fills the inner vessel, while the outer volume
1561 provides insulation through a vacuum jacket equipped with layers of aluminized mylar
1562 superinsulation. The inner vessel is a cylinder of 130 cm length and 76.2 cm diameter,
1563 containing about 550 L of LAr, corresponding to a mass of 0.77 ton. We run the signal
1564 cables for the LArTPC and the high voltage feedthrough through a “chimney” at the
1565 top and mid-length of the cryostat.

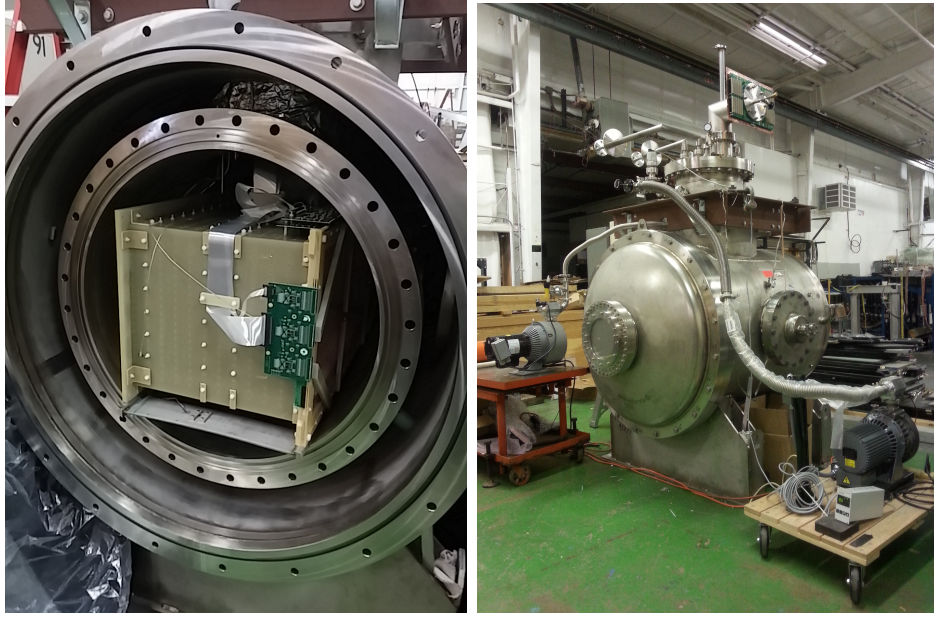


Figure 3.7: Left: the LArIAT TPC in the inner volume of the open cryostat. Right: cryostat fully sealed ready to be transported to FTBF.

Given the different scopes of the ArgoNeuT and LArIAT detectors, we made several modifications to the ArgoNeuT cryostat in order to use it in LArIAT. In particular, the modifications shown in Figure 3.8 were necessary to account for the beam of charged particles entering the TPC and to employ the new FTBF liquid argon purification system. We added a “beam window” on the front outer end cap and an “excluder” on the inner endcap, with the purpose of minimizing the amount of non-instrumented material upstream of the TPC’s active volume. The amount of non-instrumented material in front of the TPC for LArIAT corresponds to ~ 0.3 electron radiation lengths (X_0), to compare against the $\sim 1.6X_0$ of ArgoNeuT. To allow studies of the scintillation light, we added a side port feedthrough which enables the mounting of the light collection system, as well as the connections for the corresponding signal and high-voltage cables (see Section 3.3.3). We modified the bottom of the cryostat adding Conflat and ISO flange sealing to connect the liquid argon transfer line to the new argon cooling and purification system.

As in any other LArTPC, argon purity is a crucial parameter for LArIAT. Indeed,

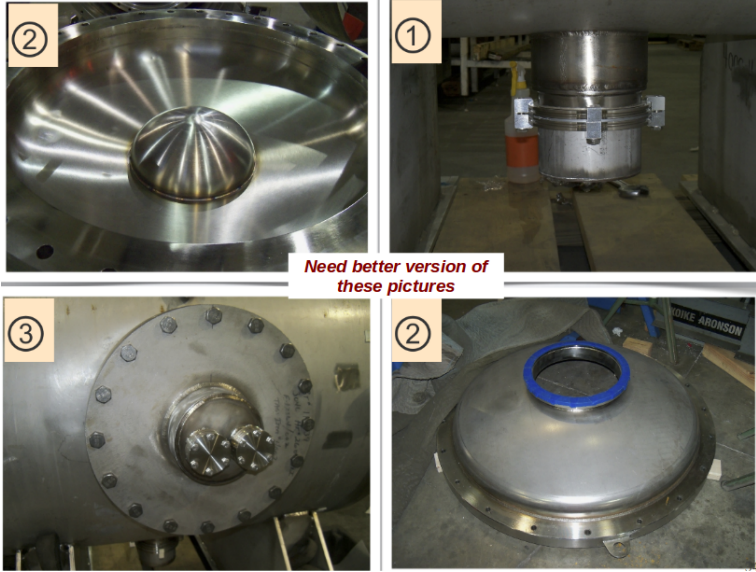


Figure 3.8: Main modifications to the ArgoNeuT cryostat: 1) outlet for connection to the purification system at the bottom of the cryostat; 2) the “beam-window” on the outer endcap and “excluder” which reduces the amount of non-instrumented material before the TPC; 3) the side port to host the light collection system.

1581 the presence of contaminants affects both the basic working principles of a LArTPC,
 1582 as shown in section 2.1.2: electronegative contaminants such as oxygen and water de-
 1583 crease the number of ionization electrons collected on the wires after drifting through
 1584 the volume. In addition, contaminants such as Nitrogen decrease the light yield
 1585 from scintillation light, especially in its slow component. In LArIAT, contaminations
 1586 should not exceed the level of 0.2 parts per billion (ppb). We achieve this level of
 1587 purity in several stages. The specifics required for the commercial argon bought for
 1588 LArIAT are 2 parts per million (ppm) oxygen, 3.5 ppm water, and 10 ppm nitrogen.
 1589 This argon is monitored with the use of commercial gas analyzer. Argon is stored in
 1590 a dewar external to LArIAT hall and filtered before filling the TPC. LArIAT uses a
 1591 filtration system designed for the Liquid Argon Purity Demonstrator (LAPD) [57]:
 1592 half of a 77 liter filter contains a 4A molecular sieve (Sigma-Aldrich [110]) able to re-
 1593 move mainly water, while the other half contains BASF CU-0226 S, a highly dispersed
 1594 copper oxide impregnated on a high surface area alumina, apt to remove mainly oxy-

1595 gen [27]. A single pass of argon in the filter is sufficient to achieve the necessary
1596 purity, unless the filter is saturated. In case the filter saturates, the media needs to
1597 be regenerated by using heated gas; this happened twice during the Run II period¹.
1598 The electron lifetime during the full LArIAT data taking are shown in Figure 2.4.
1599 The filtered argon reaches the inner vessel via a liquid feedthrough which is routed to
1600 the bottom of the cryostat. Argon is not recirculated in the system; rather, it boils
1601 off and vents to the atmosphere. During data taking, we replenish the argon in the
1602 cryostat every 6 hours to keep the TPC high voltage feedthrough and cold electronics
1603 always submerged. In fact, we constantly monitor the level, temperature, and pres-
1604 sure of the argon both in the commercial dewar and inside the cryostat during data
1605 taking.

1606 **3.3.2 LArTPC: Charge Collection**

1607 The LArIAT Liquid Argon Time Projection Chamber is a rectangular box of dimen-
1608 sions 47 cm (drift) x 40 cm (height) x 90 cm (length), containing 170 liters of Liquid
1609 Argon. The LArTPC three major subcomponents are

- 1610 1) the cathode and field cage,
- 1611 2) the wire planes,
- 1612 3) the read-out electronics.

1613 **Cathode and field cage**

1614 A G10 plain sheet with copper metallization on one of the 40 x 90 cm inner surfaces
1615 forms the cathode. A high-voltage feedthrough on the top of the LArIAT cryostat
1616 delivers the high voltage to the cathode; the purpose of the high voltage system

1. We deemed the filter regeneration necessary every time the electron lifetime dropped under 100 μs.

1617 (Figure 3.9) is to drift ionization electrons from the interaction of charged particles
1618 in the liquid argon to the wire planes. The power supply used in this system is a
1619 Glassman LX125N16 [70] capable of generating up to -125 kV and 16 mA of current,
1620 but operated at -23.5kV during LArIAT Run-II. The power supply is connected via
1621 high voltage cables to a series of filter pots before finally reaching the cathode.

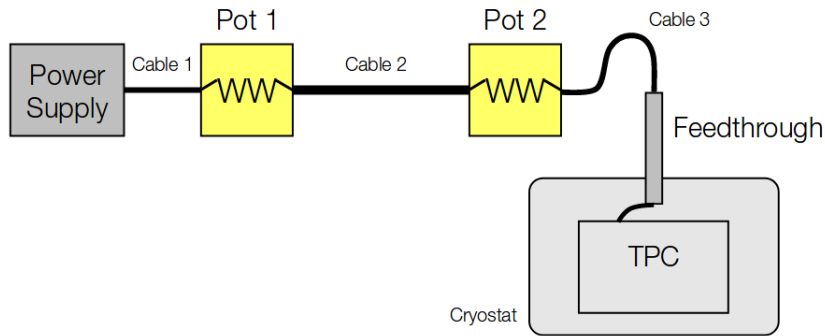


Figure 3.9: Schematic of the LArIAT high voltage system.

1622 The field cage is made of twenty-three parallel copper rings framing the inner walls
1623 of the G10 TPC structure. A network of voltage-dividing resistors connected to the
1624 field cage rings steps down the high voltage from the cathode to form a uniform electric
1625 field. The electric field over the entire TPC drift volume is 486 V/cm, as measured
1626 in appendix A. The maximum drift length, i.e. the distance between cathode and
1627 anode planes, is 47 cm.

1628 Wire planes

1629 LArIAT Run-II has three wire planes separated by 4 mm spaces: in order of increasing
1630 distance from the cathode, they are the shield, the induction and the collection plane.
1631 The “wire pitch”, i.e., the distance between two adjacent wires in a given plane, is
1632 4 mm. The shield plane counts 225 parallel wires of equal length oriented vertically.
1633 This plane is not connected with the read-out electronics; rather it shields the outer
1634 planes from extremely long induction signals due to the ionization in the whole drift

volume. As the shield plane acts almost like a Faraday cage, the resulting shape of signals in the first instrumented plane (induction) is easier to reconstruct. Both the induction and collection planes count 240 parallel wires of different length oriented at 60° from the vertical with opposite signs. Electrons moving past the induction plane will induce a bipolar pulse on its wires; the drifting electrons will be then collected on the collection plane's wires, forming a unipolar pulse.

The three wire planes and the cathode form three drift volumes, as shown in Figure 3.10. The main drift volume is defined as the region between the cathode plane and the shield plane (C-S). The other two drift regions are those between the shield plane and the induction plane (S-I), and between the induction plane and the collection plane (I-C). The electric field in these regions is chosen to satisfy the charge transparency condition and allow for 100% transmission of the drifting electrons through the shield and the induction planes.

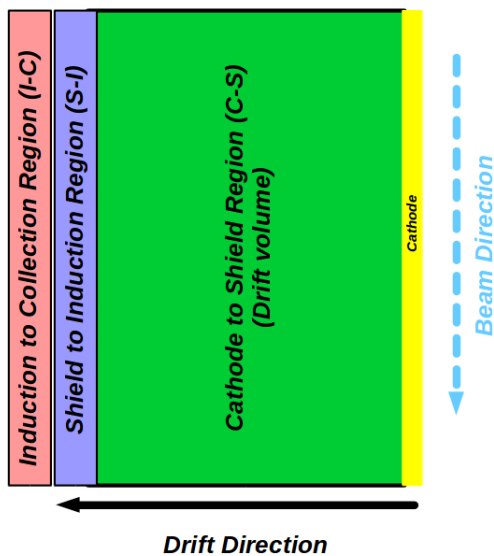


Figure 3.10: Schematic of the three drift regions inside the LArIAT TPC: the main drift volume between the cathode and the shield plane (C-S) in green, the region between the shield plane and the induction plane (S-I) in purple, and the region between the induction plane and the collection plane (I-C) in pink.

Table 3.1 provides the default voltages applied to the cathode and the shield,

1649 induction, and collection plane.

Table 3.1: Cathode and anode planes default voltages

Cathode	Shield	Induction	Collection
-23.17 kV	-298.8 V	-18.5 V	338.5 V

1650 **Electronics**

1651 Dedicated electronics read the induction and collection plane wires, for a total of
1652 480-channel analog signal path from the TPC wires to the signal digitizers. A digital
1653 control system for the TPC-mounted electronics, a power supply, and a distribution
1654 system complete the front-end system. Figure 3.11 shows a block diagram of the
1655 overall system. The direct readout of the ionization electrons in liquid argon forms
1656 typically small signals on the wires, which need amplification in oder to be processed.
1657 LArIAT performs the amplification stage directly in cold with amplifiers mounted
1658 on the TPC frame inside the liquid argon. The BNL ASICs adopted in LArIAT are
1659 designated as LArASIC, version 4-star and are the same used by the MicroBooNE
1660 experiment [60]. The signal from the ASICs are driven to the other end of the readout
1661 chain, to the CAEN V1740 digitizers [35]. The CAEN V1740 has a 12 bit resolution
1662 and a maximum input range of 2 VDC, resulting in about 180 ADC count for a
1663 crossing MIP.

1664 **3.3.3 LArTPC: Light Collection System**

1665 The collection of scintillation photons is the second mechanism of particle detection
1666 in argon other than the ionization electrons. Over the course of LArIAT's three years
1667 of data taking, the light collection system changed several times. We describe here
1668 the light collection system for Run II. Two PMTs, a 3-inch diameter Hamamatsu
1669 R-11065 and 2-inch diameter ETL D757KFL [7], as well as three SiPMs arrays (two
1670 Hamamatsu S11828-3344M 4x4 arrays and one single-channel SensL MicroFB-60035)

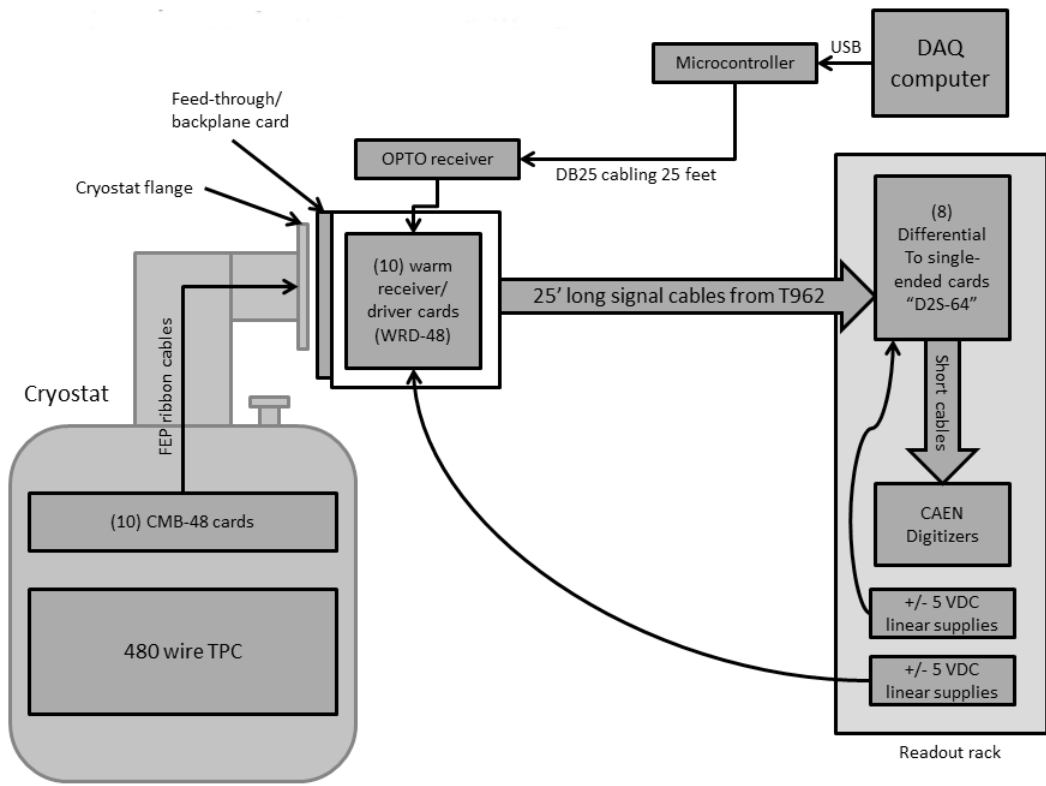


Figure 3.11: Overview of LArIAT Front End electronics.

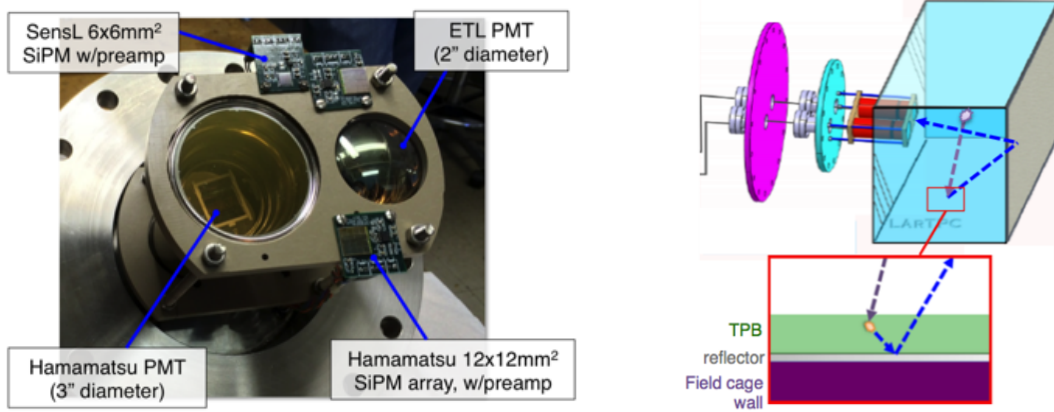


Figure 3.12: LArIAT’s photodetector system for observing LAr scintillation light inside the TPC (left), and a simplified schematic of VUV light being wavelength-shifting along the TPB-coated reflecting foils (right).

1671 are mounted on the PEEK support structure. PEEK screws into an access flange
 1672 as shown in Figure 3.12, on the anode side, leaving approximately 5 cm of clearance
 1673 from the collection plane.

1674 Liquid argon scintillates in vacuum-ultraviolet (VUV) range at 128 nm; since
 1675 cryogenic PMTs are not sensitive to VUV wavelengths, we need to shift the light to a
 1676 range that is visible to the PMTs. In LArIAT, the wavelength shifting is achieved by
 1677 installing highly-reflective 3M VIKUITI dielectric substrate foils coated with a thin
 1678 layer of tetraphenyl-butadiene (TPB) on the four unbiased walls of the TPC. The
 1679 scintillation light interaction with the TPB emits one or more visible photons, which
 1680 are then reflected into the chamber. Thus, the light yield increases and results in
 1681 higher uniformity of light across the TPC active volume, allowing the possibility of
 1682 light-based calorimetry, currently under study.

1683 For Run II, we coated the windows of the ETL PMT and the SensL SiPM with
 1684 a thin layer of TPB. In doing so, some of the VUV scintillation light converts into
 1685 visible right at the sensor faces, keeping information on the direction of the light
 1686 source. Information about the light directionality is hindered for the light reflected
 1687 on foils, as the reflection is uniform in angle.

1688 3.4 Trigger and DAQ

1689 The LArIAT DAQ and trigger system governs the read out of all the many subsystems
1690 forming LArIAT. The CAEN V1495 module [34] and its user-programmable FPGA
1691 are the core of this system. Every 10 ns, this module checks for matches between
1692 sixteen logical inputs and user-defined patterns in the trigger menu; if it finds a match
1693 for two consecutive clock ticks, that trigger fires.

1694 LArIAT receives three logic signals from the Fermilab accelerator complex related
1695 to the beam timing which we use as input triggers: a pulse just before the beam, a
1696 pulse indicating beam-on, and a beam-off pulse.

1697 The beam instruments, the cosmic ray taggers, and the light collection system
1698 provide the other NIM-standard logic pulse inputs to the trigger decision. We auto-
1699 matically log the trigger inputs configuration with the rest of the DAQ configuration
1700 at the beginning of each run.

1701 Fundamental inputs to the trigger card come from the TOF (see section 3.2.3)
1702 and the wire chambers (see section 3.2.2), as activity in these systems points to the
1703 presence of a charged particle in tertiary beam line. In particular, the discriminated
1704 pulses from the TOF PMTs form a NIM logic pulse for the trigger logic. We ask
1705 for a coincidence within a 20 ns window for all the pulses from the PMTs looking at
1706 the same scintillator block and use a delayed coincidence between the upstream and
1707 downstream paddle to inform the trigger decision. In order to form a coincidence
1708 between the upstream and downstream paddles, we delay the upstream paddle coin-
1709 cidence by 20 ns and widen it by 100 ns. The delay and widening are necessary to
1710 account for both lightspeed particles and slower particles (high-mass) to travel the
1711 6.5 m between the upstream and the downstream paddles. For the read out of the
1712 wire chambers, we use a total of sixteen multi-hit TDCs [73], four per chamber: two
1713 TDC per plane (horizontal and vertical), sixty-four wires per TDC. In each TDC, we
1714 keep the logical “OR” for any signal over threshold from the sixty-four wires. We

1715 then require a coincidence between the “OR” for the horizontal TDCs and the “OR”
1716 for the vertical TDCs: with this logic we make sure that at least one horizontal wire
1717 and one vertical wire saw significant signal in one wire chamber. The single logical
1718 pulse from each of the four wire chambers feeds into the first four inputs to the V1495
1719 trigger card. We require a coincidence within 20 ns of at least three logical inputs to
1720 form a trigger.

1721 The cosmic towers (see Section 3.2.5) provide another primary input to the trigger,
1722 in order to capture long tracks from cosmic muons crossing the TPC. We use NIM
1723 modules to require coincidences between one upper and one lower paddle set of any
1724 opposite cosmic towers. The OR all the opposite towers’ coincidences is fed as an
1725 input to the trigger card.

1726 We use the signal from the cryogenic PMTs (see Section 3.3.3) to form several
1727 interesting triggers. The coincidence of signals from all the PMT pulses within \sim 20 ns
1728 is an indication of ionizing radiation in the TPC and forms a trigger input. The
1729 coincidence of two subsequent scintillation logic pulses delayed by a maximum of $7 \mu\text{s}$
1730 forms the Michel electron trigger.

1731 **3.5 Control Systems**

1732 LArIAT is a complex ensemble of systems which needed to be monitored simultane-
1733 ously during data taking. We performed the monitoring of the systems operations
1734 with a slow control system, a DAQ monitoring system and a low level data quality
1735 monitoring described in the following sections.

1736 **Slow Control**

1737 We used the Synoptic Java Web Start framework [19] as a real-time display of subsys-
1738 tem conditions. Synoptic provides a Graphical User Interface that talks to the Fer-

milab Accelerator Control System via the ACNET protocol. Its simple GUI allowed us to change the operating parameters and to graph the trends of several variables of interest for all of the tertiary beam detectors. Among the most important quantities monitored by Synoptic there are the level of argon in both the inner vessel and the external dewar, the operating voltages of cathode and wire planes, of the PMTs and SiPMs, and of the four wire chambers, as well as the magnet temperatures. Figure 3.13 shows an example of the monitoring system. LArIAT uses the Accelerator Control NETwork system (ACNET) to monitor the beam conditions of the MCcenter beamline. For example, the horizontal and vertical position of the beam at the first two wire chambers (WC1 and WC2) are shown in 3.14 as seen by the shifter during data taking.

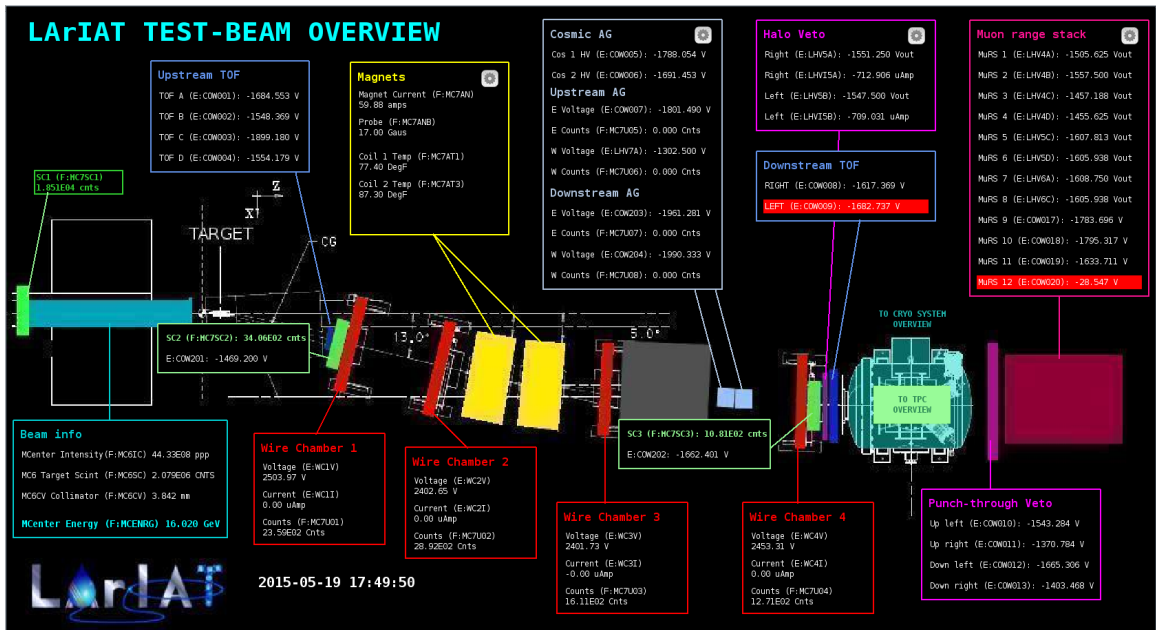


Figure 3.13: Interface of the Synoptic slow control system

1750 DAQ Monitoring

We monitor the data taking and the run time evolution with the Run Status Webpage (<http://lariat-wbm.fnal.gov/lariat/run.html>), a webpage updated in real-time. The

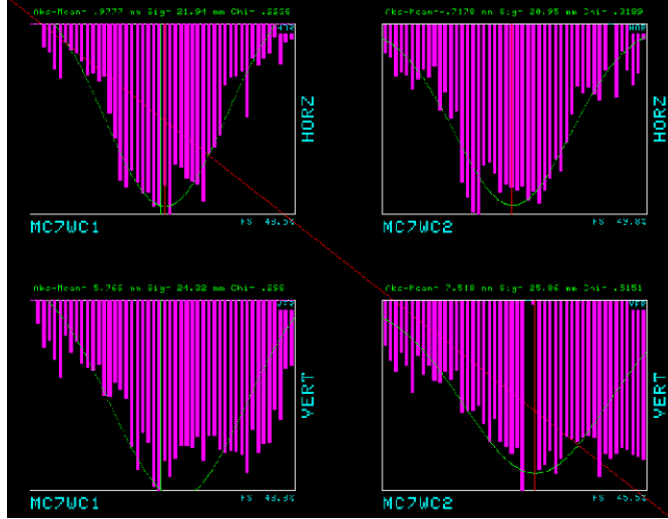


Figure 3.14: Beam position at the upstream wire chambers monitored with ACNET.

1753 page displays, among other information, the total number of triggers in the event,
 1754 the total number of detectors triggered during a beam spill, the trigger patterns, the
 1755 number of times a particular trigger pattern was satisfied during a beam spill, and
 1756 the current time relative to the Fermilab accelerator complex supercycle. A screen
 1757 shot of the page is show in figure 3.15.

1758 Data Quality Monitoring

1759 We employ two systems to ensure the quality of our data during data taking: the
 1760 Near-Real-Time Data Quality Monitoring and the Event Viewer.

1761 The Near-Real-Time Data Quality Monitoring (DQM) is a webpage which receives
 1762 updates from all the VME boards in the trigger system and displays the results of
 1763 a quick analysis of the DAQ stream of raw data on a spill-by-spill basis. The DQM
 1764 allows the shifter to monitor almost in real time (typically with a 2-minute delay)
 1765 a series of low level-quantities and compare them to past collections of beam spills.
 1766 Some of the variables monitored in the DQM are the pedestal mean and RMS on
 1767 CAEN digitizer boards of the TPC wires and PMTs of the beamline detectors, the
 1768 hit occupancy and timing plots on the wire chambers, and number of data fragments

1769 recorded that are used to build a TPC event. Abnormal values for low-level quantity
1770 in the data activates a series of alarms in the DQM; this quick feedback on the DAQ
1771 and beam conditions is fundamental to assure a fast debugging of the detector and a
1772 very efficient data taking during beam uptime.

1773 The online Event Viewer displays a two dimensional representation (Wire vs Time)
1774 of LArIAT TPC events on both the Induction and the Collection planes in near real
1775 time. The raw pulses collected by the DAQ on each wire are plotted as a function
1776 of drift time, resulting in an image of the TPC event easily readable by the shifter.
1777 This tool guarantees a particularly good check of the TPC operation which activate
1778 an immediate feedback for troubleshooting a number of issues. For example, it is
1779 easy for the shifter to spot high occupancy events and request a reduction of the
1780 primary beam intensity, or to spot a decrease of the argon purity which requires the
1781 regeneration of filters, or to catch the presence of electronic noise and reboot the
1782 ASICs. An example of high occupancy event is shown in 3.16.

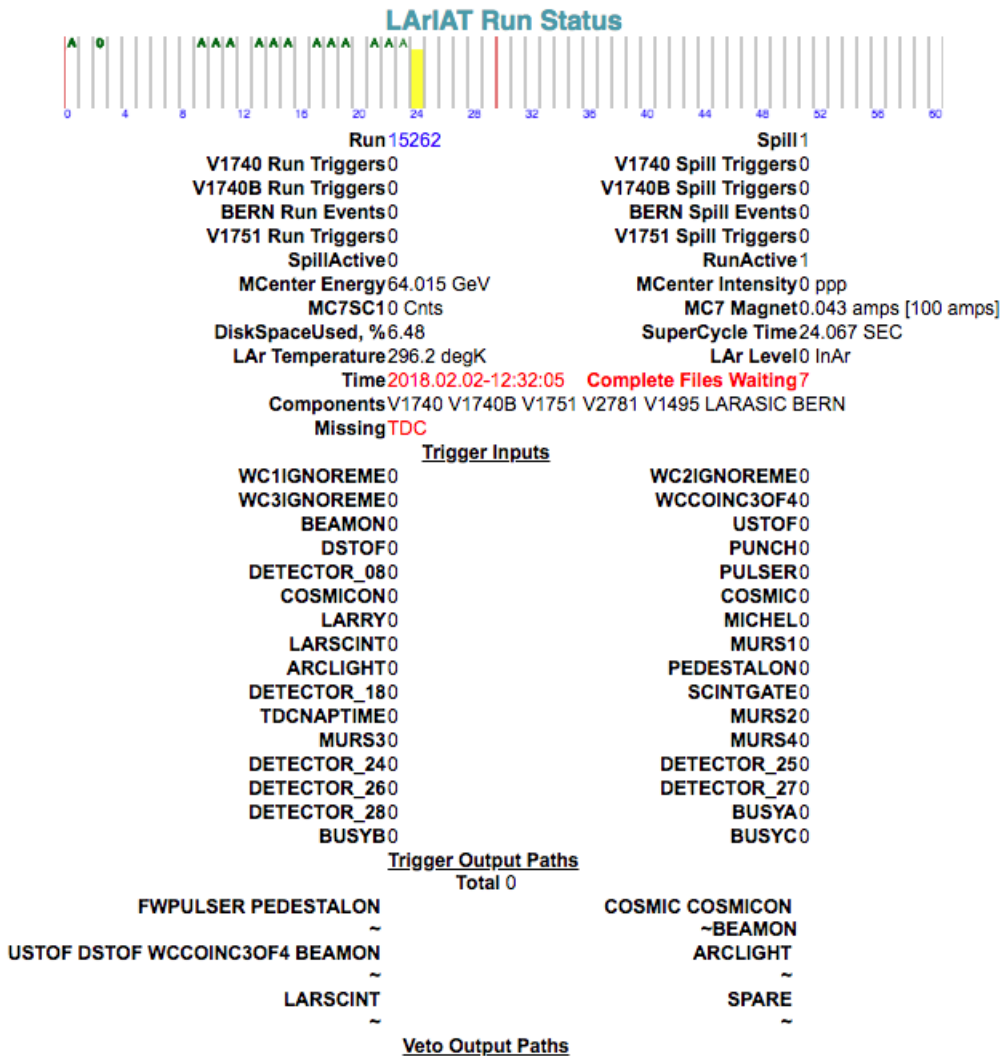


Figure 3.15: Run Status page at LArIAT downtime. At the top the yellow bar displays the current position in the Fermilab supercycle. Interesting information to be monitored by the shifter were the run number and number of spills, time elapsed from data taking (here in red), the energy of the secondary beam and the trigger paths.

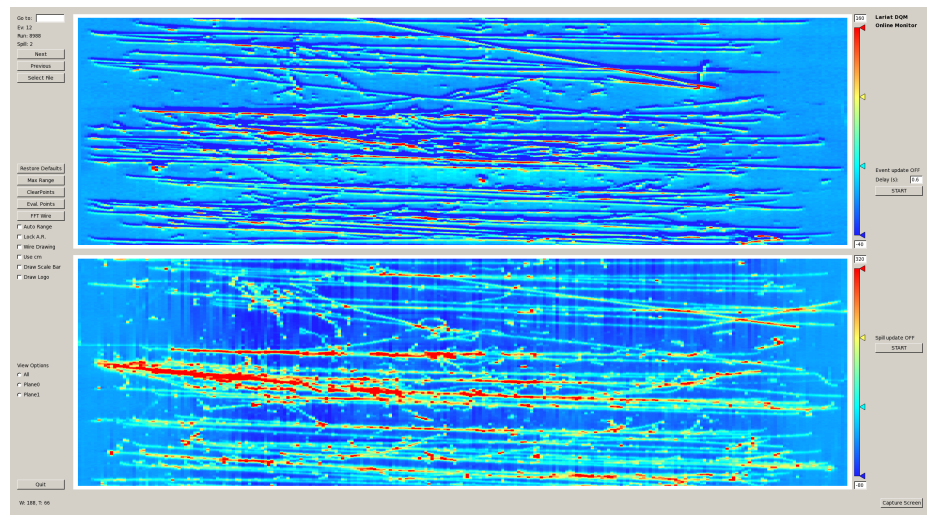


Figure 3.16: High occupancy event display: induction plane (top) and collection plane (bottom).

¹⁷⁸³ **Chapter 4**

¹⁷⁸⁴ **Total Hadronic Cross Section**

¹⁷⁸⁵ **Measurement Methodology**

¹⁷⁸⁶ “Like a lemon to the lime and the bubble to the bee”

¹⁷⁸⁷ – Eazy-E, 1993 –

¹⁷⁸⁸ This chapter describes the general procedure employed to measure total hadronic
¹⁷⁸⁹ interaction cross sections on Ar in LArIAT. Albeit with small differences, both the
¹⁷⁹⁰ (π^- ,Ar) and (K^+ ,Ar) total hadronic cross section measurements rely on the same
¹⁷⁹¹ procedure. We start by selecting the particle of interest using a combination of
¹⁷⁹² beamline detectors and TPC information (Section 4.1). We then perform a handshake
¹⁷⁹³ between the beamline information and the TPC tracking to assure the selection of
¹⁷⁹⁴ the correct TPC track (Section 4.2) associated to the corresponding beam particle.
¹⁷⁹⁵ We then apply the “thin slice” method to measure the “raw” hadronic cross section
¹⁷⁹⁶ (Section 4.3). A series of corrections are then evaluated and applied to obtain the
¹⁷⁹⁷ final cross section (Section 4.3.3).

¹⁷⁹⁸ At the end of this chapter, we show a sanity check of the methodology by apply-
¹⁷⁹⁹ ing the thin slice method employing only MC truth information and retrieving the
¹⁸⁰⁰ expected MC cross section for pions and kaons (Section 4.4).

1801 **4.1 Event Selection**

1802 The measurement of the (π^- ,Ar) and (K^+ ,Ar) total hadronic cross section in LArIAT
1803 starts by selecting the pool of pion or kaon candidates and measuring their momentum
1804 before they enter the LAr volume. This is done through the series of selections on
1805 beamline and TPC information described in the next sections. The summary of the
1806 event selection in data is reported in Table 4.1.

1807 **4.1.1 Selection of Beamline Events**

1808 We leverage the beamline particle identification and momentum measurement before
1809 entering the TPC as an input to evaluate the kinetic energy for the hadrons used in
1810 the cross sections measurements. To this end, we select the LArIAT data to keep
1811 only events whose wire chamber and time of flight information is registered (line 1 in
1812 in Table 4.1). Additionally, we perform a check of the plausibility of the trajectory
1813 inside the beamline detectors: given the position of the hits in the four wire chambers,
1814 we make sure the particle's trajectory does not cross any impenetrable material such
1815 as the collimator and the magnets steel (line 2 in in Table 4.1).

	Run-II Neg Pol	Run-II Pos Pol
1. Events Reconstructed in Beamline	158396	260810
2. Events with Plausible Trajectory	147468	240954
3. Beamline $\pi^-/\mu^-/e^-$ Candidate	138481	N.A.
4. Beamline K^+ Candidate	N.A	2837
5. Events Surviving Pile Up Filter	108929	2389
6. Events with WC2TPC Match	41757	1081
7. Events Surviving Shower Filter	40841	N.A.
8. Available Events For Cross Section	40841	1081

Table 4.1: Number of data events for Run-II Negative and Positive polarity

1816 **4.1.2 Particle Identification in the Beamline**

1817 In data, the main tool to establish the identity of the hadron of interest is the LArIAT
1818 tertiary beamline, in its function of mass spectrometer. We combine the measurement
1819 of the time of flight, TOF , and the beamline momentum, p_{Beam} , to reconstruct the
1820 invariant mass of the particles in the beamline, m_{Beam} , as follows

$$m_{Beam} = \frac{p_{Beam}}{c} \sqrt{\left(\frac{TOF * c}{l}\right)^2 - 1}, \quad (4.1)$$

1821 where c is the speed of light and l is the length of the particle's trajectory between
1822 the time of flight paddles.

1823 Figure 4.1 shows the mass distribution for the Run II negative polarity runs on
1824 the left and positive polarity runs on the right. We perform the classification of events
1825 into the different samples as follows:

- 1826 • $\pi/\mu/e$: mass $< 350 \text{ MeV}/c^2$
1827 • kaon: $350 \text{ MeV} < \text{mass} < 650 \text{ MeV}/c^2$
1828 • proton: $650 \text{ MeV} < \text{mass} < 3000 \text{ MeV}/c^2$.

1829 Lines 3 and 4 in Table 4.1 show the number of negative $\pi/\mu/e$ and positive K
1830 candidates which pass the mass selection for LArIAT Run-II data.

1831 **4.1.3 TPC Selection: Halo Mitigation**

1832 The secondary beam impinging on LArIAT secondary target produces a plethora of
1833 particles which propagates downstream. The presence of upstream and downstream
1834 collimators greatly abates the number of particles tracing down the LArIAT tertiary
1835 beamline. However, it is possible that more than one particle sneaks into the LArTPC
1836 during its readout time: the TPC readout is triggered by the particle firing the series

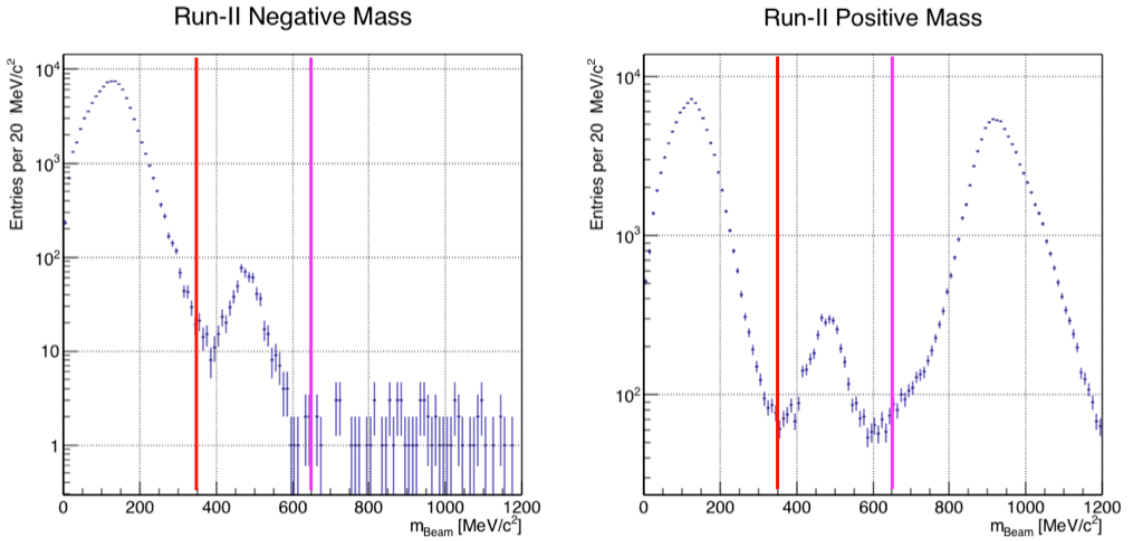


Figure 4.1: Distribution of the beamline mass as calculated according to equation 4.1 for the Run-II events reconstructed in the beamline, negative polarity runs on the left and positive polarity runs on the right. The classification of the events into $\pi^\pm/\mu^\pm/e^\pm$, K^\pm , or (anti)proton is based on these distributions, whose selection cut are represented by the vertical colored lines.

1837 of beamline detectors along our tertiary beamline, but particles from the beam halo
 1838 might also be present in the TPC at the same time. We call “pile up” the additional
 1839 traces in the TPC. We adjusted the primary beam intensity between LArIAT Run I
 1840 and Run II to reduce the presence of events with high pile up particles in the data
 1841 sample. For the cross section analyses, we remove events with more than 4 tracks in
 1842 the first 14 cm upstream portion of the TPC from the sample (line 5 in Table 4.1).

1843 **4.1.4 TPC Selection: Shower Removal**

1844 In the case of the (π^-, Ar) cross section, the resolution of beamline mass spectrometer
 1845 is not sufficient to select a beam of pure pions. In fact, muons which are close in mass
 1846 to the pions and relativistic electrons survive the selection on the beamline mass. It
 1847 is important to notice that the composition of the negative polarity beam is mostly
 1848 pions, as will be discussed in section 5.2.1. Still, we devise a selection on the TPC

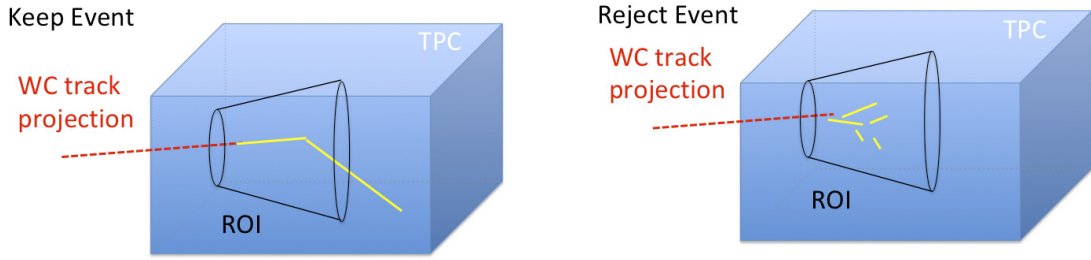


Figure 4.2: Visual rendering of the shower filter. The ROI is a cut cone, with a small radius of 4 cm, a big radius of 10 cm and an height of 42 cm (corresponding to 3 radiation lengths for electrons in Argon).

1849 information to mitigate the presence of electrons in the sample used for the pion
 1850 cross section. The selection relies on the different topologies of a pion and an electron
 1851 event when propagating in liquid argon: while the former will trace a track inside the
 1852 TPC active volume, the latter will tend to “shower”, i.e. interact with the medium,
 1853 producing bremsstrahlung photons which pair convert into several short tracks. In
 1854 order to remove the shower topology, we create a region of interest (ROI) around the
 1855 TPC track corresponding to the beamline particle. We look for short tracks contained
 1856 in the ROI, as depicted in figure 4.4: if more than 5 tracks shorter than 10 cm are
 1857 in the ROI, we reject the event. Line 7 in Table 4.1 shows the number of events
 1858 surviving this selection.

1859 **4.2 Beamlne and TPC Handshake: the Wire Cham- 1860 ber to TPC Match**

1861 For each event passing the selection on its beamline information, we need to identify
 1862 the track inside the TPC corresponding to the particle which triggered the beamline
 1863 detectors, a procedure we refer to as “WC to TPC match” (WC2TPC for short). In
 1864 general, the TPC tracking algorithm can reconstruct more than one track in the event,
 1865 partially due to the fact that hadrons interact in the chamber and partially because

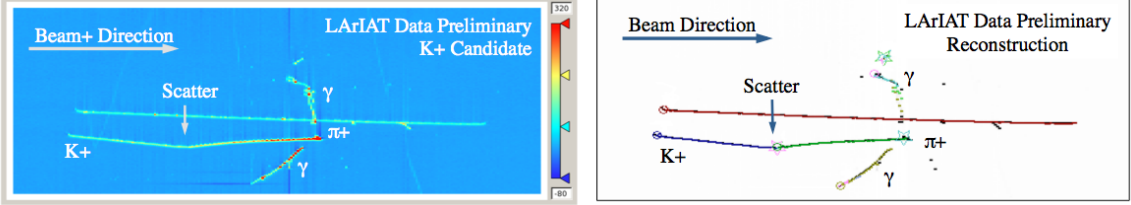


Figure 4.3: Kaon candidate event: on the right, event display showing raw quantities; on the left, event display showing reconstructed tracks. In the reconstructed event display, different colors represent different track objects. A kink is visible in the kaon ionization, signature of a hadronic interaction: the tracking correctly stops at the kink position and two tracks are formed. An additional pile-up track is so present in the event (top track in red).

1866 of pile up particles during the triggered TPC readout time, as shown in figure 4.3.

1867 We attempt to uniquely match one wire chamber track (see Section 3.2.2) to one
 1868 and only one reconstructed TPC track. In order to determine if a match is present,
 1869 we apply a geometrical selection on the relative position of the wire chamber and
 1870 TPC tracks. We start by considering only TPC tracks whose first point is in the first
 1871 2 cm upstream portion of the TPC for the match. We project the wire chamber track
 1872 to the TPC front face where we define the coordinates of the projected point as x_{FF}
 1873 and y_{FF} . For each considered TPC track, we define ΔX as the difference between
 1874 the x position of the most upstream point of the TPC track and x_{FF} . ΔY is defined
 1875 analogously. We define the radius difference, ΔR , as $\Delta R = \sqrt{\Delta X^2 + \Delta Y^2}$. We define
 1876 as α the angle between the incident WC track and the TPC track in the plane that
 1877 contains them. If $\Delta R < 4$ cm, $\alpha < 8^\circ$, a match between WC-track and TPC track is
 1878 found. We describe how we determine the value for the radius and angular selection
 1879 in Section ???. We discard events with multiple WC2TPC matches. We use only those
 1880 TPC tracks that are matched to WC tracks in the cross section calculation. Line 6
 1881 in Table 4.1 shows the number of events where a unique WC2TPC match was found.
 1882 In MC, we mimic the matching between the WC and the TPC track by construct-
 1883 ing an artificial WC track using truth information at wire chamber four. We then
 1884 apply the same WC to TPC matching algorithm as in data.

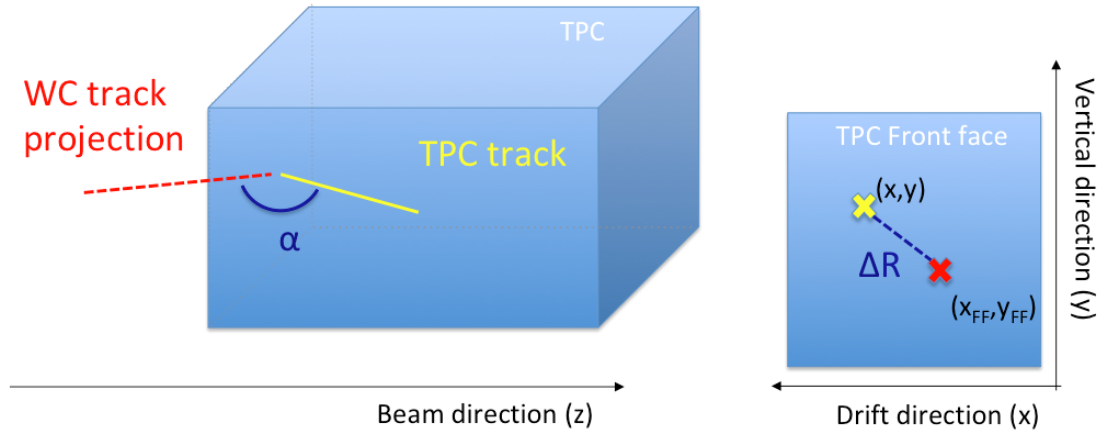


Figure 4.4: Visual rendering of the wire chamber to TPC match.

1885 4.3 The Thin Slice Method

1886 Once we have selected the 40841 beamline pion candidates and the 1081 beamline
1887 kaon candidates, and we have identified the TPC corresponding track, we apply the
1888 thin slice method to measure the cross section, as the following sections describe.

1889 4.3.1 Cross Sections on Thin Target

1890 Cross section measurements on a thin target have been the bread and butter of
1891 nuclear and particle experimentalists since the Geiger-Marsden experiments [67]. At
1892 their core, this type of experiments consists in shooting a beam of particles with a
1893 known flux on a thin slab of material and recording the outgoing flux.

1894 In general even in the case of thin target, the target is not a single particle,
1895 but rather a slab of material containing many diffusion centers. The so-called “thin
1896 target” approximation assumes that the target centers are uniformly distributed in
1897 the material and that the target is thin compared to the projectile interaction length,
1898 so that no center of interaction sits in front of another. In this approximation, the
1899 ratio between the number of particles interacting in the target N_{Int} and the number of
1900 incident particles N_{Inc} on the target estimates the interaction probability $P_{\text{Interacting}}$,

1901 which is the complementary to one of the survival probability $P_{Survival}$. Equation 4.2

$$P_{Survival} = 1 - P_{Interacting} = 1 - \frac{N_{Int}}{N_{Inc}} = e^{-\sigma_{TOT} n \delta X} \quad (4.2)$$

1902 describes the probability for a particle to survive the thin target. This formula relates
1903 the interaction probability to the total hadronic cross section (σ_{TOT}), the density of
1904 the target centers (n)¹ and the thickness of the target along the incident hadron
1905 direction (δX). If the target is thin compared to the interaction length of the process
1906 considered, we can Taylor expand the exponential function in equation 4.2 and find
1907 a simple proportionality relationship between the cross section and the number of
1908 incident and interacting particles, as shown in equation 4.3:

$$1 - \frac{N_{Int}}{N_{Inc}} = 1 - \sigma_{TOT} n \delta X + O(\delta X^2). \quad (4.3)$$

1909 Solving for the cross section, we find:

$$\sigma_{TOT} = \frac{1}{n \delta X} \frac{N_{Int}}{N_{Inc}}. \quad (4.4)$$

1910 4.3.2 Not-so-Thin Target: Slicing the Liquid Argon Volume

1911 The interaction length of pions and kaons in liquid argon is expected to be of the
1912 order of 50 cm for pions and 100 cm for kaons. Thus, the LArIAT TPC, with its 90
1913 cm of length, is not a thin target. However, the fine-grained tracking of the LArIAT
1914 LArTPC allows us to treat the argon volume as a sequence of many adjacent thin
1915 targets.

1916 As described in Chapter 3, LArIAT induction and collection planes consist of 240
1917 wires each at 4 mm spacing. The wires are oriented at +/- 60° from the vertical

1. The scattering center density in the target, n , relates to the argon density ρ , the Avogadro number N_A and the argon molar mass m_A as $n = \frac{\rho N_A}{m_A}$.

1918 direction, while the beam direction is oriented 3 degrees off the z axis in the XZ
 1919 plane. The collection wires collect signals proportional to the energy deposited by
 1920 the hadron along its path in a $\delta X = 4 \text{ mm}/(\sin(60^\circ)\cos(3^\circ)) \approx 4.7 \text{ mm}$ slab of liquid
 1921 argon. Thus, one can think to slice the TPC into many thin targets of $\delta X = 4.7 \text{ mm}$
 1922 thickness along the direction of the incident particle, making a measurement at each
 1923 wire along the path.

1924 Considering each slice j a “thin target”, we can apply the cross section calculation
 1925 from Equation 4.4 iteratively, evaluating the kinetic energy of the hadron as it enters
 1926 each slice, E_j^{kin} . For each WC2TPC matched particle, the energy of the hadron
 1927 entering the TPC is known thanks to the momentum and mass determination by the
 1928 tertiary beamline,

$$E_{FrontFace}^{kin} = \sqrt{p_{Beam}^2 - m_{Beam}^2} - m_{Beam} - E_{loss}, \quad (4.5)$$

1929 where E_{loss} is a correction for the kinetic energy loss in the uninstrumented material
 1930 between the beamline and the TPC front face. While propagating through the target,
 1931 the kinetic energy of the hadron at each slab is determined by subtracting the energy
 1932 deposited by the particle in the previous slabs. For example, at the j^{th} slab of a track,
 1933 the kinetic energy will be

$$E_j^{kin} = E_{FrontFace}^{kin} - \sum_{i < j} E_{Dep,i}, \quad (4.6)$$

1934 where $E_{Dep,i}$ is the energy deposited at each argon slice before the j^{th} point as mea-
 1935 sured by the calorimetry associated with the tracking.

1936 If the particle enters a slice, it contributes to the $N_{Inc}(E^{kin})$ distribution in the
 1937 energy bin corresponding to its kinetic energy in that slice. While into the slice, a
 1938 hadron may or may not interact. If it interacts in the slice, it contributes also to the
 1939 $N_{Int}(E^{kin})$ distribution in the appropriate energy bin; this occurrence corresponds to

	min	max
X	1 cm	46 cm
Y	-15 cm	15 cm
Z	0 cm	86 cm

Table 4.2: Fiducial volume boundaries used to determine cross section interaction point.

the end of the hadron tracking. If the hadron does not interact, it will enter the next slice and the interaction evaluation starts again. The process is applied to all the hadrons in the sample; the cross section as a function of kinetic energy, $\sigma_{TOT}(E^{kin})$ is then evaluated to be proportional to the ratio $\frac{N_{Int}(E^{kin})}{N_{Inc}(E^{kin})}$ – bin by bin ratio.

Our goal is to measure the total interaction cross section, independently from the topology of the interaction. Thus, we determine that a hadron interacted simply by requiring that the last point of the WC2TPC matched track lies in a slice within the fiducial volume, whose boundaries are defined in Table 4.2. If the TPC track ends within the fiducial volume, its last point will be the interaction point; if the track crosses the boundaries of the fiducial volume, the track will be considered “through going” and no interaction point will be found. The only points of the hadronic candidate track considered to fill the N_{Int} and N_{Inc} distributions are the ones contained in the fiducial volume.

A notable background pertinent only to the N_{Int} distribution are cases in which the hadrons decays inside the TPC. In those cases in fact, the tracking ends inside the TPC but the interaction is not hadronic. The handling of decay background is treated in a slightly different way for the pion and kaon section, details can be found in sections 5.3 and 7.1 respectively.

4.3.3 Corrections to the Raw Cross Section

Equation 4.4 is a prescription for measuring the cross section in case of a pure beam of the hadron of interest and 100% efficiency in the determination of the interaction

1961 point. For example, if LArIAT had a beam of pure pions and were 100% efficient in
 1962 determining the interaction point within the TPC, the pion cross section as a function
 1963 of kinetic energy (estimated at the central value of the energy bin E_i) would be given
 1964 by

$$\sigma_{TOT}^{\pi^-}(E_i) = \frac{1}{n\delta X} \frac{N_{Int}^{\pi^-}(E_i)}{N_{Inc}^{\pi^-}(E_i)}. \quad (4.7)$$

1965 Unfortunately, this is not the case. In fact, the selection used to isolate pions in
 1966 the LArIAT beam allows for the presence of some muons and electrons as background,
 1967 while the kaon selection allows for a small contamination of protons (see Section 5.2.1).
 1968 Also, the LArIAT TPC tracking algorithm is not 100% efficient in determining the
 1969 interaction point. Therefore we need to apply two corrections evaluated on the MC in
 1970 order to extract the final cross section from LArIAT data: i) a background subtraction
 1971 and ii) a correction for reconstruction effects. Still using the pion case as example,
 1972 we estimate the pion cross section in each energy bin changing Equation 4.7 into

$$\sigma_{TOT}^{\pi^-}(E_i) = \frac{1}{n \delta X} \frac{N_{Int}^{\pi^-}(E_i)}{N_{Inc}^{\pi^-}(E_i)} = \frac{1}{n \delta X} \frac{\epsilon^{Inc}(E_i)[N_{Int}^{TOT}(E_i) - B_{Int}(E_i)]}{\epsilon^{Int}(E_i)[N_{Inc}^{TOT}(E_i) - B_{Inc}(E_i)]}, \quad (4.8)$$

1973 where $N_{Int}^{TOT}(E_i)$ and $N_{Inc}^{TOT}(E_i)$ is the measured content of the interacting and
 1974 incident histograms for events that pass the event selection, $B_{Int}(E_i)$ and $B_{Inc}(E_i)$
 1975 represent the contributions from the background to the interacting and incident his-
 1976 tograms respectively, and $\epsilon^{Int}(E_i)$ and $\epsilon^{Inc}(E_i)$ are the corrections for reconstruction
 1977 effects.

1978 As we will show in section 5.3, the background subtraction for the interacting and
 1979 incident histograms can be translated into corresponding relative pion content factors
 1980 $C_{Int}^{\pi MC}(E_i)$ and $C_{Inc}^{\pi MC}(E_i)$ and the cross section re-written as follows

$$\sigma_{TOT}^{\pi^-}(E_i) = \frac{1}{n \delta X} \frac{\epsilon^{Inc}(E_i)}{\epsilon^{Int}(E_i)} \frac{C_{Int}^{\pi MC}(E_i)}{C_{Inc}^{\pi MC}(E_i)} \frac{N_{Int}^{TOT}(E_i)}{N_{Inc}^{TOT}(E_i)}. \quad (4.9)$$

1981 4.4 Procedure testing with MC truth quantities

1982 The (π^-, Ar) and (K^+, Ar) total hadronic cross section implemented in Geant4 can
1983 be used as a tool to validate the measurement methodology. We describe here a
1984 closure test done on Monte Carlo to prove that the methodology of slicing the TPC
1985 retrieves the underlying cross section distribution implemented in Geant4 within the
1986 MC statistical uncertainty.

1987 For pions and kaons in the considered energy range, the Geant4 inelastic model
1988 adopted is “BertiniCascade”; the pion elastic cross sections are tabulated from Chips,
1989 while the kaon elastic cross sections are tabulated on Gheisha and Chips.

1990 For the validation test, we fire a sample of pions and a sample of kaons inside
1991 the LArIAT TPC active volume using the Data Driven Monte Carlo, a procedure
1992 described in Section 5.2.2. We apply the thin-sliced method using only true quantities
1993 to calculate the hadron kinetic energy at each slab in order to decouple reconstruction
1994 effects from possible issues with the methodology. For each slab of 4.7 mm length
1995 along the path of the hadron, we integrate the true energy deposition as given by
1996 the Geant4 transport model. Then, we recursively subtracted it from the hadron
1997 kinetic energy at the TPC front face to evaluate the kinetic energy at each slab until
1998 the true interaction point is reached. Since the MC is a pure beam of the hadron of
1999 interest and truth information is used to retrieve the interaction point, no background
2000 correction or reconstruction effects correction is applied. Doing so, we obtain the true
2001 interacting and incident distributions for the considered hadron, whose ratio leads to
2002 the true MC cross section as a function of the hadron kinetic energy.

2003 Figure 4.5 shows the total hadronic cross section for argon implemented in Geant4
2004 10.03.p1 (solid lines) overlaid with the true MC cross section as obtained with the
2005 sliced TPC method (markers) for pions on the left and kaons on the right; the total
2006 cross section is shown in green. For completeness, we also report the contributions
2007 from the elastic cross section (in blue) and the inelastic cross section (in red), available

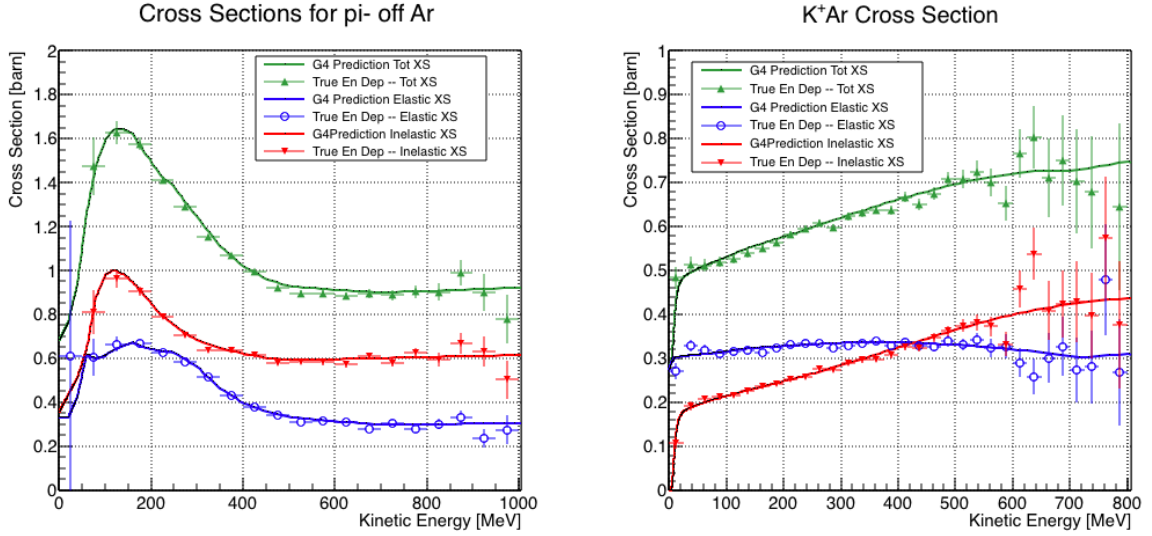


Figure 4.5: Hadronic cross sections for (π^- ,Ar) on the left and (K^+ ,Ar) on the right as implemented in Geant4 10.03.p1 (solid lines) overlaid the true MC cross section as obtained with the sliced TPC method (markers). The total cross section is shown in green, the elastic cross section in blue and the inelastic cross section in red.

2008 at the MC level. The nice agreement with the Geant4 distribution and the cross
 2009 section obtained with the sliced TPC method gives us confidence in the validity of
 2010 the methodology.

2011 **Chapter 5**

2012 **Data and MC preparation for the**
2013 **Cross Section Measurements**

2014 “*Il dolce non lo mangi mai, ma qualche volta ti rifai.*
2015 *Abbracciami*”
2016 – Pietro Ciampi, 1971 –

2017 This chapter describes the work done on the data and Monte Carlo samples in
2018 preparation for the cross section analyses. This entails the choice of the datasets
2019 and the production of the information needed to construct the Monte Carlo Simula-
2020 tion (Section 5.1), the construction and use of said Monte Carlo simulation (section
2021 5.2), the study of backgrounds for the pion cross section (Section 5.3), the study of
2022 the energy loss between WC4 and TPC (Section 5.4), the study of the tracking in the
2023 TPC (Section 5.5), and study of the calorimetry response (Section 5.6).

2024 **5.1 Cross Section Analyses Data Sets**

2025 We choose LArIAT Run-II as the data period for the (π^- ,Ar) and (K^+ ,Ar) total
2026 hadronic cross section analyses. Data taking for the this period started on 03/15/2016

2027 and ended on 07/31/2016. Since we are interested in beamline and TPC information,
2028 we ask basic requirements on the operational status of the time of flight counters, wire
2029 chambers and TPC to form the good run list for this period, which we informally call
2030 “lovely runs”.

2031 The subset of lovely runs chosen for the (π^-, Ar) total hadronic cross section
2032 analysis includes only the -60A and -100A magnet configurations in negative polarity,
2033 even if LArIAT explored several other beamline configurations during Run-II. The -
2034 60A and -100A combined data set accounts for approximately 90% of the total Run-II
2035 negative polarity runs. The choice of these two main beamline settings limits the need
2036 for the production of many different MC sets and related corrections, still maintaining
2037 a high number of events.

2038 Similarly, the subset of lovely runs chosen for the (K^+, Ar) total hadronic cross
2039 section analysis includes only the +60A and +100A magnet configurations in positive
2040 polarity. It should be noted that kaons are extremely rare in the +60A sample, thus
2041 the data sample for the (K^+, Ar) cross section after the mass selection is about 90%
2042 +100A runs, as shown in Table 5.1.

2043 For these first measurements that make use of both the LArIAT beamline and
2044 TPC information, we choose strict requirements on the reconstruction of the WC
2045 tracks, the so-called “Picky Track” sample (see Section 3.2.2), where we require a
2046 single hit in each and every wire chamber detector to reconstruct the WC track. This
2047 choice presents two advantages: the uncertainty on the momentum reconstruction
2048 for the “Picky Tracks” sample is smaller compared to the “High Yield” sample, and
2049 the comparison with the beamline MC results is straightforward. A possible future
2050 update and cross check of these analysis would be the use of the High Yield sample,
2051 where the statistics is about three times higher.

2052 The breakdown of beamline events as a function of the magnets settings is shown
2053 in Table 5.1. The choice of the data sets determines the production of beamline MC

2054 and serves as basis for the production of Data Driven MC, as shown in the next
2055 sections.

2056 5.2 Construction of a Monte Carlo Simulation for 2057 LArIAT

2058 For the simulation of LArIAT events and for the simulation of the datasets' particle
2059 make up, we use a combination of two MC generators: the G4Beamline Monte Carlo
2060 and the Data Driven single particle Monte Carlo (DDMC). We use the G4Beamline
2061 MC to simulate the particle transport in the LArIAT tertiary beamline and calculate
2062 the particle composition of the beam just after the last Wire Chamber (WC4). We
2063 use the DDMC to simulate the particles after WC4 along the beamline, close to the
2064 beam window in the LAr cryostat and in the TPC.

2065 5.2.1 G4Beamline

2066 G4Beamline simulates the beam collision at the LArIAT secondary target, the energy
2067 deposited by the particles in the LArIAT beamline detectors, and the action of the
2068 LArIAT magnets, effectively accounting for particle transport through the beamline
2069 from the LArIAT target until “Big Disk”, a fictional, void detector located just before
2070 the LArIAT cryostat. At the moment of this writing, G4Beamline does not simulated
2071 the responses of the beamline detectors. It is possible to interrogate the truth level
2072 information of the simulated particles in several points of the geometry. In order

	I = 60 A	I = 100 A	Total
Data Events after $\pi/\mu/e$ Mass Selection	67068	71413	138481
Data Events after K Mass Selection	274	2563	2837

Table 5.1: Number of data events which fit the $\pi/\mu/e$ or K mass hypothesis as a function of magnet settings.

2073 to ease the handshake between G4Beamline and the DDMC, we ask for the beam
2074 composition just after WC4. Since LArIAT data are taken under different beam
2075 conditions, we need to simulate separately the beam composition according to the
2076 magnets' settings and the secondary pion beam intensity with G4Beamline. For the
2077 pion cross section analysis the relevant beam conditions are secondary pion beam
2078 energy of 64 GeV, negative polarity magnet with current of 100 A and 60 A. For the
2079 kaon cross section analysis the relevant beam conditions is a secondary pion beam
2080 energy of 64 GeV, positive polarity magnet with current of 100 A.

2081 **Beam Composition for Negative Pion Cross Section**

2082 Even if pions are by far the biggest beam component in negative polarity runs, the
2083 LArIAT tertiary beam is not a pure pion beam. While useful to discriminate between
2084 pions, kaons, and (anti)protons, the beamline detectors are not sensitive enough to
2085 discriminate among the lighter particles in the beam: electrons, muons and pions
2086 fall under the same mass hypothesis. Thus, we need to assess the contamination
2087 from beamline particles other than pions in the event selections used for the pion
2088 cross section analysis and correct for this background. The first step of this process is
2089 assessing the percentage of electrons and muons in the $\pi/\mu/e$ beamline candidates via
2090 the G4Beamline MC, as we deem the percentage of kaons and antiprotons negligible
2091 after the mass selection ($\pm 1\%$). Since the beamline composition is a function of
2092 the magnet settings, we simulate separately events for magnet current of -60A and
2093 -100A. Figure 5.1 shows the momentum predictions from G4Beamline overlaid with
2094 data for the 60A runs (left) and for the 100A runs (right). The predictions for
2095 electrons, muons and pions have been staggered and their sum is area normalized
2096 to data. Albeit not perfect, these plots show a reasonable agreement in momentum
2097 shapes between data and MC. We attribute the difference in shape (longer tail in
2098 data) to a two approximations performed in the MC. Firstly, G4Beamline lacks the

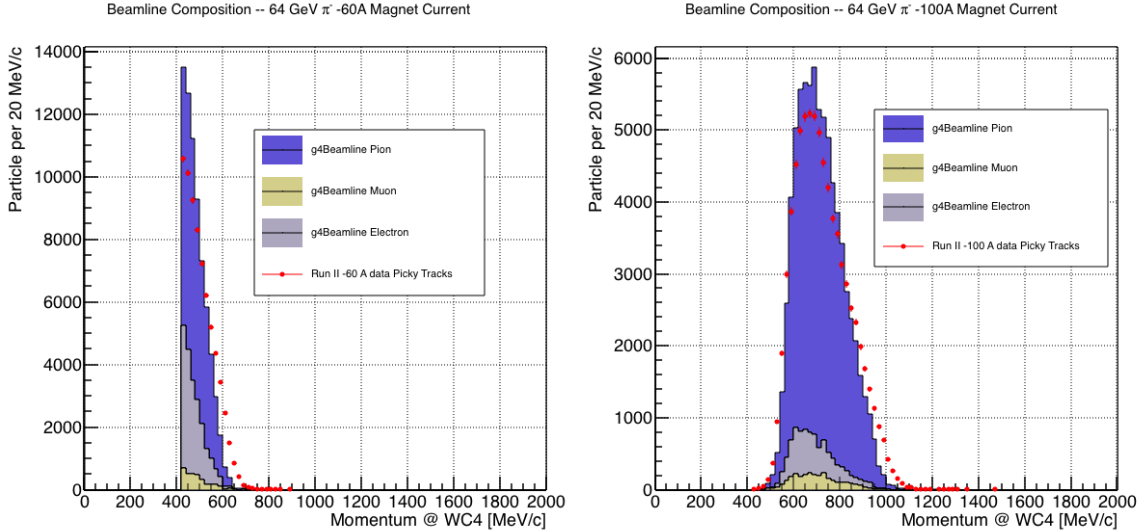


Figure 5.1: Beam composition for the -60A runs (left) and -100A runs (right). The solid blue plot represents the simulated pion content, the yellow plot represents the simulated muon content and the grey plot represents the simulated electron content. The plots are area normalized to the number of data events, shown in red.

	I = -60 A	I = -100 A
G4Pions	68.8 %	87.4 %
G4Muons	4.6 %	3.7 %
G4Electrons	26.6 %	8.9 %

Table 5.2: Simulated beamline composition per magnet settings

simulation of the WC efficiency which is momentum dependent and leads to enhance the number events in the center of the momentum distribution. Secondly, G4Beamline stop tracking pions and their products if they decay after WC1; in data, pion decays in flight can still create a trigger if the produced muon travels thought the beamline detectors. In the pion cross section analysis, these differences between data and the G4Beamline prediction are accounted for as a systematic uncertainty related to the beam composition (see Section 6.2.1).

Table 5.2 shows the beam composition per magnet setting after the mass selection according to the G4Beamline simulation.

The estimated beam composition is used as a basis to estimate the background contamination in the (π^-, Ar) cross section measurement, whose full treatment is

2110 described in section 5.3.

2111 Beam Composition for Positive Kaon Cross Section

2112 In the positive polarity runs, the tertiary beam composition is mainly pions and
2113 protons. The left side of Figure 5.2 shows the predictions for the momentum spectra
2114 for the 100A positive runs according to G4Beamline (solid colors) overlaid with data
2115 (black points). Since the LArIAT beamline detectors can discriminate between kaons
2116 and other particles, we do not rely on the G4Beamline simulation to estimate the
2117 beamline contamination in the pool of kaon candidates (as in the case of the pion
2118 cross section), but rather we use a data driven approach. The basic idea of this data
2119 driven approach is to estimate the bleed over from high and low mass peaks under
2120 the kaon peak by fitting the tails of the $\pi/\mu/e$ and proton mass distributions, as
2121 shown in Figure 5.2 right side. Since the shape of the tails is unknown, the estimate
2122 is done multiple times varying the range and shape for reasonable functions. For
2123 example, to estimate the proton content under the kaon peak, we start by fitting the
2124 left tail of the proton mass distribution with a gaussian function between $650 \text{ MeV}/c^2$
2125 and $750 \text{ MeV}/c^2$. We extend the fit function under the kaon peak and integrate the
2126 extended fit function between $350-650 \text{ MeV}/c^2$. We integrate the mass histogram
2127 in the same range and calculate the proton contamination as the ratio between the
2128 two integrals. We repeat this procedure for several fit shapes (gaussian, linear and
2129 exponential functions) and tail ranges. Finally, we calculate the contamination as
2130 the weighted average of single estimates, where the weights are calculated to be the
2131 $1./|1 - \chi^2|$ of the tail fits. The procedure is repeated for lighter particles mass peak
2132 independently. With 12 iterations of this method we find a proton contamination of
2133 $5.0 \pm 2.0 \%$ and a contamination from the lighter particles of $0.2 \pm 0.5 \%$. The
2134 estimate of the proton background is currently not used in the kaon cross section
2135 analysis, but it is a fundamental step to retrieve the true kaon cross section which

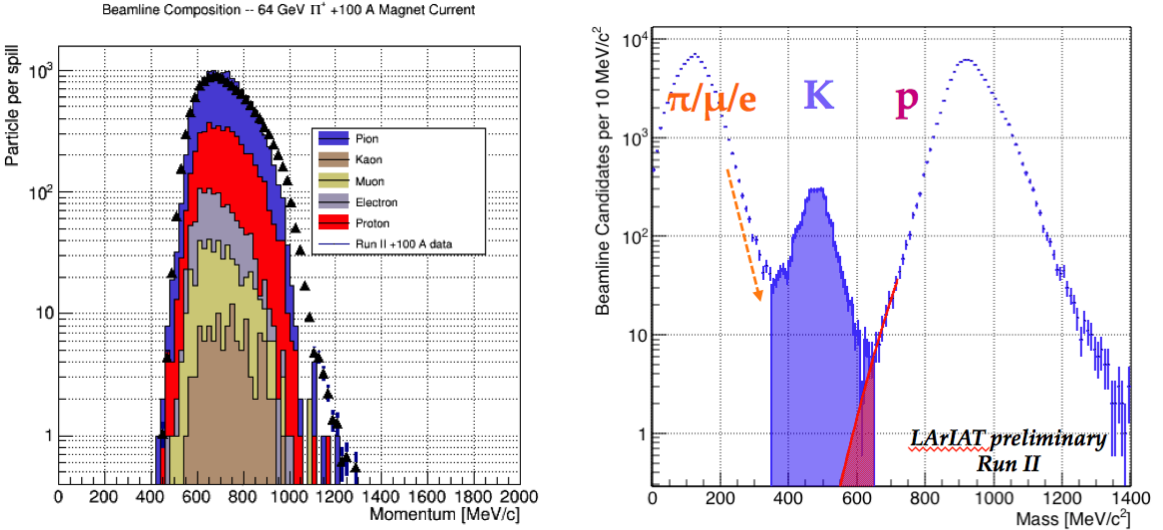


Figure 5.2: *Left:* Beam composition for the +100A runs after WC4 (no mass selection applied). The solid colors represent the contributions from the G4Beamline simulated particles: blue plot represents the simulated pion content, the yellow plot represents the simulated muon content and the grey plot represents the simulated positron content, the red the proton content and the mustard the kaon content. The plots are area normalized to the number of data events, shown in black. *Right:* Mass distribution for the Run-II positive runs, where the area under the kaon mass peak is highlighted in purple. The area under the extension of a possible fit for the proton tail is highlighted in red.

2136 will be implemented in the further development of the analysis.

2137 5.2.2 Data Driven MC

2138 The Data Driven single particle Monte Carlo (DDMC) is a single particle gun which
2139 simulates the particle transport from WC4 into the TPC leveraging on the beamline
2140 data information. The DDMC uses the data momentum and position at WC4 to
2141 derive the event generation: a general sketch of the DDMC workflow is shown in
2142 Figure 5.3.

2143 When producing a DDMC sample, beamline data from a particular running pe-
2144 riod and/or running condition are selected first. For example, data for the negative
2145 60A runs and for the negative 100A runs inform the event generation stage of two
2146 different DDMC samples. Figure 5.4 schematically shows the data quantities of in-

terest leveraged from data: the momentum (P_x, P_y, P_z) and position (X, Y) at WC4.
For each data event, we obtain the particle position (X, Y) at WC4 directly from the
data measurement; we calculate the components of the momentum using the beam-
line measurement of the momentum magnitude in conjunction with the hits on WC3
and WC4 to determine the direction of the momentum vector, as described in section
3.2.2. The momentum and position of the selected data events form a 5-dimensional
series of tuples. The DDMC event generator samples from the joint distribution
of these five quantities using a 5-dimensional hit-or-miss sampling procedure. This
sampling generates MC events with the same momentum and position distributions
as data, with the additional benefit of accounting for the correlations between the
 P_x, P_y, P_z, X, Y variables. As an example, the results of the DDMC generation com-
pared to data for the kaon +100A sample are shown in figure 5.5 for the P_z, X and Y
distributions; as expected, MC and data agree within the statistical uncertainty by
construction. A LArSoft simulation module then launches single particle MC from
 $z = -100$ cm (the location of the WC4) using the generated events. The particles
are free to decay and interact in their path from WC4 to the TPC according to the
Geant4 simulation.

Using the DDMC technique ensures that the MC and data particles have very
similar momentum, position and angular distributions at WC4 and allows us to use
the MC sample in several occasions: to estimate the background contamination to
the pion cross section (see Section 5.3), to calibrate the energy loss upstream of the
TPC (see Section 5.4), and to study the tracking and the calorimetric performance
in the LArTPC (sections 5.5 and 5.6). A small caveat is in order here: the DDMC is
a single particle Monte Carlo, which means that the beam pile-up is not simulated.

We generate six samples for the pion cross section measurement: three samples
of ~ 330000 pions, muons and electrons to simulate the negative 60A runs, and three
samples of ~ 340000 pions, muons and electrons for the negative 100A runs. We

2174 generate a sample of 195000 kaons for the kaon cross section analysis.

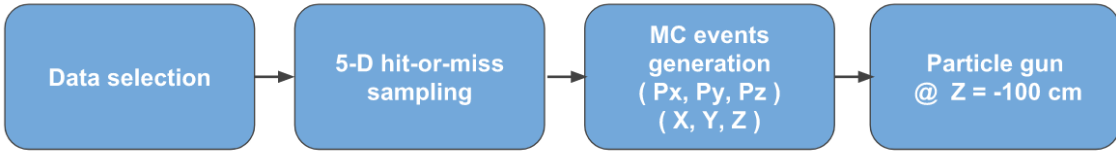


Figure 5.3: Workflow for Data Driven single particle Monte Carlo production.

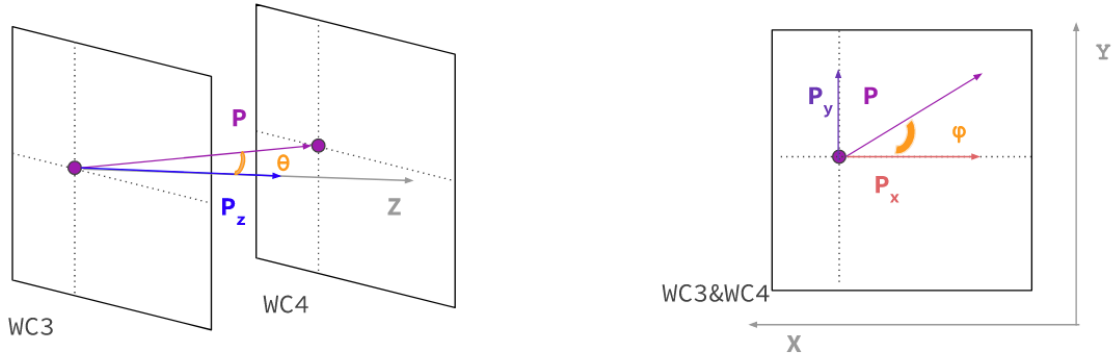


Figure 5.4: Scheme of the quantities of interest for the DDMC event generation: P_x, P_y, P_z, X, Y at WC4.

2175 5.3 Estimate of Backgrounds in the Pion Cross Section

2176 We use the beamline simulation and the DDMC simulation to estimate the background in the total hadronic pion cross section. Two categories of background exists for the negative pion cross section measurement: the background related to the pion alternative processes to hadronic interaction inside the LArTPC, discussed in Section 5.3.1 and the background related to the beamline contamination, discussed in Section 5.3.2.

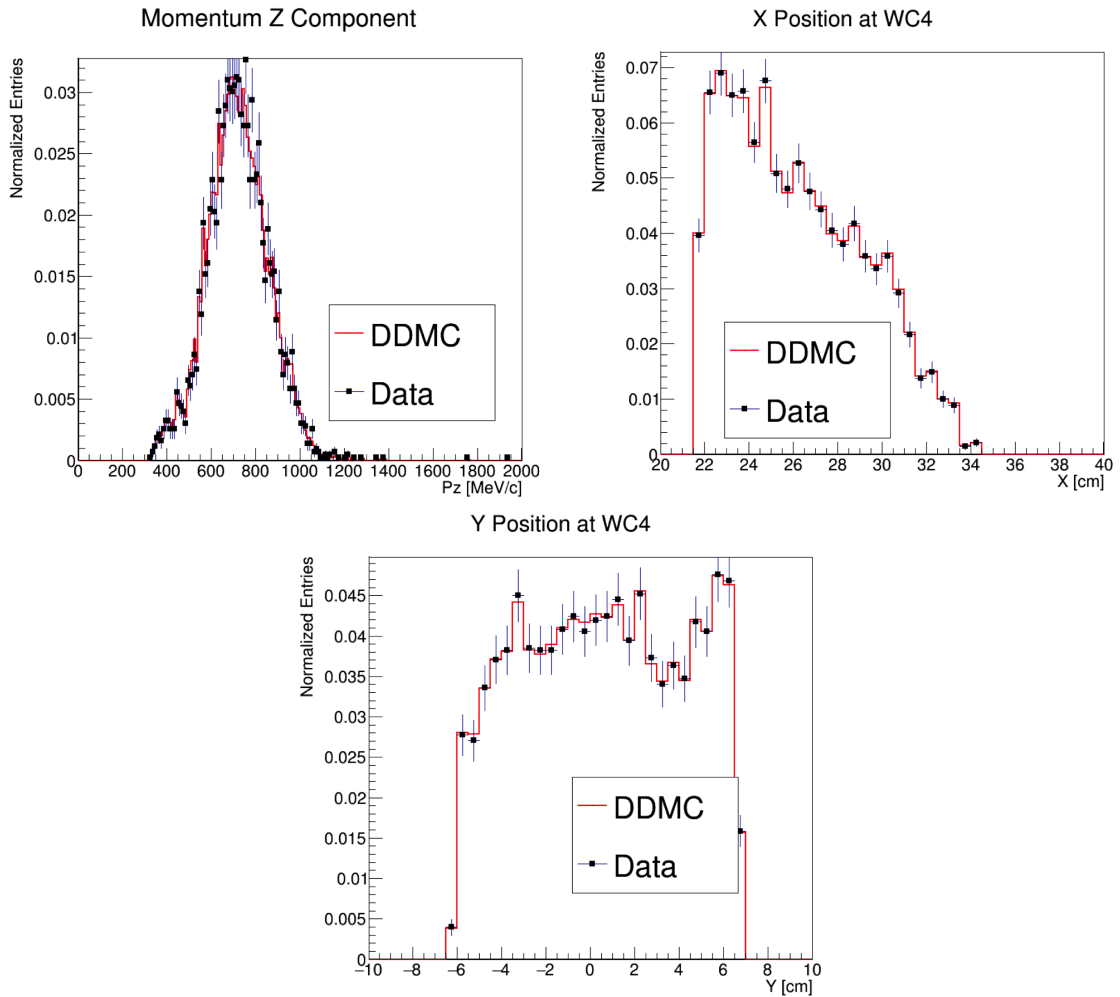


Figure 5.5: Comparison between generated quantities and data distributions for the 100A kaon sample: Z component of the momentum at WC4 (top left), X position at Wire Chamber 4 (top right), Y position at Wire Chamber 4 (bottom).

2183 **5.3.1 Background from Pion Capture and Decay**

2184 Our goal is to measure the total hadronic cross section for negative pions in argon.
2185 Since pion capture can be classified as an electromagnetic process and pion decay is a
2186 weak process (as discussed in Section 1.4.1), capture and decay represent alternative
2187 processes to the hadronic interaction, resulting therefore into a background for the
2188 cross section analysis. We present here a study of capture and decay in Monte Carlo
2189 and the solution we adopted to remove their occurrence in the data sample.

2190 For this MC study, we use a sample of MC pions generated according to the
2191 –60A beam profile with the DDMC (see Section 5.2.2). It is important to notice
2192 that capture occurs predominantly at rest, while decay may occur both in flight
2193 and at rest. Thus, we can highly mitigate capture and decay at rest by removing
2194 pions whose kinetic energy at the TPC front face is low enough to be completely
2195 released by ionization in the TPC, eventually bringing the pion to stop within the
2196 fiducial volume. This translates into a beam momentum selection, where we keep
2197 only events whose WC momentum is above a certain threshold. Figure 5.6 shows the
2198 true momentum distribution for the primary pions¹ that arrive to the TPC (pink),
2199 that capture (green) or decay (blue) inside the TPC, on a linear scale (left) and on a
2200 log scale (right) vertical axis.

2201 In order to choose the selection value for the wire chamber momentum, it is
2202 beneficial to estimate the fraction of MC capture and decay events that survive the
2203 momentum selection as a function of the momentum threshold, and compare it with
2204 the survival fraction for all the 60A events. This is done in figure 5.7. We define the
2205 survival ratio simply as the number of events surviving the true momentum selection
2206 divided by the number of events of that category. We calculate the survival ratio

1. We use here the Geant4 denomination “primary” to indicate that the pion considered does not undergo interactions modifying its energy before getting to the TPC. In fact, not every pion shot from wire chamber four will arrive to the TPC as primary, some will decay or interact before the TPC.

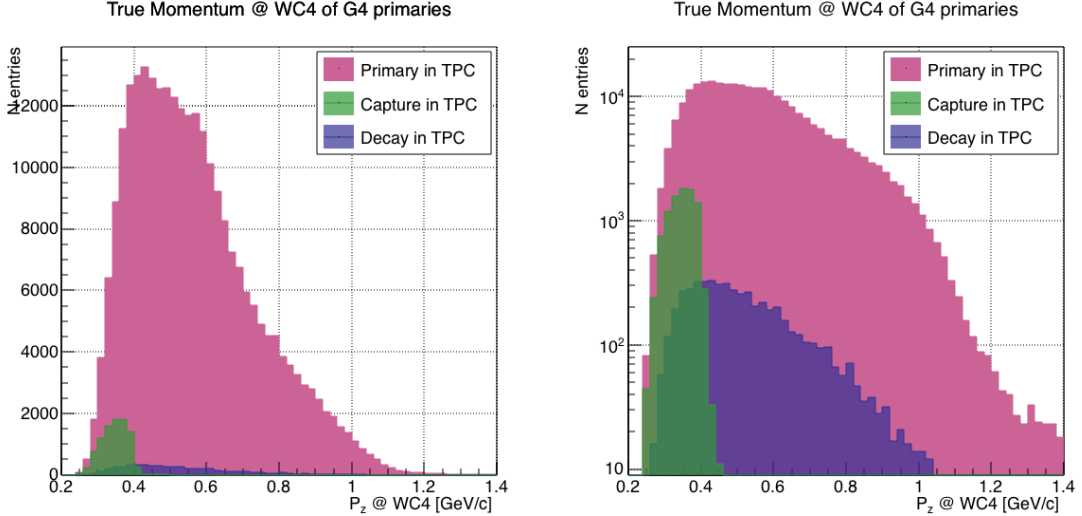


Figure 5.6: MC momentum distribution at wire chamber 4 for every simulated pion arriving in the TPC (pink), ending its life in capture (green) or in decay (blue) in the TPC, linear vertical axis on the left, logarithmic on the right.

2207 separately for the three event categories explained above: total (pink), capture (green)
 2208 and decay (blue). Selecting pions with momentum greater than 420 MeV/c removes
 2209 $\sim 99\%$ the capture events while maintaining about 80% of the 60A data sample and
 2210 almost the entire 100A sample. Figure 5.8 shows the ratio of events which end their
 2211 life in capture (green) or decay (blue) over the total number of events as a function
 2212 of the true MC momentum at WC4. This ratio is slightly dependent on the inelastic
 2213 cross section implemented in Geant4, as we are able to register a pion capture (or
 2214 decay) only if it did not interact inelastically in the TPC. We choose a momentum
 2215 threshold of 420 MeV/c because the percentage of capture events drops below 1% and
 2216 the percentage of decays is never above 2% for momenta greater than 420 MeV/c.
 2217 After the momentum selection, we evaluate the contribution of capture and decay to
 2218 be a negligibly small background to the cross section measurement compared to the
 2219 background related to the beamline which we will address in the next section.

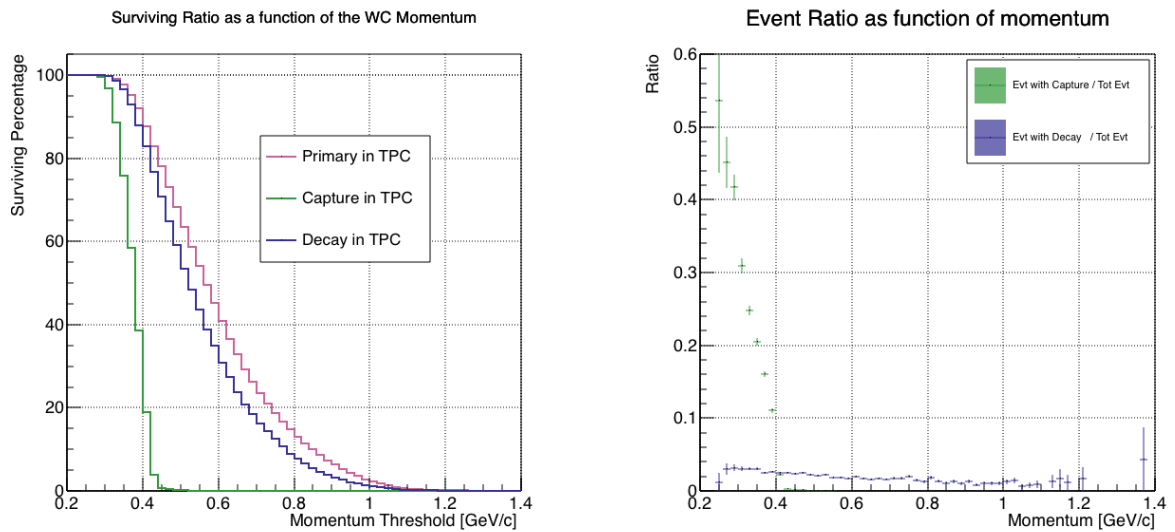


Figure 5.7: Survival ratio as a function of selection threshold on MC momentum at wire chamber four for every simulated pion arriving in the TPC (pink), capture (green) or in decay (blue).

Figure 5.8: Ratio between the capture (green) and decay (blue) events over the total number of events as a function of the MC momentum at wire chamber four.

2220 **5.3.2 Contributions from the Beamline Background**

2221 We define beamline background every TPC track matched to the WC track which is
2222 not a primary pion. Potentially, there are 4 different types of beamline background:

2223 1) electrons,

2224 2) muons,

2225 3) secondaries from pion interactions in beamline elements,

2226 4) matched pile up events.

2227 The first step to quantify the effect of the beamline background on the pion cross
2228 section is to estimate what percentage of events used in the cross section calculation is
2229 not a primary pion. We start by noting that the last type of background, the “matched
2230 pile up” events, is a negligible fraction, because of the definition of the WC2TPC
2231 match: we deem the probability of a single match with a halo particle in the absence of
2232 a beamline particle² negligibly small. As shown in Section 5.2.1, we use G4Beamline
2233 to estimate the percentage of pions, muons and electrons at WC4, obtaining the
2234 composition shown in Table 5.2. The next step is to simulate those pions, muons and
2235 electrons from WC4 to the TPC with the DDMC and evaluate their contribution to
2236 the cross section. To do so, we start by generating the same number of electrons,
2237 muons and pions with the DDMC and we apply the same selection chain applied in
2238 data (i.e. track multiplicity rejection, WC2TPC match and shower rejection) on the
2239 three samples. The number of events per particle species surviving this selection is
2240 shown on table 5.3. In order to reproduce the data beamline composition, we weight
2241 each event of a given particle species according to the estimated content for that
2242 species as found with the G4Beamline simulation. In case of 60A runs, for example,
2243 the weights are 0.688 for pions, 0.046 for muons and 0.266 for electrons.

2. Events with multiple WC2TPC matches are always rejected.

	Magnet Current -60A			Magnet Current -100 A		
	MC π^-	MC μ^-	MC e^-	MC π^-	MC μ^-	MC e^-
Total Initial events	334500	334500	334500	344500	344500	344500
After Multiplicity Rejection	330668	333420	198065	326576	344208	201380
After WC2TPC Selection	218239	296333	91139	230418	300228	98834
Evts After Shower Rejection	208063	288914	20293	219882	293585	17780
Selection Survival Rate	62.2%	86.4%	6.1%	63.8%	85.2%	5.2%
Beam Composition @WC4	68.8%	4.6 %	26.6 %	87.4 %	3.7 %	8.9 %
Expected Composition in XS sample	88.5%	8.2%	3.3 %	94.0%	5.3%	0.7%

Table 5.3: MC selection flow per particle species.

2244 It should be noted that pions may interact hadronically in the steel (cryostat wall)
 2245 or in the non-instrumented argon upstream to the TPC front face while traveling the
 2246 length of between WC4 and the TPC. Or, they could decay in flight between WC4
 2247 and the TPC. One of the interaction or decay products can leak into the TPC and
 2248 be matched with the WC track, contributing to the pool of events used for the cross
 2249 section calculation. We call this type of particles “secondaries” from pion events,
 2250 with a terminology inspired by Geant4. We estimate the number of secondaries using
 2251 the DDMC pion sample. The percentage of secondaries is given by the number of
 2252 matched WC2TPC tracks whose corresponding particle is not flagged as primary by
 2253 Geant4. The secondary particles to primary pion ratio is 4.9% in the 60A sample and
 2254 4.3% in the 100A sample.

2255 We evaluate the beamline background contribution to the cross section by pro-
 2256 ducing the interacting and incident histograms for the signal and background events
 2257 surviving the selection, staggering the contributions for each particle species, as shown
 2258 in Figure 5.9 for the -60A case and in Figure 5.10 for the -100A case. From those
 2259 histograms, we are able to evaluate the contribution of pions and beamline back-
 2260 grounds to each bin of the interacting and incident histograms separately and obtain

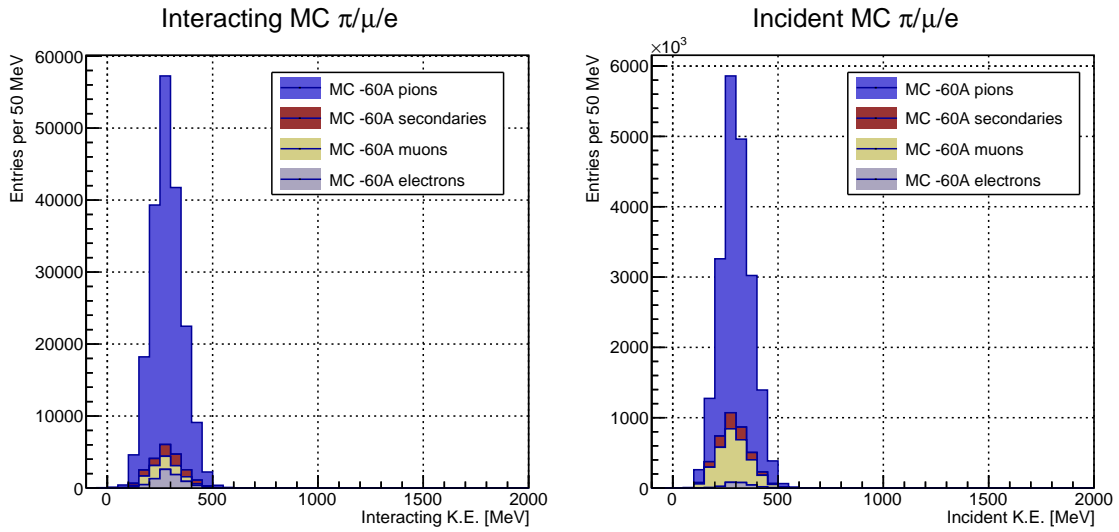


Figure 5.9: Left: staggered contributions to the interacting kinetic energy distribution for electron (grey), muons (yellow) and pion (blue) in the 60A simulation sample. Right: staggered contributions to the incident kinetic energy distribution for electron (grey), muons (yellow) and pion (blue) in the 60A simulation sample.

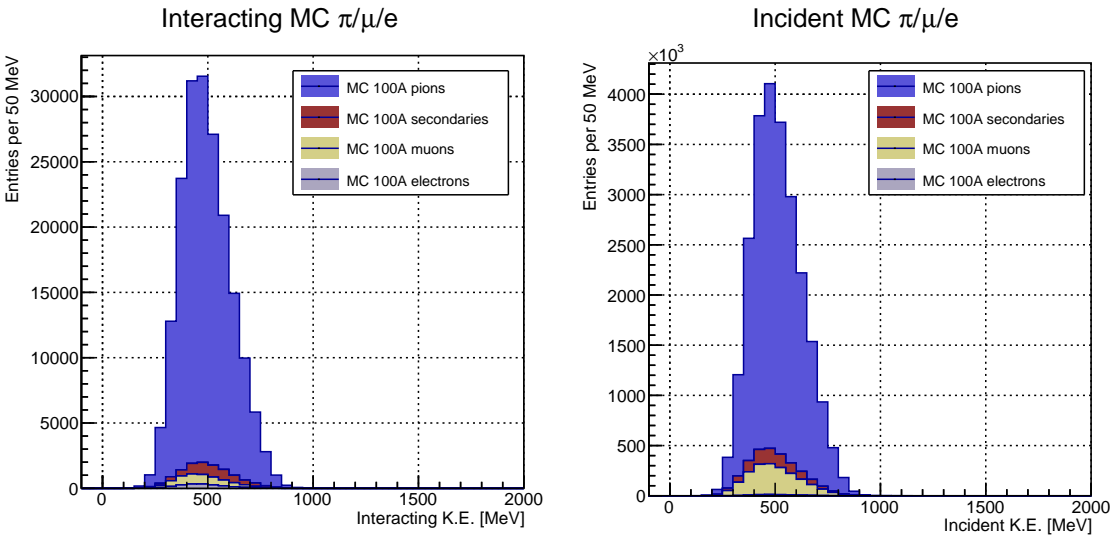


Figure 5.10: Left: staggered contributions to the interacting kinetic energy distribution for electron (grey), muons (yellow) and pion (blue) in the 100A simulation sample. Right: staggered contributions to the incident kinetic energy distribution for electron (grey), muons (yellow) and pion (blue) in the 100A simulation sample.

2261 the relative pion content. The relative pion content in each bin for the interacting
 2262 and incident histograms represents the correction applied to data. We take here the
 2263 interacting histogram as example, noting that the derivation of the correction for the
 2264 incident histogram is identical. The number of entries in each bin of the interacting
 2265 histogram (Figure 5.9 left) is $N_{\text{Int}}^{\text{TOT}}(E_i)$, equal to the sum of the pions and beamline
 2266 backgrounds flagged as interacting in that bin, namely

$$N_{\text{Int}}^{\text{TOT}}(E_i) = N_{\text{Int}}^{\pi}(E_i) + \underbrace{N_{\text{Int}}^{\mu}(E_i) + N_{\text{Int}}^e(E_i) + N_{\text{Int}}^{\text{Secondary}}(E_i)}_{B_{\text{Int}}(E_i)}. \quad (5.1)$$

2267 Thus, the relative pion content to each bin in MC can be calculated as follows

$$C_{\text{Int}}^{\pi MC}(E_i) = \frac{N_{\text{Int}}^{\pi MC}}{N_{\text{Int}}^{\text{TOTMC}}(E_i)} = \frac{N_{\text{Int}}^{\text{TOTMC}}(E_i) - B_{\text{Int}}^{\text{MC}}(E_i)}{N_{\text{Int}}^{\text{TOTMC}}(E_i)}. \quad (5.2)$$

2268 In order to evaluate the pion content of each bin in data, we scale the measured
 2269 bin by the corresponding relative pion content found in MC, as follows

$$N_{\text{Int}}^{\pi \text{RecoData}} = N_{\text{Int}}^{\text{TOTData}}(E_i) - B_{\text{Int}}^{\text{Data}}(E_i) = C_{\text{Int}}^{\pi MC}(E_i)N_{\text{Int}}^{\text{TOTData}}(E_i). \quad (5.3)$$

2270 The pion content is evaluated separately in the interacting and incident his-
 2271 tograms. Their ratio determines a correction to the measured raw cross section.
 2272 For example, the measured raw cross section of a sample with enhanced muons con-
 2273 tent will tend to be lower than the raw cross section of a muon free sample. This is
 2274 because most of the muons will cross the TPC without stopping, thus contributing
 2275 almost exclusively to the incident histogram, forcing the pion content to be lower in
 2276 the incident histogram than in the interacting; thus, the correction will tend to en-
 2277 hance the cross section. We present the estimation of $C_{\text{Int}}^{\pi MC}(E_i)$ and $C_{\text{Inc}}^{\pi MC}(E_i)$ and
 2278 their associated systematic uncertainty in chapter discussing the pion cross section
 2279 measurement (Figure 6.4).

2280 5.4 Estimate of Energy Loss before the TPC

2281 The beamline particles travel a path from where their momentum is measured in
2282 the beamline until they are tracked again inside the TPC. In the LArIAT geometry,
2283 a particle leaving the WC4 will encounter the materials listed in Table 5.4 before
2284 being registered again. The energy lost by the particle in this non-instrumented
2285 material modifies the particle's kinetic energy and directly affects the cross section
2286 measurement, as shown in equation 4.5.

Material	density [g/cm ³]	width [cm]
Fiberglass laminate (G10)	1.7	1.28
Liquid Argon	1.4	3.20
Stainless Steel	7.7	0.23
Titanium	4.5	0.04
Air	$1.2 \cdot 10^{-3}$	89.43
Plastic Scintillator	1.03	1.20 (+ 1.30)

Table 5.4: LArIAT material budget from WC4 to the TPC Front Face.

We derive an estimate of the energy loss between the beamline momentum measurement and the TPC (E_{loss}) from the pion and kaon DDMC samples, since this quantity is not measurable directly on data. The E_{loss} distribution for the 60A and 100A pion sample is shown in figure 5.11, left and right respectively. The E_{loss} distribution for the whole kaon sample is shown in figure 5.12. A clear double peaked structure is visible. After a long investigation on the origin of this unexpected shape, we determined that its origin is due to the particles either missing or hitting the HALO paddle (see Section 3.2.4 for the HALO paddle description): a schematic rendering of this occurrence is shown in figure 5.13. The kinematic at WC4 determines the trajectory of a particle and indicates whether or not it will hit the halo paddle, whose positioning and central hole size were not sufficiently well defined when the beamline instrumentation was installed. In figure 5.14 , we plot the true horizontal component of the momentum P_x versus the true X position at WC4 for pions missing

the halo paddle (left) and for pions hitting the halo paddle (right) for the -60A MC simulation runs – analogous plots are obtained with the -100A pion simulation and with the kaon simulation. These distributions can be separated drawing a line in this position-momentum space. We use a logistic regression [13] as a classifier to find the best separating line, shown in both plots as the red line. We classify as “hitting the halo paddle” all pions whose P_x and X are such that

$$P_x + 0.02 * X - 0.4 < 0$$

and as “missing the halo paddle” all pions whose P_x and X are such that

$$P_x + 0.02 * X - 0.4 > 0,$$

where the coefficients of the line are empirically found by the logistic regression estimation. Overall, this simple method classifies in the right category (hit or miss) about 86% of the pion events. In MC, we assign $E_{loss} = 32 \pm 4$ MeV for pion events classified as “hitting the halo paddle”; we assign $E_{loss} = 24 \pm 3$ MeV for pion events classified as “missing the halo paddle”. These values are the average and width of the two landau distributions underneath the double peaked distribution. We apply the same classifier on data.

A late scan of the simulated geometry showed an excess of 3 cm of uninstrumented argon compared with the surveyed detector geometry. This excess has an effect on the E_{loss} : MC particles traverse more uninstrumented material (i.e. loose more energy in the argon before the TPC front face) than data particles. We account for this difference by assigning in data $E_{loss} = 24 \pm 6$ MeV for pion events classified as “hitting the halo paddle” and $E_{loss} = 17 \pm 6$ MeV for pion events classified as “missing the halo paddle”, where the uncertainty is derived as the standard deviation of the double peaked distribution.

2302 The summary of the values for used for E_{Loss} for the pion sample is listed in table
 2303 5.5 with the analogous results for the study on the kaon case.

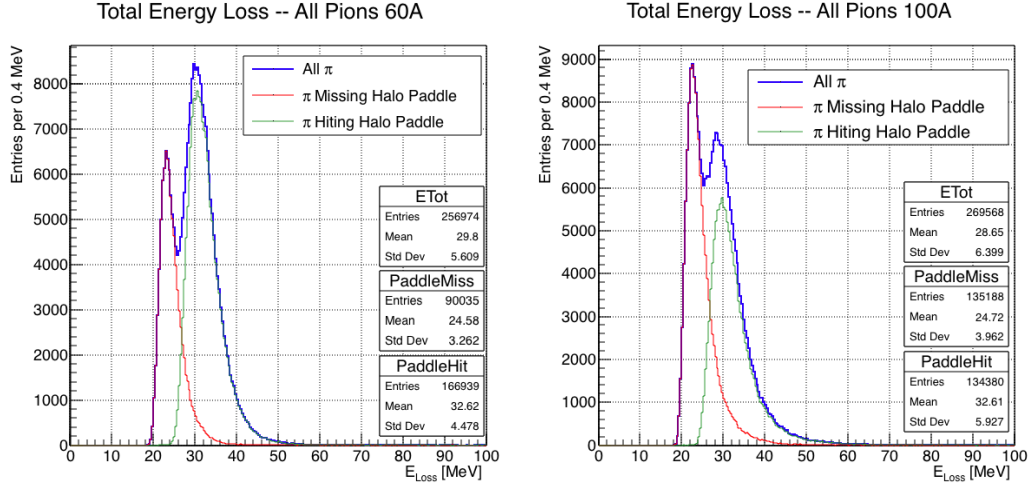


Figure 5.11: True energy loss between WC4 and the TPC front face according to the MC simulation of negative pions of the 60A runs (left) and of the 100A runs (right). The distribution for the whole data sample is shown in blue, the distribution for the pions missing the halo is shown in red, and the distribution for the pions hitting the halo is shown in green.

2304 5.5 Tracking Studies

2305 The tracking of hadrons in the TPC determines both the beamline to TPC hand-
 2306 shake and the identification of the interaction point within the TPC. Thus, it plays
 2307 a fundamental role in the cross section measurements. We performed several studies
 2308 geared towards the optimization of the LArSoft software package for tracking in the
 2309 TPC. In particular, we studied a suitable set of parameters for the WC2TPC match

	E_{loss} [MeV]	
	Hitting Halo	Missing Halo
Pion MC	32 ± 4	24 ± 3
Pion Data	25 ± 6	17 ± 6
Kaon MC	38 ± 6	31 ± 5
Kaon Data	26 ± 7	22 ± 7

Table 5.5: Energy loss for pions and kaons.

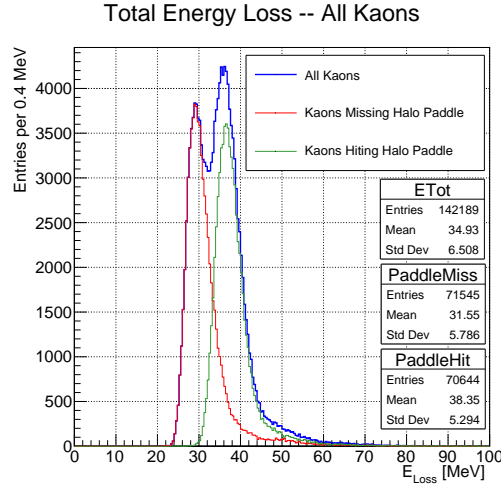


Figure 5.12: True energy loss between WC4 and the TPC front face according to the MC simulation of positive kaons in the 60A and 100A combined sample. The distribution for the whole data sample is shown in blue, the distribution for the kaons missing the halo is shown in red, and the distribution for the kaons hitting the halo is shown in green.

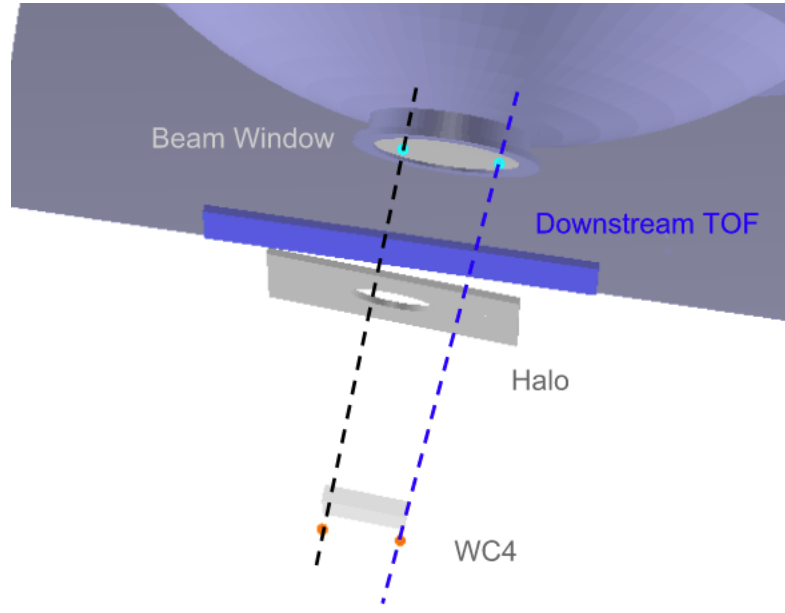


Figure 5.13: Schematic rendering of the particle path between WC4 and the TPC front face. The paddle with the hollow central circle represents the Halo paddle. We illustrate two possible trajectories: in black, a trajectory that miss the paddle and goes through the hole in the Halo, in blue a trajectory that hits the Halo paddle and goes through the scintillation material.

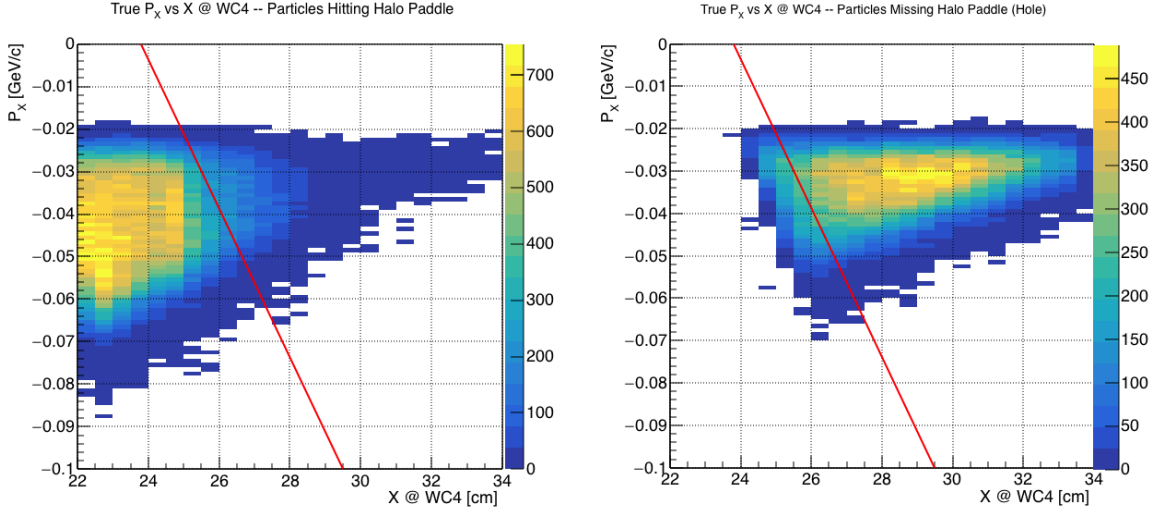


Figure 5.14: Horizontal component of the true momentum vs the horizontal position at WC4 for MC simulated pions of the 60A runs. The plot on the left shows the distribution for pion that miss the halo paddle and the plot on the right shows the distributions for pions that hit the halo. The form of the classifier is overlaid to both plots (red line).

and we optimized the clustering algorithm to maximize the efficiency of finding the interaction point on MC. Given the technical nature of these studies, we report them in Appendix B. We only report here the evaluation of the angular resolution of the tracking algorithm in data and MC, due to its important implications on the physics measurement.

5.5.1 Angular Resolution

Scope of this study is to understand and compare the tracking performances and the angular resolution of the TPC tracking on data and MC. We use the angular resolution of the tracking to determine the value of smallest angle that the tracking algorithms allow to reconstruct with a non-zero efficiency, effectively determining a selection on the distribution of the scattering angle of hadronic interaction entering the cross section measurement.

We start by selecting all the WC2TPC matched tracks used for the cross sec-

tion analysis. These tracks can contain from a minimum of 3 3D-space points to a maximum of 240 3D-space points. We fit a straight line to all the 3D-space points associated with the track. For each track we calculate the average distance between each point in space and the fit line as follows

$$\bar{d} = \frac{\sum_i^N d_i}{N}, \quad (5.4)$$

where N is the number of 3D-space points of the track and d_i is the distance of the i -th space point to the line fit. Several tests to compare the goodness of fit between data and MC have been considered. We decided to use \bar{d} for its straightforward interpretation. The \bar{d} distribution for data and MC is shown in Figure 5.17 for pions and in Figure 5.19 for kaons and shows a relatively good agreement between data and MC.

A visual representation of the procedure used to evaluate the angular resolution is shown in Figure 5.15. For each track, we order the space points according to their Z position along the positive beam direction (panel a) and we split them in two sets: the first set contains all the points belonging to the first half of the track and the second set contains all the points belonging the second half of the track. We remove the last four points in the first set and the first four points in the second set, so to have a gap in the middle of the original track (panel b). We fit the first and the second set of points with two lines (panel c). We then calculate the angle between the fit of the first and second half α (panel d). The angle α determines the angular resolution of the tracking. The distributions for data and MC for α are given in Figure 5.18 for pions and in Figure 5.20 for kaons. The mean of the data and MC angular resolution are reported in Table 5.6 for pions and kaons in data and MC.

Interaction angles smaller than the angular resolution are indistinguishable for the reconstruction. Therefore, we assess our ability to measure the cross section

2347 to be limited to interaction angles greater than 5.0 deg. More accurate studies of
 2348 the angular resolution as a function of the kinetic energy and track length, albeit
 2349 interesting, are left for an improvement of the analysis.

2350 As we discussed in Section 1.4.1, several different interaction topologies are in-
 2351 cluded as signal in the total hadronic cross section. The ability to detect a minimum
 2352 interaction angle and to stop the tracking accordingly mainly effects two interaction
 2353 channels: the pion elastic interaction (see Table 1.4, second line) and the pion in-
 2354 elastic interaction in case of neutral particle emission (see Table 1.4, fourth line); the
 2355 overall effect of this limitation is to reduced the cross section measurement to the
 2356 measurement of the cross section relative to interaction angles greater than a ~ 5.0
 2357 deg . It is beneficial to take a moment to describe the definition of interaction angle.
 2358 In case of elastic scattering, the definition is straightforward: the interaction angle is
 2359 the angle between the incoming and outgoing hadron, i.e.

$$\theta = \cos^{-1} \left(\frac{\vec{p}_{\text{incoming}} \cdot \vec{p}_{\text{outgoing}}}{|\vec{p}_{\text{incoming}}| |\vec{p}_{\text{outgoing}}|} \right). \quad (5.5)$$

2360 In case of the reaction channel, the presence of several topologies requires a more
 2361 complex definition, as shown in figure 5.16. We define the scattering angle as the
 2362 biggest of the angles between the incoming hadron and the visible daughters, where
 2363 the visible daughters are charged particles that travel more than the average pitch
 2364 length ($\delta X = 47$ mm) in the detector (see panel a); in case all the daughters are
 2365 invisible, the angle is assigned to be 90 deg (see panel b). We chose this working
 2366 definition of scattering angle for inelastic scattering keeping in mind how our tracking
 2367 reconstruction works: the tracking will stop correctly if none of the daughters is visible

	Data	MC
Pions	$\bar{\alpha}_{Data} = (5.0 \pm 4.5)$ deg	$\bar{\alpha}_{MC} = (4.5 \pm 3.9)$ deg
Kaons	$\bar{\alpha}_{Data} = (4.3 \pm 3.7)$ deg	$\bar{\alpha}_{MC} = (4.4 \pm 3.6)$ deg

Table 5.6: Angular resolution for Pion and Kaon tracking in both data and MC.

2368 in the detector and it is likely to stop correctly if multiple visible daughters form
2369 an interaction vertex. The only “dangerous” case is the production of one charged
2370 daughter plus neutrals, which we can study with this working definition of scattering
2371 angle (see panel c).

2372 Once we fix the scattering angle definition, we can study the effects of the angular
2373 resolution on the cross section by plotting the true Geant4 total hadronic cross section
2374 for interaction angles greater than a minimum interaction angle. The left side of
2375 Figure 5.21 shows the true Geant4 cross section for interaction angles greater than 0
2376 deg (green), 4.5 deg (red) corresponding to the MC angular resolution, 5.0 deg (blue)
2377 corresponding to the data angular resolution, and 9.0 deg (yellow). A small 0.5 deg
2378 systematic shift between the mean of the data and MC angular resolution is present,
2379 which has a negligible impact on the cross section. The right side of Figure 5.21 shows
2380 the ratio between the true cross section for interaction angles greater than 5 deg and
2381 the true interaction cross section for all angles; the cross section for angles greater
2382 than 5° accounts for more than 80% than the total cross section in every energy bin.

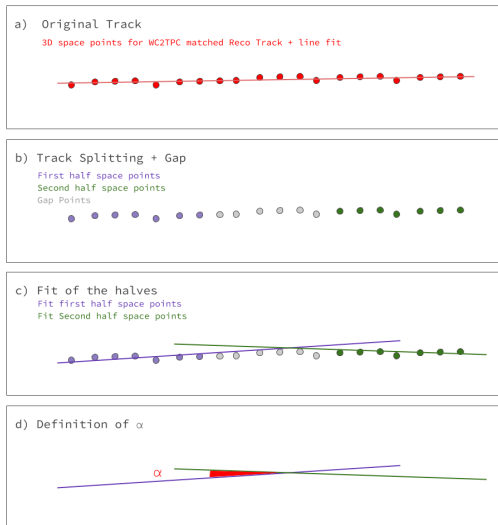


Figure 5.15: A visual representation of the procedure used to evaluate the angular resolution.

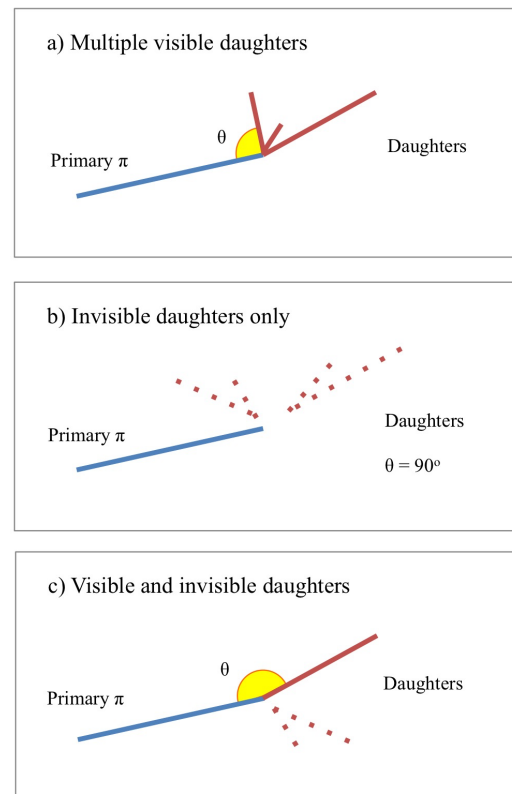


Figure 5.16: A visual representation of the scattering angle definition in case of inelastic scattering.

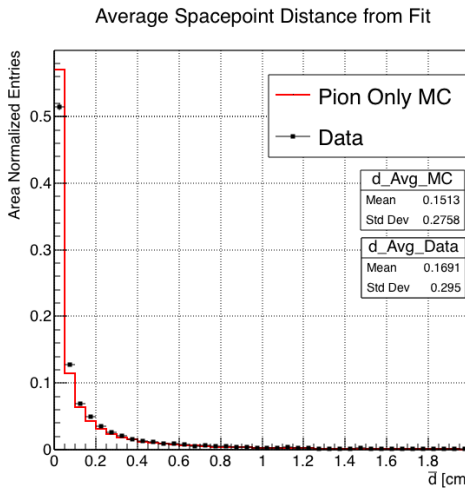


Figure 5.17: Distributions of the average distance between each 3D point in space and the fit line, \bar{d} for the data used in the pion cross section analysis and the pion only DDMC. The distributions are area normalized.

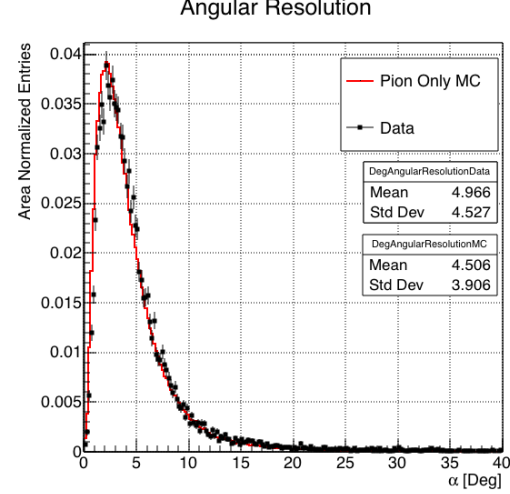


Figure 5.18: Distributions of angular resolution α for data used in the pion cross section analysis and pion only DDMC. The distributions are area normalized.

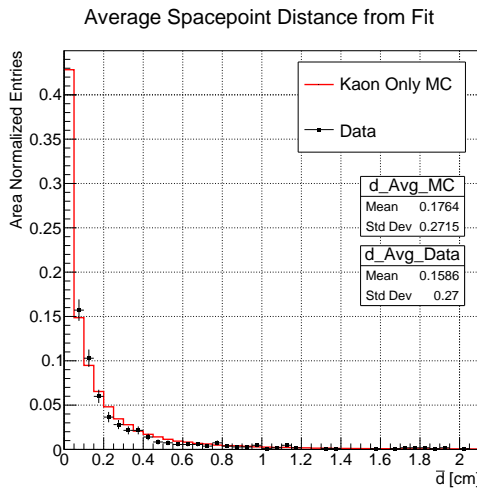


Figure 5.19: Distributions of the average distance between each 3D point in space and the fit line, \bar{d} for the data used in the kaon cross section analysis and the kaon only DDMC. The distributions are area normalized.

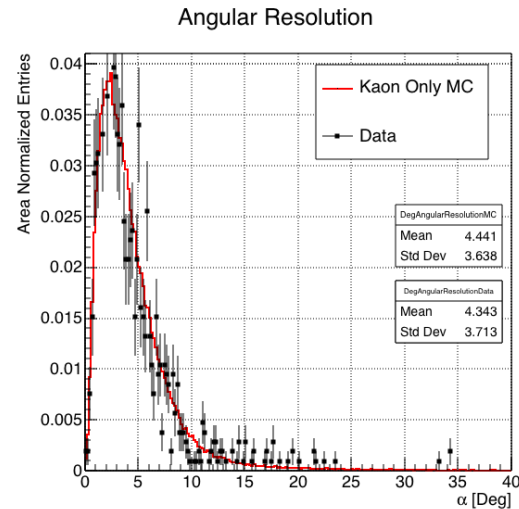


Figure 5.20: Distributions of angular resolution α for data used in the kaon cross section analysis and kaon only DDMC. The distributions are area normalized.

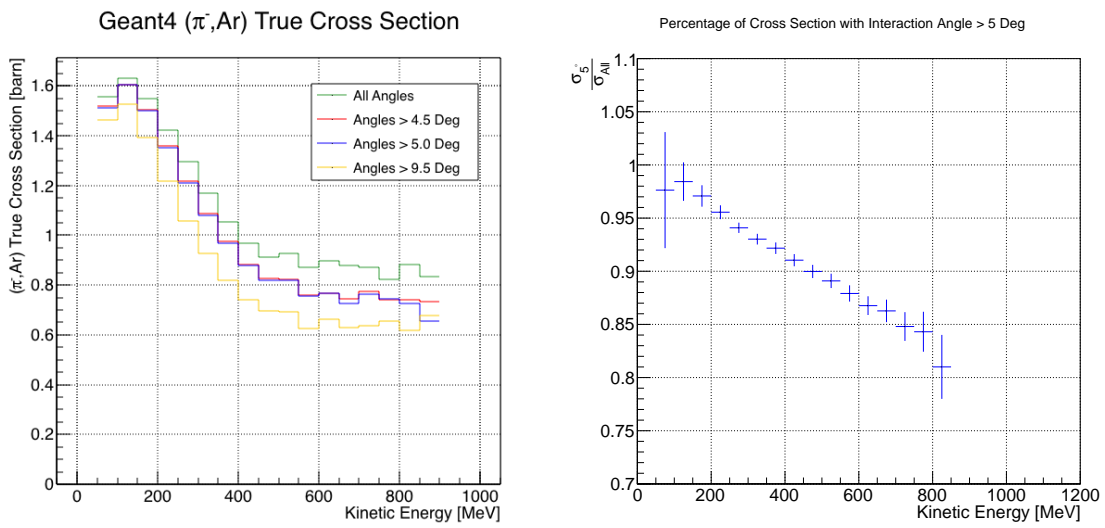


Figure 5.21: *Left:* True (π^-, Ar) cross section for interaction angles greater than 0 deg (green), 4.5 deg (red), 5.0 deg (blue) and 9.0 deg (yellow). *Right:* Ratio between the true cross section for interaction angles greater than 5 deg and the true interaction cross section for all angles.

2383 **5.6 Calorimetry Studies**

2384 The measured kinetic energy of a hadron candidate at each argon slab determines
2385 which bins of the interacting and incident histograms a selected event is going to fill.
2386 Thus, the energy measurement provided by the LArTPC is fundamental for the cross
2387 section analysis. In Appendix C, we describe how we calibrate the TPC calorimetric
2388 response. In this section, we describe how we measure the kinetic energy of the
2389 hadrons in the TPC.

2390 **5.6.1 Kinetic Energy Measurement**

2391 In this section, we define the measurement on the kinetic energy and determine the
2392 related uncertainty. We will propagate this uncertainty into the cross section mea-
2393 surement, as discussed in Section 6.1.2 for the pion cross section and in Section ??
2394 for the kaon cross section.

2395 The kinetic energy of a hadron at the j^{th} slice of argon in the TPC is given by

$$KE_j = \sqrt{p_{\text{Beam}}^2 + m_{\text{Beam}}^2} - m_{\text{Beam}} - E_{\text{Loss}} - E_{\text{FF-j}}, \quad (5.6)$$

2396 where p_{Beam} is the momentum measured by the beamline detectors, m_{Beam} is the
2397 mass of the hadron as reported in the PDG, E_{Loss} is the energy loss between the
2398 beamline and the TPC, and $E_{\text{FF-j}}$ is the energy that the hadron deposited from the
2399 TPC front face until the j^{th} slice. The uncertainty on KE_j is then given by

$$\delta KE_j = \sqrt{\delta p_{\text{Beam}}^2 + \delta E_{\text{Loss}}^2 + \delta E_{\text{dep FF-j}}^2}, \quad (5.7)$$

2400 where we have dropped the uncertainty on the mass, since it is orders of magnitude
2401 smaller than the other uncertainties. We assume the relative uncertainty on p_{Beam} to
2402 be 2%, and the uncertainty on the energy loss upstream to be 7 MeV, as calculated

2403 in Section 5.4. We describe the estimate of the uncertainty on $E_{\text{FF-j}}$ in the rest of
2404 this section.

2405 The energy deposited by the hadron from the TPC front face until the j^{th} slice is
2406 the sum of the measured energy deposited in each previous slabs E_i , i.e.

$$E_{\text{FF-j}} = \sum_{i < j} E_i, \quad (5.8)$$

2407 where E_i is measured in each slab as the product of the stopping power, dE/dX_i ,
2408 and the track pitch for that point. Since the measurements of the energy deposited
2409 in each slab rely on the same global calorimetric procedure and tracking algorithms,
2410 we assume conservatively that that the measurements of E_i are not independent from
2411 one another; thus, the uncertainty on $E_{\text{FF-j}}$ becomes

$$\delta E_{\text{FF-j}} = \sum_{i < j} \delta E_i = (j - 1)\delta E_i, \quad (5.9)$$

2412 where δE_i is the uncertainty on the energy loss in one slab of argon.

2413 The left side of Figure 5.22 shows the distribution of the energy deposited in each
2414 slab of argon, for the 60A negative pion dataset in black and for the pion only MC
2415 in blue. The analogous plot for the -100A negative pion data set is show on the right
2416 side of Figure 5.22. The distributions are fitted with a landau displayed in red for
2417 data and in teal for MC. The uncertainty on E_i is given by the width of the Landau
2418 fit to the data. A small systematic uncertainty is given by a 1.0% difference between
2419 the most probable value of the landau fits in data and MC.

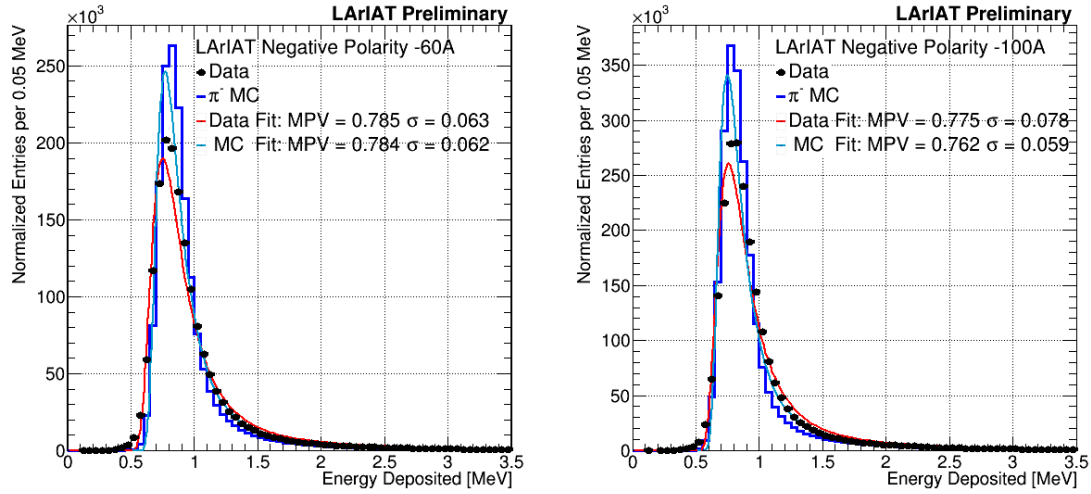


Figure 5.22: Energy deposited E_i in a single slab of argon for the pion -60A runs (left) and -100A runs (right). The data is shown in black, the MC in blue. The distributions are fitted with a landau displayed in red for data and in teal for MC.

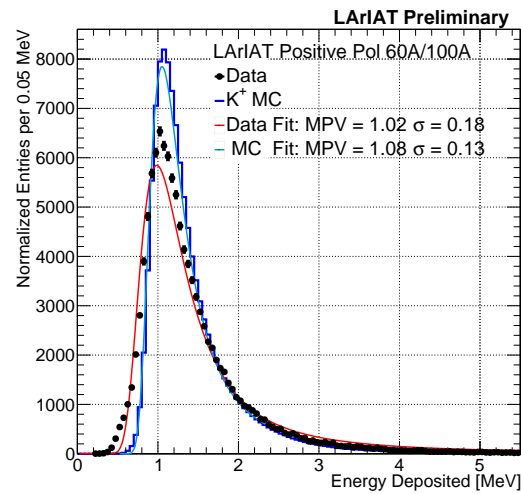


Figure 5.23: Energy deposited E_i in a single slab of argon for the kaons of the +60A runs and +100A runs. The data is shown in black, the MC in blue. The distributions are fitted with a landau displayed in red for data and in teal for MC.

2420 **Chapter 6**

2421 **Negative Pion Cross Section**
2422 **Measurement**

2423 “*Y ella es flama que se eleva, Y es un pájaro a volar.*
2424 *En la noche que se incendia, estrella de oscuridad*
2425 *que busca entre la tiniebla, la dulce hoguera del beso.*”
2426 – Lila Downs, 2002 –

2427 In this chapter, we show the result of the thin slice method to measure the (π^- -
2428 Ar) total hadronic cross section. In Section 6.1, we start by measuring the raw cross
2429 section, i.e. the cross section obtained exclusively using data reconstruction, without
2430 any additional corrections. In Section 6.2, we apply the statistical subtraction of the
2431 background contributions based on simulation and the correction for reconstruction
2432 effects. The final results are presented in Section 6.3.

2433 **6.1 Raw Cross Section**

2434 We measure the raw (π^- -Ar) total hadronic cross section as a function of the kinetic
2435 energy in the two chosen data sets, the -60A and -100A negative runs. As we will

clarify in Section 6.2, the corrections to the raw cross section depend on the beam settings and need to be calculated independently for the two datasets. Thus, we present here the measurement of the raw cross section on the two datasets separately.

As stated in section 4.3.2, the raw cross section is given by the equation 4.4

$$\sigma_{TOT}(E_i) = \frac{1}{n \delta X} \frac{N_{Int}^{TOT}(E_i)}{N_{Inc}^{TOT}(E_i)}, \quad (4.4)$$

where N_{Int}^{TOT} is the measured number of particles interacting at kinetic energy E_i , N_{Inc}^{TOT} is the measured number of particles incident on an argon slice at kinetic energy E_i , n is the density of the target centers and δX is the thickness of the argon slice. The density of the target centers and the slab thickness are $n = 0.021 \cdot 10^{24} \text{ cm}^{-3}$ and $\delta X = 0.47 \text{ cm}$, respectively.

Figure 6.1 shows the distribution of N_{Int}^{TOT} as a function of the kinetic energy for the 60A dataset on the left and for the 100A dataset on the right. The data central points are represented by black dots, the statistical uncertainty is shown in black, while the systematic uncertainty is shown in red. Data is displayed over the N_{Int}^{TOT} distribution obtained with a MC sample of pions, muon and electrons weighted by the beam composition (additional details on the composition will be provided in Section ??). The contribution from the simulated pions is shown in blue, the one from secondaries in red, the one from muons in yellow and the ones from electrons in gray. The simulated pion's and backgrounds' contributions are stacked; the sum of the integrals from each particle species is normalized to the integral of the data.

Figure 6.2 shows the distribution of N_{Inc}^{TOT} for the 60A dataset on the left and for the 100A dataset on the right. Data is displayed over the MC. The same color scheme and normalization procedure is used for both the interacting and incident histograms.

Figure 6.3 shows the raw cross section for the 60A dataset on the left and for the 100A dataset on the right, statistical uncertainty in black and systematic uncertainty

2460 in red. The raw data cross section is overlaid to the reconstructed cross section for the
 2461 MC sample, displayed in azure. Since the background contributions and the detector
 2462 effects for the 60A and 100A sample are different, it is premature to compare the raw
 2463 cross sections obtained from the two samples at this point.

2464 We describe the calculation of the statistical uncertainty for the interacting, in-
 2465 cident and cross section distributions in Section 6.1.1; we describe the procedure to
 2466 calculate the corresponding systematics uncertainty on Section 6.1.2.

2467 6.1.1 Statistical Uncertainty

2468 The statistical uncertainty for a given kinetic energy bin of the cross section is cal-
 2469 culated by error propagation from the statistical uncertainty on $N_{\text{Inc}}^{\text{TOT}}$ and $N_{\text{Int}}^{\text{TOT}}$
 2470 correspondent bin. Since the number of incident particles in each energy bin is given
 2471 by a simple counting, we assume that $N_{\text{Inc}}^{\text{TOT}}$ is distributed as a poissonian with mean
 2472 and variance equal to $N_{\text{Inc}}^{\text{TOT}}$ in each bin. On the other hand, $N_{\text{Int}}^{\text{TOT}}$ follows a bino-
 2473 mial distribution: a particle in a given energy bin might or might not interact. The
 2474 variance for the binomial is given by

$$\text{Var}[N_{\text{Int}}^{\text{TOT}}] = \mathcal{N}P_{\text{Interacting}}(1 - P_{\text{Interacting}}). \quad (6.1)$$

2475 Since the interaction probability $P_{\text{Interacting}}$ is estimated by $\frac{N_{\text{Int}}^{\text{TOT}}}{N_{\text{Inc}}^{\text{TOT}}}$ and the number
 2476 of tries \mathcal{N} is $N_{\text{Inc}}^{\text{TOT}}$, equation 6.1 translates into

$$\text{Var}[N_{\text{Int}}^{\text{TOT}}] = N_{\text{Inc}}^{\text{TOT}} \frac{N_{\text{Int}}^{\text{TOT}}}{N_{\text{Inc}}^{\text{TOT}}} \left(1 - \frac{N_{\text{Int}}^{\text{TOT}}}{N_{\text{Inc}}^{\text{TOT}}}\right) = N_{\text{Int}}^{\text{TOT}} \left(1 - \frac{N_{\text{Int}}^{\text{TOT}}}{N_{\text{Inc}}^{\text{TOT}}}\right). \quad (6.2)$$

2477 $N_{\text{Inc}}^{\text{TOT}}$ and $N_{\text{Int}}^{\text{TOT}}$ are not independent. In fact, the population of a given bin for
 2478 the interacting histogram always implies at least the population of the same bin in
 2479 the incident histogram (and possibly other incidents bins at higher energies). Thus,

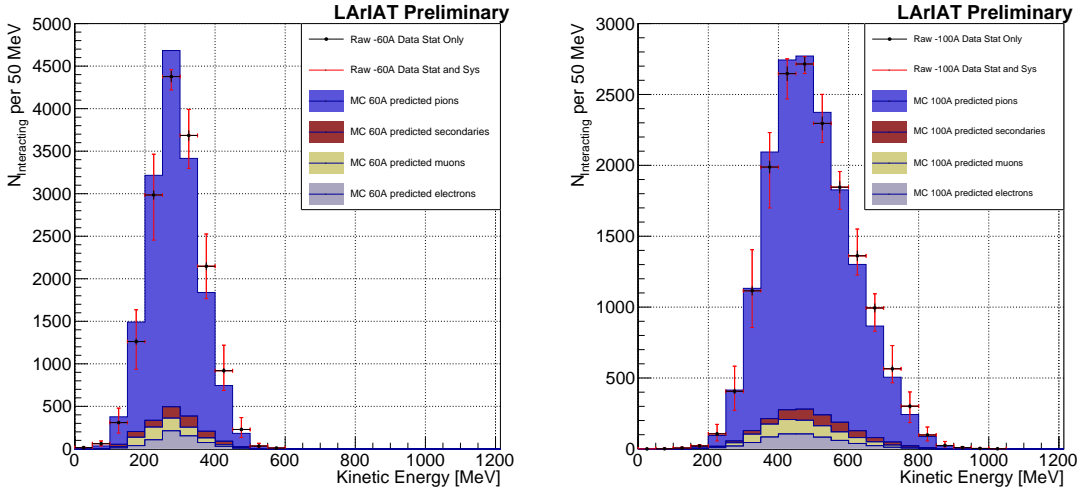


Figure 6.1: Raw number of interacting pion candidates as a function of the reconstructed kinetic energy for the 60A runs (left) and for the 100A runs (right). The statistical uncertainties are shown in black, the systematic uncertainties in red.

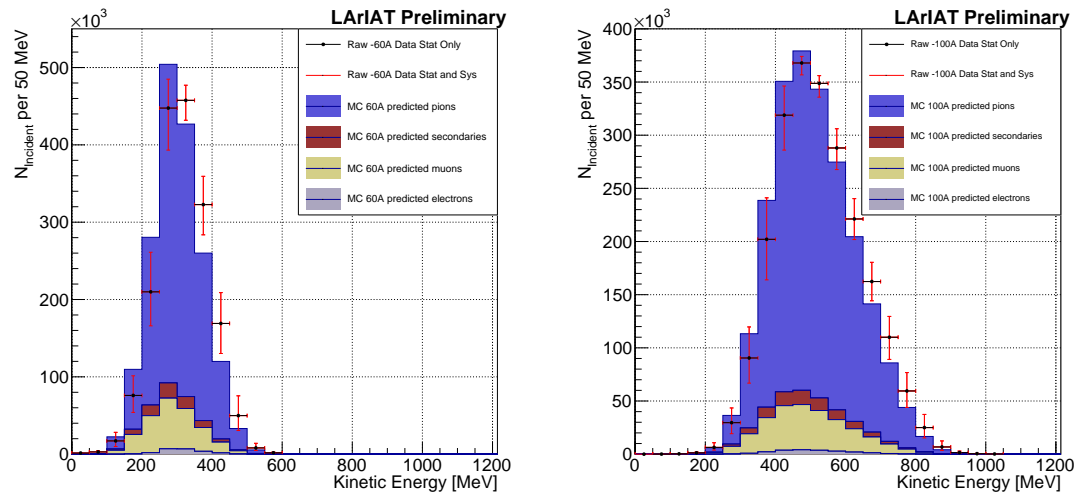


Figure 6.2: Raw number of incident pion candidates as a function of the reconstructed kinetic energy for the 60A runs (left) and for the 100A runs (right). The statistical uncertainty is shown in black, the systematic uncertainties in red.

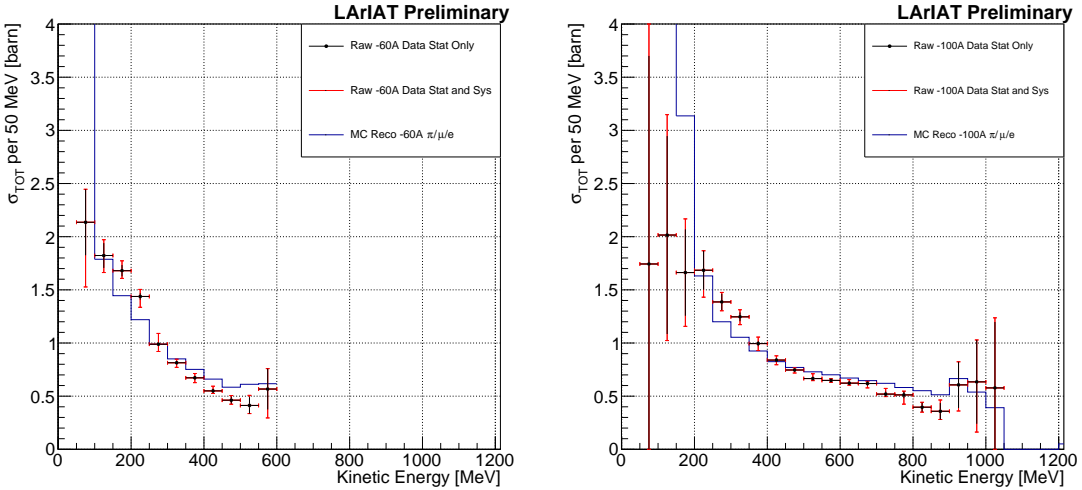


Figure 6.3: Raw (π^- -Ar) total hadronic cross section for the 60A runs (left) and for the 100A runs (right). The statistical uncertainty is shown in black, the systematic uncertainties in red. The raw cross section obtained with a MC mixed sample of pions, muon and electrons in the percentage predicted by G4Beamline is shown in azure.

2480 we conservatively calculate the statistical uncertainty on the cross section as

$$\delta\sigma_{TOT}(E) = \sigma_{TOT}(E) \left(\frac{\delta N_{Int}^{TOT}}{N_{Int}^{TOT}} + \frac{\delta N_{Inc}^{TOT}}{N_{Inc}^{TOT}} \right) \quad (6.3)$$

2481 where:

$$\delta N_{Inc}^{TOT} = \sqrt{N_{Inc}^{TOT}} \quad (6.4)$$

$$\delta N_{Int}^{TOT} = \sqrt{N_{Int}^{TOT} \left(1 - \frac{N_{Int}^{TOT}}{N_{Inc}^{TOT}} \right)}. \quad (6.5)$$

2482 6.1.2 Treatment of Systematics

2483 The only systematic effect considered in the measurement of the raw cross section
 2484 results from the propagation of the uncertainty associate with the measurement of
 2485 the kinetic energy at each argon slab. As shown in Section 5.6.1, the uncertainty on
 2486 the kinetic energy of a pion candidate at the j^{th} slab of argon is given by

$$\delta KE_j = \sqrt{\delta p_{Beam}^2 + \delta E_{Loss}^2 + \delta E_{dep\ FF-j}^2} \quad (6.6)$$

$$= \sqrt{(2\% p_{Beam})^2 + (6 [\text{MeV}])^2 + (j - 1)^2 (\sim 0.08 [\text{MeV}])^2}. \quad (6.7)$$

2487 We propagate this uncertainty by varying the energy measurement KE_j at each
 2488 argon slab. We measure N_{Inc}^{TOT} , N_{Int}^{TOT} and the cross section in three cases: first
 2489 assigning the measured KE_j at each kinetic energy sampling, then assigning $KE_j +$
 2490 δKE_j , and finally assigning $KE_j - \delta KE_j$. The difference between the values obtained
 2491 using the KE_j sampling and the maximum and minimum values in each kinetic energy
 2492 bin determines the systematic uncertainty.

2493 6.2 Corrections to the Raw Cross Section

2494 As described in section 4.3.3, we need to apply a background correction and an
 2495 efficiency correction in order to derive the pion cross section from the raw cross
 2496 section. The cross section is given in equation 4.9,

$$\sigma_{TOT}^{\pi^-}(E_i) = \frac{1}{n \delta X} \frac{\epsilon^{Inc}(E_i)}{\epsilon^{Int}(E_i)} \frac{C_{Int}^{\pi MC}(E_i)}{C_{Inc}^{\pi MC}(E_i)} \frac{N_{Int}^{TOT}(E_i)}{N_{Inc}^{TOT}(E_i)}. \quad (4.9)$$

2497 Section 6.2.1 describes the evaluation of pion content in the interacting and inci-
 2498 dent histograms, ($C_{Int}^{\pi MC}(E_i)$ and $C_{Inc}^{\pi MC}(E_i)$) and the propagation to the cross section
 2499 measurement of the relative systematic uncertainties.

2500 Section 6.2.2 describes the procedure employed to obtain the efficiency corrections
 2501 $\epsilon^{Int}(E_i)$ and $\epsilon^{Inc}(E_i)$ and the propagation to the cross section measurement of the
 2502 relative uncertainties.

2503 **6.2.1 Background subtraction**

2504 We use the procedure described in 5.3.2 to evaluate the relative pion content in
2505 the interacting histogram $C_{\text{Int}}^{\pi MC}(E_i)$ and the relative pion content in the incident
2506 $C_{\text{Inc}}^{\pi MC}(E_i)$. We start by evaluating the relative pion content assuming the beamline
2507 composition simulated by G4Beamline, whose pion, muon and electron percentages
2508 per beam setting are reported again in the first line of Table 6.1. The left side of
2509 Figure 6.4 shows the MC estimated relative pion content for the interacting histogram
2510 as function of kinetic energy for the 60A runs (top) and 100A runs (bottom). The
2511 right side of the same figure shows the MC estimated relative pion content for the
2512 incident histogram as function of kinetic energy for the 60A runs (top) and 100A
2513 runs (bottom). In Figure 6.4 the central curves displayed in light blue are obtained
2514 using the beamline composition as predicted by G4Beamline: these are the correction
2515 curves for the relative pion content applied to data in equation 4.9.

2516 So, the question now becomes: how well do we know the beamline composition?
2517 In absence of additional data constraints, we take a 100% systematic uncertainty on
2518 the electron content, reported in lines 3 and 4 of Table 6.1. The effect of doubling or
2519 halving the electron percentage in the beam on the pion relative content is displayed
2520 in red in Figure 6.4. We reserve a slightly different treatment for the muon content.
2521 Since G4Beamline tracks only particles which cross all the wire chambers, pion events
2522 that decay in flight from WC1 to WC4 are not recorded by G4Beamline. Pion decays
2523 in the beamline could trigger the beamline detectors in data, if the produced muon
2524 propagates forward along the beamline. Thus, we take the G4Beamline prediction
2525 for muons as a lower bound in the composition: the effect of doubling the muon
2526 content (line 2 in Table 6.1) is shown in blue on Figure 6.4. A future study of data
2527 from additional beamline detectors such as the Aerogel Chernkov detectors [43] or the
2528 muon range stack (see Section 3.2.4) has the potential of a narrowing the systematics
2529 uncertainty coming from the beamline composition.

2530 We propagate the uncertainty on the beamline composition as a systematic un-
2531 certainty to the cross section by varying the beam composition for all the cases listed
2532 in Table 6.1 and evaluating variation of obtained data cross sections in each bin. This
2533 systematic uncertainty is summed in quadrature with the statistical uncertainty and
2534 the systematic uncertainty related to the kinetic energy measurement.

2535 6.2.2 Correction for Reconstruction Effects

2536 The interaction point for a particle in the selected sample for the total hadronic cross
2537 section analysis is the last point of its track that lies inside the LArTPC fiducial
2538 volume. This definition holds regardless the type of the interaction, i.e. if the TPC
2539 track ends within the fiducial volume, its last point will be the interaction point, no
2540 matter what the products of the interaction look like; on the other hand, if the track
2541 crosses the boundaries of the fiducial volume, the particle will be considered “through
2542 going” and no interaction point will be found. Given this definition, it is evident that
2543 we rely on the tracking algorithm to discern where the interaction occurred in the
2544 TPC and correctly end the tracking. The tracking algorithm has an intrinsic angle
2545 resolution as shown in section 5.5.1, which limits its efficiency, especially in the case
2546 of elastic scattering occurring at low angles. **Plus, there are instances where INSERT**
2547 **HERE THE STUFF ABOUT THE MIGRATION** Thus, we need to apply a correction
2548 accounting for mis-reconstruction of the interaction point in order to retrieve the true
2549 cross section. This correction is evaluated separately for the interacting and incident
2550 histograms bin by bin, namely $\epsilon^{\text{int}}(E_i)$ and $\epsilon^{\text{inc}}(E_i)$, and applied in the cross section
2551 formula as shown in equation 4.9.

2552 Reconstruction Effects Correction: Procedure

2553 We describe here the procedure to calculate the mis-reconstruction correction taking
2554 the interacting distribution as example and noting that the procedure is identical for

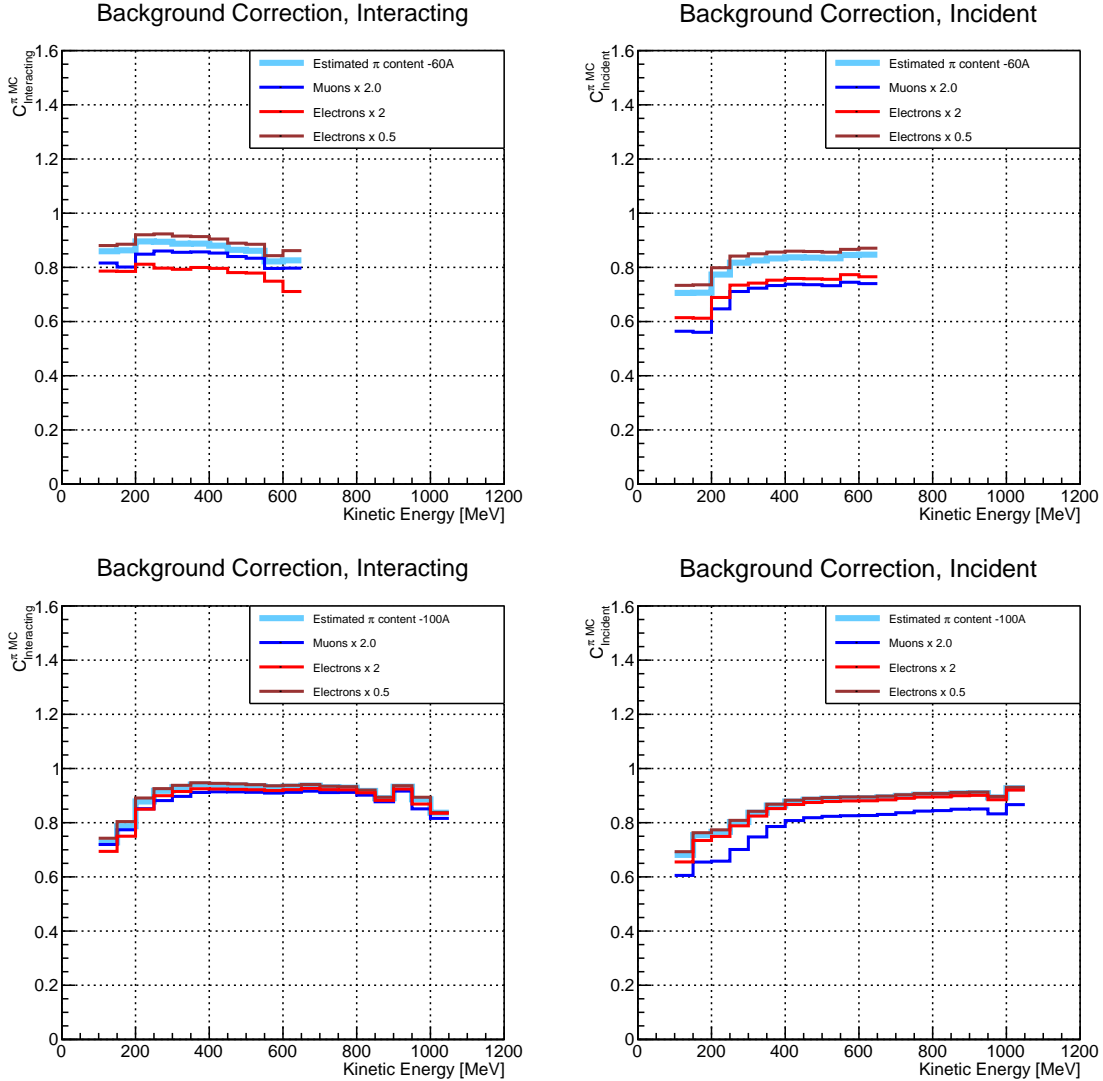


Figure 6.4: *Left:* MC estimated relative pion content for interacting histogram a function of kinetic energy for the 60A runs (top) and 100A runs (bottom), predicted background content in azure and muon and electron content variation in blue and red. *Right:* MC estimated relative pion content for incident histogram a function of kinetic energy for the 60A runs (top) and 100A (bottom), predicted background content in azure and muon and electron content variation in blue and red

2555 the incident distribution.

2556 In section 5.5.1, we estimated the angular resolution for data and MC to be
2557 $\bar{\alpha}_{Data} = (5.0 \pm 4.5)$ deg and $\bar{\alpha}_{MC} = (4.5 \pm 3.9)$ deg, respectively. Most interaction
2558 angles smaller than the angular resolution will thus be indistinguishable for the re-
2559 construction. Thus, we claim we are able to measure the cross section for interaction
2560 angles greater than 5.0 deg. Geant4 simulates interactions at all angles, as shown in
2561 figure 6.7. In order to calculate the correction for reconstruction effects, we select
2562 events which have an interaction angle greater than a given α_{res} to construct the true
2563 interacting and incident histograms (the denominator of the correction).

2564 We derive the correction $\epsilon^{int}(E_i)$ on a set of pure pion MC, calculating its value bin
2565 by bin as the ratio between the true bin content and the correspondent reconstructed
2566 bin content. The true interacting distribution is obtained applying the thin slice
2567 method on true MC energy deposition up to the MC flagged true interaction point
2568 for interaction angles greater than 5° . The reconstructed MC interacting distribution
2569 is obtained treating the MC events through the same reconstruction process as data:
2570 the interaction point is given by the end of the tracking and its energy is given by
2571 the reconstructed calorimetric information. The correction is then applied to in data
2572 bin by bin. In formulae, the correction is calculated to be

$$\epsilon^{Int}(E_i) = \frac{N_{\text{Interacting}}^{\pi \text{ Reco MC}}(E_i)}{N_{\text{Interacting}}^{\pi \text{ True MC}}(E_i)}, \quad (6.8)$$

2573 where $N_{\text{Int}}^{\pi \text{ True MC}}(E_i)$ is the content of the i -th bin in the true interacting his-
2574 togram, and $N_{\text{Int}}^{\pi \text{ Reco MC}}(E_i)$ is the content of the i -th bin in the reconstructed inter-
2575 acting histogram. The correction is applied to data as follows

$$N_{\text{Int}}^{\pi \text{ Data}}(E_i) = \frac{N_{\text{Int}}^{\pi \text{ Reco Data}}(E_i)}{\epsilon^{Int}(E_i)} = N_{\text{Int}}^{\pi \text{ Reco Data}}(E_i) \frac{N_{\text{Int}}^{\pi \text{ True MC}}(E_i)}{N_{\text{Int}}^{\pi \text{ Reco MC}}(E_i)}. \quad (6.9)$$

2576 where $N_{\text{Int}}^{\pi \text{ Reco Data}}(E_i)$ is the background subtracted bin content of the i -th bin in
2577 for the reconstructed interacting histogram for data, i.e.

$$N_{\text{Int}}^{\pi \text{ Reco Data}}(E_i) = N_{\text{Int}}^{\text{TOT Data}}(E_i) - B_{\text{Int}}^{\text{Data}}(E_i) = C_{\text{Int}}^{\pi \text{ MC}}(E_i) N_{\text{Int}}^{\text{TOT Data}}(E_i). \quad (6.10)$$

2578 The systematics on this correction is estimated by varying the value of α_{res} be-
2579 tween 0 deg and 4.5 deg and propagating the uncertainty on the cross section.

2580 Figure 6.5 shows $\epsilon^{\text{Int}}(E_i)$ in the left side and $\epsilon^{\text{Inc}}(E_i)$ on the right as a function of
2581 the kinetic energy for the 60A runs and their systematic uncertainty. Similarly, figure
2582 6.6 shows $\epsilon^{\text{Int}}(E_i)$ in the left side and $\epsilon^{\text{Inc}}(E_i)$ on the right as a function of the kinetic
2583 energy for the 100A runs and their systematic uncertainty.

	Magnet Current -60A			Magnet Current -100 A		
	MC π^-	MC μ^-	MC e^-	MC π^-	MC μ^-	MC e^-
Expected Composition	68.8 %	4.6 %	26.6 %	87.4 %	3.7 %	8.9 %
Composition 2x Muons	64.2 %	9.2 %	26.6 %	83.7 %	7.4 %	8.9 %
Composition 2x Electrons	42.2 %	4.6 %	53.2 %	78.5 %	3.7 %	17.8 %
Composition 0.5x Electrons	82.1 %	4.6 %	13.3 %	91.9 %	3.7 %	4.4 %

Table 6.1: Beam composition variation for the study of systematics due to beam contamination.

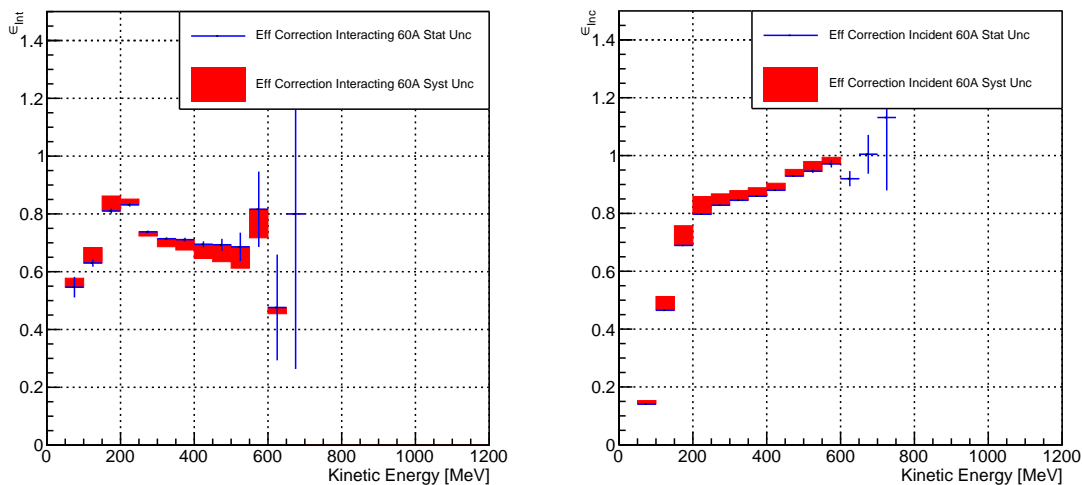


Figure 6.5: *Left:* Reconstruction effects correction on the 60A interacting histogram, statistical uncertainty in blue, systematic uncertainty in red. *Right:* Reconstruction effects correction on the 60A incident histogram, statistical uncertainty in blue, systematic uncertainty in red.

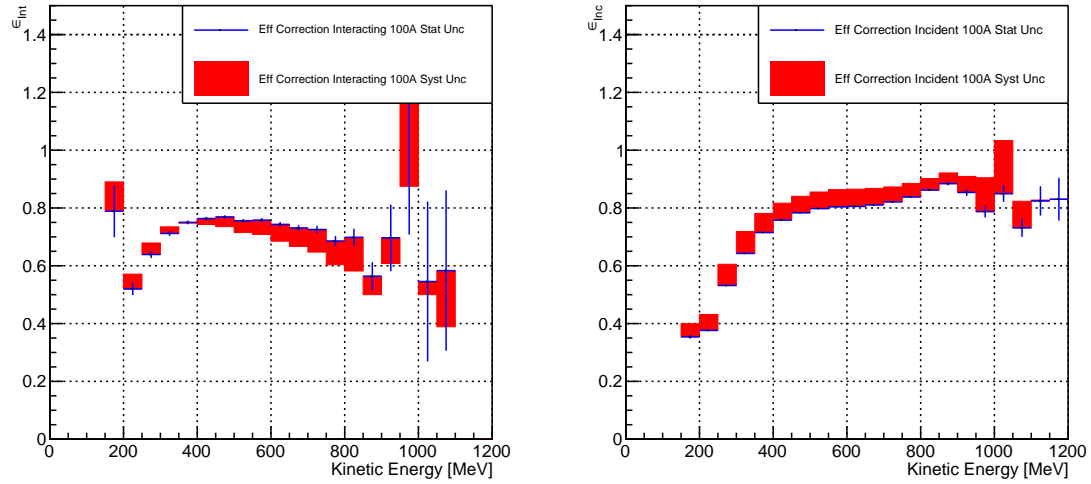


Figure 6.6: *Left*: Reconstruction effects correction on the 100A interacting histogram, statistical uncertainty in blue, systematic uncertainty in red. *Right*: Reconstruction effects correction on the 100A incident histogram, statistical uncertainty in blue, systematic uncertainty in red.

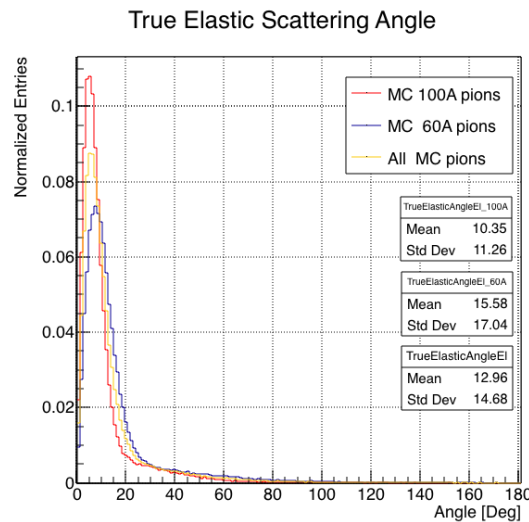


Figure 6.7: Distribution of the true scattering angle for a pion elastic scattering off the argon nucleus as simulated by Geant4.

2584 **6.3 Results**

2585 Figure 6.8 show the measurement of the (π^- -Ar) total hadronic cross section for
2586 scattering angles greater than 5° , as the result of the background subtraction and
2587 reconstruction effects correction to the raw cross section. The top left plot is the
2588 measurement obtained on the 60A data, statistical uncertainty in black and system-
2589 atic uncertainty in red. The top right plot is the measurement obtained on the 100A
2590 data, statistical uncertainty in black and systematic uncertainty in blue. The bottom
2591 plot shows the two measurements overlaid. In all three plot, the Geant4 prediction
2592 for the total hadronic cross section for angle scattering greater than 5° is displayed
2593 in green.

2594 The systematic uncertainty on the cross section is the sum in quadrature of the
2595 statistical uncertainty, the systematic uncertainty related to the kinetic energy mea-
2596 surement, the systematic uncertainty related to the beam composition and the sys-
2597 tematic uncertainty related to the reconstruction effects correction.

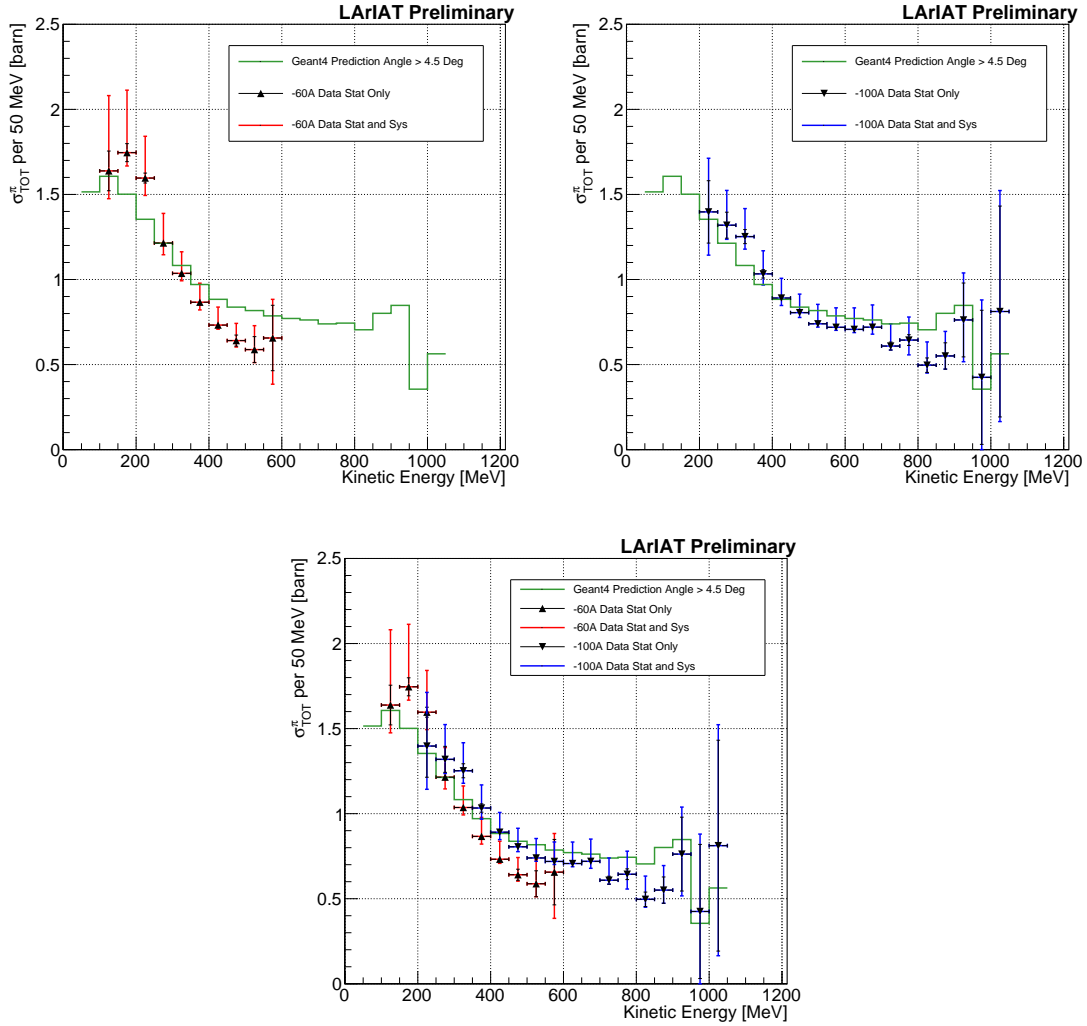


Figure 6.8: *Top Left:* (π^- -Ar) total hadronic cross section for scattering angles greater than 5° measured in the 60A sample, statistical uncertainty in black and systematic uncertainty in red. The Geant4 prediction for the total hadronic cross section for angle scattering greater than 5° is displayed in green.

Top Right: (π^- -Ar) total hadronic cross section for scattering angles greater than 5° measured in the 100A sample, statistical uncertainty in black and systematic uncertainty in blue. The Geant4 prediction for the total hadronic cross section for angle scattering greater than 5° is displayed in green.

Bottom: (π^- -Ar) total hadronic cross section measurements in the 60A and 100A samples overlaid with the Geant4 prediction (green).

2598 **Chapter 7**

2599 **Positive Kaon Cross Section**

2600 **Measurement**

2601 “Beat-up little seagull, on a marble stair
2602 Tryin’ to find the ocean, lookin’ everywhere.”
2603 – Nina Simone, 1978 –

2604 In this chapter, we show the result of the thin slice method to measure the (K^+ -
2605 Ar) total hadronic cross section. In Section 7.1, we start by measuring the raw
2606 cross section. In Section 7.2, we apply a statistical subtraction of the background
2607 contributions based on simulation and a correction for reconstruction effects. The
2608 final results are presented in Section 7.3.

2609 **7.1 Raw Cross Section**

2610 We measure the raw (K^+ -Ar) total hadronic cross section as a function of the kinetic
2611 energy in the combined +60A and +100A dataset.

2612 Similar to the pion case, the raw cross section is given by the equation 4.4

$$\sigma_{TOT}(E_i) = \frac{1}{n\delta X} \frac{N_{Int}^{TOT}(E_i)}{N_{Inc}^{TOT}(E_i)}, \quad (4.4)$$

2613 where N_{Int}^{TOT} is the measured number of particles interacting at kinetic energy E_i ,
2614 N_{Inc}^{TOT} is the measured number of particles incident on an argon slice at kinetic energy
2615 E_i , n is the density of the target centers and δX is the thickness of the argon slice.
2616 The density of the target centers and the slab thickness are $n = 0.021 \cdot 10^{24} \text{ cm}^{-3}$ and
2617 $\delta X = 0.47 \text{ cm}$, respectively.

2618 As in the case of pions, kaons might decay or interact between WC4 and the TPC
2619 front face. Some of the interaction products may be wrongly matched to the WC
2620 track, forming the “secondary” particle’s background in the kaon sample. We estimate
2621 the effect of the contamination of secondaries through the DDMC kaon sample. Figure
2622 7.1 shows the distribution of N_{Int}^{TOT} as a function of the kinetic energy. The data
2623 central points are represented by black dots, the statistical uncertainty is shown in
2624 black, while the systematic uncertainty is shown in red. Data is displayed over the
2625 N_{Int}^{TOT} distribution obtained with a DDMC sample of kaons shot from WC4. The
2626 contribution from the simulated kaons which interact hadronically is shown in pink,
2627 the contributions from kaon decay is shown in orange and the one from secondaries
2628 in red. The simulated kaon’s and secondaries’ contributions are stacked; the sum of
2629 their integrals is normalized to the integral of the data.

2630 Figure 7.2 shows the distribution of N_{Inc}^{TOT} . Data is displayed over the MC. For
2631 the N_{Inc}^{TOT} distribution we do not make a distinction between kaons that decay or
2632 interact hadronically because any kaon contributes to the flux of incident particles at
2633 given kinetic energy independently from its final interaction. The same normalization
2634 procedure is used for both the interacting and incident histograms.

2635 Figure 7.3 shows the raw cross section, statistical uncertainty in black and system-

atic uncertainty in red. The raw data cross section is overlaid to the reconstructed cross section for the MC mixed sample, displayed in azure. We calculate the statistical uncertainty for the interacting, incident and cross section distributions in a similar fashion to the pion case as described in Section 6.1.1.

As in the pion case, the only systematic effect considered in the measurement of the raw cross section results from the propagation of the uncertainty associate with the measurement of the kinetic energy at each argon slab. For kaons, the uncertainty on the kinetic energy of a candidate at the j^{th} slab of argon is given by

$$\delta KE_j = \sqrt{\delta p_{Beam}^2 + \delta E_{Loss}^2 + \delta E_{dep\ FF-j}^2} \quad (7.1)$$

$$= \sqrt{(2\% p_{Beam})^2 + (7\text{ [MeV]})^2 + (j - 1)^2(\sim 0.18\text{ [MeV]})^2}. \quad (7.2)$$

We propagate this uncertainty by varying the energy measurement KE_j at each argon slab. We measure N_{Inc}^{TOT} , N_{Int}^{TOT} and the cross section in three cases: first assigning the measured KE_j at each kinetic energy sampling, then assigning $KE_j + \delta KE_j$, and finally assigning $KE_j - \delta KE_j$. The difference between the values obtained using the KE_j sampling and the maximum and minimum values in each kinetic energy bin determines the systematic uncertainty.

7.2 Corrections to the Raw Cross Section

As described in section 4.3.3, we need to apply a background correction and a correction for reconstruction effects in order to derive the kaon cross section from the raw cross section. The cross section is given in equation 4.9,

$$\sigma_{TOT}^{K^+}(E_i) = \frac{1}{n\delta X} \frac{\epsilon^{Inc}(E_i)}{\epsilon^{Int}(E_i)} \frac{C_{Int}^{KMC}(E_i)}{C_{Inc}^{KMC}(E_i)} \frac{N_{Int}^{TOT}(E_i)}{N_{Inc}^{TOT}(E_i)}. \quad (4.9)$$

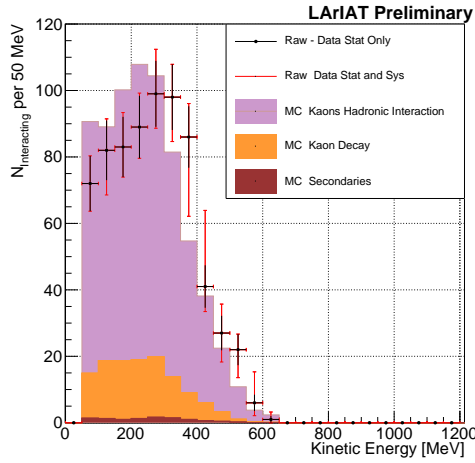


Figure 7.1: Raw number of interacting kaon candidates as a function of the reconstructed kinetic energy. The statistical uncertainties are shown in black, the systematic uncertainties in red.

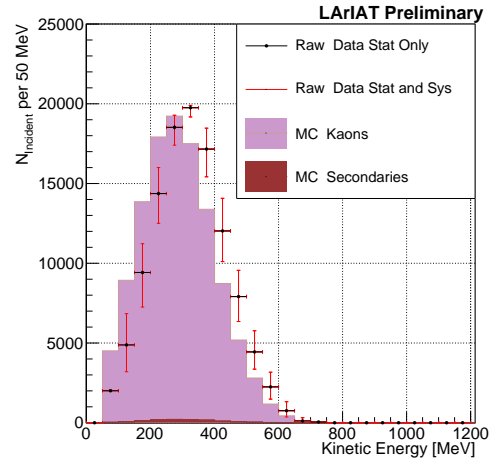


Figure 7.2: Raw number of incident kaon candidates as a function of the reconstructed kinetic energy. The statistical uncertainty is shown in black, the systematic uncertainties in red.

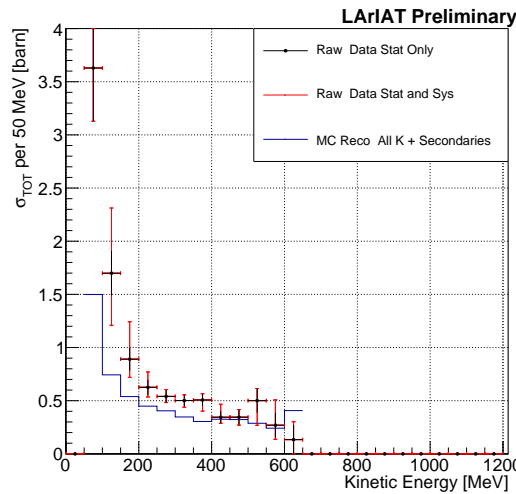


Figure 7.3: Raw (K^+ -Ar) total hadronic cross section. The statistical uncertainty is shown in black, the systematic uncertainties in red. The raw cross section obtained with a MC sample of kaons is shown in blue. For the MC cross section, we include the contributions from secondaries.

2654 Currently, the only background considered for the kaon hadronic cross section
2655 comes from the presence of secondaries and decay interaction points. A further de-
2656 velopment of the analysis will need to account for the presence of a small proton
2657 contamination. Figure 7.4 shows the relative kaon content suitable for the hadronic
2658 cross section for the interacting and incident histograms.

2659 As described in 6.2.2 for the pion case, we derive the correction on a set of pure
2660 kaon MC, calculating its value bin by bin as the ratio between the true bin content
2661 and the correspondent reconstructed bin content. The correction is then applied
2662 to the relevant bin in data. The correction for reconstruction effects is evaluated
2663 separately for the interacting and incident histograms, namely $\epsilon^{\text{int}}(E_i)$ and $\epsilon^{\text{inc}}(E_i)$,
2664 and propagated to the cross section as shown in equation 4.9.

2665 In section 5.5.1, we estimated the angular resolution for data and MC to be
2666 $\bar{\alpha}_{\text{Data}} = (4.3 \pm 3.7) \text{ deg}$ and $\bar{\alpha}_{\text{MC}} = (4.4 \pm 3.6) \text{ deg}$, respectively. Most interaction
2667 angles smaller than the angular resolution will thus be indistinguishable for the re-
2668 construction. Thus, we claim we are able to measure the cross section for interaction
2669 angles greater than 4.5 deg. Geant4 simulates interactions at all angles: in order to
2670 calculate the efficiency correction, we select events which have an interaction angle
2671 greater than a α_{res} to construct the true interacting and incident histograms (the de-
2672 nominator of the efficiency correction). The systematics on the efficiency correction
2673 is estimated by varying the value of α_{res} between 0 deg and 4.5 deg and propagating
2674 the uncertainty on the cross section.

2675 Figure 7.5 shows $\epsilon^{\text{Int}}(E_i)$ in the left side and $\epsilon^{\text{Inc}}(E_i)$ on the right as a function of
2676 the kinetic energy for the kaon sample and their systematic uncertainty.

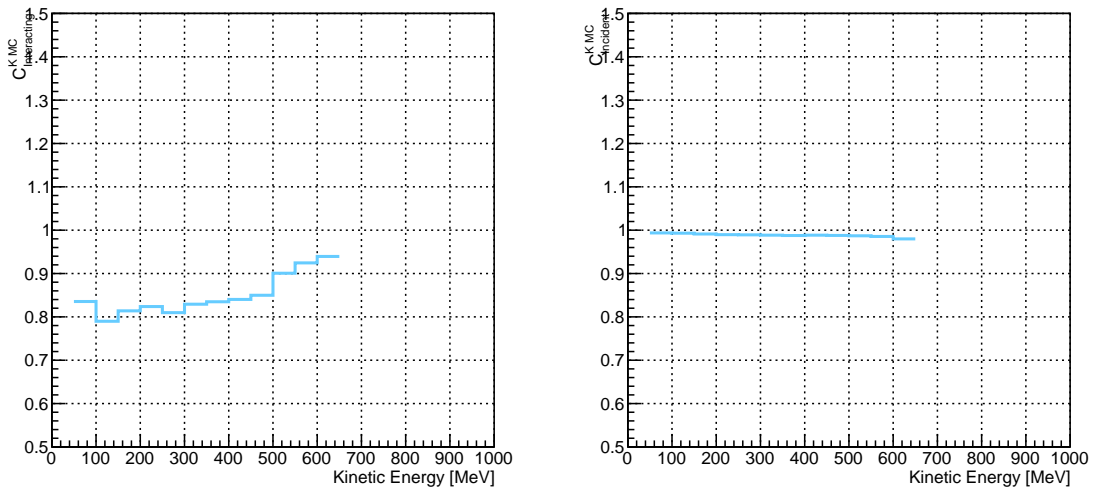


Figure 7.4: *Left:* MC estimated relative kaon content for kaons interacting hadronically as function of kinetic energy. *Right:* MC estimated relative kaon content for incident histogram a function of kinetic energy.

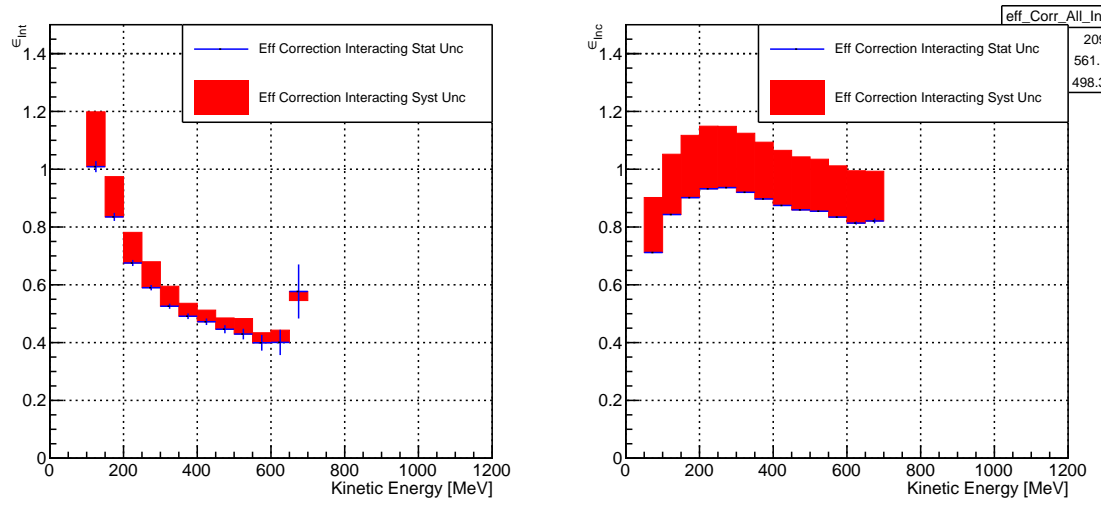


Figure 7.5: *Left:* Efficiency correction on the interacting histogram, statistical uncertainty in blue, systematic uncertainty in red. *Right:* Efficiency correction on the incident histogram, statistical uncertainty in blue, systematic uncertainty in red.

2677 7.3 Results

2678 Figure 7.6 show the measurement of the (K^+ -Ar) total hadronic cross section for
 2679 scattering angles greater than 5° , as the result of the background subtraction and
 2680 efficiency correction to the raw cross section. The plot shows the measurement ob-
 2681 tained on the full dataset, statistical uncertainty in black and systematic uncertainty
 2682 in red. The Geant4 prediction for the total hadronic cross section for angle scattering
 2683 greater than 5° is displayed in green.

2684 The systematic uncertainty on the cross section is the sum in quadrature of the
 2685 statistical uncertainty, the systematic uncertainty related to the kinetic energy mea-
 2686 surement and the systematic uncertainty related to the efficiency correction.

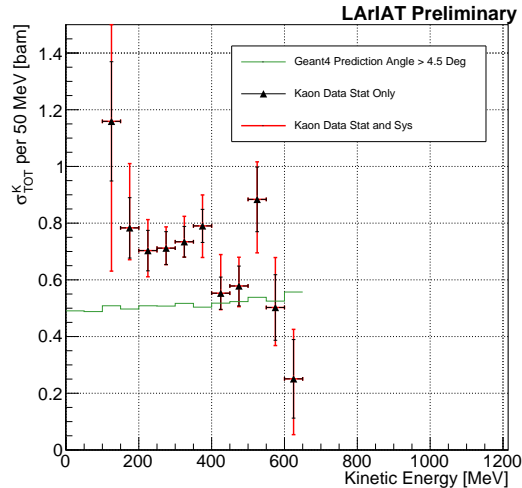


Figure 7.6: (K^+ -Ar) total hadronic cross section for scattering angles greater than 5° measured in the 60A sample, statistical uncertainty in black and systematic un-
certainty in red. The Geant4 prediction for the total hadronic cross section for angle scattering greater than 5° is displayed in green.

2687 **Chapter 8**

2688 **Conclusions**

2689 In the era of neutrino precision measurements, of huge liquid argon detectors and
2690 of massive amount of information from LArTPCs, a renewed interest for an ancient
2691 measurement arises: the measurement of hadronic interactions with matter. With
2692 this work, we presented the first ever (π^- -Ar) and (K^+ -Ar) total hadronic cross
2693 section measurements as a function of the hadron kinetic energy. These analyses are
2694 the first physics analyses developed by the LArIAT experiment. Both the analysis
2695 follow a similar workflow and they rely on beam line detector information as well as
2696 both calorimetry and tracking in the TPC.

2697 In order to measure (π^- -Ar) total hadronic argon cross sections, we start by
2698 selecting pion beamline candidates through a series of selections on the beamline
2699 and TPC information apt to maximize the number of pions in the selection over
2700 the number of muons and electrons. We use the LArIAT beamline MC to estimate
2701 the beam composition of the selected beamline candidates and we propagate them
2702 to the LArIAT TPC constructing a properly weighted sample with the DDMC. We
2703 apply the thin slice method on the pion candidates and obtain the raw cross section
2704 measurement. From the simulated sample, we obtain two corrections accounting for
2705 the beamline background contamination and for detector effects. Finally, we apply

2706 the corrections to data and measure the true cross section.

2707 In order to measure (K^+ -Ar) total hadronic argon cross sections, we follow a
2708 similar procedure, i.e. we apply the thin slice method on kaon candidates identified
2709 in the beamline to obtain the raw cross section. We apply a background correction and
2710 a correction for detector effects to the raw cross section. The background correction
2711 accounts for the presence of secondary particles in both the interacting and incident
2712 histograms and for the presence of decay events in the interacting plot.

2713 The final results for the (π^- -Ar) and (K^+ -Ar) total hadronic cross section are
2714 shown side by side in figure 8.1.

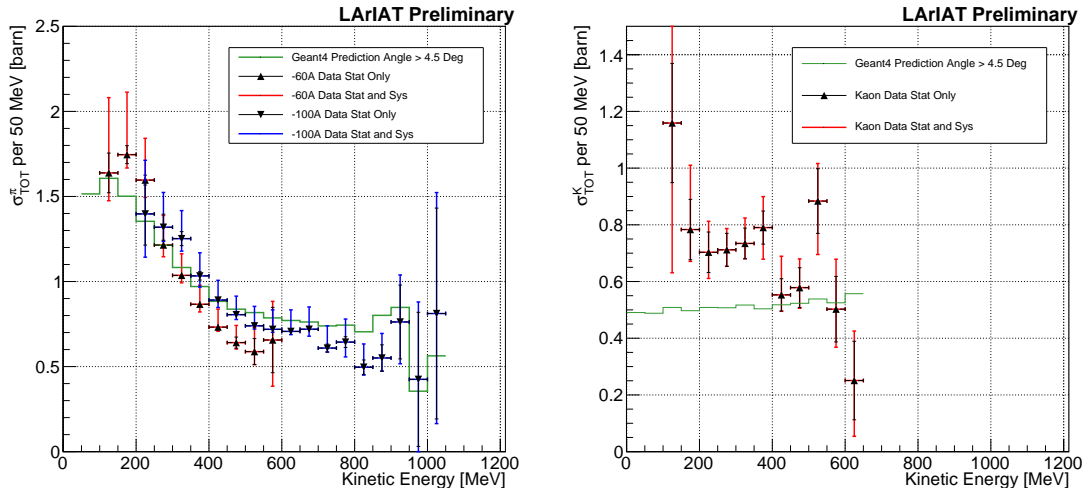


Figure 8.1: *Left:* (π^- -Ar) total hadronic cross section measurements in the 60A and 100A samples overlaid with the Geant4 prediction (green). *Right:* (K^+ -Ar) total hadronic cross section for scattering angles greater than 5° measured in the 60A sample, statistical uncertainty in black and systematic uncertainty in red. The Geant4 prediction for the total hadronic cross section for angle scattering greater than 5° is displayed in green.

2715 These analyses' will serve as a basis for the future cross section measurements of
2716 pions and kaons for the exclusive channels in LArIAT.

2717 **Appendix A**

2718 **Measurement of LArIAT Electric
2719 Field**

2720 The electric field of a LArTPC in the drift volume is a fundamental quantity for
2721 the proper functionality of this technology, as it affects almost every reconstructed
2722 quantity such as the position of hits or their collected charge. Given its importance,
2723 we calculate the electric field for LArIAT with a single line diagram from our HV
2724 circuit and we cross check the obtained value with a measurement relying only on
2725 TPC data.

2726 Before getting into the details of the measurement procedures, it is important to
2727 explicit the relationship between some quantities in play. The electric field and the
2728 drift velocity (v_{drift}) are related as follows

$$v_{drift} = \mu(E_{field}, T)E_{field}, \quad (\text{A.1})$$

2729 where μ is the electron mobility, which depends on the electric field and on the
2730 temperature (T). The empirical formula for this dependency is described in [115]
2731 and shown in Figure A.1 for several argon temperatures.

2732 The relationship between the drift time (t_{drift}) and the drift velocity is trivially

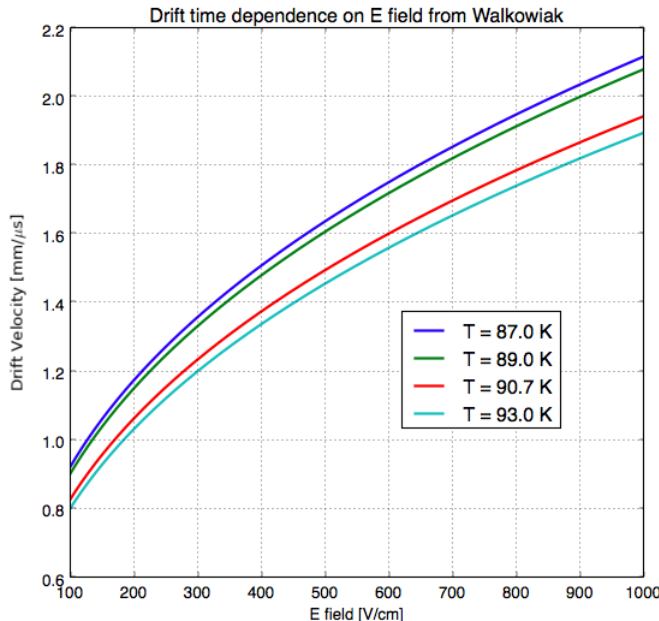


Figure A.1: Drift velocity dependence on electric field for several temperatures. The slope of the line at any one point represents the electron mobility for that given temperature and electric field.

Table A.1: Electric field and drift velocities in LArIAT smaller drift volumes

	Shield-Induction	Induction-Collection
E_{field}	700.63 V/cm	892.5 V/cm
v_{drift}	1.73 mm/μs	1.90 mm/μs
t_{drift}	2.31 μs	2.11 μs

2733 given by

$$t_{drift} = \Delta x / v_{drift}, \quad (\text{A.2})$$

2734 where Δx is the distance between the edges of the drift region. Table A.1 reports the

2735 values of the electric field, drift velocity, and drift times for the smaller drift volumes.

2736 With these basic parameters established, we can now move on to calculating the

2737 electric field in the main drift region (between the cathode and the shield plane).

2738 Single line diagram method

2739 The electric field strength in the LArIAT main drift volume can be determined know-
 2740 ing the voltage applied to the cathode, the voltage applied at the shield plane, and the
 2741 distance between them. We assume the distance between the cathode and the shield
 2742 plane to be 470 mm and any length contraction due to the liquid argon is negligibly
 2743 small (~ 2 mm).

2744 The voltage applied to the cathode can be calculated using Ohm's law and the
 2745 single line diagram shown in Figure A.2. A set of two of filter pots for emergency
 2746 power dissipation are positioned between the Glassman power supply and the cathode,
 2747 one at each end of the feeder cable, each with an internal resistance of $40 \text{ M}\Omega$.

2748 Given the TPC resistor chain, the total TPC impedance is $6 \text{ G}\Omega$. Since the total
 2749 resistance on the circuit is driven by the TPC impedance, we expect the resulting
 2750 current to be

$$I = V_{PS}/R_{tot} = -23.5 \text{ kV}/6 \text{ G}\Omega \sim 4 \mu\text{A}, \quad (\text{A.3})$$

2751 which we measure with the Glassman power supply, shown in Figure A.3.

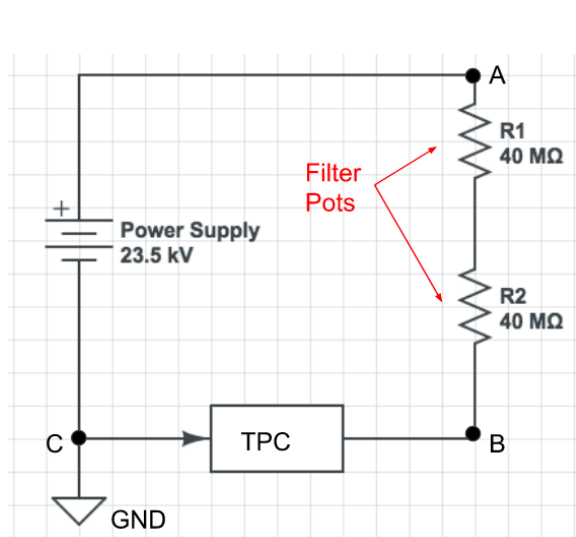


Figure A.2: LArIAT HV simple schematics.

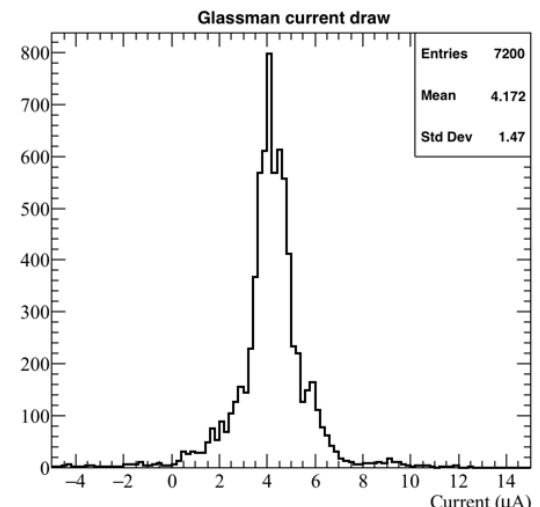


Figure A.3: Current reading from the Glassman between May 25th and May 30th, 2016 (typical Run-II conditions).

2752 Using this current, the voltage at the cathode is calculated as

$$V_{BC} = V_{PS} - (I \times R_{eq}) = -23.5 \text{ kV} + (0.00417 \text{ mA} \times 80 \text{ M}\Omega) = -23.17 \text{ kV}, \quad (\text{A.4})$$

2753 where I is the current and R_{eq} is the equivalent resistor representing the two filter
2754 pots. The electric field is then calculated to be

$$E_{\text{field}} = \frac{V_{BC} - V_{\text{shield}}}{\Delta x} = 486.54 \text{ V/cm}. \quad (\text{A.5})$$

2755 **E field using cathode-anode piercing tracks**

2756 We devise an independent method to measure the drift time (and consequently drift
2757 velocity and electric field) using TPC cathode to anode piercing tracks. We use this
2758 method as a cross check to the single line method. The basic idea is simple:

- 2759 0. Select cosmic ray events with only 1 reconstructed track
- 2760 1. Reduce the events to the one containing tracks that cross both anode and cath-
- 2761 ode
- 2762 2. Identify the first and last hit of the track
- 2763 3. Measure the time difference between these two hits (Δt).

2764 This method works under the assumptions that the time it takes for a cosmic particle
2765 to cross the chamber ($\sim \text{ns}$) is small compared to the charge drift time ($\sim \text{hundreds}$
2766 of μs).

2767 We choose cosmic events to allow for a high number of anode to cathode piercing
2768 tracks (ACP tracks), rejecting beam events where the particles travel almost perpen-
2769 dicularly to drift direction. We select events with only one reconstructed track to
2770 maximize the chance of selecting a single crossing muon (no-michel electron). We
2771 utilize ACP tracks because their hits span the full drift length of the TPC, see figure

2772 A.4, allowing us to define where the first and last hit of the tracks are located in space
2773 regardless of our assumption of the electric field.

2774 One of the main features of this method is that it doesn't rely on the measurement
2775 of the trigger time. Since Δt is the time difference between the first and last hit of a
2776 track and we assume the charge started drifting at the same time for both hits, the
2777 measurement of the absolute beginning of drift time t_0 is unnecessary. We boost the
2778 presence of ACP tracks in the cosmic sample by imposing the following requirements
2779 on tracks:

- 2780 • vertical position (Y) of first and last hits within ± 18 cm from TPC center
2781 (avoid Top-Bottom tracks)
- 2782 • horizontal position (Z) of first and last hits within 2 and 86 cm from TPC front
2783 face (avoid through going tracks)
- 2784 • track length greater than 48 cm (more likely to be crossing)
- 2785 • angle from the drift direction (phi in figure A.5) smaller than 50 deg (more
2786 reliable tracking)
- 2787 • angle from the beam direction (theta in figure A.5) greater than 50 deg (more
2788 reliable tracking)

2789 Tracks passing all these selection requirements are used for the Δt calculation.

2790 For each track passing our selection, we loop through the associated hits to retrieve
2791 the timing information. The analysis is performed separately on hits on the collection
2792 plane and induction plane, but lead to consistent results. As an example of the time
2793 difference, figures A.6 and A.7 represent the difference in time between the last and
2794 first hit of the selected tracks for Run-II Positive Polarity sample on the collection
2795 and induction plane respectively. We fit with a Gaussian to the peak of the Δt
2796 distributions to extract the mean drift time and the uncertainty associated with it.

2797 The long tail at low Δt represents contamination of non-ACP tracks in the track
2798 selection. We apply the same procedure to Run-I and Run-II, positive and negative
2799 polarity alike.

2800 To convert Δt recorded for the hits on the induction plane to the drift time we
2801 employ the formula

$$t_{drift} = \Delta t - t_{S-I} \quad (\text{A.6})$$

2802 where t_{drift} is the time the charge takes to drift in the main volume between the
2803 cathode and the shield plane and t_{S-I} is the time it takes for the charge to drift from
2804 the shield plane to the induction plane. In Table A.1 we calculated the drift velocity
2805 in the S-I region, thus we can calculate t_{S-I} as

$$t_{S-I} = \frac{l_{S-I}}{v_{S-I}} = \frac{4mm}{1.73mm/\mu s} \quad (\text{A.7})$$

2806 where l_{S-I} is the distance between the shield and induction plane and v_{S-I} is the drift
2807 velocity in the same region. A completely analogous procedure is followed for the hits
2808 on the collection plane, taking into account the time the charge spent in drifting from
2809 shield to induction as well as between the induction and collection plane. The value
2810 for Δt_{drift} , the calculated drift velocity (v_{drift}), and corresponding drift electric field
2811 for the various run periods is given in Table A.2 and are consistent with the electric
2812 field value calculated with the single line diagram method.

Delta t_{drift} , drift v and E field with ACP tracks

Data Period	Δt_{Drift} [μs]	Drift velocity [mm/ μs]	E field [V/cm]
RunI Positive Polarity Induction	311.1 ± 2.4	1.51 ± 0.01	486.6 ± 21
RunI Positive Polarity Collection	310.9 ± 2.6	1.51 ± 0.01	487.2 ± 21
RunII Positive Polarity Induction	315.7 ± 2.8	1.49 ± 0.01	467.9 ± 21
RunII Positive Polarity Collection	315.7 ± 2.7	1.49 ± 0.01	467.9 ± 21
RunII Negative Polarity Induction	315.9 ± 2.6	1.49 ± 0.01	467.1 ± 21
RunII Negative Polarity Collection	315.1 ± 2.8	1.49 ± 0.01	470.3 ± 21
Average Values	314.1	1.50 ± 0.01	474.3 ± 21

Table A.2: Δt for the different data samples used for the Anode-Cathode Piercing tracks study.

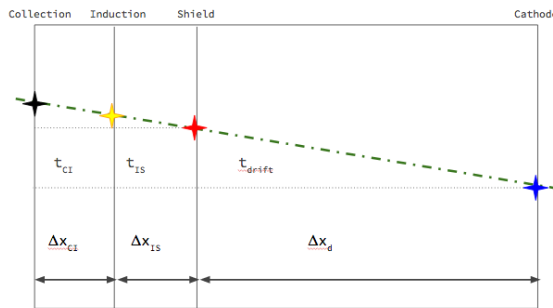


Figure A.4: Pictorial representation of the YX view of the TPC. The distance within the anode planes and between the shield plane and the cathode is purposely out of proportion to illustrate the time difference between hits on collection and induction. An ACP track is shown as an example.

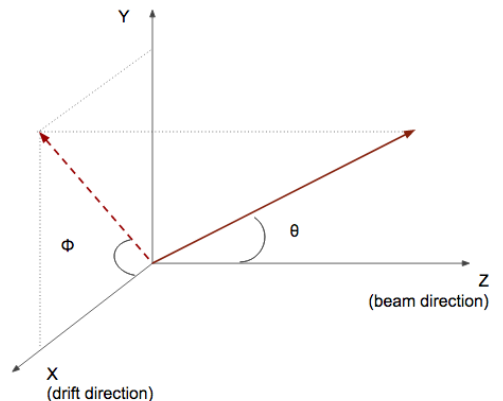


Figure A.5: Angle definition in the context of LArIAT coordinate system.

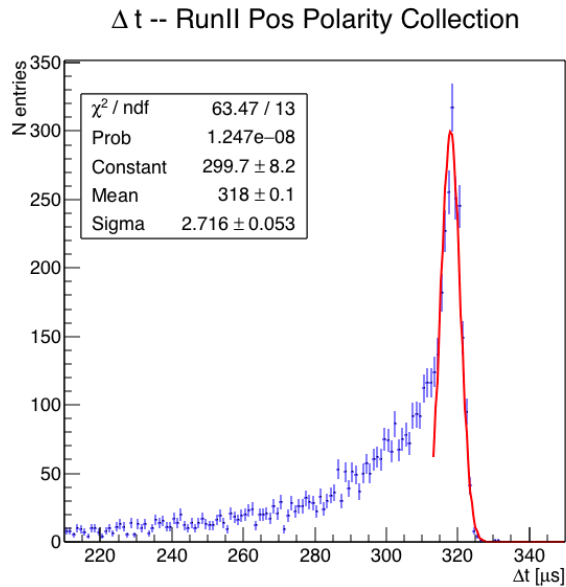


Figure A.6: Collection plane Δt fit for Run II positive polarity ACP data selected tracks.

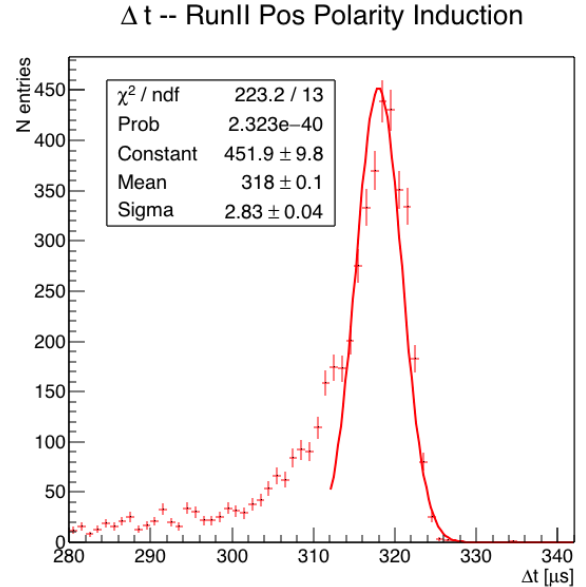


Figure A.7: Induction plane Δt fit for Run II positive polarity ACP data selected tracks.

2813 **Appendix B**

2814 **Additional Tracking Studies for**
2815 **LArIAT Cross Section Analyses**

2816 In this section, we describe two studies. The first is a justification of the selection
2817 criteria for the beamline handshake with the TPC information. We perform this
2818 study to boost the correct identification of the particles in the TPC associated with
2819 the beamline information, while maintaining sufficient statistics for the cross section
2820 measurement. The second study is an optimization of the tracking algorithm, with
2821 the scope of maximizing the identification of the hadronic interaction point inside the
2822 TPC. These two studies are related, since the optimization of the tracking is per-
2823 formed on TPC tracks which have been matched to the wire chamber track; in turn,
2824 the tracking algorithm for TPC tracks determines the number of reconstructed tracks
2825 in each event used to try the matching with the wire chamber track. Starting with
2826 a sensible tracking reconstruction, we perform the WC2TPC matching optimization
2827 first, then the tracking optimization. The WC2TPC match purity and efficiency are
2828 then calculated again with the optimized tracking.

2829 **B.0.1 Study of WC to TPC Match**

2830 Scope of this study is assessing the performances of the WC2TPC match on Monte
2831 Carlo (see Section 4.2) and decide the selection values we will use on data. A
2832 word of caution is necessary here. With this study, we want to minimize pathologies
2833 associated with the presence of the primary hadron itself, e.g. the incorrect association
2834 between the beamline hadron and its decay products inside the TPC. Assessing the
2835 contamination from pile-up¹, albeit related, is beyond the scope of this study.

2836 In MC, we are able to define a correct WC2TPC match using the Geant4 truth
2837 information. We are thus able to count how many times the WC tracks is associated
2838 with the wrong TPC reconstructed track.

2839 We define a correct match if the all following conditions are met:

- 2840 - the length of the true primary Geant4 track in the TPC is greater than 2 cm,
2841 - the length of the reconstructed track length is greater than 2 cm,
2842 - the Z position of the first reconstructed point is within 2 cm from the TPC
2843 front face
2844 - the distance between the reconstructed track and the true entering point is the
2845 minimum compared with all the other reconstructed tracks.

2846 In order to count the wrong matches, we consider all the reconstructed tracks
2847 whose Z position of the first reconstructed point lies within 2 cm from the TPC front
2848 face. Events with true length in TPC < 2 cm are included. Since hadrons are shot
2849 100 cm upstream from the TPC front face, the following two scenarios are possible
2850 from a truth standpoint:

2851 [Ta] the primary hadron decays or interact strongly before getting to the TPC,

1. We remind the reader that the DDMC is a single particle Monte Carlo, where the beam pile up is not simulated.

2852 [Tb] the primary hadron enters the TPC.

2853 As described in Section 4.2, we define a WC2TPC match according to the relative
2854 position of the WC and TPC track parametrized with ΔR and the angle between
2855 them, parametrized with α . Once we choose the selection values r_T and α_T to de-
2856 termine a reconstructed WC2TPC match, the following five scenarios are possible in
2857 the truth to reconstruction interplay :

2858 1) only the correct track is matched

2859 2) only one wrong track is matched

2860 3) the correct track and one (or more) wrong tracks are matched

2861 4) multiple wrong tracks matched.

2862 5) no reconstructed tracks are matched

2863 Since we keep only events with one and only one match, we discard cases 3), 4)
2864 and 5) from the events used in the cross section measurement. For each set of r_T and
2865 α_T selection value, we define purity and efficiency of the selection as follows:

$$\text{Efficiency} = \frac{\text{Number of events correctly matched}}{\text{Number of events with primary in TPC}}, \quad (\text{B.1})$$

$$\text{Purity} = \frac{\text{Number of events correctly matched}}{\text{Total number of matched events}}. \quad (\text{B.2})$$

2866 Figure B.1 shows the efficiency (left) and purity (right) for WC2TPC match as
2867 a function of the radius, r_T , and angle, α_T , selection value. It is apparent how both
2868 efficiency and purity are fairly flat as a function of the radius selection value at a
2869 given angle. This is not surprising. Since we are studying a single particle gun Monte
2870 Carlo sample, the wrong matches can occur only for mis-tracking of the primary or

for association with decay products; decay products will tend to be produced at large angles compared to the primary, but could be fairly close to the in x and y projection of the primary. The radius cut would play a key role in removing pile up events.

For LArIAT cross section measurements, we generally prefer purity over efficiency, since a sample of particles of a pure species will lead to a better measurement. Obviously, purity should be balanced with a sensible efficiency to avoid rejecting the whole sample.

We choose $(\alpha_T, r_T) = (8 \text{ deg}, 4 \text{ cm})$ and get a MC 85% efficiency and 98% purity for the kaon sample and a MC 95% efficiency and 90% purity for the pion sample.

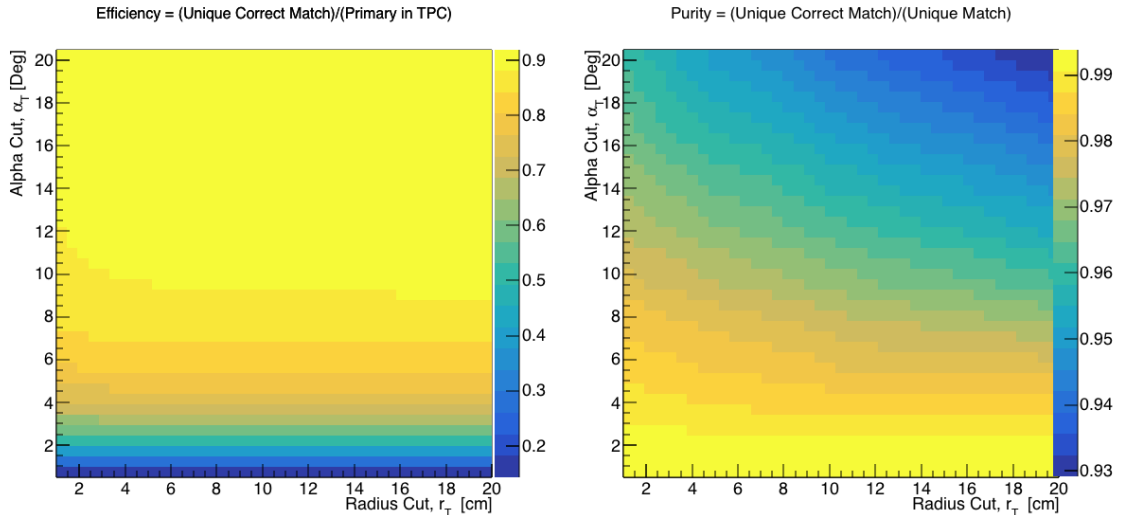


Figure B.1: Efficiency (left) and purity (right) for WC2TPC match as a function of the radius and angle selections for the kaon sample.

2880 B.0.2 Tracking Optimization

We perform an optimization of the clustering algorithm (see Section 2.1.5) with the scope of maximizing the efficiency of finding the interaction point for the total hadronic cross section measurements. We define as the interaction point the most downstream point of a WC2TPC matched TPC tracks within the TPC fiducial volume. Since all the WC2TPC tracks are by definition beam particles, tracks travel

2886 from upstream to downstream in the TPC; thus, identifying the interaction point
2887 means to stop the tracking correctly.

2888 TrajCluster is the package used to cluster hits in LArIAT; this package counts more
2889 than 20 tunable parameters. A standard method to develop clustering algorithms and
2890 checking their performances is to “hand scan”, which means recognizing the effect of
2891 parameters tuning by looking at a series of data event displays. Albeit we recognize
2892 the importance of hand scanning as a great diagnosis tool, we developed a fully
2893 automated optimization package which compares MC reconstructed information to
2894 MC truth.

2895 We start by defining a figure of merit in order to discern what makes a parameter
2896 configuration better than an other. We chose the percentage of events whose recon-
2897 structed and true length differ less than 2 cm. We then identify the parameters in
2898 TrajCluster that are most important to correctly stop the tracking and an appropriate
2899 range of values for each of them. We chose to optimize the parameters that leverage
2900 on the angle between consecutive groups of hits, the number of hits use in the cluster
2901 fit and the average hit charge to stop the tracking. We define a configuration space
2902 with all possible combination of values for the chosen parameters and we perform
2903 reconstruction one combination at a time: the combination with the highest figure of
2904 merit determines the optimized tracking reconstruction.

2905 We chose construct the combination space using a total of 5 parameters, 3 values
2906 each and two iterations of the method (for a total of 486 combinations). We run the
2907 combinations on a sample of 100000 pion events. After the optimization, the most
2908 upstream point of the tracking is correctly identified 99.5% of the times, the most
2909 downstream point is correctly identified 62.5% of the times, the tracking stops short
2910 about 15% of the times and misses the interaction point 22.5% of the times. Hand
2911 scanning confirmed that the missed interaction points happen in the vast majority of
2912 cases for very shallow angles, as shown in the event display in Figure, or in the case

2913 of angles visible only in one projection plane. We also noticed that the premature
2914 stopping of the tracks is often related to the presence of delta rays parallel to the
2915 track. We see room of improvement, such as the delta ray removal and a forced track
2916 breaking in case of a kink present in a single plane, for a future analysis. **ADD evd**

2917 The procedure behind this optimization package is virtually applicable to any
2918 LArSoft module where it is possible to define figure of merit.

2919 **Appendix C**

2920 **Energy Calibration**

2921 Scope of the energy calibration is to identify the factors which convert the charge
2922 collected (dQ) to energy deposited in the chamber (dE). As described in section
2923 2.1.5, this is a multi-step procedure. In LArIAT, we first correct the raw charge by
2924 the electronic noise on the considered wire [103], then by the electron lifetime [104],
2925 and then by the recombination using the ArgoNeut recombination values. Lastly, we
2926 apply overall calibration of the energy, i.e. we determine the “calorimetry constants”
2927 using the procedure described in this section.

2928 We independently determine the calorimetry constants for Data and Monte Carlo
2929 in the LArIAT Run-II Data samples using a parametrization of the stopping power
2930 (a.k.a. energy deposited per unit length, dE/dX) as a function of momentum. This is
2931 done by comparing the stopping power measured on reconstructed quantities against
2932 the Bethe-Bloch theoretical prediction for various particle species (see Equation 2.1).
2933 We obtain the theoretical expectation for the dE/dX most probable value of pions
2934 (π), muons (μ), kaons (K), and protons (p) in the momentum range most relevant
2935 for LArIAT (Figure C.1) using the tables provided by the Particle Data Group [101]
2936 for liquid argon [1].

2937 The basic idea of this calibration technique is to utilize a sample of beamline

2938 events with known particle species and momentum to measure the dE/dX of the
2939 corresponding tracks in the TPC. In particular, we decided to use positive pions as
2940 calibration sample and samples from all the other particle species as cross check. Once
2941 the dE/dX of the positive pion sample has been measured at various momenta, we
2942 tune to calorimetry constants within the reconstruction software to align the measured
2943 values to match the theoretical ones found in Figure C.1.

2944 In data, we start by selecting a sample of beamline positive pion beamline can-
2945 didates without any restriction on their measured momentum¹. We then apply the
2946 WC2TPC match and subtract the energy loss upstream to the TPC front face, de-
2947 termining the momentum at the TPC front face. For each surviving pion candidate,
2948 we measure the dE/dx at each of the first 12 spacepoints associated the 3D recon-
2949 structed track, corresponding to a ~ 5 cm portion. These dE/dX measurements are
2950 then put into a histogram that corresponds to measured momentum of the track.
2951 The dE/dX histograms are sampled every 50 MeV/c in momentum (e.g. 150 MeV/c
2952 $< P < 200$ MeV/c, 200 MeV/c $< P < 250$ /c MeV, etc...). This process of selecting,
2953 sampling, and recording the dE/dX for various momentum bins is repeated over the
2954 entire sample of events, allowing us to collect sufficient statistic in most of the mo-
2955 mentum bins between 150 MeV/c and 1100 MeV/c. On average, pions and muons
2956 only lose ~ 10 MeV in this 5 cm section of the track and protons lose ~ 20 MeV. Thus
2957 choosing 50 MeV/c size bins for our histograms covers the energy spread within those
2958 bins due to energy loss from ionization for all the particle species identifiable in the
2959 beamline. Each 50 MeV/c momentum binned dE/dX histogram is now fit with a
2960 simple Landau function. The most probable value (MPV) and the associated error
2961 on the MPV from the fit are extracted and plotted against the theoretical prediction
2962 Figure C.1. Depending on the outcome of the data-prediction comparison, we modify
2963 the calorimetry constants and we repeat the procedure until a qualitative agreement

1. it should be noted that some muon and position contamination is present in the π^+ sample

2964 is achieved. We perform this tuning for the collection and induction plane separately.
 2965 As a cross check to the calorimetry constants determined using the positive pions,
 2966 we lock the constants and plot the dE/dx versus momentum distribution of all the
 2967 other particle species identifiable in the beamline data ($\pi/\mu/e$, K , p, in both polarities)
 2968 against the corresponding Beth-Bloch prediction. The agreement between data
 2969 from the other particle species and the predictions is the expected result of this cross
 2970 check. The results of the tuning and cross check for Run-II data on the collection
 2971 plane is shown in Figure C.2 negative polarity data on top, positive polarity data on
 2972 the bottom.

2973 In MC, we simulate the corresponding positive pion sample with the DDMC (see
 2974 section 5.2.2) and follow the same steps as in data. More details on the calorimetry
 2975 tuning can be found in [79].

2976 **Add agreement between data and MC for dedx for pions**

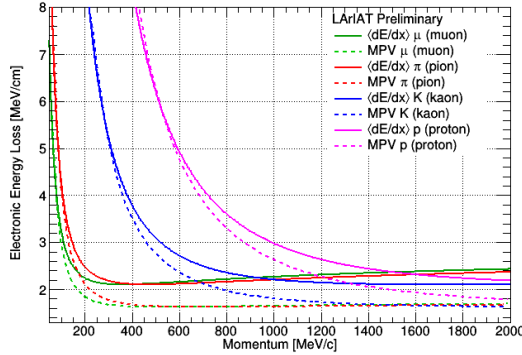


Figure C.1: Stopping power for pions, muons, kaons, and protons in liquid argon over the momentum range most relevant for LArIAT according to the Beth-Bloch equation. The solid lines represent the prediction for the mean energy dE/dX , while the dashed lines are the predictions for the MPV.

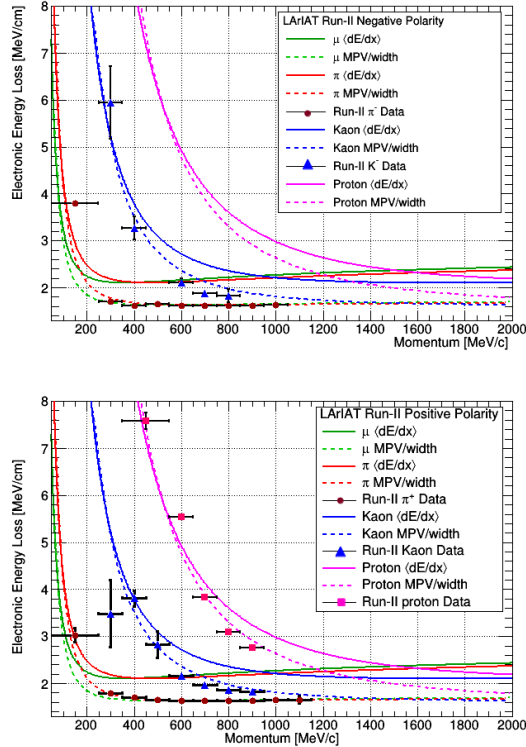


Figure C.2: Stopping power versus Momentum for Run-II negative (top) and positive (bottom) polarity data. We achieve the agreement between the Bethe-Bloch predictions and the distribution obtained with of the positive pions (top plot, red dots) by tuning the calorimetry constants. Once the calorimetry constants are locked in, the agreement between the other particle species and the Bethe-Bloch predictions follows naturally.

²⁹⁷⁷ Bibliography

- ²⁹⁷⁸ [1] PDG Tables for Liquid Argon. . Technical report.
- ²⁹⁷⁹ [2] Precision electroweak measurements on the Z resonance. *Physics Reports*,
²⁹⁸⁰ 427(5):257 – 454, 2006.
- ²⁹⁸¹ [3] K. Abe, J. Amey, C. Andreopoulos, M. Antonova, S. Aoki, A. Ariga, D. Au-
²⁹⁸² tiero, S. Ban, M. Barbi, G. J. Barker, G. Barr, C. Barry, P. Bartet-Friburg,
²⁹⁸³ M. Batkiewicz, V. Berardi, S. Berkman, S. Bhadra, S. Bienstock, A. Blondel,
²⁹⁸⁴ S. Bolognesi, S. Bordoni, S. B. Boyd, D. Brailsford, A. Bravar, C. Bronner,
²⁹⁸⁵ M. Buizza Avanzini, R. G. Calland, T. Campbell, S. Cao, S. L. Cartwright,
²⁹⁸⁶ M. G. Catanesi, A. Cervera, C. Checchia, D. Cherdack, N. Chikuma,
²⁹⁸⁷ G. Christodoulou, A. Clifton, J. Coleman, G. Collazuol, D. Coplowe, A. Cudd,
²⁹⁸⁸ A. Dabrowska, G. De Rosa, T. Dealtry, P. F. Denner, S. R. Dennis, C. Densham,
²⁹⁸⁹ D. Dewhurst, F. Di Lodovico, S. Di Luise, S. Dolan, O. Drapier, K. E. Duffy,
²⁹⁹⁰ J. Dumarchez, M. Dziewiecki, S. Emery-Schrenk, A. Ereditato, T. Feusels,
²⁹⁹¹ A. J. Finch, G. A. Fiorentini, M. Friend, Y. Fujii, D. Fukuda, Y. Fukuda,
²⁹⁹² V. Galymov, A. Garcia, C. Giganti, F. Gizzarelli, T. Golan, M. Gonin, D. R.
²⁹⁹³ Hadley, L. Haegel, M. D. Haigh, D. Hansen, J. Harada, M. Hartz, T. Hasegawa,
²⁹⁹⁴ N. C. Hastings, T. Hayashino, Y. Hayato, R. L. Helmer, A. Hillairet, T. Hiraki,
²⁹⁹⁵ A. Hiramatsu, S. Hirota, M. Hogan, J. Holeczek, F. Hosomi, K. Huang, A. K.
²⁹⁹⁶ Ichikawa, M. Ikeda, J. Imber, J. Insler, R. A. Intonti, T. Ishida, T. Ishii, E. Iwai,
²⁹⁹⁷ K. Iwamoto, A. Izmaylov, B. Jamieson, M. Jiang, S. Johnson, P. Jonsson,

2998 C. K. Jung, M. Kabirnezhad, A. C. Kaboth, T. Kajita, H. Kakuno, J. Kameda,
2999 D. Karlen, T. Katori, E. Kearns, M. Khabibullin, A. Khotjantsev, H. Kim,
3000 J. Kim, S. King, J. Kisiel, A. Knight, A. Knox, T. Kobayashi, L. Koch, T. Koga,
3001 A. Konaka, K. Kondo, L. L. Kormos, A. Korzenev, Y. Koshio, K. Kowalik,
3002 W. Kropp, Y. Kudenko, R. Kurjata, T. Kutter, J. Lagoda, I. Lamont, M. Lam-
3003 oureux, E. Larkin, P. Lasorak, M. Laveder, M. Lawe, M. Licciardi, T. Lindner,
3004 Z. J. Liptak, R. P. Litchfield, X. Li, A. Longhin, J. P. Lopez, T. Lou, L. Ludovici,
3005 X. Lu, L. Magaletti, K. Mahn, M. Malek, S. Manly, A. D. Marino, J. F. Martin,
3006 P. Martins, S. Martynenko, T. Maruyama, V. Matveev, K. Mavrokordis, W. Y.
3007 Ma, E. Mazzucato, M. McCarthy, N. McCauley, K. S. McFarland, C. McGrew,
3008 A. Mefodiev, C. Metelko, M. Mezzetto, P. Mijakowski, A. Minamino, O. Mi-
3009 neev, S. Mine, A. Missent, M. Miura, S. Moriyama, Th. A. Mueller, J. Myslik,
3010 T. Nakadaira, M. Nakahata, K. G. Nakamura, K. Nakamura, K. D. Nakamura,
3011 Y. Nakanishi, S. Nakayama, T. Nakaya, K. Nakayoshi, C. Nantais, C. Nielsen,
3012 M. Nirko, K. Nishikawa, Y. Nishimura, P. Novella, J. Nowak, H. M. O'Keeffe,
3013 K. Okumura, T. Okusawa, W. Oryszczak, S. M. Oser, T. Ovsyannikova, R. A.
3014 Owen, Y. Oyama, V. Palladino, J. L. Palomino, V. Paolone, N. D. Patel,
3015 P. Paudyal, M. Pavin, D. Payne, J. D. Perkin, Y. Petrov, L. Pickard, L. Pick-
3016 ering, E. S. Pinzon Guerra, C. Pistillo, B. Popov, M. Posiadala-Zezula, J.-M.
3017 Poutissou, R. Poutissou, P. Przewlocki, B. Quilain, T. Radermacher, E. Radi-
3018 cioni, P. N. Ratoff, M. Ravonel, M. A. Rayner, A. Redij, E. Reinherz-Aronis,
3019 C. Riccio, P. A. Rodrigues, E. Rondio, B. Rossi, S. Roth, A. Rubbia, A. Rychter,
3020 K. Sakashita, F. Sánchez, E. Scantamburlo, K. Scholberg, J. Schwehr, M. Scott,
3021 Y. Seiya, T. Sekiguchi, H. Sekiya, D. Sgalaberna, R. Shah, A. Shaikhiev,
3022 F. Shaker, D. Shaw, M. Shiozawa, T. Shirahige, S. Short, M. Smy, J. T.
3023 Sobczyk, H. Sobel, M. Sorel, L. Southwell, J. Steinmann, T. Stewart, P. Stowell,
3024 Y. Suda, S. Suvorov, A. Suzuki, S. Y. Suzuki, Y. Suzuki, R. Tacik, M. Tada,

- 3025 A. Takeda, Y. Takeuchi, H. K. Tanaka, H. A. Tanaka, D. Terhorst, R. Terri,
3026 T. Thakore, L. F. Thompson, S. Tobayama, W. Toki, T. Tomura, C. Touramani,
3027 nis, T. Tsukamoto, M. Tzanov, Y. Uchida, M. Vagins, Z. Vallari, G. Vasseur,
3028 T. Vladislavljevic, T. Wachala, C. W. Walter, D. Wark, M. O. Wascko, A. We-
3029 ber, R. Wendell, R. J. Wilkes, M. J. Wilking, C. Wilkinson, J. R. Wilson, R. J.
3030 Wilson, C. Wret, Y. Yamada, K. Yamamoto, M. Yamamoto, C. Yanagisawa,
3031 T. Yano, S. Yen, N. Yershov, M. Yokoyama, K. Yoshida, T. Yuan, M. Yu, A. Za-
3032 lewska, J. Zalipska, L. Zambelli, K. Zaremba, M. Ziembicki, E. D. Zimmerman,
3033 M. Zito, and J. Źmuda. Combined analysis of neutrino and antineutrino oscil-
3034 lations at t2k. *Phys. Rev. Lett.*, 118:151801, Apr 2017.
- 3035 [4] K. Abe, Y. Haga, Y. Hayato, M. Ikeda, K. Iyogi, J. Kameda, Y. Kishimoto,
3036 M. Miura, S. Moriyama, M. Nakahata, T. Nakajima, Y. Nakano, S. Nakayama,
3037 A. Orii, H. Sekiya, M. Shiozawa, A. Takeda, H. Tanaka, T. Tomura, R. A. Wen-
3038 dell, R. Akutsu, T. Irvine, T. Kajita, K. Kaneyuki, Y. Nishimura, E. Richard,
3039 K. Okumura, L. Labarga, P. Fernandez, J. Gustafson, C. Kachulis, E. Kearns,
3040 J. L. Raaf, J. L. Stone, L. R. Sulak, S. Berkman, C. M. Nantais, H. A.
3041 Tanaka, S. Tobayama, M. Goldhaber, W. R. Kropp, S. Mine, P. Weatherly,
3042 M. B. Smy, H. W. Sobel, V. Takhistov, K. S. Ganezer, B. L. Hartfiel, J. Hill,
3043 N. Hong, J. Y. Kim, I. T. Lim, R. G. Park, A. Himmel, Z. Li, E. O’Sullivan,
3044 K. Scholberg, C. W. Walter, T. Wongjirad, T. Ishizuka, S. Tasaka, J. S. Jang,
3045 J. G. Learned, S. Matsuno, S. N. Smith, M. Friend, T. Hasegawa, T. Ishida,
3046 T. Ishii, T. Kobayashi, T. Nakadaira, K. Nakamura, Y. Oyama, K. Sakashita,
3047 T. Sekiguchi, T. Tsukamoto, A. T. Suzuki, Y. Takeuchi, T. Yano, S. V. Cao,
3048 T. Hiraki, S. Hirota, K. Huang, T. Kikawa, A. Minamino, T. Nakaya, K. Suzuki,
3049 Y. Fukuda, K. Choi, Y. Itow, T. Suzuki, P. Mijakowski, K. Frankiewicz, J. Hig-
3050 night, J. Imber, C. K. Jung, X. Li, J. L. Palomino, M. J. Wilking, C. Yanag-
3051 isawa, D. Fukuda, H. Ishino, T. Kayano, A. Kibayashi, Y. Koshio, T. Mori,

- 3052 M. Sakuda, C. Xu, Y. Kuno, R. Tacik, S. B. Kim, H. Okazawa, Y. Choi,
3053 K. Nishijima, M. Koshiba, Y. Totsuka, Y. Suda, M. Yokoyama, C. Bronner,
3054 M. Hartz, K. Martens, Ll. Marti, Y. Suzuki, M. R. Vagins, J. F. Martin, A. Kon-
3055 aka, S. Chen, Y. Zhang, and R. J. Wilkes. Search for proton decay via $p \rightarrow e^+ \pi^0$
3056 and $p \rightarrow \mu^+ \pi^0$ in 0.31 megaton · years exposure of the super-kamiokande water
3057 cherenkov detector. *Phys. Rev. D*, 95:012004, Jan 2017.
- 3058 [5] R Acciarri, C Adams, J Asaadi, B Baller, T Bolton, C Bromberg, F Ca-
3059 vanna, E Church, D Edmunds, A Ereditato, S Farooq, B Fleming, H Greenlee,
3060 G Horton-Smith, C James, E Klein, K Lang, P Laurens, D McKee, R Mehdiyev,
3061 B Page, O Palamara, K Partyka, G Rameika, B Rebel, M Soderberg, J Spitz,
3062 A M Szelc, M Weber, M Wojcik, T Yang, and G P Zeller. A study of electron
3063 recombination using highly ionizing particles in the argoneut liquid argon tpc.
3064 *Journal of Instrumentation*, 8(08):P08005, 2013.
- 3065 [6] R Acciarri, M Antonello, B Baibussinov, M Baldo-Ceolin, P Benetti,
3066 F Calaprice, E Calligarich, M Cambiaghi, N Canci, F Carbonara, F Cavanna,
3067 S Centro, A G Cocco, F Di Pompeo, G Fiorillo, C Galbiati, V Gallo, L Grandi,
3068 G Meng, I Modena, C Montanari, O Palamara, L Pandola, G B Piano Mortari,
3069 F Pietropaolo, G L Raselli, M Roncadelli, M Rossella, C Rubbia, E Segreto,
3070 A M Szelc, S Ventura, and C Vignoli. Effects of nitrogen contamination in
3071 liquid argon. *Journal of Instrumentation*, 5(06):P06003, 2010.
- 3072 [7] R. Acciarri et al. Demonstration and Comparison of Operation of Photomulti-
3073 plier Tubes at Liquid Argon Temperature. *JINST*, 7:P01016, 2012.
- 3074 [8] R. Acciarri et al. Design and Construction of the MicroBooNE Detector. *JINST*,
3075 12(02):P02017, 2017.

- 3076 [9] R. Acciarri et al. First Observation of Low Energy Electron Neutrinos in a
3077 Liquid Argon Time Projection Chamber. *Phys. Rev.*, D95(7):072005, 2017.
3078 [Phys. Rev.D95,072005(2017)].
- 3079 [10] M Adamowski, B Carls, E Dvorak, A Hahn, W Jaskierny, C Johnson, H Jostlein,
3080 C Kendziora, S Lockwitz, B Pahlka, R Plunkett, S Pordes, B Rebel, R Schmitt,
3081 M Stancari, T Tope, E Voirin, and T Yang. The liquid argon purity demon-
3082 strator. *Journal of Instrumentation*, 9(07):P07005, 2014.
- 3083 [11] C. Adams et al. The Long-Baseline Neutrino Experiment: Exploring Funda-
3084 mental Symmetries of the Universe. 2013.
- 3085 [12] P. Adamson, L. Aliaga, D. Ambrose, N. Anfimov, A. Antoshkin, E. Arrieta-
3086 Diaz, K. Augsten, A. Aurisano, C. Backhouse, M. Baird, B. A. Bambah,
3087 K. Bays, B. Behera, S. Bending, R. Bernstein, V. Bhatnagar, B. Bhuyan,
3088 J. Bian, T. Blackburn, A. Bolshakova, C. Bromberg, J. Brown, G. Brunetti,
3089 N. Buchanan, A. Butkevich, V. Bychkov, M. Campbell, E. Catano-Mur, S. Chil-
3090 dress, B. C. Choudhary, B. Chowdhury, T. E. Coan, J. A. B. Coelho, M. Colo,
3091 J. Cooper, L. Corwin, L. Cremonesi, D. Cronin-Hennessy, G. S. Davies, J. P.
3092 Davies, P. F. Derwent, R. Dharmapalan, P. Ding, Z. Djurcic, E. C. Dukes,
3093 H. Duyang, S. Edayath, R. Ehrlich, G. J. Feldman, M. J. Frank, M. Gabrielyan,
3094 H. R. Gallagher, S. Germani, T. Ghosh, A. Giri, R. A. Gomes, M. C. Goodman,
3095 V. Grichine, R. Group, D. Grover, B. Guo, A. Habig, J. Hartnell, R. Hatcher,
3096 A. Hatzikoutelis, K. Heller, A. Himmel, A. Holin, J. Hylen, F. Jediny, M. Judah,
3097 G. K. Kafka, D. Kalra, S. M. S. Kasahara, S. Kasetti, R. Keloth, L. Kolupaeva,
3098 S. Kotelnikov, I. Kourbanis, A. Kreymer, A. Kumar, S. Kurbanov, K. Lang,
3099 W. M. Lee, S. Lin, J. Liu, M. Lokajicek, J. Lozier, S. Luchuk, K. Maan, S. Mag-
3100 ill, W. A. Mann, M. L. Marshak, K. Matera, V. Matveev, D. P. Méndez, M. D.
3101 Messier, H. Meyer, T. Miao, W. H. Miller, S. R. Mishra, R. Mohanta, A. Moren,

- 3102 L. Mualem, M. Muether, S. Mufson, R. Murphy, J. Musser, J. K. Nelson,
3103 R. Nichol, E. Niner, A. Norman, T. Nosek, Y. Oksuzian, A. Olshevskiy, T. Ol-
3104 son, J. Paley, P. Pandey, R. B. Patterson, G. Pawloski, D. Pershey, O. Petrova,
3105 R. Petti, S. Phan-Budd, R. K. Plunkett, R. Poling, B. Potukuchi, C. Principato,
3106 F. Psihas, A. Radovic, R. A. Rameika, B. Rebel, B. Reed, D. Rocco, P. Rojas,
3107 V. Ryabov, K. Sachdev, P. Sail, O. Samoylov, M. C. Sanchez, R. Schroeter,
3108 J. Sepulveda-Quiroz, P. Shanahan, A. Sheshukov, J. Singh, J. Singh, P. Singh,
3109 V. Singh, J. Smolik, N. Solomey, E. Song, A. Sousa, K. Soustruznik, M. Strait,
3110 L. Suter, R. L. Talaga, M. C. Tamsett, P. Tas, R. B. Thayyullathil, J. Thomas,
3111 X. Tian, S. C. Tognini, J. Tripathi, A. Tsaris, J. Urheim, P. Vahle, J. Vasel,
3112 L. Vinton, A. Vold, T. Vrba, B. Wang, M. Wetstein, D. Whittington, S. G. Wo-
3113 jcicki, J. Wolcott, N. Yadav, S. Yang, J. Zalesak, B. Zamorano, and R. Zwaska.
3114 Constraints on oscillation parameters from ν_e appearance and ν_μ disappearance
3115 in nova. *Phys. Rev. Lett.*, 118:231801, Jun 2017.
- 3116 [13] Alan Agresti. *Categorical Data Analysis*. Wiley Series in Probability and Statis-
3117 tics. Wiley, 2013.
- 3118 [14] A. Aguilar-Arevalo et al. Evidence for neutrino oscillations from the observation
3119 of anti-neutrino(electron) appearance in a anti-neutrino(muon) beam. *Phys.*
3120 *Rev.*, D64:112007, 2001.
- 3121 [15] A. A. Aguilar-Arevalo et al. Improved Search for $\bar{\nu}_\mu \rightarrow \bar{\nu}_e$ Oscillations in the
3122 MiniBooNE Experiment. *Phys. Rev. Lett.*, 110:161801, 2013.
- 3123 [16] S. Amoruso et al. Study of electron recombination in liquid argon with the
3124 ICARUS TPC. *Nucl. Instrum. Meth.*, A523:275–286, 2004.
- 3125 [17] C. Anderson et al. The ArgoNeuT Detector in the NuMI Low-Energy beam
3126 line at Fermilab. *JINST*, 7:P10019, 2012.

- 3127 [18] C. Andreopoulos et al. The GENIE Neutrino Monte Carlo Generator. *Nucl.*
3128 *Instrum. Meth.*, A614:87–104, 2010.
- 3129 [19] Timofei Bolshakov Andrey Petrov. Java synoptic toolkit. Technical report,
3130 Sept 2010.
- 3131 [20] M. Antonello, B. Baibussinov, P. Benetti, E. Calligarich, N. Canci, S. Cen-
3132 tro, A. Cesana, K. Cieslik, D. B. Cline, A. G. Cocco, A. Dabrowska, D. De-
3133 qual, A. Dermenev, R. Dolfini, C. Farnese, A. Fava, A. Ferrari, G. Fiorillo,
3134 D. Gibin, S. Gninenko, A. Guglielmi, M. Haranczyk, J. Holeczek, A. Ivashkin,
3135 J. Kisiel, I. Kochanek, J. Lagoda, S. Mania, A. Menegolli, G. Meng, C. Monta-
3136 nari, S. Otwinowski, A. Piazzoli, P. Picchi, F. Pietropaolo, P. Plonski, A. Rap-
3137 poldi, G. L. Raselli, M. Rossella, C. Rubbia, P. Sala, A. Scaramelli, E. Seg-
3138 reto, F. Sergiampietri, D. Stefan, J. Stepaniak, R. Sulej, M. Szarska, M. Ter-
3139 rani, F. Varanini, S. Ventura, C. Vignoli, H. Wang, X. Yang, A. Zalewska,
3140 and K. Zaremba. Precise 3d track reconstruction algorithm for the ICARUS
3141 t600 liquid argon time projection chamber detector. *Advances in High Energy*
3142 *Physics*, 2013:1–16, 2013.
- 3143 [21] M. Antonello et al. A Proposal for a Three Detector Short-Baseline Neutrino
3144 Oscillation Program in the Fermilab Booster Neutrino Beam. 2015.
- 3145 [22] D. Ashery, I. Navon, G. Azuelos, H. K. Walter, H. J. Pfeiffer, and F. W.
3146 Schlepütz. True absorption and scattering of pions on nuclei. *Phys. Rev. C*,
3147 23:2173–2185, May 1981.
- 3148 [23] C. Athanassopoulos et al. Evidence for $\nu(\mu) \rightarrow \nu(e)$ neutrino oscillations
3149 from LSND. *Phys. Rev. Lett.*, 81:1774–1777, 1998.

- 3150 [24] Borut Bajc, Junji Hisano, Takumi Kuwahara, and Yuji Omura. Threshold
3151 corrections to dimension-six proton decay operators in non-minimal {SUSY}
3152 $\text{su}(5)$ {GUTs}. *Nuclear Physics B*, 910:1 – 22, 2016.
- 3153 [25] B. Baller. Trajcluster user guide. Technical report, apr 2016.
- 3154 [26] Gary Barker. Neutrino event reconstruction in a liquid argon TPC. *Journal of*
3155 *Physics: Conference Series*, 308:012015, jul 2011.
- 3156 [27] BASF Corp. 100 Park Avenue, Florham Park, NJ 07932 USA.
- 3157 [28] R. Becker-Szendy, C. B. Bratton, D. R. Cady, D. Casper, R. Claus, M. Crouch,
3158 S. T. Dye, W. Gajewski, M. Goldhaber, T. J. Haines, P. G. Halverson, T. W.
3159 Jones, D. Kielczewska, W. R. Kropp, J. G. Learned, J. M. LoSecco, C. Mc-
3160 Grew, S. Matsuno, J. Matthews, M. S. Mudah, L. Price, F. Reines, J. Schultz,
3161 D. Sinclair, H. W. Sobel, J. L. Stone, L. R. Sulak, R. Svoboda, G. Thornton,
3162 and J. C. van der Velde. Search for proton decay into $e^+ + \pi^0$ in the imb-3
3163 detector. *Phys. Rev. D*, 42:2974–2976, Nov 1990.
- 3164 [29] J B Birks. Scintillations from organic crystals: Specific fluorescence and relative
3165 response to different radiations. *Proceedings of the Physical Society. Section A*,
3166 64(10):874, 1951.
- 3167 [30] A. Bodek and J. L. Ritchie. Further studies of fermi-motion effects in lepton
3168 scattering from nuclear targets. *Phys. Rev. D*, 24:1400–1402, Sep 1981.
- 3169 [31] Mark G. Boulay and A. Hime. Direct WIMP detection using scintillation time
3170 discrimination in liquid argon. 2004.
- 3171 [32] D. V. Bugg, R. S. Gilmore, K. M. Knight, D. C. Salter, G. H. Stafford, E. J. N.
3172 Wilson, J. D. Davies, J. D. Dowell, P. M. Hattersley, R. J. Homer, A. W. O'dell,

- 3173 A. A. Carter, R. J. Tapper, and K. F. Riley. Kaon-nucleon total cross sections
3174 from 0.6 to 2.65 gev/ *c. Phys. Rev.*, 168:1466–1475, Apr 1968.
- 3175 [33] W. M. Burton and B. A. Powell. Fluorescence of tetraphenyl-butadiene in the
3176 vacuum ultraviolet. *Applied Optics*, 12(1):87, jan 1973.
- 3177 [34] CAEN. Caen v1495 data sheet. Technical report, jan 2018.
- 3178 [35] CAEN. Caen v1740 data sheet. Technical report, jan 2018.
- 3179 [36] A. S. Carroll, I. H. Chiang, C. B. Dover, T. F. Kycia, K. K. Li, P. O. Mazur,
3180 D. N. Michael, P. M. Mockett, D. C. Rahm, and R. Rubinstein. Pion-nucleus
3181 total cross sections in the (3,3) resonance region. *Phys. Rev. C*, 14:635–638,
3182 Aug 1976.
- 3183 [37] D. Casper. The nuance neutrino physics simulation, and the future. *Nuclear
3184 Physics B - Proceedings Supplements*, 112(1-3):161–170, nov 2002.
- 3185 [38] F. Cavanna et al. LArIAT: Liquid Argon In A Testbeam. 2014.
- 3186 [39] A. Cervera, A. Donini, M.B. Gavela, J.J. Gomez Cádenas, P. Hernández,
3187 O. Mena, and S. Rigolin. Golden measurements at a neutrino factory. *Nu-
3188 clear Physics B*, 579(1-2):17–55, jul 2000.
- 3189 [40] E. Church. LArSoft: A Software Package for Liquid Argon Time Projection
3190 Drift Chambers. 2013.
- 3191 [41] ATLAS Collaboration. Observation of a new particle in the search for the
3192 standard model higgs boson with the ATLAS detector at the LHC. *Physics
3193 Letters B*, 716(1):1–29, sep 2012.
- 3194 [42] CMS Collaboration. Observation of a new boson at a mass of 125 gev with the
3195 cms experiment at the lhc. *Physics Letters B*, 716(1):30 – 61, 2012.

- 3196 [43] The LArIAT Collaboration. The liquid argon in a testbeam (lariat) experiment.
3197 Technical report, In Preparation 2018.
- 3198 [44] Stefano Dell’Oro, Simone Marcocci, Matteo Viel, and Francesco Vissani. Neu-
3199 trinoless double beta decay: 2015 review. *Advances in High Energy Physics*,
3200 2016:1–37, 2016.
- 3201 [45] S.E. Derenzo, A.R. Kirschbaum, P.H. Eberhard, R.R. Ross, and F.T. Solmitz.
3202 Test of a liquid argon chamber with 20 m rms resolution. *Nuclear Instruments
3203 and Methods*, 122:319 – 327, 1974.
- 3204 [46] Savas Dimopoulos, Stuart Raby, and Frank Wilczek. Proton Decay in Super-
3205 symmetric Models. *Phys. Lett.*, B112:133, 1982.
- 3206 [47] D. Drakoulakos et al. Proposal to perform a high-statistics neutrino scattering
3207 experiment using a fine-grained detector in the NuMI beam. 2004.
- 3208 [48] A Ereditato, C C Hsu, S Janos, I Kreslo, M Messina, C Rudolf von Rohr,
3209 B Rossi, T Strauss, M S Weber, and M Zeller. Design and operation of
3210 argontube: a 5 m long drift liquid argon tpc. *Journal of Instrumentation*,
3211 8(07):P07002, 2013.
- 3212 [49] Torleif Ericson and Wolfram Weise. *Pions and Nuclei (The International Series
3213 of Monographs on Physics)*. Oxford University Press, 1988.
- 3214 [50] A.A. Aguilar-Arevalo et al. The miniboone detector. *Nuclear Instruments and
3215 Methods in Physics Research Section A: Accelerators, Spectrometers, Detectors
3216 and Associated Equipment*, 599(1):28 – 46, 2009.
- 3217 [51] Antonio Bueno et al. Nucleon decay searches with large liquid argon TPC de-
3218 tectors at shallow depths: atmospheric neutrinos and cosmogenic backgrounds.
3219 *Journal of High Energy Physics*, 2007(04):041–041, apr 2007.

- 3220 [52] A.S. Clough et al. Pion-nucleus total cross sections from 88 to 860 MeV. *Nuclear*
3221 *Physics B*, 76(1):15–28, jul 1974.
- 3222 [53] B.W. Allardycce et al. Pion reaction cross sections and nuclear sizes. *Nuclear*
3223 *Physics A*, 209(1):1 – 51, 1973.
- 3224 [54] C Athanassopoulos et al. The liquid scintillator neutrino detector and LAMPF
3225 neutrino source. *Nuclear Instruments and Methods in Physics Research Section*
3226 *A: Accelerators, Spectrometers, Detectors and Associated Equipment*, 388(1-
3227 2):149–172, mar 1997.
- 3228 [55] F. Binon et al. Scattering of negative pions on carbon. *Nuclear Physics B*,
3229 17(1):168 – 188, 1970.
- 3230 [56] L. Aliaga et al. Minerva neutrino detector response measured with test beam
3231 data. *Nuclear Instruments and Methods in Physics Research Section A: Ac-*
3232 *celerators, Spectrometers, Detectors and Associated Equipment*, 789:28 – 42,
3233 2015.
- 3234 [57] M Adamowski et al. The liquid argon purity demonstrator. *Journal of Instru-*
3235 *mentation*, 9(07):P07005, 2014.
- 3236 [58] P. Vilain et al. Coherent single charged pion production by neutrinos. *Physics*
3237 *Letters B*, 313(1-2):267–275, aug 1993.
- 3238 [59] R. Acciarri et al. Convolutional neural networks applied to neutrino events
3239 in a liquid argon time projection chamber. *Journal of Instrumentation*,
3240 12(03):P03011, 2017.
- 3241 [60] R. Acciarri et al. Design and construction of the MicroBooNE detector. *Journal*
3242 *of Instrumentation*, 12(02):P02017–P02017, feb 2017.

- 3243 [61] C. E. Aalseth et al.l. DarkSide-20k: A 20 tonne two-phase LAr TPC for direct
3244 dark matter detection at LNGS. *The European Physical Journal Plus*, 133(3),
3245 mar 2018.
- 3246 [62] H Fenker. Standard beam pwc for fermilab. Technical report, Fermi National
3247 Accelerator Lab., Batavia, IL (USA), 1983.
- 3248 [63] H Fesbach. Theoretical nuclear physics: Nuclear reactions. 1992.
- 3249 [64] J. A. Formaggio and G. P. Zeller. From ev to eev: Neutrino cross sections across
3250 energy scales. *Rev. Mod. Phys.*, 84:1307–1341, Sep 2012.
- 3251 [65] E. Friedman et al. K+ nucleus reaction and total cross-sections: New analysis
3252 of transmission experiments. *Phys. Rev.*, C55:1304–1311, 1997.
- 3253 [66] V.M. Gehman, S.R. Seibert, K. Rielage, A. Hime, Y. Sun, D.-M. Mei,
3254 J. Maassen, and D. Moore. Fluorescence efficiency and visible re-emission
3255 spectrum of tetraphenyl butadiene films at extreme ultraviolet wavelengths.
3256 *Nuclear Instruments and Methods in Physics Research Section A: Accelerators,*
3257 *Spectrometers, Detectors and Associated Equipment*, 654(1):116 – 121, 2011.
- 3258 [67] H. Geiger and E. Marsden. On a diffuse reflection of the formula-particles.
3259 *Proceedings of the Royal Society A: Mathematical, Physical and Engineering*
3260 *Sciences*, 82(557):495–500, jul 1909.
- 3261 [68] Howard Georgi and S. L. Glashow. Unity of all elementary-particle forces. *Phys.*
3262 *Rev. Lett.*, 32:438–441, Feb 1974.
- 3263 [69] D.Y. Wong (editor) G.L. Shaw (Editor). *Pion-nucleon Scattering*. John Wiley
3264 & Sons Inc, 1969.
- 3265 [70] Glassman High Voltage, Inc., Precision Regulated High Voltage DC Power Sup-
3266 ply.

- 3267 [71] D S Gorbunov. Sterile neutrinos and their role in particle physics and cosmology.
3268 *Physics-Uspekhi*, 57(5):503, 2014.
- 3269 [72] C. Green, J. Kowalkowski, M. Paterno, M. Fischler, L. Garren, and Q. Lu. The
3270 Art Framework. *J. Phys. Conf. Ser.*, 396:022020, 2012.
- 3271 [73] S. Hansen, D. Jensen, G. Savage, E. Skup, and A. Soha. Fermilab test beam
3272 multi-wire proportional chamber tracking system upgrade. June 2014. Interna-
3273 tional Conference on Technology and Instrumentation in Particle Physics (TIPP
3274 2014).
- 3275 [74] J. Harada. Non-maximal θ_{23} , large θ_{13} and tri-bimaximal θ_{12} via quark-
3276 lepton complementarity at next-to-leading order. *EPL (Europhysics Letters)*,
3277 103(2):21001, 2013.
- 3278 [75] Peter W. Higgs. Broken symmetries and the masses of gauge bosons. *Physical*
3279 *Review Letters*, 13(16):508–509, oct 1964.
- 3280 [76] P.W. Higgs. Broken symmetries, massless particles and gauge fields. *Physics*
3281 *Letters*, 12(2):132–133, sep 1964.
- 3282 [77] H J Hilke. Time projection chambers. *Reports on Progress in Physics*,
3283 73(11):116201, 2010.
- 3284 [78] N. Ishida, M. Chen, T. Doke, K. Hasuike, A. Hitachi, M. Gaudreau, M. Kase,
3285 Y. Kawada, J. Kikuchi, T. Komiyama, K. Kuwahara, K. Masuda, H. Okada,
3286 Y.H. Qu, M. Suzuki, and T. Takahashi. Attenuation length measurements of
3287 scintillation light in liquid rare gases and their mixtures using an improved
3288 reflection suppresser. *Nuclear Instruments and Methods in Physics Research*
3289 *Section A: Accelerators, Spectrometers, Detectors and Associated Equipment*,
3290 384(2-3):380–386, jan 1997.

- 3291 [79] G. Pulliam J. Asaadi, E. Gramellini. Determination of the electron lifetime in
3292 lariat. Technical report, August 2017.
- 3293 [80] George Jaffé. Zur theorie der ionisation in kolonnen. *Annalen der Physik*,
3294 347(12):303–344, 1913.
- 3295 [81] C. Jarlskog. A basis independent formulation of the connection between quark
3296 mass matrices, CP violation and experiment. *Zeitschrift für Physik C Particles
3297 and Fields*, 29(3):491–497, sep 1985.
- 3298 [82] B J P Jones, C S Chiu, J M Conrad, C M Ignarra, T Katori, and M Toups. A
3299 measurement of the absorption of liquid argon scintillation light by dissolved ni-
3300 tragen at the part-per-million level. *Journal of Instrumentation*, 8(07):P07011,
3301 2013.
- 3302 [83] Benjamin J. P. Jones. *Sterile Neutrinos in Cold Climates*. PhD thesis, MIT,
3303 2015.
- 3304 [84] Cezary Juszczak, Jarosław A. Nowak, and Jan T. Sobczyk. Simulations from
3305 a new neutrino event generator. *Nuclear Physics B - Proceedings Supplements*,
3306 159:211–216, sep 2006.
- 3307 [85] D. I. Kazakov. Beyond the standard model: In search of supersymmetry. In
3308 *2000 European School of high-energy physics, Caramulo, Portugal, 20 Aug-2
3309 Sep 2000: Proceedings*, pages 125–199, 2000.
- 3310 [86] Dae-Gyu Lee, R. N. Mohapatra, M. K. Parida, and Merostar Rani. Predic-
3311 tions for the proton lifetime in minimal nonsupersymmetric $so(10)$ models: An
3312 update. *Phys. Rev. D*, 51:229–235, Jan 1995.

- 3313 [87] M A Leigui de Oliveira. Expression of Interest for a Full-Scale Detector Engi-
3314 neering Test and Test Beam Calibration of a Single-Phase LAr TPC. Technical
3315 Report CERN-SPSC-2014-027. SPSC-EOI-011, CERN, Geneva, Oct 2014.
- 3316 [88] W. H. Lippincott, K. J. Coakley, D. Gastler, A. Hime, E. Kearns, D. N. McK-
3317 insey, J. A. Nikkel, and L. C. Stonehill. Scintillation time dependence and pulse
3318 shape discrimination in liquid argon. *Phys. Rev. C*, 78:035801, Sep 2008.
- 3319 [89] Jorge L. Lopez and Dimitri V. Nanopoulos. Flipped SU(5): Origins and re-
3320 cent developments. In *15th Johns Hopkins Workshop on Current Problems*
3321 *in Particle Theory: Particle Physics from Underground to Heaven Baltimore,*
3322 *Maryland, August 26-28, 1991*, pages 277–297, 1991.
- 3323 [90] Vincent Lucas and Stuart Raby. Nucleon decay in a realistic so(10) susy gut.
3324 *Phys. Rev. D*, 55:6986–7009, Jun 1997.
- 3325 [91] Ettore Majorana. Teoria simmetrica dell'elettrone e del positrone. *Il Nuovo*
3326 *Cimento*, 14(4):171–184, apr 1937.
- 3327 [92] Hisakazu Minakata and Alexei Yu. Smirnov. Neutrino mixing and quark-lepton
3328 complementarity. *Phys. Rev. D*, 70:073009, Oct 2004.
- 3329 [93] M. Mooney. The microboone experiment and the impact of space charge effects.
3330 2015.
- 3331 [94] E. Morikawa, R. Reininger, P. Gürtler, V. Saile, and P. Laporte. Argon, kryp-
3332 ton, and xenon excimer luminescence: From the dilute gas to the condensed
3333 phase. *The Journal of Chemical Physics*, 91(3):1469–1477, aug 1989.
- 3334 [95] FM Newcomer, S Tedja, R Van Berg, J Van der Spiegel, and HH Williams.
3335 A fast, low power, amplifier-shaper-discriminator for high rate straw tracking
3336 systems. *IEEE Transactions on Nuclear Science*, 40(4):630–636, 1993.

- 3337 [96] Emmy Noether. Invariant variation problems. *Transport Theory and Statistical*
3338 *Physics*, 1(3):186–207, jan 1971.
- 3339 [97] I. Nutini. Study of charged particles interaction processes on ar in the 0.2 - 2.0
3340 GeV energy range through combined information from ionization free charge
3341 and scintillation light. Technical report, jan 2015.
- 3342 [98] D. R. Nygren. The time projection chamber: A new 4π detector for charged
3343 particles. Technical report, 1974.
- 3344 [99] L. Onsager. Initial recombination of ions. *Phys. Rev.*, 54:554–557, Oct 1938.
- 3345 [100] S. Pascoli, S.T. Petcov, and A. Riotto. Leptogenesis and low energy cp-violation
3346 in neutrino physics. *Nuclear Physics B*, 774(1):1 – 52, 2007.
- 3347 [101] C. Patrignani et al. Review of Particle Physics. *Chin. Phys.*, C40(10):100001,
3348 2016.
- 3349 [102] B. Pontecorvo. Neutrino Experiments and the Problem of Conservation of
3350 Leptonic Charge. *Sov. Phys. JETP*, 26:984–988, 1968. [Zh. Eksp. Teor.
3351 Fiz.53,1717(1967)].
- 3352 [103] T. Yang R. Acciarri. Investigation of the non-uniformity observed in the wire
3353 response to charge in lariat run 1. Technical report, February 2017.
- 3354 [104] T. Yang R. Acciarri, M. Stancari. Determination of the electron lifetime in
3355 lariat. Technical report, March 2016.
- 3356 [105] Martti Raidal. Relation between the neutrino and quark mixing angles and
3357 grand unification. *Phys. Rev. Lett.*, 93:161801, Oct 2004.
- 3358 [106] Steve Ritz et al. Building for Discovery: Strategic Plan for U.S. Particle Physics
3359 in the Global Context. 2014.

- 3360 [107] C. Rubbia. The Liquid Argon Time Projection Chamber: A New Concept for
3361 Neutrino Detectors. 1977.
- 3362 [108] L.M. Saunders. Electromagnetic production of pions from nuclei. *Nucl. Phys.*,
3363 *B7*: 293-310(1968).
- 3364 [109] Qaisar Shafi and Zurab Tavartkiladze. Neutrino democracy, fermion mass hier-
3365 archies, and proton decay from 5d su(5). *Phys. Rev. D*, 67:075007, Apr 2003.
- 3366 [110] Sigma-Aldrich, P.O. Box 14508, St. Louis, MO 63178 USA.
- 3367 [111] R. K. Teague and C. J. Pings. Refractive index and the lorentz–lorenz function
3368 for gaseous and liquid argon, including a study of the coexistence curve near the
3369 critical state. *The Journal of Chemical Physics*, 48(11):4973–4984, jun 1968.
- 3370 [112] J. Thomas and D. A. Imel. Recombination of electron-ion pairs in liquid argon
3371 and liquid xenon. *Phys. Rev. A*, 36:614–616, Jul 1987.
- 3372 [113] D.R.O. Morrison N. Rivoire V. Flaminio, W.G. Moorhead. Compilation of
3373 Cross Sections I: π^+ and π^- Induced Reactions. *CERN-HERA*, pages 83–01,
3374 1983.
- 3375 [114] D.R.O. Morrison N. Rivoire V. Flaminio, W.G. Moorhead. Compilation of
3376 Cross Sections II: K^+ and K^- Induced Reactions. *CERN-HERA*, pages 83–02,
3377 1983.
- 3378 [115] W. Walkowiak. Drift velocity of free electrons in liquid argon. *Nuclear Instru-
3379 ments and Methods in Physics Research Section A: Accelerators, Spectrometers,*
3380 *Detectors and Associated Equipment*, 449(1-2):288–294, jul 2000.
- 3381 [116] Hermann Weyl. Gravitation and the electron. *Proceedings of the National
3382 Academy of Sciences of the United States of America*, 15(4):323–334, 1929.

- 3383 [117] Colin et al Wilkin. A comparison of pi+ and pi- total cross-sections of light
3384 nuclei near the 3-3 resonance. *Nucl. Phys.*, B62:61–85, 1973.
- 3385 [118] D. H. Wright and M. H. Kelsey. The Geant4 Bertini Cascade. *Nucl. Instrum.*
3386 *Meth.*, A804:175–188, 2015.
- 3387 [119] C. S. Wu, E. Ambler, R. W. Hayward, D. D. Hoppes, and R. P. Hudson.
3388 Experimental test of parity conservation in beta decay. *Phys. Rev.*, 105:1413–
3389 1415, Feb 1957.
- 3390 [120] N Yahlali, L M P Fernandes, K Gonzlez, A N C Garcia, and A Soriano. Imaging
3391 with sipms in noble-gas detectors. *Journal of Instrumentation*, 8(01):C01003,
3392 2013.
- 3393 [121] T. Yanagida. Horizontal symmetry and masses of neutrinos. *Progress of Theo-*
3394 *retical Physics*, 64(3):1103–1105, sep 1980.